Department of Mechanical Engineering

Performance Enhancement of Inclined Solar Chimney Power Plant Using Underneath Air-Vents and Thermal Storage Medium

Wilson Phua Yuen Zheng

This thesis is presented for the Degree of

Master of Philosophy (Mechanical Engineering)

of

Curtin University

March 2018

DECLARATION

To the best of my knowledge and belief this thesis contains no material previously published by any other person except where due acknowledgment has been made.

This thesis contains no material which has been accepted for the award of any other degree or diploma in any university.

Signature: …….

Date: ……...

ACKNOWLEDGEMENTS

This research was funded by Ministry of Higher Education under the Fundamental Research Grant Scheme (FRGS) with Grant Reference Code: FRGS/1/2016/TK07/CURTIN/03/3. The author wishes to acknowledge the funding body for the support and opportunity to have earned advanced knowledge in this research. Acknowledgement also goes to Curtin University, Malaysia for supporting my study in this research through the Fee Waiver Scheme.

My sincere thanks goes to the Project Main Supervisor and Principal Investigator, Dr. Aja Ogboo Chikere. I also wish to extend my thanks to the Thesis Committee members, Dr. Wong Kiing Ing and Dr. Sukanta Roy who have contributed in their individual capacities to the success of this thesis completion. I also send my unalloyed appreciation to my parents Mr. Phua Mui Chiang and Mrs. Hii Hung Chuo for their moral support and encouragement in the course of my studies. Worth acknowledging are the supports of other staff members of Faculty of Engineering and Science most especially Dr. Law Ming Chiat, Office of Research and Development, and School of Graduate studies for their support and encouragement in accessing research facilities which contributed to the success of this research. I also wish to acknowledge the friendships of other Curtin University research students who share their ideas in research which has in one way or the other assisted me to pull through my study.

ABSTRACT

Solar chimney power plant (SCPP) is a solar thermal energy conversion system. The SCPP converts solar energy into thermal energy and indirectly to mechanical/electrical energy using air as the working fluid to drive a staged wind turbine connected to generator. Thus, the SCPP employs greenhouse, chimney and wind turbine technologies. At the collector (greenhouse), the absorber converts the solar radiation to thermal energy where the heated absorber in turn warms the adjacent air, thus induces buoyancy-driven flow. The kinetic energy in the buoyant air is harnessed and converted to mechanical/electrical energy using a turbine-generator. The main challenge of SCPP technology is the serial energy conversion process leading to low efficiency of the plant. The total efficiency of the SCPP is the product of the efficiencies of the three technologies of the plant. The solar collector has efficiency of over 20% but incurs high thermal losses rated at over 30%. The turbine has been rated the most efficient component of the SCPP at over 60% due to the shrouded location of the turbine. The chimney has the least efficiency which is due to the dependence of the performance on the height of the chimney. For 1000 m tall chimney, the efficiency is about 3%. To enhance the total performance of SCPP, the collector and chimney efficiency need to be improved. This research focus on improving the efficiency of the collector of inclined SCPP through the use of underneath air-vents. The study employed numerical method using a Computational Fluid Dynamics software, Star-CCM+. In the system modelling and simulation, radiation modelling principles were adopted under condition of steady state. The study showed that with the use of underneath air-vents, there was 4.25% and 4.64% reduction in convection and radiation heat transfer respectively from the collector cover to the ambient at 1000 W/m^2. It was also observed that the air mass flow rate was increased by 210% and consequently the power output of the plant improved by 60%. The study revealed that for a 100 m^2 inclined collector used in the study, 15 number of air-vents were required for optimum performance enhancement. Considering the effect of thermal loss through the absorber and the capacity of the absorber to act as heat storage medium, it was observed that an absorber thickness of 0.3 m was economical and effective for thermal storage in the inclined SCPP with 100 m^2 collector. The study also showed that the system without chimney could operate but with reduced efficiency as compared with the system incorporated with chimney.

TABLE OF CONTENTS

LIST OF FIGURES

LIST OF TABLES

NOMENCLATURE

Symbol	Description	Unit
A_{ap}	Absorber area	m^2
A_c	Cover area	m^2
A_{coll}	Collector area	m^2
$A_{air-channel}$	Area of the air flow channel	m^2
α	Thermal diffusivity	m^2/s
β	Tilt angle of the collector	°
β_λ	Extinction coefficient	N/A
$\beta'_{t,ap-air}$	Coefficient of volumetric expansion of thin film of air near the absorber	m^3/m^3°C
$\beta'_{t,air-c}$	Coefficient of volumetric expansion of thin film of air near the cover	m^3/m^3°C
C_p	Specific heat capacity of air	kJ/kg·K
cp_{ap-air}	Thin film air specific heat near the absorber	kJ/kg·K
cp_{air-c}	Thin film air specific heat near the cover	kJ/kg·K
E_{coll}	Input energy at solar collector	W
ε	Turbulent dissipation rate	m^2/s^3
ε_{ap}	Emittance of the absorber	N/A
ε_c	Emittance of the transparent cover	N/A
$\vec{F}$	External body force	N
g	Gravitational acceleration	m/s^2
G_k	Turbulent kinetic energy due to mean velocity gradient	J/kg
G_b	Turbulent kinetic energy due to buoyancy	J/kg
h	Convective Heat Transfer Coefficient	W/m^2·K
h_{cond-b}	Conduction heat transfer coefficient through the absorber's back	W/m^2·C
$h_{conv,air-c}$	Convective heat transfer coefficient from the collector's air to the cover	W/m^2·C
$h_{conv,ap-air}$	Convection heat transfer coefficient from the absorber to the collector's air	W/m^2·C

$h_{conv,c-air}$	Convective heat transfer coefficient from the cover to the collector's air	W/m^2·C
$h_{conv,c-amb}$	Convective heat transfer coefficient from the cover to the ambient	W/m^2·C
$h_{rad,ap-c}$	Radiation heat transfer coefficient from the absorber to cover	W/m^2·C
$h_{rad,c-sky}$	Radiation heat transfer coefficient from the cover to the sky	W/m^2·C
h_w	Heat loss coefficient by convection from the cover to the ambient due to wind effect	W/m^2·C
H_{ap-c}	Height between the absorber and the cover	m
H_{tot}	Total height of chimney	m
I	Solar radiation intensity	W/m^2
I_λ	Radiation Intensity at Wavelength, λ	W/m^2
$I_{b\lambda}$	Black Body Intensity at Wavelength, λ	W/m^2
$I_{pb\lambda}$	Particle Black Body Intensity	W/m^2
k	Turbulent Kinetic Energy	J/kg
$k_{a\lambda}$	Absorption coefficient at wavelength λ	m^{-1}
$k_{s\lambda}$	Scattering coefficient at wavelength λ	m^{-1}
$k_{pa\lambda}$	Particle absorption coefficient at wavelength λ	m^{-1}
$k_{ps\lambda}$	Particle scattering coefficient at wavelength λ	m^{-1}
$k_{t,air-c}$	Thermal conductivity of a thin film air near the cover	W/m·K
$k_{t,ap-air}$	Thermal conductivity of a thin film air near the absorber	W/m·K
$\dot{m}_{air}$	Mass flow rate of air	kg/s
μ	Dynamic Viscosity	kg/m·s
μ_{air-c}	Dynamic viscosity of the thin film air near the cover	kg/m·s
μ_{ap-air}	Dynamic viscosity of the thin film air near the absorber	kg/m·s
μ_t	Turbulent Viscosity	m^2/s
Nu_{air-c}	Nusselt number for the air near the cover	N/A
Nu_{ap-air}	Nusselt number for the air near the absorber	N/A
η_{ch}	Chimney efficiency	%
η_{coll}	Collector efficiency	%

η_{sys}	System efficiency	%
η_{turb}	Turbine efficiency	%
p	Pressure	Pa
p_0	Total Pressure at the Inlet	Pa
p_{gauge}	Gauge Pressure	Pa
$P_{air-tot}$	Air power	W
$P_{elec-out}$	Electrical power output	W
Δp_{tot}	Change in pressure between the ambient and the air in the SCPP	Pa
q	Heat Flux at the Surface of the Wall	W/m^2
$q_{air-conv}$	Convective heat transfer from the collector's air to the cover	J
$q_{ap-conv}$	Energy transfer by convection from the absorber	J
q_{ap-rad}	Energy transfer by radiation from the absorber	J
$q_{ap-cond}$	Energy transfer through the absorber to the back by conduction	J
$q_{c-conv-amb}$	Convective heat transfer from the cover to the ambient	J
$q_{c-rad-sky}$	Radiation heat transfer from the cover to the sky	J
q_{rad}	Radiative Heat Flux	W/m^2
q_u	Useful energy gain	J
Ra_{air-c}	Rayleigh number for the air near the cover	N/A
Ra_{ap-air}	Rayleigh number of the air near the absorber	N/A
S_{ap}	Energy absorbed by the absorber	W/m^2
S_c	Energy absorbed by the cover	W/m^2
S_k	User defined source term in turbulence equations	N/A
S_ε	User defined source term in turbulence equations	N/A
S_m	Source term in momentum equation	N/A
T	Temperature	K
T_∞	Reference Temperature	K
T_{air}	Temperature of collector's air	K
T_{ap}	Temperature of absorber	K
T_b	Temperature of absorber's back	K

T_c	Temperature of transparent cover	K
T_{amb}	Ambient temperature	K
T_{ref}	Operating temperature	K
T_{sky}	Sky temperature	K
T_s	Local solid temperature	K
T_W	Wall surface temperature	K
$T_{t,air-c}$	Temperature of the air near the cover	K
$T_{t,ap-air}$	Temperature of the air near the absorber	K
$\bar{\bar{\tau}}$	Stress tensor	Pa
ρ	Density	kg/m^3
ρ_{air-c}	The air densities for the air near the cover	kg/m^3
ρ_{amb}	Density of ambient air	kg/m^3
ρ_{ap-air}	Air density for the air near the absorber	kg/m^3
ρ_{air}	Density of collector's air	kg/m^3
$\vec{v}$	Air Velocity	m/s
Y_m	Fluctuating dilation	N/A
Ω	Solid angle in radiative heat transfer equation	°

N/A refers to dimensionless units.

Chapter 1
Introduction

1.1 Research Background

1.1.1 Global Energy Demand

Energy represents the capacity of a physical system or a body to perform work. Energy is essential for all types of activities in the world, considering both living organisms and non-living matter (Siraj 2012). Global advancements are strongly based on energy availability which could lead to technological advancement, career opportunities, economic development, food production, security, poverty reductions and so on (Siraj 2012, Al-Kayiem et al. 2016). According to Al-Kayiem et al. (2016), energy demand is dependent on five different factors which include wealth status of a nation, the statistics of weather and climate conditions throughout the year, human populations, the efficient consumption of energy resources, and the energy conversion technologies. The global energy demand has been greatly influenced by the global human population growth which was rated at 1.23 % per year for the years between 2000 and 2015 (World-Bank 2017). This growing energy demand can be attributed to the increased economic growth and advanced lifestyles of luxury among individuals as well as technological advancements. The growing energy demand of the globe has mainly be mitigated by the use of non-renewable energy resources such as fossil fuels (oil, gas and coal) and nuclear energy. The use of these non-renewable energy resources contribute to environmental degradations such as acid rain, greenhouse gas emission, global warming and the depletion of natural resources.

The continuous growing demand of energy in the world can be seen from the primary energy consumption per year. Table 1.1 shows global energy consumption in Millions Tons of Oil Equivalent (MTOE) considering the primary energy resources for years 2010 to 2016 (BP 2011, 2012, 2013, 2014, 2015, 2016, 2017). A representation of the individual energy resource usage of Table 1.1 in percentage to the total energy consumption is presented in Table 1.2. In 2016, fossil fuel based energy consumed globally reached 11,354.30 MTOE out of the total of 13276.30 MTOE consumed in same year. This represents about 86% of the global energy supply. The energy demand growth is projected by Council (2013) to be double of the 2010 consumption by year 2050.

Table 1.1: World's Primary Energy Usage (Millions Tons of Oil Equivalent) (BP 2011, 2012, 2013, 2014, 2015, 2016, 2017)

Year	Primary Energy Mix (Millions Tons of Oil Equivalent - MTOE)							
	Oil	Natural Gas	Coal	Fossil Fuel	Nuclear Energy	Hydro-Power	Renewable Energy	Total
2010	4031.90	2843.10	3532.00	10407.00	626.30	778.90	165.50	11977.70
2011	4081.40	2914.20	3628.80	10624.40	600.40	794.70	205.60	12225.10
2012	4138.90	2986.30	3723.70	10848.90	559.90	833.60	240.80	12483.20
2013	4179.10	3052.80	3867.00	11098.90	563.70	861.60	283.00	12807.20
2014	4251.60	3081.50	3911.20	11244.30	575.50	884.30	316.60	13020.70
2015	4331.30	3135.20	3839.90	11306.40	583.10	892.90	364.90	13147.30
2016	4418.20	3204.10	3732.00	11354.30	592.10	910.30	419.60	13276.30

Table 1.2: Percentage Contribution by Various Energy Sources (BP 2011, 2012, 2013, 2014, 2015, 2016, 2017)

Year	Percentage Contribution by Various Energy Sources (%)							
	Oil	Natural Gas	Coal	Fossil Fuel	Nuclear Energy	Hydro-Power	Renewable Energy	Total
2010	33.66	23.74	29.49	86.89	5.23	6.50	1.38	100.00
2011	33.39	23.84	29.68	86.91	4.91	6.50	1.68	100.00
2012	33.16	23.92	29.83	86.91	4.49	6.68	1.93	100.00
2013	32.63	23.84	30.19	86.66	4.40	6.73	2.21	100.00
2014	32.65	23.67	30.04	86.36	4.42	6.79	2.43	100.00
2015	32.94	23.85	29.21	86.00	4.44	6.79	2.78	100.00
2016	33.28	24.13	28.11	85.52	4.46	6.86	3.16	100.00

This increasing demand of energy if depends only on fossil will be a great burden on the environment, thus requires a shift to more environmental friendly energy resources.

1.1.2 Development, Fossil Fuel Energy and the Environment

In a report by UNEP (2012), Asia-Pacific region represented the world's fastest growing economies. However, as the economy in this region continues to grow, the vast majority of the energy demand is mostly supplied from fossil energy resources. For example, Malaysia

consumes over 90% fossil fuel to sustain her economic development (BP 2016, 2017). According to ADB (2014), it is expected that the world's energy requirement will increase by one third of 2010 consumption by 2035, of which Asian countries such as China, India, and other developing regions will consume about 60 % of the global total.

Fossil fuels (oil, natural gas and coal) are usually combusted for energy and power generation in plants. The combustion of the fuels produce carbon dioxide which is considered the dominant/primary greenhouse gas emitted to the atmosphere. According to IPCC (2014), 65 % of the carbon dioxide released in the atmosphere is due to the burning of fossil fuels and other industrial processes. In addition to that, about 25 % (about 17% of globally emitted greenhouse gas) of the greenhouse gas emitted globally to the environment come from electrical power generation plants (IPCC 2014). The use of fossil fuels as the major primary source of energy to drive a nation's economy have the consequences of environmental (air and water) pollutions. The global dependent on fossil fuels as source of energy has been attributed to the increasing effect of global warming due to the large emission of greenhouse gases to the atmosphere. The negative effects of fossil fuel usage on the environment have received considerable critical attention in the topics like climate changes, sea level rise, heat waves and droughts. Awareness regarding the need to limit the overwhelming dependence on fossil fuels has been raised because of the fact that the use of fossil fuels poses a large threat to the environment. The use of fossil fuel threatens water security due to the illegal disposal of waste oils to the water bodies thus causing water pollution (Rafindadi et al. 2014). It was reported by ADB (2013) that Asia-Pacific region faces increased threat to water security and affects sustainable livelihoods. Water pollution also has negative consequences on the marine biodiversity.

Moreover, there is an urgent need to address the problems with the depletion of the fossil fuels resources. In light of the recent growing energy crisis and the widespread consumption of fossil fuels, the limited supply of these non-renewable energy resources has become a serious concern (Khan et al. 2016). Höök et al. (2010) developed theories on the formation of conventional energy resources and they predicted that the supply of fossil fuels would run out by the year 2100. Therefore, it is important to preserve the fossil fuel resources like oil for other sustainable industrial purposes and develop alternate energy generation processes that are more environmental friendly.

1.1.3 Solar Energy Based Power Generating Systems

Renewable energy has long been the interest quest in the field of electricity power generation. Considering the various renewable sources of energy, solar energy is considered the Earth's predominant source of energy but time and location dependent. The radiant heat and light coming from the Sun can be converted directly or indirectly into different forms of energy. However, it is known that the solar power is being disadvantaged by the low efficiencies of the energy conversion systems (Dennis 2006). One of the drawbacks of solar power systems is the initial investment cost which restrains the masses from investing into the energy system. The economic disadvantage is associated with the increased costs of the installation of solar energy technologies while producing only a relatively small amount of energy compared to other conventional energy system, thus characterized of low efficiency. As a result, the solar power still remains considerably a high cost energy option when compared to conventional energy sources such as the fossil fuels, nuclear and hydropower.

In recent years, there has been an increasing interest in utilizing the solar energy for electricity generation and various reviews have stated that the advantages of the solar technologies outweigh their disadvantages (Al-Kayiem et al. 2016, Kannan et al. 2016, Khan et al. 2016). For examples, some of the benefits of solar energy include free and abundant supply, and its environmentally friendly nature (Al-Kayiem et al. 2016). Solar energy also is inexhaustible in supply which has recorded 1.8×10^{14} kW/hr interception on the earth surface out of the total 3.8×10^{23} kW/hr emitted by the Sun (Panwar et al. 2011). The unlimited source of solar energy makes it a promising option to provide continuous supply of electricity to meet the global energy demand (Kannan et al. 2016). Asian countries receive a reasonably high amount of solar radiation throughout the year. Even though the Asian countries receive higher solar radiation from the Sun with longer sunshine duration as compared to other temperate countries, solar energy is yet to be effectively harnessed in this region.

The existing body of research on solar energy also suggests that this renewable energy has become more socially acceptable. The reason behind the public acceptance of the solar power technologies is to combat environmental degradation caused by the massive burning of the fossil fuels (Khan et al. 2016). Solar energy is said to be the cleanest form of energy that can be used to generate electricity, without causing harm to the environment. According to Khan et al. (2016), the construction of solar energy based power generating plants could prove to be beneficial in the long term, as initial investments on the solar power plants would serve to

provide sustainable energy future for both urban and technologically less developed areas. Extensive researches have been carried out to improve the cost effectiveness of solar technologies for electricity production to allow the possibilities for the development of commercial solar power generation plants in the near future. On top of that, as the radiation intensity varies with locations, countries which receive a reasonable amount of solar radiation would not have issues with the reliability of energy supply (Khan et al. 2016).

Solar energy can be converted directly and indirectly to electrical power using different energy conversion systems. Example of well-known technology for the direct conversion of solar energy into electrical energy is the use of the photovoltaic cells. The solar thermal energy conversion systems are used for indirect generation of electricity from the solar energy. The solar thermal systems can be classified as either low temperatures or high temperatures solar thermal systems. High temperatures solar thermal systems include parabolic trough solar collectors, solar power tower (heliostat), parabolic reflector, linear Fresnel concentrators, solar oven, dish concentrator etc. (Energy 2015). Low temperatures solar thermal systems are mainly flat-plate solar collectors which the Solar Chimney Power Plant finds its origin.

Solar chimney power plant (SCPP) is a low temperature solar thermal system which combines three technologies (greenhouse technology, chimney technology and wind turbine technology) in a serial conversion of solar energy to electrical energy. The SCPP energy conversion processes include the conversion of solar energy into thermal energy at the collector absorber, conversion of the thermal energy at the absorber to kinetic energy in the buoyant air, conversion of the kinetic energy in the air into mechanical work using the turbine and conversion of the mechanical work into electrical power through the rotation of a connected shaft from the turbine to the generator.

1.1.4 Solar Chimney Power Plant

Solar chimney power plant (SCPP) as illustrated in Figure 1.1. has attracted several researches in the quest to find a commercial procedure of generating electricity. The interest in SCPP can be attributed to the maturity of the three technologies upon which the system operates. The technologies include greenhouse technology, chimney technology and turbine technology. The system operates at low temperature working fluid and can be maintained while in operation. The greenhouse is an open-solar-air collector design which has transparent cover raised some distance above the ground. The ground represents the absorber while the transparent cover

allows the penetration of the sun into the collector as well as prevents the thermal energy generated in the greenhouse from leaving. The collector absorbs both direct and diffused solar radiation and utilizes them to generate heat in the greenhouse. At the collector (greenhouse), the absorber converts the energy from the sun to thermal energy where the heated absorber in turns warms up the adjacent air, thus creates buoyancy driven flow. The kinetic energy in the buoyant air is harnessed and converted to mechanical/electrical energy using turbine-generator. The above described energy conversion process shows the serial conversion process which occurs in the SCPP, thus leading to low efficiency of the plant. The energy conversions of the SCPP can be categorized into four different types (Al-Kayiem et al. 2016). For instance, the plant's absorber material as shown in Figure 1.2 is utilized to convert the solar radiant energy into thermal energy. The heated air in the solar collector gains kinetic energy and moves toward the chimney to exhaust to the atmosphere as shown in Figure 1.3. Through the use of a turbine as illustrated in Figure 1.4 which consists of a wind rotor, the kinetic energy in the working fluid is converted into mechanical energy, in the form of rotational energy. The turbine is connected to an electric generator, where the conversion of mechanical energy into electrical energy takes place.

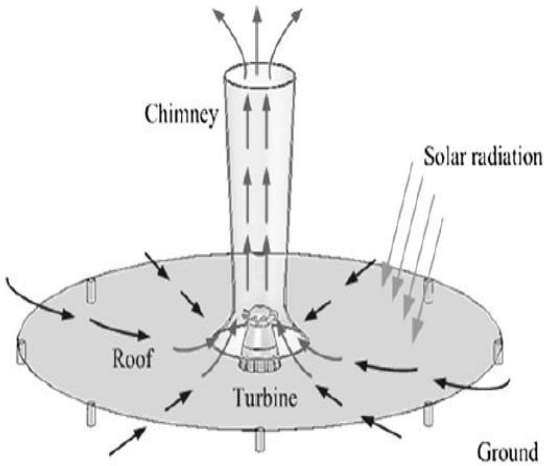

Figure 1.1: Schematic of Solar Chimney Power Plant (SCPP) by (Koonsrisuk et al. 2013)

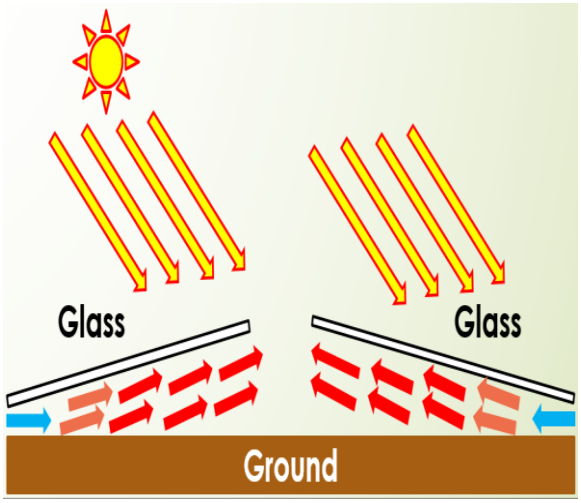

Figure 1.2: The collector component of SCPP which consists of transparent cover roof and ground absorber

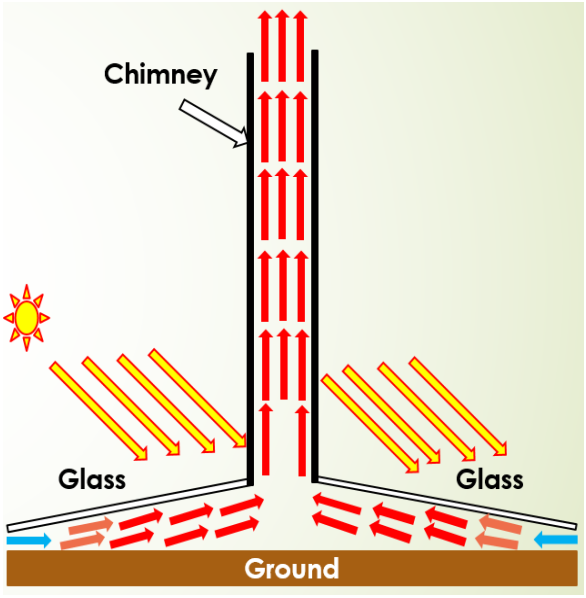

Figure 1.3: The chimney component of the SCPP

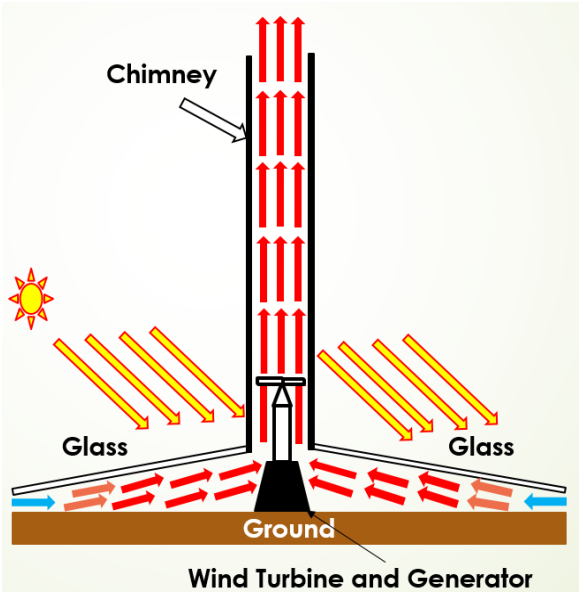

Figure 1.4: Installation of Wind Turbine and Generator at the Chimney Base

1.1.5 Solar Chimney Power Plant Challenges

The main challenge of SCPP technology is the serial energy conversion process leading to low efficiency of the plant. The total efficiency of the SCPP is the product of the efficiencies of the three technologies of the plant. The solar collector has efficiency of about 20% and characterized of high thermal losses of over 30%. The turbine has been rated the most effective and efficient component of the SCPP due to the location of the turbine which lead to over 60% energy conversion efficiency. The chimney has the least efficiency which is due to the dependence of the performance on the height of the chimney where 1000 m tall chimney has efficiency of about 3%. Most literatures have suggested that increasing the SCPP size will increase the plant's efficiency, however increasing the collector size also increases the thermal losses while increasing the chimney height increases the investment cost and engineering challenge of the chimney construction.

Overall, the SCPP suffers a drawback as a result of low efficiency, which is less than 2%. The major contributors to the poor efficiency of the plant are the collector high thermal losses and the chimney low efficiency. The difference in the densities of the ambient air and the system air creates the pressure difference which promotes the stack effect in the chimney and enhances the exhausting rate of the buoyant air to the ambient. When the air temperature exceeds that of

the transparent cover, it losses heat to the transparent cover and consequently to the atmosphere thus affecting the pressure in the system (Haaf et al. 1983). Moreover, the solar collector's efficiency is also affected by the climatic condition of the geographical location where the SCPP is being installed. Haaf et al. (1983) showed that higher ambient temperature leads to reduced output/performance of the SCPP considering the driving force is a function of difference in temperature between the system's air and the ambient/surrounding air temperatures.

In the design of the SCPP, the open-solar-air collector has fixed inlet height which allows the system to operate at low and high solar radiation intensities. During the hours of high solar radiation intensity, the system experiences excessive thermal losses. This applies to the inclined solar chimney power plant. In the inclined solar chimney, this situation can be mitigated to enhance power output by the plant. The SCPP also faces the challenge of little or no power generation in the night due to lack of energy supply from the sun or alternative sources. The energy generated by the SCPP fluctuates over the day and varies with time of the year due to the position of the sun at various time and season. Conventional SCPP requires a large expanse of flat land with no competing values. Furthermore, the mass flow rate of air in the SCPP is limited to the collector size and the stack effect of the chimney.

1.2 Research Gaps and Project Novelty

Most researchers in the field of SCPP have determined that the plant's performance can be enhanced through increased air mass flow rate in the system. However, the idea for combined heat and mass transfer for improved buoyancy and reduced thermal loss has not been developed. Researchers have only attempted to show that an increase in the air mass flow rate at the collector's outlet causes the plant's performance to improve. Most studies have only focused on optimizing the geometrical parameters and the total size of the SCPP to achieve a higher air mass flow rate. Manipulating and optimizing the plant geometrical dimensions and sizes were common objectives published in most papers which had consequences of high investment cost and increased thermal losses. However, an attempt to naturally induce higher amount of air-stream into the system has not been investigated. Air-vents at the collector's absorber are proposed in this study to induce additional air-stream into the system, thus, increasing the mass flow rate of the working fluid in the greenhouse with respect to the increase in the temperature of the greenhouse. The influx of lower temperature air from the air vents

reduces the temperature of the system air, which consequently reduces the radiation heat transfer from the absorber to the cover and from the system's air to the cover. Combining the heat transfer effect and the mass flow rate increase, the air power to the turbine increases which is expected to improve the power output from the turbine and the total performance of the plant.

To date, there has been no investigation on the effects of air-vents on the solar collector's performance. The new design of the inclined SCPP with underneath air-vents has not been developed thus this study. On top of that, much uncertainty still exists about the possibilities of increasing the thermal storage of SCPP by manipulating the concrete absorber's thickness as the increase in thickness increases the cost of the collector while low absorber thickness leads to thermal losses through the collector back. To take advantage of the absorber and reduce thermal losses through the back, the optimum sizes for the collector absorber need to be determined. The use of inclined collector has the advantage of acting as chimney and collector but has not been investigated if it can eliminate the need for additional chimney thus this investigation to determine the plant operation without chimney.

1.3 Research Questions

The study is designed to answer the following research questions:

No.	Questions	Rationale
1.	How can the heat losses associated to the collector be reduced in order to improve the plant's performance?	The collector incurs over 30% thermal loss which degrades the collector efficiency
2.	Can the system's air mass flow rate be increased under fixed collector inlet without enlarging the size of the collector and the chimney?	At fixed collector inlet height, the greenhouse gets saturated at about 600 W/m^2, thus increase thermal losses.
3.	Considering a specific plant's size, is there a way to improve the turbine's power output?	The power output of the turbine is dependent on the power available in the buoyant air.
4.	What thickness of the collector absorber offers optimum thermal storage for improved power generation at night?	The SCPP operation is limited to the availability of stored energy in the absorber for night operations.

5.	Can the SCPP operate effective with the removal of the chimney and what design meets this requirement?	The chimney enhances buoyancy in the SCPP and has been considered to consume about 50% of the plant initial cost.

1.4 Research Aim and Objectives

The main aim of this research is to study the possible enhancement of the performance of inclined solar chimney power plant using underneath air-vents. The study also aims at developing a prototype model that could be employed to prove the concept of the system for electrical power generation. The air-vents are expected to improve the performance of the solar collector component by reducing the collector thermal losses and enhance air mass flow rate as well as the power output of the plant. The influx of lower temperature air into the system through the underneath air-vents can improve heat removal factor from the absorber, thus reduces the absorber temperature. This reduces the re-radiation from the absorber to the transparent cover, and it also reduces the heat transfer from the collector's air to the transparent cover. The reduction in the re-radiation and convective heat transfer from the absorber and air respectively to the cover reduces the cover temperatures and thermal losses from the cover to the ambient. The inclusion of underneath air-vents at the collector's absorber is then expected to increase the air mass flow rate and air power available to the turbine, thus increase the power output.

Considering the lack of operation of the system in the night, this research also numerically investigates the concrete absorber thickness suitable for thermal storage and the effects of including water tubes at the absorber on the performance of the collector of the inclined solar chimney power plant. The use of concrete as the collector absorber will reduce the re-radiation heat transfer from the absorber to the transparent cover thereby storing the excess thermal energy. Besides, the thickness of the absorber will increase the thermal storage in the collector. The use of thermal storage provides continuous power generation even in the absence of solar energy. Addition of water tubes will also be tested on thermal storage and performance enhancement. Another objective of the research is to numerically investigate the operation of the inclined solar chimney power plant without chimney for 100 m^2 collector, as the collector tilt angle creates height advantage for the buoyancy driven flow of the air.

To achieve the aims of this research, the following research objectives will be achieved as summarized below:

1. Numerically model the new design of inclined SCPP using Star CCM+ to evaluate the fluid flow and thermal fields in the system for different designs (with or without air vents).
2. To determine the number of air vents required for optimum performance enhancement of the collector and reduce thermal losses for a 100 m^2 collector.
3. Numerically investigate the absorber thickness suitable for thermal storage and the effects of including water tubes at the absorber on the performance of the collector of the inclined SCPP
4. Numerically investigate the operation of the inclined solar chimney power plant without chimney for 100 m^2 collector and a case with 20 m high chimney.

1.5 Significance of the Solar Chimney Power Plant Project

Although the overall efficiency of the Solar Chimney Power Plant (SCPP) is low, the issue with the total efficiency is still well tolerated with the plant's low costs of construction, operation and maintenance (Schlaich 1995). When the SCPP is compared to other types of solar power concentrating systems, the SCPP can use both the diffused and the direct solar radiation (Schlaich 1995). In the scenario where the sky is frequently being overcast, the SCPP can still operate under the effect of the diffused solar radiation. Furthermore, the SCPP relies on the collector's absorber for the absorption of the solar radiant energy and this absorber is capable to store the excess thermal energy without having to pay any extra costs. During the day, when the solar energy is available, some of the radiated energy would be stored in the absorber and the heat energy release would take place during the night. The SCPP is also a reliable system for the generation of electricity as it is not liable to fail or malfunction easily, considering that the only mechanical moving parts are the turbine and the generator components (Schlaich 1995). The building materials can also be sourced locally without having the need to purchase high technologies components.

The SCPP research project has various commercial and industrial values, too. As an example, the SCPP is a competitive and attractive technology which utilizes the inexhaustible source of solar energy. The operating principle of the SCPP system is relatively simple and the cost of maintenance is low. This project helps to meet the energy requirements of people in the

mountainous regions of Malaysia. The results of this study can be employed in the design of inclined SCPP for parks and mountainous regions to meet the energy of the people. It also improves the power generation from renewable energy that can be connected to the grid. Furthermore, this research makes a significant contribution to knowledge and it has scientific theoretical context. This study introduces a new procedure of mass flow rate enhancement by the use of air vents at the collector, thus enhance the power output. The novel theories or knowledge include a new idea for combined heat and mass transfer for improved buoyancy and reduced thermal loss. The project presents a new design of solar chimney power plant. Moreover, it involves the design of a low cost inclined SCPP for enhanced power output. The use of the collector absorber and water tubes as thermal storage materials will also enhance the duration of night operation of the plant.

1.6 Summary

Solar Chimney Power Plant (SCPP) converts solar energy into thermal energy and indirectly to mechanical and electrical energy. The SCPP has low efficiency and many studies have been carried out both experimentally and numerically to enhance the performance of the SCPP. To date, there has been no investigation on the effects of air-vents on the SCPP performance. The current research aims to develop a new design of an inclined SCPP with underneath air-vents. This study also identifies the possibility of enhancing the collector's thermal storage through the use of the concrete absorber material and water storage medium to improve the power generation at night. Novel designs of inclined SCPP without additional chimney component are introduced in this project as the inclination of the collector creates a height advantage for the buoyancy driven flow of the air.

Chapter 2
Literature Review

2.1 Introduction to the Literature Review

The historic progress and the timeline of the Solar Chimney Power Plant (SCPP) are presented in this chapter. A review of the SCPP numerical model is provided. The review critically examines the methods with respect to the boundary conditions and the modelling procedures employed in the various papers selected from major researchers in this field. In this chapter, various enhancement models of the SCPP are introduced.

2.2 Solar Chimney Power Plant Timeline

The principle of stack effect which refers to the upward trajectory of air along the chimney tower had already been used for the past centuries. The first system which used the concept of the chimney effect was idealized and developed by a well-known Italian polymath, known as Leonardo da Vinci (1452 – 1519). In the system, a fireplace was located at the base of a chimney which created the temperature differences between the outside air and the indoor air. The lower pressure of the hot air then caused the air to rise through the chimney, which subsequently resulted in the rotation of a windmill installed above the fireplace (Fluri 2008, Calder 1970, Pastohr et al. 2004). The windmill was also connected to a barbeque spit roaster.

In 1903, a colonel in the Spanish army, who was named as Isidoro Cabanyes, made a proposal regarding the working concept of a solar chimney power plant in a magazine (Lorenzo 2002). The proposal of the project was termed as a solar engine project and it showed an assembly between an air heater and a house which consisted of a chimney. In the conceptual design, blades of propellers were found in the interior of the house which served to harness the energy in the hot rising air for the purpose of electricity production (Lorenzo 2002, dos Santos Bernardes 2010, Cabanyes 1903). In 1926, an engineer known as Prof. Bernard Dubos suggested an idea for the development of a solar chimney on a mountain slope. The design involved a solar chimney being supported on a slope of a high mountain.

Prof. Bernard Dubos' ideas of the power plant were then published by a German author, Hanns Gunther, in 1931 (dos Santos Bernardes 2010, Zhou et al. 2010, Günther 2012). Hanns Gunther evaluated the proposed solar chimney design by Prof. Bernard Dubos and a statement was

made in which the air velocity would reach a peak value of 50 m/s in the chimney. The kinetic energy of the upward movement of air particles through the chimney could be used to rotate wind turbines. Hanns Gunther also developed an experimental model based on Prof. Bernard Dubos' proposed conceptual design. In the experimental set-up, a thin flat sheet was used to represent Sahara Desert whereas solar thermal energy was modelled by using a spirit lamp that produced an open flame.

In 1956, Ridley invented a design which combined two solar chimneys into one single assembly (Ridley 1956). A patent was granted by the Great Britain Patent to Ridley. In the design, the heat source to the wall of the first solar chimney was obtained from the hot air generated in the greenhouse collector. A turbine was staged at the first chimney's base in which cold air would be extracted from a tunnel which was attached to the second solar chimney. The cold air was then supplied to the turbine. The temperature difference caused a continuous updraft of air which allowed an uninterrupted generation of power from the solar heat. Another patent was also granted to the design of Nazare in 1964, in which the design involved a divergent solar updraft tower (Nazare 1964). The chimney employed a diffuser-shaped tower to induce the updraft wind and to focus the wind energy to the throat of the chimney.

Despite having a complete information about the working principles of a solar chimney, it appeared that the concept did not receive much attention up to the 1970s. The reason behind this was due to the discovery of oil which provided a new source of fuel. Consequently, this was followed by a rapid economic growth in the oil production sector. However, the oil boom lasted for a short period before major industrial countries of the world started facing the oil crisis in 1973. The shortages of the oil resources prompted the need to shift the primary energy supply from fossil fuels to renewable energy resources (Al-Kayiem et al. 2016). The oil crisis had led to a renewed interest in utilizing the existing renewable energy technologies, whereby solar chimney power plant was one of the systems which attracted huge attention among researchers. One of the significant and notable advancements to the solar chimney system ever since the oil crisis in 1973 was the patents granted to Lucier's design between the years 1975 and 1981 (Lucier 1978, 1981).

In 1978, Prof Schlaich presented the technologies of the solar chimney power plants (SCPP) at a conference (Pasumarthi et al. 1998). In 1981, the conceptual design of the SCPP was proposed by Schlaich Bergermann Partner structural engineering firm and in 1982, a pilot plant was constructed in Manzanares, Spain. The pilot plant in Manzanares operated for a total

duration of 7 years from 1982 until 1989 (Schlaich 1995). The principles of the SCPP technology was published by (Haaf et al. 1983). The preliminary test results from the Manzanares power plant were reported by Haaf (1984) and it was proven that the SCPP concept was technically viable for commercial electrical power generation using the energy from the sun.

The experimental SCPP prototype in Manzanares produced a peak power output of 50 kW (Schlaich 1995). A vertical 195 m tall chimney tower was constructed at the center of the solar collector and the diameter of the chimney was 10 m (Schlaich 1995, Haaf 1984). The greenhouse collector consisted of a transparent roof with a diameter of 240 m and the ground which performed as the absorber. The height of the transparent cover above the ground was 2 m, which allowed for an accessible entrance to the turbine located at the chimney's base. This permitted the maintenance of the wind turbine. The purpose of the design and the development of the Manzanares SCPP prototype was to validate, through the use of experimental measurements, the performance determined from theoretical calculations (Schlaich 1995). In addition to that, the effect of the installation of different components on the SCPP's performance under real operating conditions was determined (Schlaich 1995).

The heated air which leaved through the chimney tower was sourced from the solar collector. According to Schlaich (1995), the height of the transparent cover was designed to increase adjacent to the base of the chimney, which reduced the friction losses during the flow of air into the central updraft tower. It was also stated by Schlaich (1995) that the transparent cover had different opacity properties towards the radiation spectrum. The transparent cover was able to transmit short wavelength of the radiation bands of the Sun while it retained the long wavelength components from the heated ground. Moreover, accumulation of dust and sand particles on the roof of the solar collector was a common occurrence which lowered the plant's efficiency. The SCPP prototype in Manzanares relied on infrequent rainstorms to remove the dust from the collector's transparent cover roof (Schlaich 1995).

The chimney tower played an important role as the plant's heat engine. Conventionally, the chimney was a pressure tube which was usually installed at the center of the solar collector to create stack effect and enhance buoyancy to the hot air. The chimney component in the Manzanares SCPP prototype had an ideal surface area to volume ratio which caused low friction losses on the air flow (Schlaich 1995). The chimney's efficiency was only dependent on its height and the ambient air temperature at ground level, and the efficiency was not

determined by the increase in temperature of the air inside the solar collector (Schlaich 1995). Hence, it was reported by Schlaich (1995) that the chimney in Manzanares could utilize the small increase in air temperature which was generated by the heat stored in the ground at night.

2.3 Computational Fluid Dynamics Modelling of the Solar Chimney Power Plant

Computational Fluid Dynamics (CFD) is one of the most commonly used methods of performing numerical simulations of fluid flows and thermal fields in the SCPP. Pastohr et al. (2004) were among first researchers to model the SCPP numerically through the combination of the main components of the power plant. These components included the solar collector, chimney, and the ground absorber, shown three dimensionally in Figure 2.1. To reduce the computation time, two dimensional axisymmetric model of the SCPP was used, as shown in Figure 2.2.

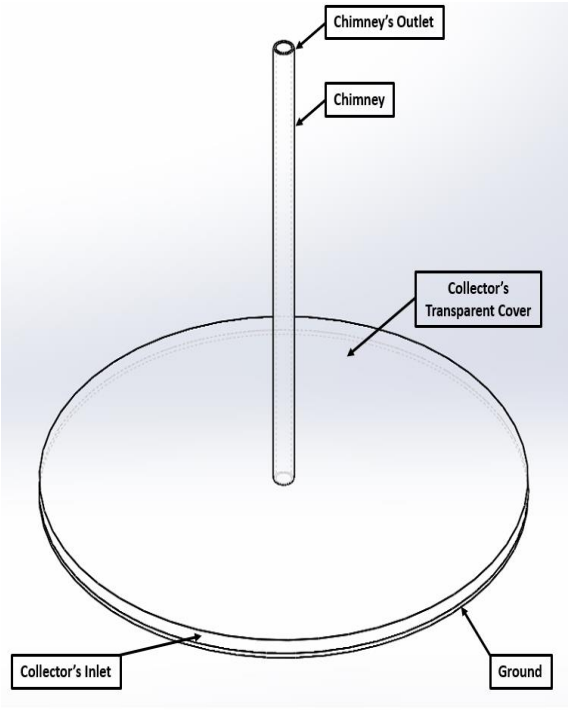

Figure 2.1: Three Dimensional Schematic of the Solar Chimney Power Plant

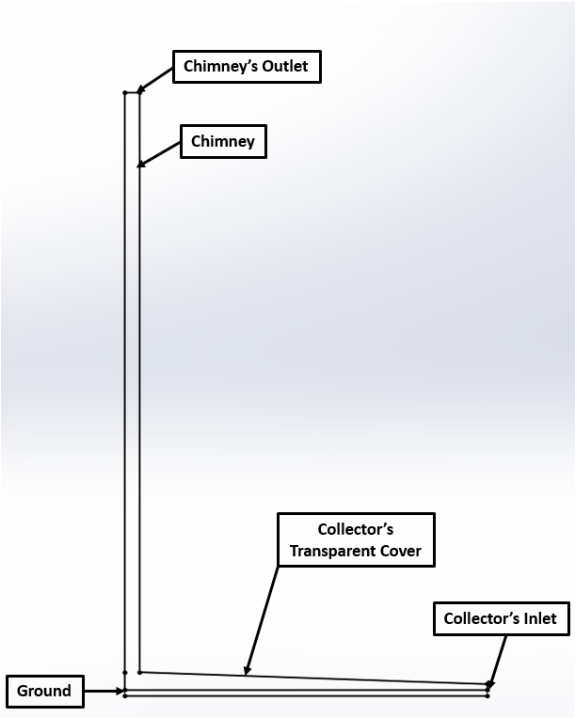

Figure 2.2: Two Dimensional Axisymmetric Model of the SCPP

The physical model of the SCPP was adapted to the structural dimensions of the prototype in Manzanares, Spain. The solar chimney had a radius of 5 m and the height of the chimney was 195 m. The radius of the collector was 122 m, with inlet and outlet height of 2 m and 6 m,

respectively. The results obtained from the CFD model were compared to those of the experimental results of Manzanares SCPP by Haaf (1984).

CFD simulation software package was used to solve the conservation of momentum equation, mass continuity equation, conservation of energy equation and turbulence equations. In the SCPP, dimensionless Rayleigh number was used to determine whether the air flow was laminar or turbulent. For instance, the transition from laminar to turbulent took place when the Rayleigh number was approximately 10^9. It was determined that the Rayleigh number of the flow inside the SCPP exceeded 10^{10}, indicating that the flow was turbulent (Xu et al. 2011, Ming et al. 2013, Pastohr et al. 2004).

The following section focus on the validity of the various numerical modelling approaches employed in the modelling and simulation of the flow and thermal field of SCPP. It reviews the various assumptions used and the boundary conditions for different CFD models. Furthermore, the review points out on the reliability of each of the numerical modelling approaches and possible flaws.

2.4 Various Numerical Modelling Approaches in SCPP

Three numerical modelling procedures were often used in the simulation of the SCPP system. The first procedure was to define a constant heat flux across the surface of the ground. This method was initially adopted by (Pastohr et al. 2004) and was later widely used in the computational studies by (Kasaeian et al. 2017, Zou et al. 2017, Zhou et al. 2017, Shirvan et al. 2017, Mehrpooya et al. 2016, Ghorbani et al. 2015, Rabehi et al. 2017, Hanna et al. 2016).

The second modelling procedure was to define the incident radiation flux by representing a thin layer below the ground's boundary as a volume heat source. Koonsrisuk et al. (2007) originally suggested the use of this procedure to model the incoming solar radiation. It was later found that the use of this method among researchers was uncommon. This method was applied in the SCPP numerical studies by Xu et al. (2011) and Hu et al. (2017). There was a major reliability issue with the use of the second modelling procedure. For instance, Huang et al. (2017) claimed that the collector's working fluid was determined to be higher than the absorber's temperature, which was physically incorrect.

The third modelling procedure involved the use of radiation modelling principle. In this approach, the radiation effect of the Sun which was introduced into the computational domain

was calculated by a solar load model. Within the solar load model, the ray tracing approach was used to apply the solar loads as the primary source of heat in the governing energy equations. The third radiation modelling principle was first introduced by Guo et al. (2014) in which they claimed that the approach produced reliable results as the radiation effects between the walls of the SCPP were considered. The use of the third modelling approach was widely accepted by researchers and was adopted in recent computational studies conducted by (Huang et al. 2017, Gholamalizadeh et al. 2017, Wang et al. 2017, Gholamalizadeh et al. 2016, Guo, Li, et al. 2016, Gholamalizadeh et al. 2014).

Furthermore, when a numerical modelling approach of the SCPP had been decided, specific assumptions were accounted for. Assumption of ignoring the influence of surrounding winds was usually applied to simplify the physical model of the SCPP. Besides, it was common for researchers to estimate the convective heat transfer coefficients specified at the transparent cover or the absorber's boundary through the use of established empirical equations. This section provides a detailed review on the validity and the reliability of the three numerical modelling procedures adopted in the SCPP simulation studies. This section also reviews the different assumptions and boundary conditions applied in the SCPP numerical models.

2.4.1 Numerical Modelling Approach 1: Defining Solar Radiation as the Boundary Condition

The first modelling approach of the SCPP was based on the specification of heat flux magnitude on the ground's boundary or the transparent cover's surface, as shown schematically in Figure 2.3. The simplicity of this method justified its widespread application among researchers in this field. Kasaeian et al. (2017) employed the first modelling procedure to investigate the influence of several turbine blades designs on the SCPP performance. The geometrical dimensions of the pilot SCPP in Manzanares were remodeled for validation purpose. Heat flux magnitude of 1000 W/m^2 was specified on the ground's boundary. An assumption was made by Kasaeian et al. (2017) in which the collector's glass cover was subjected to convection heat transfer. However, they did not report the value of the convective heat transfer coefficient used in their study. Kasaeian et al. (2017)'s model resulted in 13 m/s upwind velocity while the experimental results of Haaf (1984) reported 15 m/s upwind velocity whereby the error percentage was 13 %. Furthermore, Kasaeian et al. (2017)'s model resulted in 18.8 °C collector's air temperature rise at 1000 W/m^2 while Haaf (1984) reported a temperature increase of 20 °C, thereby leading to 6 % error percentage. It was also determined that the error

percentage was 48 % when the comparison was made between the experimental power output and the power output calculated from the numerical model. These results showed that there was an over prediction of the thermal loss occurring from the collector's glass cover to the ambient, which explained the lower upwind velocity and collector's air temperature rise in Kasaeian et al. (2017)'s study.

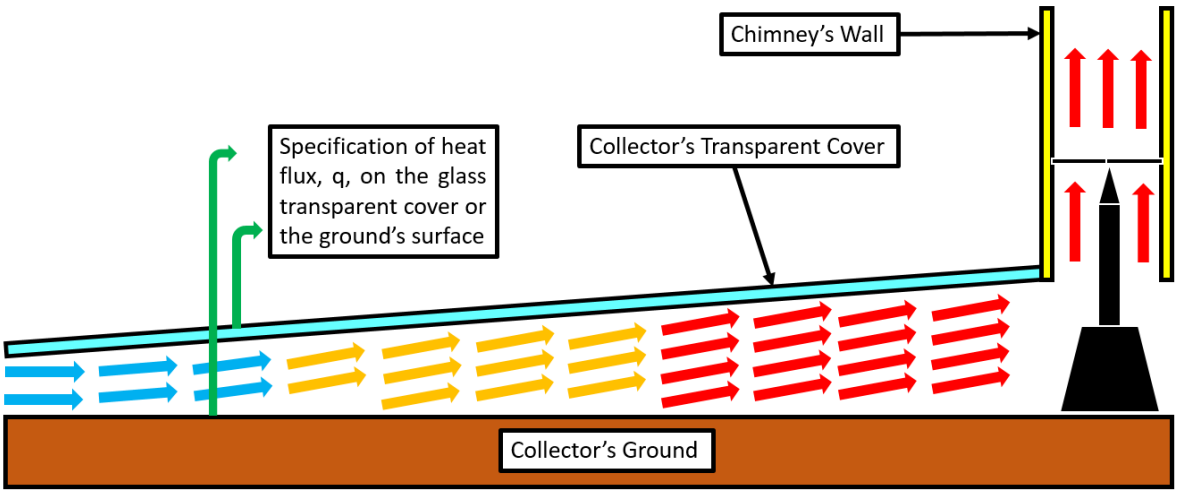

Figure 2.3: Schematic Representation of the First Modelling Approach

Zou et al. (2017) adopted the first modelling approach in which the solar irradiation was defined as a constant heat flux across the ground absorber's surface. Moreover, the influence of atmospheric wind was taken into consideration when modelling the solar collector. Convective heat transfer boundary condition was also applied at the collector's glass cover, where the convection heat transfer coefficient was calculated using an empirical equation developed by Zou et al. (2015). Based on the results obtained through validation, the error percentage between the numerical model by Zou et al. (2017) and the experimental pilot SCPP in Manzanares by Haaf (1984) was found to increase considerably with higher solar radiation intensities. This suggested that when empirical equation was used to predict the convective heat transfer coefficient at the glass cover, the thermal loss from the roof to the ambient was overestimated, considering higher solar irradiation.

Zhou et al. (2017) applied similar methodology in the modelling of the SCPP, in which the source of heat energy from the Sun was defined as a heat flux boundary condition at the absorber. The heat flux was specified as 247.5 W/m^2 in their study. In addition to that, their investigation considered the mechanism of forced convection as a result of external wind. In Zhou et al. (2017)'s computational model, the effect of radiation heat transfer between the walls of the SCPP was not included. Subsequent to the numerical analysis, the results were compared

with the experimental data of Manzanares pilot SCPP reported by Haaf (1984). It was found that Zhou et al. (2017) estimated a lower upwind velocity of 8.65 m/s whereas the experimental data reported 8.96 m/s. A possible explanation for the variation in both numerical and experimental results was that the consideration of forced convection might over-estimate the heat energy losses from the collector's glass cover.

Shirvan et al. (2017) performed simulations on the SCPP to identify the best design parameters for improving the plant's power output. The first modelling approach was employed, whereby the heat fluxes applicable to the different hours of the day were specified at the surface of the ground. Furthermore, Shirvan et al. (2017) implemented a convective heat transfer coefficient of 5 $W/m^2 \cdot K$ at the glass boundary and the wall interface between the absorber and the collector's working fluid. From the results of their simulation, the air temperature at the chimney's base was underestimated in the early hours of the morning, when compared to the experimental results of Manzanares SCPP reported by Haaf (1984). However, when the SCPP system was simulated at a higher solar radiation intensity, the air temperature was overestimated. These results proved that the implementation of convective heat transfer boundary condition at the wall interface of the glass and the ground was not reliable to match the actual operating conditions of the SCPP.

In a computational study of the SCPP by Mehrpooya et al. (2016), the first modelling approach was used to simulate the SCPP system. A constant heat flux of 800 W/m^2 was set at the ground's surface. The model did not include external wind effect, but instead, the glass cover was subjected to convection with a heat transfer coefficient value of 8 $W/m^2 \cdot K$. Moreover, convection heat transfer boundary was implemented at the interface between the glass and the collector's air, and at the interface between the absorber and the collector's air. A high error percentage of 21.19 % was determined between the numerical results of Mehrpooya et al. (2016) and the experimental data of Haaf (1984) at 800 W/m^2, which reported upwind air velocity of 11.1 m/s and 14.1 m/s, respectively. Therefore, it was evident that the application of convection heat transfer boundary led to significant heat losses associated to the solar collector.

Ghorbani et al. (2015) established a numerical model of a SCPP hybrid system which consisted of a solar chimney and a dry cooling tower. Although the novel design combined the operation of a solar chimney and a heat rejection device, the geometrical dimensions of the hybrid power plant were adapted to the structural dimensions of Manzanares SCPP for validation and further

analysis. The modelling procedure by Ghorbani et al. (2015) was based on the first approach in which the solar radiation was defined as a boundary condition. However, instead of setting the heat flux magnitude on the ground's surface, the heat flux was specified on the transparent cover. Assumption was made regarding the heat transfer by convection at the transparent cover, whereby the convective heat transfer coefficient was 10 $W/m^2 \cdot K$. Validation of the numerical results was only carried out at 1000 W/m^2 solar radiation intensity. For instance, the numerical results by Ghorbani et al. (2015) showed good agreement with the experimental data by Haaf (1984) with error percentages of 1.1 % and 0.4 % for the collector's air temperature rise and the updraft velocity, respectively. However, a major drawback with the validation was that it was only carried out at 1000 W/m^2 solar irradiation. It was not known whether there would be a large variation between the simulation and experimental results when the solar radiation intensity was lowered.

Rabehi et al. (2017) developed a CFD model of the Manzanares pilot SCPP and validated the model results with the experimental data by Haaf (1984). Subsequent to the validation procedure, Rabehi et al. (2017) relied on the meteorological data measured at four different sites in Algeria to determine the electrical power output of the SCPP in these regions. In the CFD model, the first modelling approach was employed in which the absorber's boundary was given a constant heat flux magnitude of 1000 W/m^2. The absorber-fluid interface was subjected to convection heat transfer coefficient of 10 $W/m^2 \cdot K$. The CFD model of Rabehi et al. (2017) overestimated the system's performance whereby the updraft air velocity was reported as 16.37 m/s, in comparison to the 15 m/s reported in Haaf (1984)'s paper. This review indicated that the use of convection heat transfer boundary at the solid fluid interface resulted in the over prediction of the system's performance.

Hanna et al. (2016) proposed a numerical model of the SCPP and the plant's dimensions were later used to fabricate an experimental test rig. Similar to the approach used by previously mentioned authors, the solar irradiation was defined as a wall boundary condition. Although the method employed by Hanna et al. (2016) was based on the first approach, they defined slightly different boundary conditions at the collector's transparent cover, ground and the solid fluid wall interface. The transparent cover and the ground were specified as temperature boundaries, while the solid fluid wall interface was defined with a constant heat flux of 525 W/m^2. The simulation results were compared to the experimental measured data obtained from the small scale SCPP built by Hanna et al. (2016). It was found that the simulation model

resulted in 8.4 % higher electrical power output. One significant disadvantage of Hanna et al. (2016)'s CFD model was the application of temperature thermal boundary condition at the transparent cover and the ground. The use of this boundary condition constrained the temperature at the respective boundaries throughout the simulation, which proved to be inconsistent with the actual SCPP's physical model.

The first numerical modelling approach of the SCPP is frequently used by researchers in this field because of its simplicity. The procedure of defining the solar radiation as a boundary condition is a reliable tool to simulate the physical model of the SCPP, but it does have its limitations. These limitations are referenced to the assumption that the energy received from the Sun is fully absorbed by the ground. As a result, there is an over estimation in the heat energy transferred from the ground to the collector's working fluid. To support the above claim, Huang et al. (2017) indicated that the ground's temperature was often found to be higher when the first numerical modelling procedure was used. The higher ground's temperature increases the temperature differences between the ambient air and the collector's working fluid, which provides a higher driving force in the system. This leads to over-estimation of the collector's performance.

On top of that, the first modelling procedure does not consider the greenhouse effect in the solar collector. It is widely known that the solar collector works on the principle of greenhouse effect in which the radiant energy is allowed to pass through glass or any transparent surfaces, but infrared energy (heat) cannot. This effect permits the collector to accumulate the heat from the solar energy. In the first modelling procedure of the SCPP, the collector's transparent cover is allowed to transmit every components of the Sun's electromagnetic spectrum. In the case where the greenhouse effect is included in the CFD model of the solar collector, the glass cover will only permit the radiation components to penetrate to the ground according to the components' transmissivity constants. This ensures that part of the radiation is absorbed by the collector's glass roof. When the greenhouse effect is not considered in the first modelling procedure, the collector's efficiency is over predicted.

2.4.2 Numerical Modelling Approach 2: Defining Solar Radiation as a Volume Heat Source

The second modelling approach of the SCPP was based on the definition of the solar radiation as a volume heat source within a thin layer below the ground's surface, shown schematically

in Figure 2.4. Hu et al. (2017) performed simulation on the SCPP equipped with divergent updraft tower by using the second modelling procedure. For instance, the thermal specification at the ground's boundary was selected as a heat source condition. A thin layer of 0.0001 m at the ground's boundary was assumed to generate 7200 kW/m^3 of heat. The uniform heat generation rated at 7200 kW/m^3 was chosen to produce the same amount of heat that would be acquired by the system when the solar radiation intensity was 1000 W/m^2. Hu et al. (2017) modelled the collector's transparent cover in such a way that the cover transferred the heat into the ambient by means of convection and radiation. The combined external radiation and convection heat transfer coefficient was 10 W/m^2·K. The simulation results by Hu et al. (2017) were consistent with the experimental data reported by Haaf (1984), which proved the feasibility of the second numerical modelling approach of the SCPP.

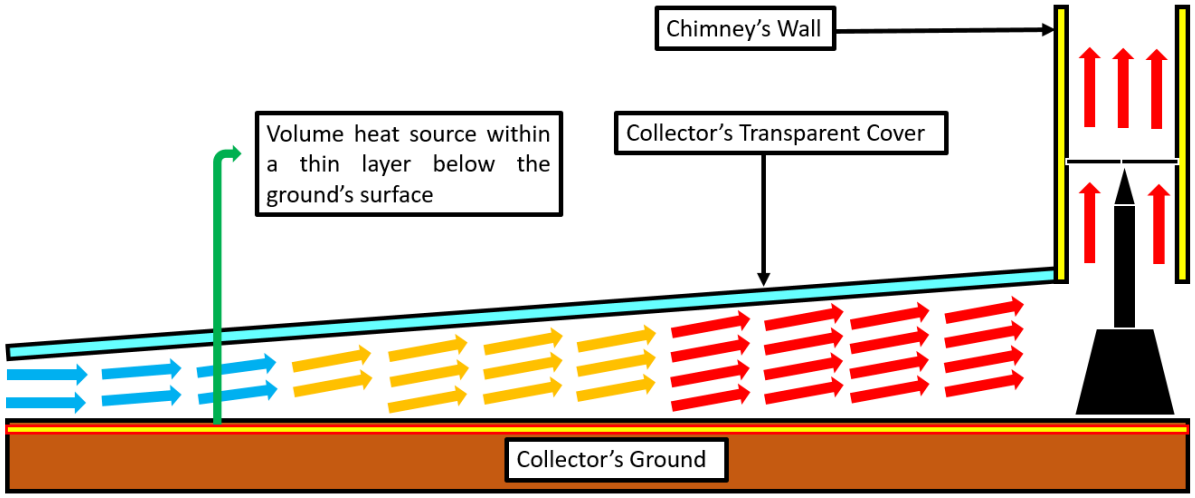

Figure 2.4: Schematic Representation of the Second Modelling Approach

The same procedure of specifying a volume heat source condition at the ground's boundary was adopted by Xu et al. (2011). In their study, the ambient wind velocity was assumed to be less than 2 m/s and therefore, the convective heat transfer boundary was applied at the collector's glass roof with a heat transfer coefficient of 10 W/m^2·K. Validation of the CFD model by Xu et al. (2011) was carried out by comparing the model results with the experimental data of Manzanares pilot SCPP reported by Haaf (1984). The percentage of error was determined to be less than 5 %. One limitation of Xu et al. (2011)'s numerical model was that the temperature of the collector's working fluid was found to be higher than the experimental results.

One major drawback of the second numerical modelling approach is the imprecise evaluation of the collector's air and the ground's average temperatures. According to a review by Huang et al. (2017), it was claimed that the approach resulted in a higher collector's air temperature as compared to the ground's temperature. This shows that the method is theoretically wrong. Therefore, the second modelling approach is rarely used by researchers as it leads to temperature field results inconsistencies and it involves potential analysis error.

2.4.3 Numerical Modelling Approach 3: Solar Load Model and Ray Tracing Method

In the third numerical modelling approach, the solar load was integrated into the computational domain. Accurate prediction of the Sun's radiation that entered the computational domain was achieved through the use of this method. Instead of defining the solar radiation as a boundary condition or a volume heat source, the solar radiation was incorporated as the primary heat sources in the conservation of energy equation. Huang et al. (2017) developed a two-dimensional numerical model of the SCPP based on this method. Moreover, it was possible to take into consideration the greenhouse effect of the solar collector when this method was employed. For instance, the Sun's radiation was classified into two categories, consisting of short wavelength component (less than 2.5 micrometer) and long wavelength component (more than 3.0 micrometer, less than 120.0 micrometer). The results obtained from Huang et al. (2017)'s model were in agreement with Haaf (1984)'s experimental data of Manzanares SCPP, which showed error percentages of 4 %, 10.2 % and 4 % for the ground's temperature, upwind velocity and air temperature rise, respectively. The difference in the upwind velocity was likely due to the specification of convection heat transfer boundary condition at the collector's glass roof, which led to over estimation of the thermal losses.

Gholamalizadeh et al. (2017) made use of the third numerical modelling approach in their study. The solar load model was activated during the simulation of the SCPP. Under the solar load model, the ray tracing algorithm was employed to compute the source of heat energy obtained from the incident solar radiation. The illumination parameters and the position of the Sun were used to model the beam propagation within the computational domain. The beam was then applied to all the wall boundaries in the domain. The resulting heat flux on the wall boundaries due to the solar radiation was calculated. Moreover, a non-grey Discrete Ordinates model was activated by Gholamalizadeh et al. (2017) to include the effect of greenhouse in the solar collector. With the use of the Discrete Ordinates model in Fluent, the collector's glass cover was specified to have high transmissivity for the visible light component. Meanwhile,

low transmissivity was set for the infrared component. From Gholamalizadeh et al. (2017)'s investigation, it was found that their model produced 36.1 kW power output while the pilot SCPP in Manzanares reported 35 to 36 kW (Haaf 1984). Both numerical and experimental results were highly consistent to one another, which proved the reliability of the third modelling approach.

2.5 Performance Enhancement Designs of the Solar Chimney Power Plants

Various enhancement models were proposed to improve the performance of the SCPP, as summarized in Table 2.1. The proposed designs were introduced and the major findings obtained from the reviews were provided.

Table 2.1: Enhancement Models of the Solar Chimney Power Plant

Authors	**Enhancement Models**	**Main Findings**
Pasumarthi et al. (1998)	Installation of an intermediate black canvas within the enclosure of the solar collector	❖ The black canvas served as an intermediate absorber surface which divided the gap between the back plate and the transparent cover into two different air-flow channels. ❖ With the separation of the air-flow on either side of the canvas, the effective area for heat transfer was increased. ❖ It was found that the mass flow rate of air and the power output of the turbine increased with the inclusion of the black canvas.
Bilgen et al. (2005)	Idea of a sloped collector on an inclined surface at a high latitude area	❖ The sloped collector had two different functions, in which it was used as a greenhouse for the absorption of solar radiation and it also performed as a chimney for the suction of air from the ambient. ❖ It was found that the performance of the sloped collector at a high latitude position was better

		than a conventional flat-plate collector at a low latitude region
Papageorgiou (2010)	Floating solar chimney technology	❖ A new design was created which replaced rigid concrete chimneys with inflated fabric (polyester) chimneys. The chimneys were filled up with lighter than air gas. ❖ Considering the use of fabric material in the construction of the solar chimneys, the initial investment cost was reduced.
Serag-Eldin (2006)	Solar chimney power plant in mountainous regions	❖ The authors presented the idea of the utilization of steep cliffs as the base design of solar chimneys. ❖ Cliffs with large valleys were desired as the valley was proposed to be used as the collector. ❖ With this idea, the cost of construction would be reduced while increasing the cycle efficiency.
Zhou, Yang, et al. (2009)	Integration of solar collector with man-made mountain hollow	❖ The authors idealized a concept where the giant hollow space in the mountain was excavated as the solar chimney. ❖ Materials usage was reduced and the design ensured a safe environment in comparison to conventional solar chimneys.
Zhou and Yang (2009)	Extension of the novel design of floating solar chimney	❖ The solar chimney was suggested to be stiffened onto a mountainside. The mountain's base was used as the collector. ❖ From their analysis, it was determined that for a collector situated in the northern hemispheres, the collector should face south.

Al-Kayiem et al. (2009)	Use of flue gas waste heat as supplementary thermal energy	❖ These researchers fabricated the first laboratory model which was numerically simulated by Al-Kayiem et al. (2012). ❖ The laboratory model consisted of an absorber plate made up of metal sheet. The absorber was sloped at an angle of 45°. A gas turbine component was utilized to supply the flue gas to the system. The model was then adapted for outdoor experiments, where the system with the absorber and the flue gas channels was comprised of two parts. The tilt angles of the first and the second parts were 15° and 45°, respectively. ❖ The experimental results were reported by Chikere et al. (2011)
Islamuddin et al. (2013), Al-Kayiem et al. (2013)	The use of waste heat energy in flue gases passing through conduits situated in the solar collector	❖ The system was modelled and simulated using ANSYS. The results proved that the use of waste heat energy in flue gases integrated to the collector enhanced the system's performance. ❖ The research and the proposed enhancement idea also contributed towards minimizing global warming as the high temperature of the flue gases was reduced prior to the release of the gases into the atmosphere.
Kashiwa et al. (2008)	Solar cyclone concept	❖ In the concept of the solar cyclone, the system was designed to yield fresh water from the atmosphere and at the same time, producing electrical power. ❖ A cyclonic separation unit was positioned at the chimney's base where the unit condensed and removed atmospheric water whereas the turbine generated energy from the air in motion.

A considerable amount of literature was published on the utilization of SCPP with an inclined collector. The following Table 2.2 focus on the enhancement studies of the SCPP considering inclined collectors and tilted transparent covers. Generally, most researchers have found that the efficiency of the collector is increased with the utilization of inclined collectors and sloped transparent covers.

Table 2.2: Performance Enhancement Studies of the Solar Chimney Power Plant with respect to Inclined Collectors and Sloped Transparent Covers

Authors	**Enhancement Studies**	**Main Findings**
Gholamalizadeh et al. (2016)	Inclination of collector's roof	❖ The roof was inclined by adjusting the height of the collector's outlet while maintaining the collector's inlet height at constant value. ❖ It was found that the collector's inclination caused an increased mass flow rate of air through the system. ❖ The efficiency of the collector and the plant's power output increased with the collector's inclination.
Patel et al. (2014)	Sloped transparent cover of the collector	❖ The authors found that a smaller collector opening led to higher values of air velocities at higher values of collector's air mass flow rate at the chimney base. ❖ For the smaller inlet opening, the heated collector's fluid was said to have a minor interaction with the surrounding air. The rate of heat transfer would be higher, which created a higher amount of air updraft in the chimney. As a result, more fresh air was drawn into the SCPP collector component and the mass flow rate of fluid significantly increased.

Hassan et al. (2018)	Performance improvement of SCPP through the variation of collector slope	❖ The study was conducted to identify the effect of the change in the collector's slope on the performance of Manzanares SCPP model. ❖ Air velocity and temperature at the exit of the collector were found to increase when the collector's slope was increased. However, the investigation revealed that when the slope of the collector was too steep, the smooth flow of buoyant air was deteriorated which caused the system's performance to degrade.
Ayadi et al. (2017)	Collector's Transparent Cover Inclination	❖ In the study, the angle of the collector's transparent cover was varied between 1°, 0°, - 1°, and - 1.5°. ❖ The study identified that the collector's transparent cover being tilted at - 1° and - 1.5° showed highest performance considering the air velocity at the collector's outlet.
Cottam et al. (2016)	Solar Collector's Canopy Profile Variation	❖ The researchers identified the impact of the different collector's canopy profiles on the plant's performance. ❖ Five different canopy profiles were investigated, which included exponential profile, flat profile, constant-gradient sloped, segmented, and segmented/stepped profile. ❖ The researchers justified that the use of flat canopy profile led to significant pressure losses at the junction between the roof and the chimney. The loss in pressure was a result of the sudden restriction of the cross-sectional area of air flow.

		❖ Exponential canopy and constant-gradient sloped profiles enhanced the performance of the collector. ❖ The authors claimed that it was necessary to design the collector's transparent roof to be sufficiently high at the junction between the roof and the chimney. An increased height of the transparent cover at this junction caused maximum kinetic energy in the air flow.
Zhou et al. (2016)	Improving performance of sloped solar collector through the use of natural anabatic winds	❖ The researchers presented a novel concept of improving the performance of a sloped collector by using natural anabatic winds. ❖ The collector was proposed to be constructed on the upper mountain slope. The collector's location on the upper mountain slope allowed the absorption of higher amount of solar radiation and additional heat sourced from the lower mountain slope. ❖ The study found that the collector's performance was improved through the use of the additional heat.
Gitan et al. (2015)	Tilted collector analysis of SCPP under Malaysia climate	❖ The investigation was conducted to identify the optimum tilt angle of the SCPP's sloped collector in Malaysia. ❖ The results obtained from the investigation showed that tilt angle of 10° produced highest power output. ❖ The authors also claimed that solar collectors inclined at 10° or 45° observed higher performance in comparison to horizontal solar collectors.

Ng (2014)	Optimization of an inclined collector's tilt angle in Malaysia	❖ Determination of the optimum tilt angles of a sloped collector had proved particularly effective in improving the collector's efficiency. ❖ The authors found that when the solar collectors were inclined at tilt angles below 20°, higher amount of solar irradiation was received.

The design concept of SCPP with thermal storage system was aimed to enhance power generation in the night. The thermal storage system involved the use of water as a heat energy storage medium. This idea ensured continuous power generation through all seasons. Due to the higher heat capacity of water as compared to the other types of fluid, the use of water storage medium could potentially absorb a higher amount of solar energy during the day. Consequently, water's high heat capacity allowed the stored heat energy to be released at a slow rate during the night without solar insolation. Furthermore, various other thermal storage systems are introduced including heat storage in underground soil and solar ponds. Table 2.3 presents the investigations of thermal storage system for the performance enhancement of SCPP.

Table 2.3: Performance Enhancement Studies of the Solar Chimney Power Plant with respect to Thermal Storage Systems

Authors	**Enhancement Studies**	**Main Findings**
Kreetz (1997)	Water-filled tight tubes in the open solar air collector	❖ The idea of the water-filled tight tubes emerged from the fundamental theory that water had a higher specific heat capacity than soil. ❖ The use of water as a heat energy storage medium enhanced power generation in the night. ❖ During the day, incident solar energy would be absorbed and stored in the tubes, whereas the heat energy release would take place during the night.
Choi et al. (2016)	Integration of SCPP with water storage layers	❖ The study was conducted to investigate the performance difference between SCPP integrated

		with thermal storage system and those without any storage system. ❖ The study found that an increase in the depth of the water storage system led to an increased power generation during the night, however, output power during the day was significantly reduced.
Guo, Wang, et al. (2016)	Consideration of underground soil heat storage in a conventional SCPP	❖ The analysis found that without the consideration of the underground soil heat storage in the SCPP, no temperature rise at the exit of the collector was observed for the period between midnight and 6 am in the morning. ❖ The model with an underground soil heat storage medium was able to predict temperature rises at the collector exit throughout the whole duration of 24 hours.
Alrobaei (2007)	Hybrid geothermal/solar energy technology	❖ The hybrid design was aimed at solving the low energy generation during the night. ❖ Coupling geothermal heat pumps with the solar chimney power plant, hot water was obtained from the underground. The hot water was distributed across the ground's surface of the solar collector using embedded pipes.
Pretorius (2007)	Improved ground heat storage using a regulating mechanism	❖ The author included an intermediate transparent cover between the roof and the ground of the solar collector, which separated the air-flow channel into top and bottom partitions. With respect to the bottom partition of the collector, an airflow regulating mechanism was proposed to be installed which enhanced the

		storage and release of heat energy from the ground absorber. ❖ During the day with high solar irradiance, the bottom partition was closed, thus, allowing the storage of heat energy in the ground. During the night, the bottom partition was opened which permitted higher release of heat energy to the air trapped under the transparent cover.
Yiping, Zhenlei, et al. (2006), Yiping, Junhong, et al. (2006), Davey (2008)	Hybrid solar chimney power plant and solar pond	❖ These authors proposed the use of solar ponds as thermal storage medium in the open solar-air collector to enhance heat storage for night operation of the SCPP. ❖ The solar collector was designed to be constructed near the saltwater ponds in which the water trapped heat in the day and released the heat for continuous operation of the plant at night.

2.6 Summary of Literature Review

The Solar Chimney Power Plant (SCPP) timeline was presented. The numerical model of the SCPP with respect to the structural dimensions of the experimental pilot SCPP in Manzanares, Spain was reviewed. The review also critically examined the various methods and approaches used with respect to the boundary conditions and the modelling procedures employed by researchers in this field. The enhancement models of the SCPP were introduced in this chapter.

Chapter 3
Methodology

3.1 Introduction to Methodology

In this chapter, Section 3.2 presents the modelling assumptions used in the current work and the description of the CFD model employed in this study. Section 3.3 explains the computational domain of the Manzanares pilot SCPP for validation purpose while Section 3.4 shows the computational domain of an inclined SCPP. Section 3.5 presents the operation equations of the SCPP which describe the governing physics behind the operation of the plant. Section 3.6 provides the governing equations used in the numerical modelling of the SCPP. Section 3.7 provides information of the boundary conditions adopted in the numerical model of the present work. Section 3.8 includes a detailed flow chart of the case studies in this work, with explanation on how the studies were conducted with respect to various manipulated and constant variables.

3.2 Numerical Modelling Assumptions and Model Description

For the numerical simulations, the system is simplified with some assumptions considering the experimental reports and numerical procedures published in this area. The necessary assumptions are as follows:

- The fluid flow in the SCPP is considered to be at steady state condition.

- Fluid flow is assumed to be incompressible. According to Hamdan (2011), the Mach number of the flow in the SCPP is below 0.3 and therefore, the incompressible flow assumption is justifiable.

- A steady-state calculation is performed using Boussinesq model where the model treats density as a constant value in all solved equations, except for the buoyancy term in the momentum equation.

- The effects of surrounding wind at the transparent cover roof are neglected in this study, thus the simulation not conducted with far-field condition.

- The walls surface which the fluid flow through are under no-slip condition.

- The turbine component is not included in the simulation as the turbine efficiency has been found to operate at over 60% efficiency, as reported by Fluri (2008).

The computational domain in this study refers to the simplified physical geometry of the SCPP. The SCPP employs basic physics of fluid flow, heat and mass transfer. The appropriate governing equations associated to the various physics of operation of SCPP are employed for the analysis of the fluid flow and thermal field in the computational domain of the plant. These governing equations compose the mathematical concepts of the physical processes in line with the working principles of the SCPP, which are used in the CFD simulation using Star-CCM+ software. The governing equations employ the boundary conditions associated with the operation of the plant to simulate the air velocities and temperatures at the base of the chimney and the collector's components temperatures.

3.3 Computational Domain of Manzanares Pilot Plant for Validation

The conventional geometry of the SCPP takes the form of the pilot plant in Manzanares, Spain. The traditional design consists of a circular open-solar-air collector which consists of a transparent roof raised and held a certain height above the ground (absorber) to form a greenhouse; a solar chimney situated at the center of the collector to create stack effect and enhance buoyancy in the hot air. At the chimney base is a single vertical axis wind turbine for energy conversion. Considering the scope of this work, the turbine component is not included in the study as the turbine efficiency has been found by other researchers to operate at over 60% efficiency. The turbine mainly converts the energy in the buoyant air into mechanical energy and with the aid of a generator, to electrical energy. For this study, a preliminary study on the Manzanares pilot plant was conducted numerically using Star-CCM+ software to validate the simulation procedures and the assumptions before conducting the full research simulations. The preliminary study used the boundary conditions and metrological data from experimental study on Manzanares pilot plant as presented in literatures for the simulation and validations. The schematic representation of the symmetrical three-dimensional model of the Manzanares pilot SCPP is shown in Figure 3.1. Since the flow is symmetrical around the y-axis of the SCPP body, only 1/32 portion of the geometry was modeled.

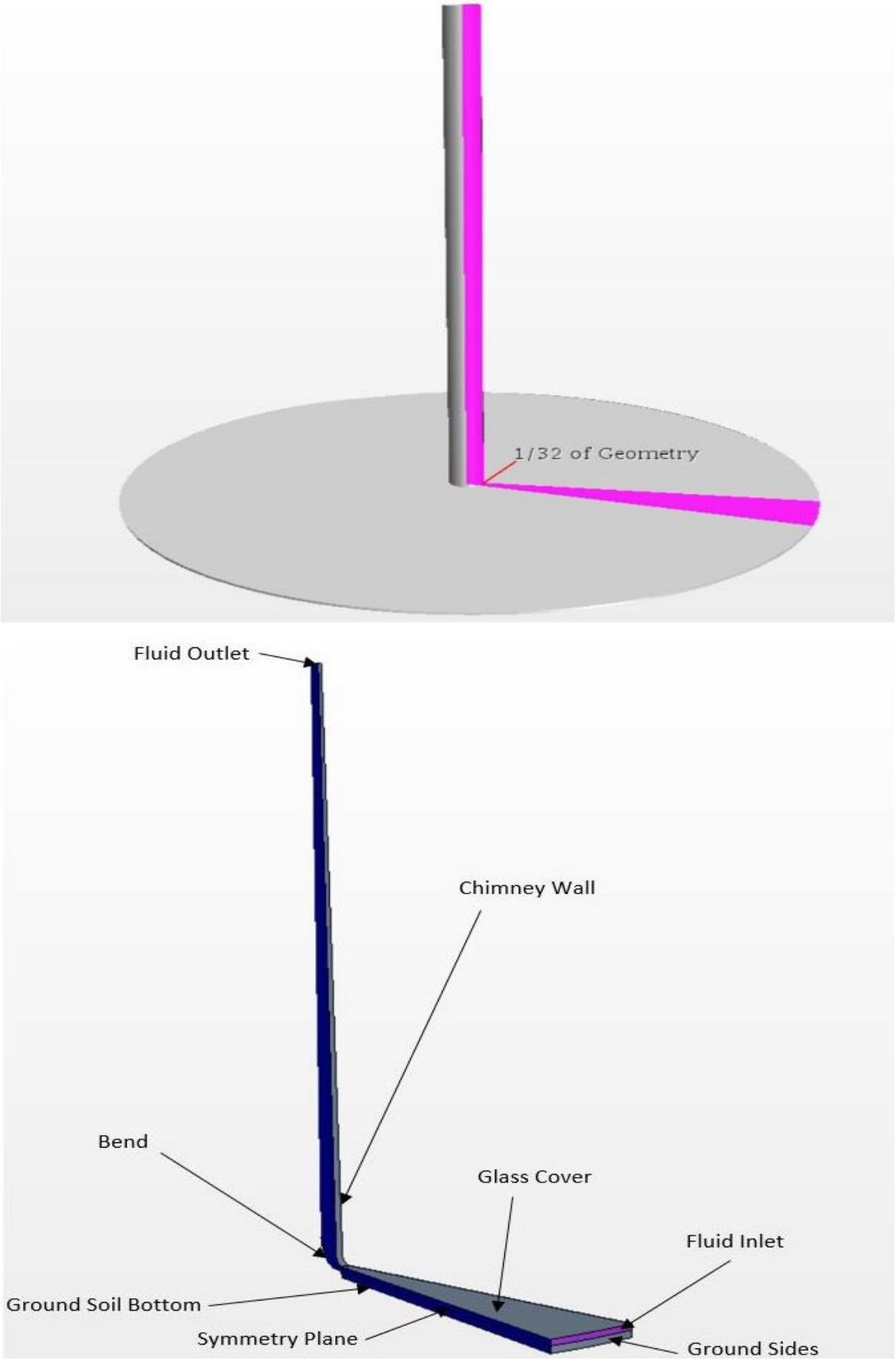

Figure 3.1: 1/32 portion of the Manzanares pilot plant CFD geometry

3.4 Computational Domain of Inclined SCPP

The model for this research study is presented in Figure 3.2 for clearer understanding of the system. The model is a south facing solar chimney power plant system inclined at 15^{o} to the horizontal. The concept is for parks electrical power generation and at mountainous locations. The collector is made of transparent cover raised some height above an absorber made of concrete to form a greenhouse and induce buoyancy in the air within open-solar-air collector region. At the south facing region, is the inlet of the collector while the west and east sides are the side walls for buoyant air sustenance in the system. At the North, the collector streamlines to meet the chimney diameter size based on the designed collector area. Different models were developed and investigated under different operating conditions. The model described above was also investigated with the inclusion of underneath air-vents at the collector component. The underneath air-vents diagrammatic representation is shown in Figure 3.3. The geometrical modelling of the proposed system was done using the modeler embedded in Star-CCM+ while the fluid flow and thermal field simulated in the Star-CCM+ simulation domain.

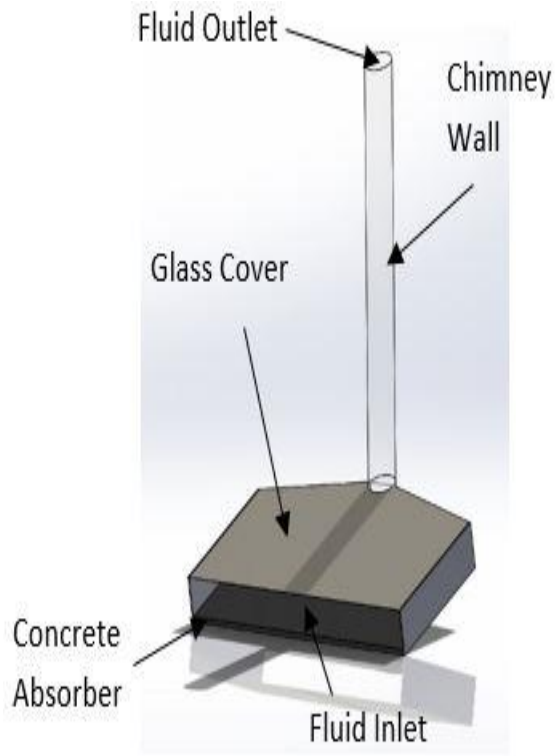

Figure 3.2: Model for this research study which is inclined at 15° to the horizontal

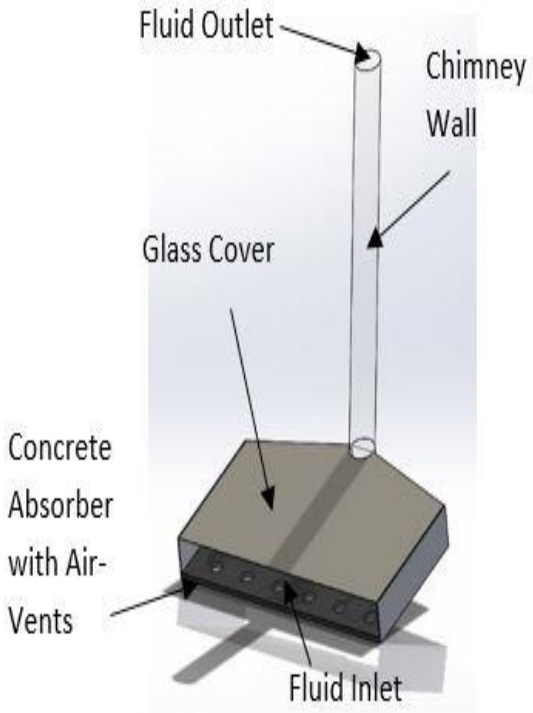

Figure 3.3: Geometry of the SCPP with air-vents at the collector's absorber

3.5 Solar Chimney Power Plant Operation Equations

The SCPP combines the technologies of the collector, the chimney and the turbine in its operation. The basic equations which describe the complete operation of the solar chimney power plant are described below considering the collector and chimney components.

3.5.1 Energy Balance at the Collector

The collector is the thermal engine where the hot buoyant air is generated thus, the energy balance of the various components are presented accordingly.

3.5.1.1 Input Energy to the Collector

The input energy at the solar collector, E_{coll}, is the product of the solar radiation intensity, I, and the area of the collector, A_{coll}, as shown in Equation 3.1.

$$E_{coll} = I \cdot A_{coll} \tag{3.1}$$

The collector area is the average surface area of the collector which is associated to the absorber and the transparent cover and defined by Equation 3.2.

$$A_{coll} = \frac{A_{ap} + A_c}{2} \tag{3.2}$$

The energy gained at the different components with respect to the input energy is described as shown in Equation 3.3.

$$E_{coll} = S_{ap}A_{ap} + S_cA_c \tag{3.3}$$

Equation 3.3 defines the distribution of the input energy into absorbed energy by the cover, represented as S_cA_c and energy absorbed by the absorber represented as $S_{ap}A_{ap}$. The total energy gained at the various components of the collector is a product of the absorbed energy and the component area.

3.5.1.2 Energy Balance at the Collector Absorber

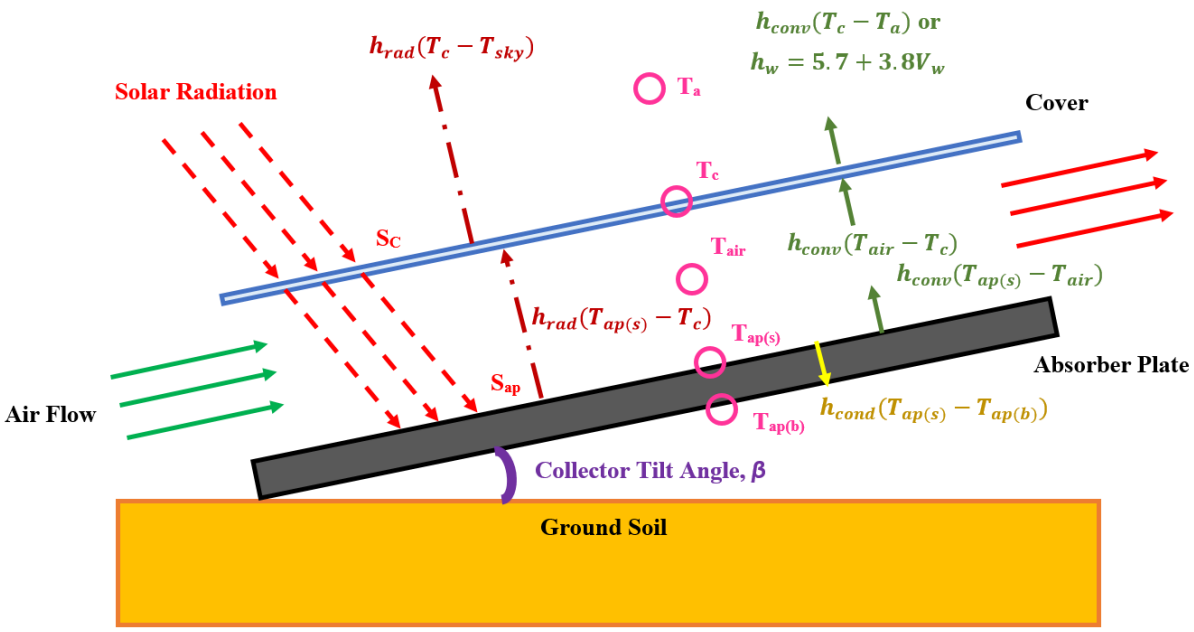

Figure 3.4: Heat Transfer Model of the Inclined Solar Collector

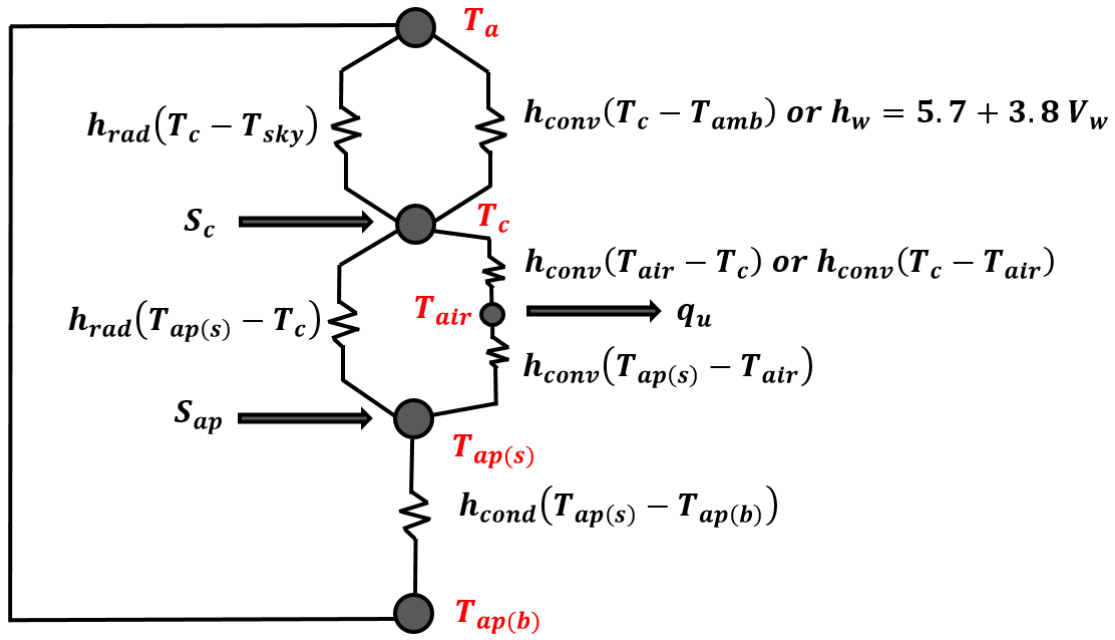

Figure 3.5: Thermal Network of Inclined SCPP

The heat transfer model of the inclined solar collector is shown in Figure 3.4. At the collector absorber, following the thermal network as shown in Figure 3.5, the thermal energy gained by the absorber is only from solar energy. Considering the first law of thermodynamics, the energy is transferred to the air by convection ($q_{ap\text{-}conv}$), through the absorber to the back by conduction

($q_{ap\text{-}cond}$), to the transparent cover by radiation ($q_{ap\text{-}rad}$) and excess stored in the absorber. A consideration of the system without thermal energy storage, Equation 3.4 describes the heat transfer process which is detailed in Equation 3.5 with respect to the different heat transfer mechanism and the components temperatures.

$$S_{ap}A_{ap} = q_{ap-rad} + q_{ap-conv} + q_{ap-cond} \tag{3.4}$$

$$S_{ap}A_{ap} + h_{rad,ap-c}A_{ap}(T_c - T_{ap}) + h_{conv,ap-air}A_{ap}(T_{air} - T_{ap}) + h_{cond-b}A_b(T_b - T_{ap}) = 0 \tag{3.5}$$

With reference to Equation 3.5, the radiation heat transfer coefficient is described using Equation 3.6 (Duffie et al. 2013).

$$h_{rad,ap-c} = \frac{\sigma(T_{ap}^2 + T_c^2)(T_{ap} + T_c)}{\left(\frac{1}{\varepsilon_{ap}} + \frac{1}{\varepsilon_c} - 1\right)} \tag{3.6}$$

The convection heat transfer is associated with the air and is described using Equation 3.7. The thermal conductivity of the thin film air near the absorber is given in Equation 3.8 (Duffie et al. 2013).

$$h_{conv,ap-air} = Nu_{ap-air}\left(\frac{k_{t,ap-air}}{H_{ap-c}}\right) \tag{3.7}$$

$$k_{t,ap-air} = 0.0257\left(\frac{T_{t,ap-air}}{293}\right)^{0.86} \tag{3.8}$$

$T_{t,ap-air}$ is determined as the average of the air temperature and the absorber temperature, as shown in Equation 3.9.

$$T_{t,ap-air} = \frac{T_{air} + T_{ap}}{2} \tag{3.9}$$

The Nusselt number for the air near the absorber is obtained from the correlations established by Raithby et al. (1998), as represented in Equation 3.10. The positive exponent indicates that only positive values of the terms in the square brackets are to be used.

$$Nu_{ap-air} = 1 + 1.44\left[1 - \frac{1708\sin(1.8\beta)^{1.6}}{Ra_{ap-air}\cos(\beta)}\right]\left[1 - \frac{1708}{Ra_{ap-air}\cos(\beta)}\right]^{+} + \left[\left(\frac{Ra_{ap-air}\cos(\beta)}{5830}\right)^{\frac{1}{3}} - 1\right]^{+} \quad 3.10$$

$$Ra_{ap-air} = \frac{g\beta'_{t,ap-air}(T_{ap} - T_{air})H^3_{ap-c}}{v_{t,ap-air}\alpha_{t,ap-air}} \quad 3.11$$

$$Ra_{ap-air} = \frac{cp_{t,ap-air}\rho^2_{t,ap-air}g\beta'_{t,ap-air}(T_{ap} - T_{air})H^3_{ap-c}}{\mu_{t,ap-air}k_{t,ap-air}}$$

$$v = \frac{\mu}{\rho}$$

$$\alpha = \frac{k}{c_p\rho} \quad 3.12$$

$$v\alpha = \frac{\mu k}{c_p\rho^2}$$

The coefficient of volumetric expansion of thin film of air near the absorber is given in Equation 3.13.

$$\beta'_{t,ap-air} = \frac{1}{T_{t,ap-air}} \quad 3.13$$

The dynamic viscosity of the thin film air near the absorber is provided by Equation 3.14 (Duffie et al. 2013).

$$\mu_{ap-air} = 1.81 \times 10^{-5}\left(\frac{T_{t,ap-air}}{293}\right)^{0.735} \quad 3.14$$

The thin air film specific heat near the absorber is shown in Equation 3.15 (Duffie et al. 2013).

$$c_{p_{ap-air}} = 1006\left(\frac{T_{t,ap-air}}{293}\right)^{0.0155} \quad 3.15$$

The air density for the air near the absorber is calculated based on Equation 3.16 (Duffie et al. 2013).

$$\rho_{ap-air} = \frac{97500}{287.045 T_{t,ap-air}} \quad 3.16$$

3.5.1.3 Energy Balance at the Collector Cover

The energy gained at the cover depends on the solar radiation intensity and the temperature of the cover which can be described into low solar radiation intensity/low cover temperature and high solar radiation/high cover temperature. In the case of low cover temperature where the cover temperature is lower than the temperature of the air, the energy balance at the cover considers energy gain as the sum of the absorbed solar energy, the re-radiated heat from the absorber to the cover and the convective heat transfer from the air to the cover while the energy losses are the radiation heat loss from the cover to the sky and the convection heat loss from the cover to the ambient (might be influenced by wind), thus can be represented using Equation 3.17. The analysis of Equation 3.17 considering the heat transfer coefficients for the cover energy balance is shown in Equation 3.18 without the effect of wind. On the other hand, when the cover temperature is higher than the air temperature, there is a convective heat transfer from the cover to the working fluid (system air), thus the energy balance equation is represented with 3.19. Similarly, the heat transfer coefficients relationship of Equation 3.19 is presented in Equation 3.20 without considering the effect of wind.

$$S_c A_c + q_{ap-rad} + q_{air-conv} = q_{c-conv-amb} + q_{c-rad-sky} \quad 3.17$$

$$S_c A_c + h_{rad,ap-c} A_{ap}(T_{ap} - T_c) + h_{conv,air-c} A_c (T_{air} - T_c) = h_{conv,c-amb} A_c (T_c - T_{amb}) + h_{rad,c-sky} A_c (T_c - T_{sky}) \quad 3.18$$

$$S_c A_c + q_{ap-rad} = q_{c-conv-amb} + q_{c-rad-sky} + q_{air-conv} \quad 3.19$$

$$S_c A_c + h_{rad,ap-c} A_{ap}(T_{ap} - T_c) = h_{conv,c-amb} A_c (T_c - T_{amb}) + h_{rad,c-sky} A_c (T_c - T_{sky}) + h_{conv,c-air} A_c (T_c - T_{air}) \quad 3.20$$

In Equation 3.18, the radiation heat transfer coefficient from the absorber to the cover is represented by Equation 3.6. On the other hand, the radiation heat transfer coefficient from the cover to the sky is given by Equation 3.21. The temperature of the sky is determined by using Equation 3.22. The convection heat transfer coefficient is given by Equation 3.23. The thermal conductivity of a thin film air near the cover is shown in Equation 3.24 (Duffie et al. 2013).

$$h_{rad,c-sky} = \frac{\sigma \varepsilon_c (T_c^2 + T_s^2)(T_c + T_s)(T_c - T_s)}{(T_c - T_a)} \quad 3.21$$

$$T_s = 0.0552 T_a^{1.5} \quad 3.22$$

$$h_{conv,air-c} = Nu_{air-c} \left(\frac{k_{t,air-c}}{H_{ap-c}} \right) \quad 3.23$$

$$k_{t,air-c} = 0.0257 \left(\frac{T_{t,air-c}}{293} \right)^{0.86} \quad 3.24$$

$T_{t,air-c}$ is determined as the average of the air temperature and the cover temperature, as shown in Equation 3.25. The Nusselt number for the air near the cover is given in Equation 3.26 (Raithby et al. 1998). Positive exponent shows that only positive values of the terms in the square brackets are to be used.

$$T_{t,air-c} = \frac{T_{air} + T_c}{2} \quad 3.25$$

$$Nu_{air-c} = 1 + 1.44 \left[1 - \frac{1708 \sin(1.8\beta)^{1.6}}{Ra_{air-c} \cos(\beta)} \right] \left[1 - \frac{1708}{Ra_{air-c} \cos(\beta)} \right]^+ + \left[\left(\frac{Ra_{air-c} \cos(\beta)}{5830} \right)^{\frac{1}{3}} - 1 \right]^+ \quad 3.26$$

The Rayleigh number for the air near the cover is shown in Equation 3.27. The kinematic viscosity and thermal diffusivity, together with their collective term are shown in Equation 3.28.

$$Ra_{air-c} = \frac{g \beta'_{t,air-c} (T_{air} - T_c) H_{ap-c}^3}{v_{t,air-c} \alpha_{t,air-c}} \quad 3.27$$

$$Ra_{air-c} = \frac{cp_{t,air-c}\rho_{t,air-c}^2 g\beta'_{t,air-c}(T_{air} - T_c)H_{ap-c}^3}{\mu_{t,air-c}k_{t,air-c}}$$

$$v = \frac{\mu}{\rho}$$

$$\alpha = \frac{k}{c_p\rho} \qquad 3.28$$

$$v\alpha = \frac{\mu k}{c_p\rho^2}$$

The coefficient of volumetric expansion of thin film of air near the cover is given in Equation 3.29.

$$\beta'_{t,air-c} = \frac{1}{T_{t,air-c}} \qquad 3.29$$

The dynamic viscosity of the thin film air near the cover is provided by Equation 3.30 (Duffie et al. 2013).

$$\mu_{air-c} = 1.81 \times 10^{-5}\left(\frac{T_{t,air-c}}{293}\right)^{0.735} \qquad 3.30$$

The thin film air specific heat near the cover is shown in Equation 3.31 (Duffie et al. 2013).

$$c_{p_{air-c}} = 1006\left(\frac{T_{t,air-c}}{293}\right)^{0.0155} \qquad 3.31$$

The air density for the air near the cover is calculated based on Equation 3.32 (Duffie et al. 2013).

$$\rho_{air-c} = \frac{97500}{287.045T_{t,air-c}} \qquad 3.32$$

In a situation where the heat loss by convection from the cover to the ambient is considered with respect to the effect of wind, the correlation developed by McAdams (1958), Equation 3.33 can be used to evaluated the thermal loss.

$$h_w = 5.7 + 3.8V_w \quad 3.33$$

3.5.1.4 Energy Balance at the Collector Air

From the energy balance, it can be seen that there are energy transfer between the air (working fluid) and the collector components (absorber and the cover). At a low solar radiation intensity, the energy gained by the air can be determined using the Equation 3.34 for a case where the air losses heat to the cover, in which Equation 3.35 describes the heat transfer modes and the temperatures of the system's components. At a high solar radiation intensity, the air gains heat from the cover and the useful energy, q_u, gained by the air is represented by Equation 3.36. The heat transfer mechanisms and different components' temperatures with respect to Equation 3.36 are represented by Equation 3.37.

$$q_{ap-conv} - q_{air-conv} = q_u \quad 3.34$$

$$h_{conv,ap-air}A_{ap}\left(T_{ap} - T_{air}\right) - h_{conv,air-c}A_c(T_c - T_{air}) = q_u \quad 3.35$$

$$q_{ap-conv} + q_{air-conv} = q_u \quad 3.36$$

$$h_{conv,ap-air}A_{ap}\left(T_{ap} - T_{air}\right) + h_{conv,air-c}A_c(T_c - T_{air}) = q_u \quad 3.37$$

The useful energy gained by the air is the driving force for the buoyant air that rotates the turbine. This useful energy can be analyzed as a function of air mass flow rate as shown in Equation 3.38.

$$q_u = \dot{m}_{air}C_{p,\,air}(T_{air} - T_a) \quad 3.38$$

In Equation 3.38, all the parameters of the useful energy gained by the air are dependent on temperature apart from the mass flow rate which remains constant for every batch of flow. To determine air mass flow rate in the system, Equation 3.39 can be employed.

$$\dot{m}_{air} = \rho_{air} A_{air-channel} \mathrm{v}_{air} \quad 3.39$$

3.5.1.5 Collector Performance Equation

For any given collector area, A_{coll}, and solar radiation intensity, I, a certain amount of useful energy is gained, q_u. Thus, the collector efficiency, η_{coll}, is the ratio of the useful energy gain to the input energy, E_{coll}, as shown in Equation 3.40. For the collector's absorber thermal energy storage capacity, the stored thermal energy, q, is calculated using Equations 3.41 and 3.42.

$$\eta_{coll} = \frac{q_u}{E_{coll}} = \frac{q_u}{A_{coll} \cdot I} \quad 3.40$$

$$q = C_{p_{concrete}} \Delta T \quad 3.41$$

$$\Delta T = T_{Concrete} - T_{Air} \quad 3.42$$

3.5.2 Chimney Operation Equations

The chimney enhances buoyancy of the air through pressure difference (stack effect) such that the velocity of the air increases. Thus the change in pressure between the ambient and the air in the SCPP, Δp_{tot}, can be determined using Equation 3.43 as presented by Schlaich et al. (2005).

$$\Delta p_{tot} = g \int_0^{H_{tot}} (\rho_{amb} - \rho_{air}) dh \quad 3.43$$

Equation 3.43 shows that Δp_{tot} increases as chimney height increases. Consequently, the pressure variation impacts the air power, $P_{air\text{-}tot}$, where air power can be determined using Equation 3.44 (Schlaich et al. 2005).

$$P_{air-tot} = \Delta p_{tot} \cdot \mathbf{v}_{air-ch} \cdot A_{ch} \quad 3.44$$

The efficiency of the chimney is determined by the enhancement it contributes to the buoyancy in the air exiting the collector as presented in Equation 3.45 (Schlaich et al. 2005).

$$\eta_{ch} = \frac{P_{air-tot}}{q_u} \quad 3.45$$

Equation 3.45 can be represented by Equation 3.46 considering the effect of chimney height with respect to the pressure difference as highlighted in Equation 3.43 and useful energy of Equation 3.38 to determine the chimney efficiency.

$$\eta_{ch} = \frac{gH_{tot}}{C_p T_a} \quad 3.46$$

3.5.3 Turbine Operation Equations

The air power generated in the system is the power available to the turbine which is converted to electrical energy. The electrical power generated in SCPP from the turbine-generator can be expressed as Equation 3.47 with the turbine efficiency equation represented in Equation 3.48.

$$P_{elec-out} = \eta_{turb} P_{air-tot} \quad 3.47$$

$$\eta_{turb} = \frac{P_{elec-out}}{P_{air-tot}} \quad 3.48$$

3.5.4 Total Performance Equations

Considering Equation 3.44 and Equation 3.47 which represent the total air power and total electrical power generated in SCPP, respectively, the plant efficiency for the cases of the plant operation with and without turbines are determined using Equations 3.49 and 3.50, respectively.

$$\eta_{sys} = \frac{P_{elec-out}}{A_{ap} I_T} \quad 3.49$$

$$\eta_{sys} = \frac{P_{air-tot}}{A_{ap} I_T} \quad 3.50$$

3.6 Numerical Modelling Governing Equations

The governing equations that are associated with the modelling of the SCPP discussed in this report are presented in detail at this section following the subsections below. The governing equations present the flow and thermal field equations, the turbulence model equations and the radiation model equations.

3.6.1 Conservation of Mass Equation

The conservation of mass or continuity equation is shown in Equation 3.51 (ANSYS 2011).

$$\nabla \cdot \vec{v} = 0 \tag{3.51}$$

In the present work, the flow is assumed to be incompressible without any mass generation or source term.

3.6.2 Conservation of Momentum Equation

The conservation of momentum equation is shown in Equation 3.52.

$$\frac{\partial}{\partial t}(\rho\vec{v}) + \nabla \cdot (\rho\vec{v}\vec{v}) = -\nabla p + \nabla \cdot (\bar{\bar{\tau}}) + \rho\vec{g} + \vec{F} \tag{3.52}$$

In Equation 3.52, p is the static pressure, $\bar{\bar{\tau}}$ is the stress tensor, $\rho\vec{g}$ is the gravitational body force and $\vec{F}$ refers to the Boussinesq term.

3.6.3 Turbulence Equations

The airflow in a SCPP is driven by the variations in density caused by temperature differences. The strength of buoyancy driven flows is determined using Rayleigh number, *Ra*. In the case where $Ra > 10^{10}$, the flow is fully turbulent. In the SCPP model of this study, considering air temperature of 325 K with a collector's air temperature increase of 20 K, the Rayleigh number is 11.45×10^{12}, indicating turbulent flow. The transport equations of turbulence k-ε model for incompressible flows are presented in Equations 3.53 and 3.54 (ANSYS 2011).

$$\frac{\partial k}{\partial t} + \frac{\partial}{\partial x_i}(k\mu_i) = \frac{\partial}{\partial x_j}\left(\alpha_k \mu_{eff} \frac{\partial k}{\partial x_j}\right) + G_k + G_b - \varepsilon - Y_m + S_k \tag{3.53}$$

$$\frac{\partial \varepsilon}{\partial t} + \frac{\partial}{\partial x_i}(\varepsilon\mu_i) = \frac{\partial}{\partial x_j}\left(\alpha_\varepsilon \mu_{eff} \frac{\partial \varepsilon}{\partial x_j}\right) + C_{1\varepsilon}\frac{\varepsilon}{k}(G_k + C_{3\varepsilon}G_b) - C_{2\varepsilon}\frac{\varepsilon^2}{k} - R_\varepsilon + S_\varepsilon \tag{3.54}$$

In Equations 3.53 and 3.54, the terms G_k and G_b respectively refer to the generation of turbulent kinetic energy due to velocity gradient and buoyancy. The model constants are $C_{1\varepsilon}$ = 1.44 and $C_{2\varepsilon}$ = 1.9, which are obtained from the established turbulent flow data of (Versteeg et al. 2007).

3.6.4 Energy Equation and Radiative Heat Transfer Equation

The energy equation is shown in Equation 3.55 (ANSYS 2011).

$$\nabla \cdot \left(\vec{v}(\rho E)\right) = \nabla \cdot k_{eff} \nabla T + \overline{\overline{\tau_{eff}}} \cdot \vec{v} + S_h \qquad 3.55$$

In Equation 3.55, S_h is the user defined volumetric heat source. In the modelling of the SCPP in the current work, the solar ray tracing algorithm integrated in the solar load model computes the heat flux resulting from incident solar radiations. The results are coupled through the user defined volumetric heat source term in the energy equation. The radiation heat transfer between the surfaces in SCPP is calculated by using Surface to Surface (S2S) radiation model. The first step employed in the S2S radiation model is the computation of the surface-to-surface interaction between each pair of surface in the computational domain. The proportion of radiation which leaves a particular surface that strikes on another surface is dependent on the emissivity properties, locations and alignments of the surfaces relative to one another. A representation of surface interaction by radiation between two elemental surfaces is shown in Figure 3.6 which is employed in the analysis of the S2S governing equations.

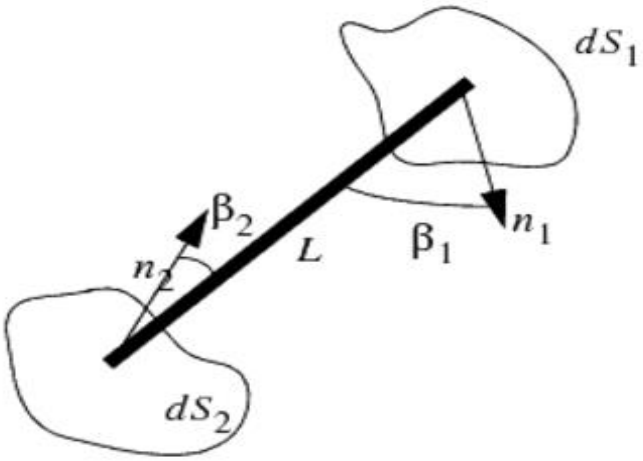

Figure 3.6: Radiation exchange between two elemental surfaces facing one another (Guide 2009)

The total amount of radiation power that elemental surface dS_1 emits which is in turn can be received by an elemental surface dS_2 is given by Equation 3.56.

$$P_{1-2} = i_1' dS_1 \cos(\beta_1) \left(\frac{dS_2 \cos(\beta_2)}{L^2} \right) \quad 3.56$$

The calculation of the view factor between the two elemental surfaces is done by dividing the power that dS_2 receives by the radiation power produced by surface dS_1, as presented by Equation 3.57.

$$dF_{1-2} = \frac{P_{1-2}}{\pi i_1' dS1} \quad 3.57$$

Assuming that the two elemental surfaces dS_1 and dS_2 take the form of two black surfaces, referred to as surfaces *i* and *j* respectively, the following revised view factor in Equation 3.58 is established to satisfy thermal equilibrium and reciprocity relation:

$$dF_{i-j} dS_i = dF_{j-1} dS_j \quad 3.58$$

3.7 Boundary Conditions and Solution Procedures

At the inlet of the solar collector, the pressure inlet boundary condition is specified and equated as the atmospheric gauge pressure, as shown in Equation 3.59.

$$p_0 = 0\ Pa \quad 3.59$$

The same boundary condition is used for the chimney's outlet, as shown in Equation 3.59. No slip boundary condition is used for the chimney's wall, the ground, and the transparent cover. The heat flux to these walls adjacent to the fluid elements is shown in Equation 3.60, which is detailed in Equation 3.61. The radiative heat flux, q_{rad}, is computed by the radiation and the solar load models in Star-CCM+.

$$q_{total} = q_{heat-gen} + q_{rad} \quad 3.60$$

$$q_{heat-gen} = \frac{k_s}{\Delta n}(T_w - T_s) \quad 3.61$$

For all the boundaries in the Solar Chimney Power Plant (SCPP) system, the optical radiation properties have to be specified. Visible light component has a lower wavelength of 1 x 10^{-7} m and an upper wavelength of 3 x 10^{-6} m. Thermal radiation component has a lower wavelength of 3 x 10^{-6} m and an upper wavelength of 1.0 m. Constant values for Surface Emissivity and Surface Transmissivity take the form of an array profile, with the first column referring to the visible light, and the second column referring to the thermal radiation. For the transparent cover, the surface emissivity is (0.08, 0.95), whereas the surface transmissivity is (0.92, 0.05). With these settings, the transparent cover is given a high transmissivity for the lower wavelengths of the Visible Light, and lower values of transmissivity for the higher wavelengths of the Thermal Radiation, as published by Gholamalizadeh et al. (2014) who used a two-band radiation model.

3.7.1 Boundary Conditions for the Manzanares SCPP in Spain for Validation Purpose

The complete boundary conditions that were used to model the Manzanares pilot SCPP for simulation is detailed in Table 3.1. The simulated results were validated against the experimental results as published in literatures. The boundaries conditions employed in the simulation were derived from the operating conditions and the weather data at Manzanares pilot plant. In this study, the heat flux was equated to zero at the wall surface of radiation model in relation to the boundary condition. Considering the solar radiation induced model, under ambient condition where there was no thermal interference from other external heat sources, the surface temperature and the surrounding air temperature were at equilibrium, and thus, the change in temperature equated to zero. Therefore, the local heat flux at the surface equals to zero which showed that there was no internal heat generation from the medium. With the introduction of radiation heat transfer model, the energy gained by the surface drive the system which caused influences on temperature of the various components of the system including the operating fluid. Moreover, the greenhouse effect was considered in the CFD model of the SCPP. For instance, constant values for surface emissivity, surface reflectivity and surface transmissivity take the form of an array profile, with the first column referring to the first spectral band which is the visible light, and the second column referring to the second spectral band which is the infrared radiation.

Table 3.1: Boundary Conditions for Manzanares SCPP Simulation Model

Boundaries	**Boundary Types**	**Values**
Inlet	Pressure Inlet	• Gauge Pressure = 0 Pa • Temperature = 305.25 K • Turbulence Intensity = 0.1 (Pastohr et al. 2004) • Turbulence Viscosity Ratio = 10.0
Symmetry Planes	Symmetry Plane	• Not Applicable
Transparent cover	Wall	• No slip • Heat Flux = 0 W/m^2
Outlet	Pressure Outlet	• Gauge Pressure = 0 Pa • Temperature = 305.25 K • Turbulence Viscosity = 0.1 (Pastohr et al. 2004) • Turbulence Viscosity Ratio = 10.0
Other Wall Surfaces	Wall	• No slip • Heat Flux = 0 W/m^2

From this baseline CFD model validation using the Manzanares SCPP, the 15° inclined SCPP of different configurations were developed for various investigations.

3.7.2 Boundary Conditions for the Inclined SCPP with Underneath Air-Vents

The inclined SCPP model has the boundary conditions specified in Table 3.2, which are applicable to both the models with and without the air-vents. With the inclusion of the air-vents at the absorber, in order to ease the modeling of the absorber, the solid shell region in Star-CCM+ was employed. On the other hand, the investigation on the absorber capability for thermal storage, the concrete absorber was modelled at varying thickness to observe the temperature distribution in the absorber and considerable thermal losses at each thickness.

Table 3.2: Boundary Conditions for Inclined SCPP with and without Air-Vents

Boundaries	**Types**	**Values**
Absorber-Fluid Interface	Wall	• No slip • Heat Flux = 0 W/m^2
Inlet, Air Vents' Inlets	Pressure Inlet	• Pressure = 0 Pa • Temperature = 305.25 K • Turbulence Intensity = 0.1 (Pastohr et al. 2004) • Turbulence Viscosity Ratio = 10.0
Transparent cover	Wall	• No slip • Heat Flux = 0 W/m^2
Outlet	Pressure Outlet	• Pressure = 0 Pa • Temperature = 305.25 K • Turbulence Viscosity = 0.1 (Pastohr et al. 2004) • Turbulence Viscosity Ratio = 10.0

3.8 Case Studies Flow Chart

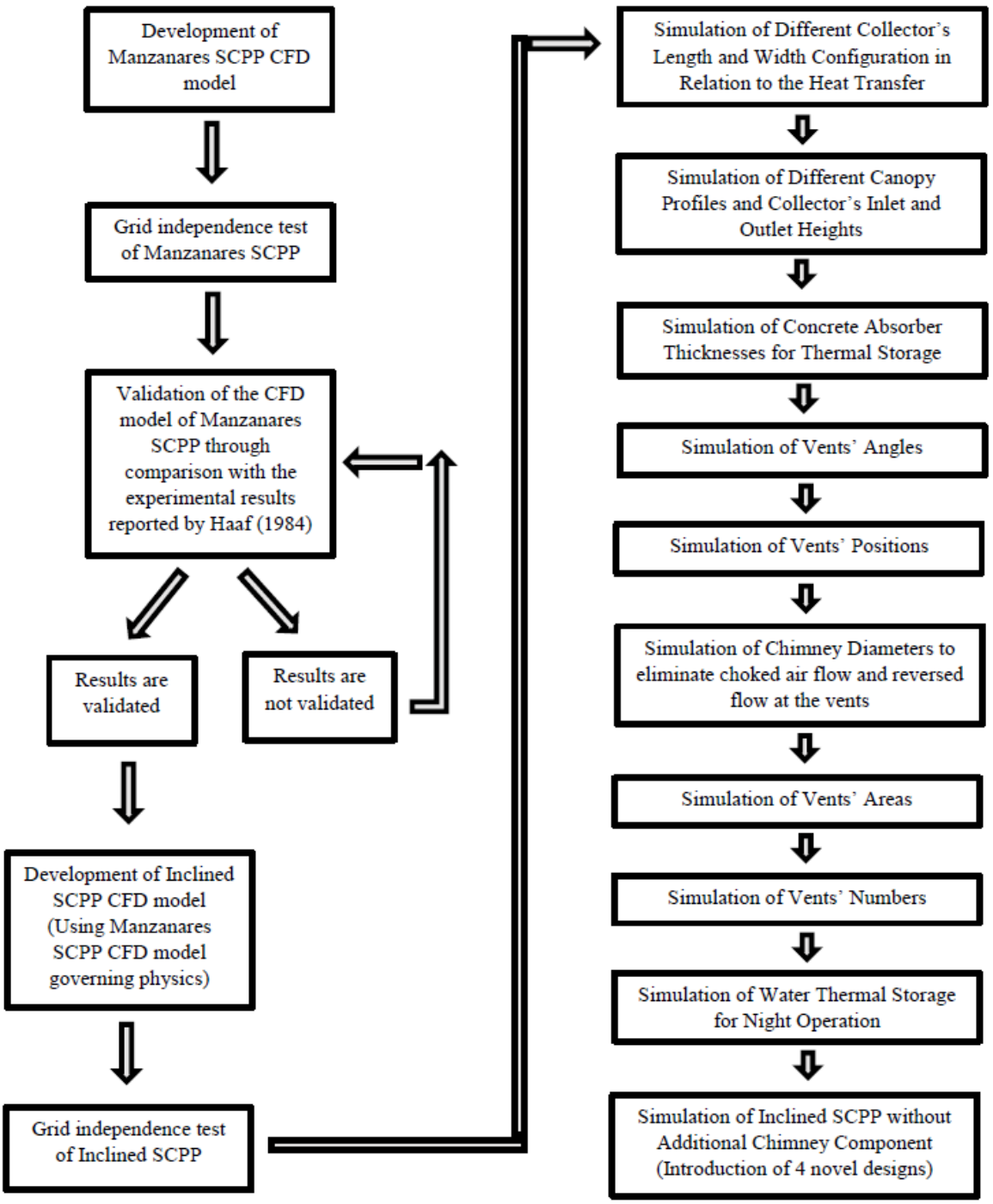

The case studies flow chart shows the steps involved in achieving the project's objectives. The Manzanares SCPP CFD model was developed and the grid independence test was conducted. The results were validated with experimental data published in the literatures. Then, similar physics were used for the inclined SCPP CFD model and grid independence test was performed. The simulation was carried out as detailed in the next section.

3.9 Investigation into the Research Objectives

3.9.1 Simulation of Different Collector's Length and Width Configuration in Relation to the Heat Transfer

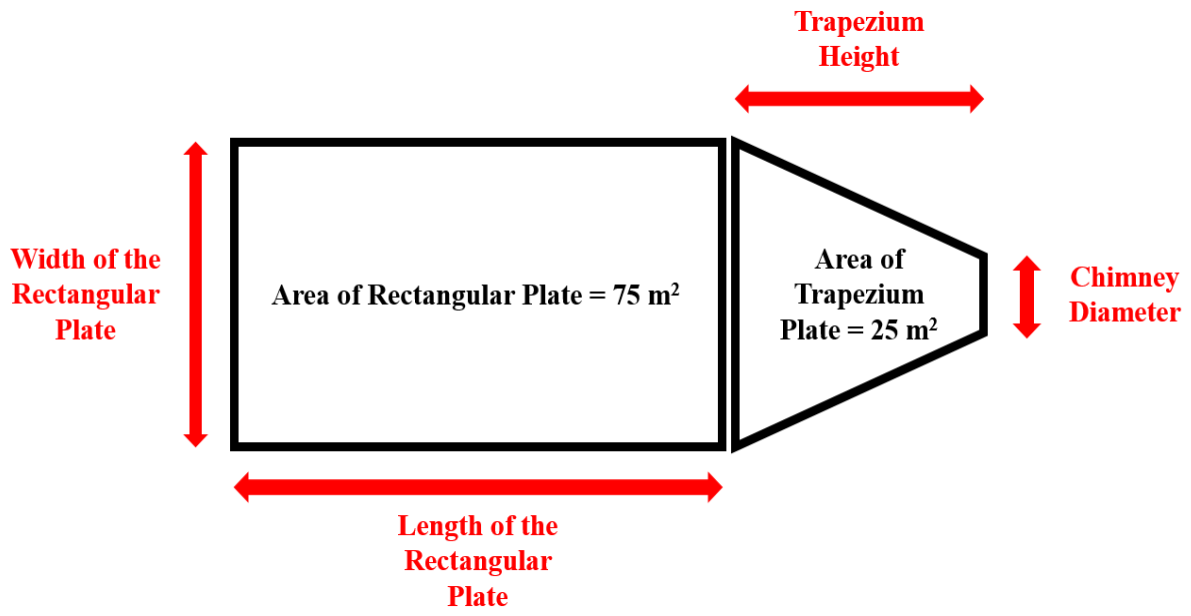

Figure 3.7: Classification of the solar collector into a rectangular plate and a streamlined trapezium section

In this study, the length and width of the solar collector's rectangular plate are varied to identify their effects on the thermal performance of the inclined solar chimney power plant (SCPP). This particular sub-objective plays an important role to achieve the main objective which is to develop a new model of the inclined SCPP. In Figure 3.7, the solar collector is divided into a rectangular plate and a streamlined trapezium section. The manipulated variables are the length and width of the rectangular plate. However, when the width of the rectangular plate is changed, the height of the trapezium plate will also be altered to maintain the trapezium's area at 25 m^2 and to fix the chimney's diameter at 0.5 m. The area of the rectangular plate is 75 m^2, which results in 100 m^2 solar collector area. The inclination angle of the solar collector is 15°. The collector inlet and outlet height is 0.5 m. The concrete absorber thickness is 0.3 m and the transparent cover thickness is 0.005 m. The simulation is done by using the solar radiation data computed by the solar calculator on the 1st of January 2017, at 12 noon, located in Miri, Sarawak. The solar radiation intensity is 1000 W/m^2. Table 3.3 shows the schematics of 12 different cases which will be investigated numerically.

Table 3.3: 12 cases showing different combinations of the collector's length and width dimensions

Case 1A: 2.5 m Length and 30 m Width	Case 1B: 5.0 m Length and 15.0 m Width	Case 1C: 7.5 m Length and 10 m Width
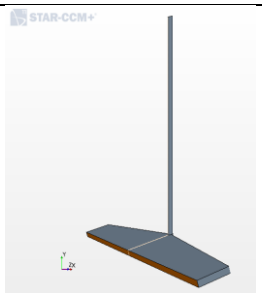	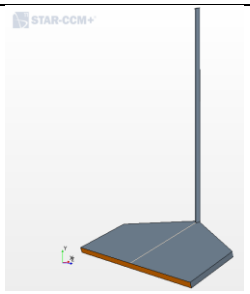	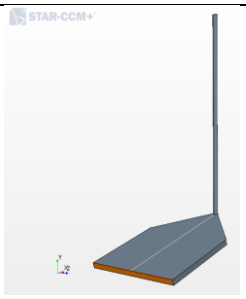
Case 1D: 10.0 m Length and 7.5 m Width	**Case 1E: 12.5 m Length and 6 m Width**	**Case 1F: 15.0 m Length and 5.0 m Width**
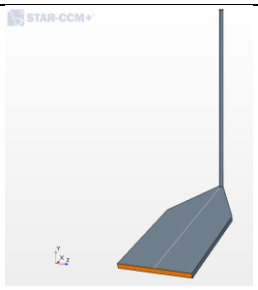	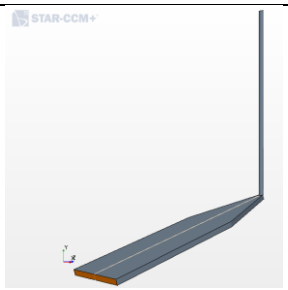	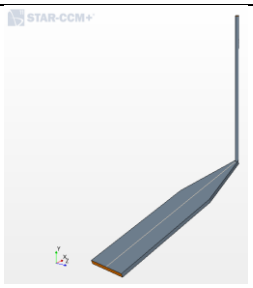
Case 1G: 17.5 m Length and 30/7 m Width	**Case 1H: 20.0 m Length and 3.75 m Width**	**Case 1I: 22.5 m Length and 10/3 m Width**
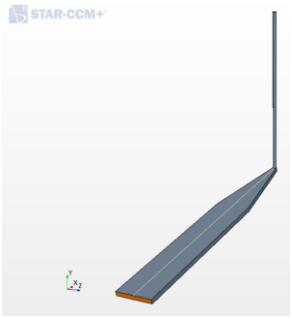	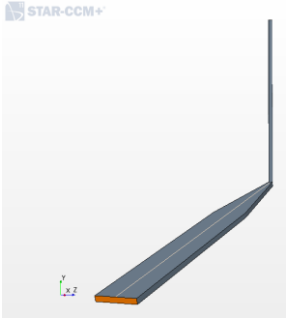	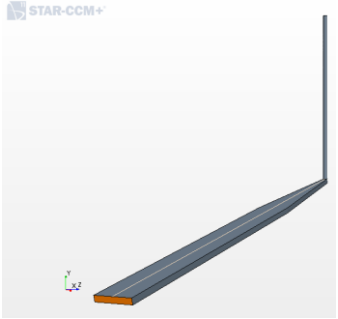
Case 1J: 25.0 m Length and 3.0 m Width	**Case 1K: 27.5 m Length and 30/11 m Width**	**Case 1L: 30.0 m Length and 2.5 m Width**
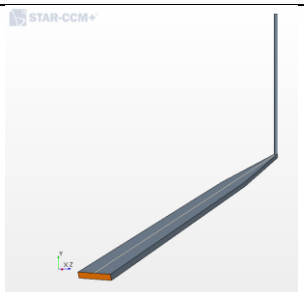	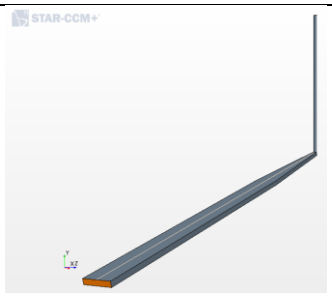	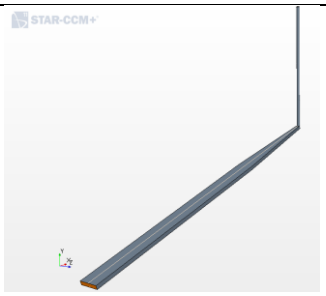

3.9.2 Simulation of Different Canopy Profiles and Collector's Inlet and Outlet Heights

In this investigation, the effects of the collector's air volume and the transparent cover roof's inclination on the inclined solar chimney power plant (SCPP)'s performance are analyzed. By setting the solar radiation intensity at a constant value of 1000 W/m^2, and by using the reference Case 1E, different volumes of the collector's air are manipulated. At this stage of the investigation, the collector's inlet and outlet heights are uniform, which represent flat canopy profiles. Five different volumes of the collector's air are simulated which consist of 30 m^3, 40 m^3, 50 m^3, 60 m^3 and 70 m^3 volumes. Then, the air volume which results in the highest electrical power output will be used to simulate the effect of the collector's roof inclination. The collector's transparent cover roof is sloped by manipulating the inlet and the outlet heights of the collector, and these combinations are shown in Table 3.4. From this table, it has to be noted that as the collector's inlet height is increased from 0.1 m to 0.6 m, the collector's outlet height is being decreased from 1.1 m to 0.6 m. With these combinations, the SCPP system will have a constant gradient slope, whereby the solar collector with an inlet height of 0.1 m and an outlet height of 1.1 m is regarded as the steepest canopy profile. The constant variables are such that the rectangular plate of the absorber has an area of 75 m^2, the area of the trapezium plate of the absorber is 25 m^2, the inclination angle of the collector is 15°, the chimney diameter is 0.5 m, the concrete absorber thickness is 0.3 m and the transparent cover thickness is 0.005 m.

Table 3.4: Different solar collector's inlet and outlet heights

0.1 m Collector Inlet and 1.1 m Collector Outlet Heights	0.2 m Collector Inlet and 1.0 m Collector Outlet Heights	0.3 m Collector Inlet and 0.9 m Collector Outlet Heights
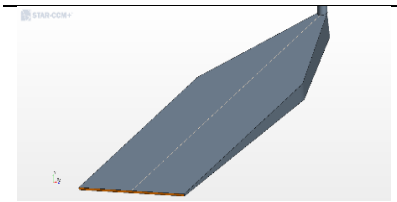	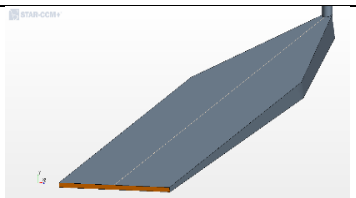	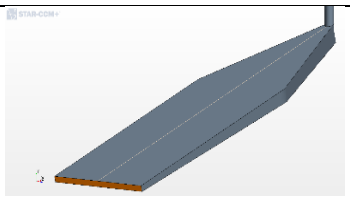
0.4 m Collector Inlet and 0.8 m Collector Outlet Heights	0.5 m Collector Inlet and 0.7 m Collector Outlet Heights	0.6 m Collector Inlet and 0.6 m Collector Outlet Heights
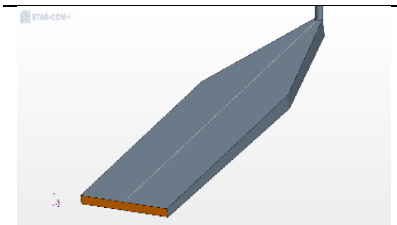	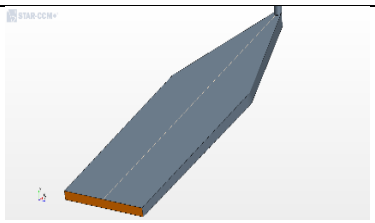	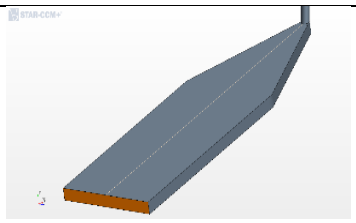

3.9.3 Simulation of Different Concrete's Absorber Thicknesses

In this particular study, the thermal storage capabilities of the concrete absorber are investigated. As the thicknesses of the concrete are manipulated, the most optimum thickness that offers a minimum cost will be selected for subsequent numerical investigation of this project. The areas of the rectangular and trapezium plates are constantly set to 75 m^2 and 25 m^2, respectively. This will result in a total solar collector area of 100 m^2. The inclination of the solar collector is 15°, in which the apex of the solar collector merges with a chimney of 0.5 m diameter. The height of the chimney is 26.85 m. The glass shell model has a thickness of 0.005 m and the effects of winds are neglected. In the case of the concrete absorber, a far-field projection distance of 5 m is modelled underneath the absorber, where the model now takes into consideration the effects of thermal losses to the ambient by both convection and radiation. The rectangular plate has 12.5 m length and 6 m width. In the solar collector, the air volume is set to 60 m^3 where the collector has an inlet height of 0.1 m and an outlet height of 1.1 m.

3.9.4 Simulation of Underneath Air Vents Oriented at Various Angles With Respect to the Horizontal Surface of the Absorber

A new model of an inclined SCPP with underneath air vents is developed in this investigation. The orientation angles of the air vents are manipulated in this study, as shown in Table 3.5. The figures shown in this table illustrate the side view of the solar collector's absorber, where the vents are installed at different angles with respect to the horizontal surface of the absorber. The angle of the vent is gradually increased from 10° to 90°. The other constant variables remain similar to the previous investigations where the solar collector occupies an area of 100 m^2. The collector is divided into rectangular and trapezoidal plate of 75 m^2 and 25 m^2 area, respectively. The collector is inclined at 15° to the horizontal ground surface. The chimney diameter is 0.5 m, with a height of 26.85 m. The transparent cover and absorber have shell thicknesses of 0.005 m and 0.3 m, respectively. The rectangular partition of the absorber has 12.5 m length and 6 m width. The collector inlet is specified to be 0.1 m while the collector outlet is set as 1.1 m. The position of the air vents is shown in Figure 3.8, where the vents are proposed to cover 6 m along the length of the collector, from the collector's inlet. This simulation involves 10 number of air vents, with each vent having a radius of 0.25 m, which results in a total vent area of 2 m^2.

Table 3.5: Different Orientation Angles of the Air Vents

Angle	Schematics
10°	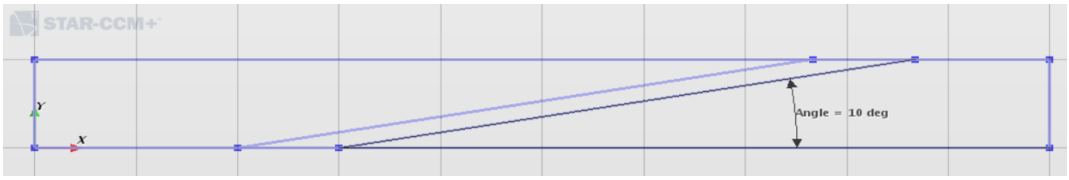
20°	
30°	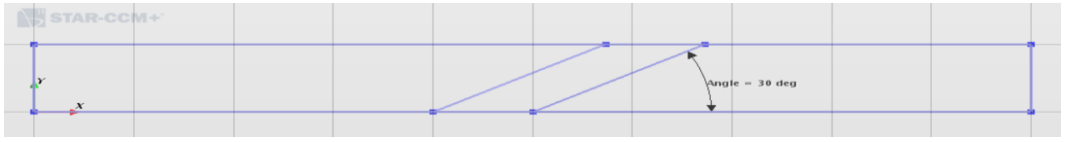
40°	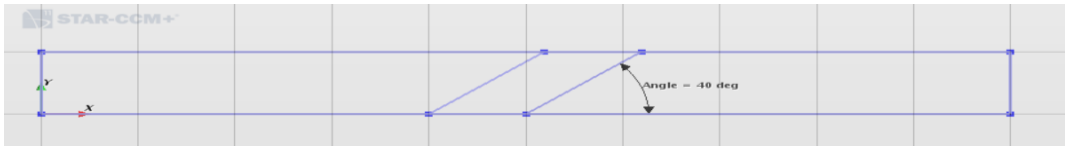
50°	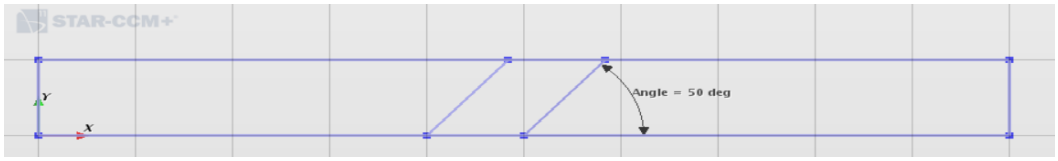
60°	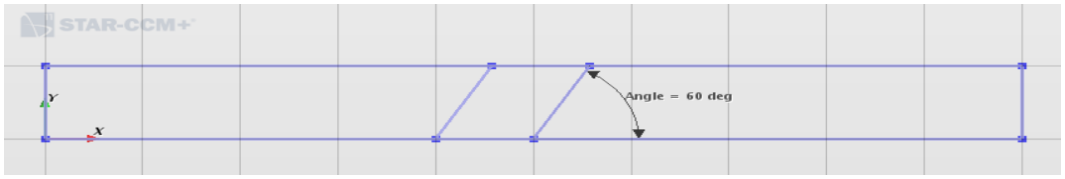
70°	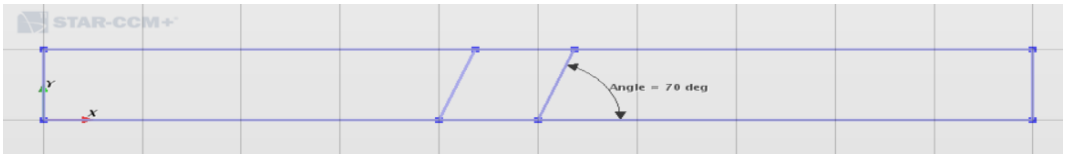
80°	
90°	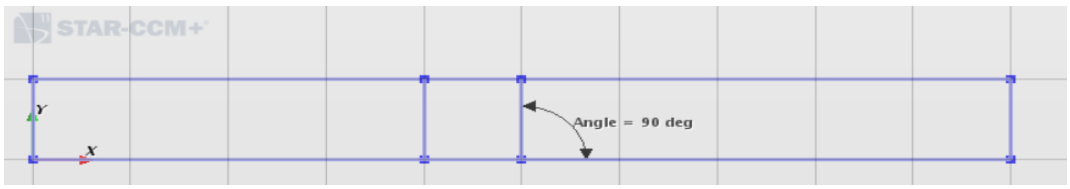

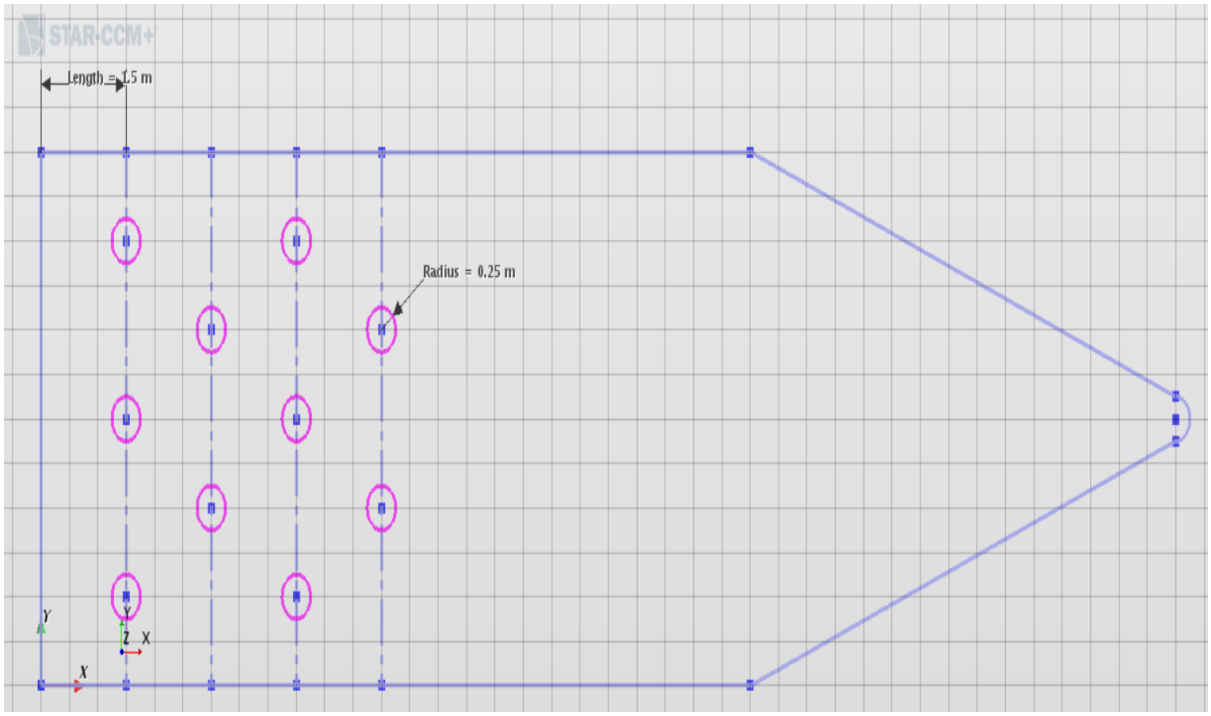

Figure 3.8: Position of the Vents

3.9.5 Simulation of the Various Air Vents' Positions in the Solar Collector

In this study, the positions of the vents in the solar collector are varied. This investigation is carried out to identify the fluid flow behavior with respect to the different positions of the vents in the solar collector. The absorber is first separated into four different partitions, which are labelled as 0 m < x ≤ 4 m, 4 m < x ≤ 8 m, 8 m < x ≤ 12 m, and 12 m < x ≤ 16 m. 10 number of air vents with 0.25 m radius each are installed in each of the partition, as shown in Table 3.6. The figures shown in this table illustrate the top view of the solar collector's absorber, in which the positions of the vents are shown. For the constant variables, the solar collector's area is fixed at 100 m^2, where the rectangular area is 75 m^2 while the trapezoidal area is 25 m^2. For the rectangular geometry of the solar collector, the length is 12.5 m while the width is 6 m. The inclination angle of the solar collector is 15°. The chimney diameter is fixed at 0.5 m throughout the investigation, where its height is 26.85 m. The glass shell has a thickness of 0.005 m and the absorber has a shell thickness of 0.3 m. The inlet height of the collector is 0.1 m while its outlet height is 1.1 m. The air vents are installed at 50° orientation angle with respect to the horizontal surface of the absorber.

Table 3.6: Different positions of the air vents

Different Partitions on the Absorber	Schematics
0 m < x ≤ 4 m	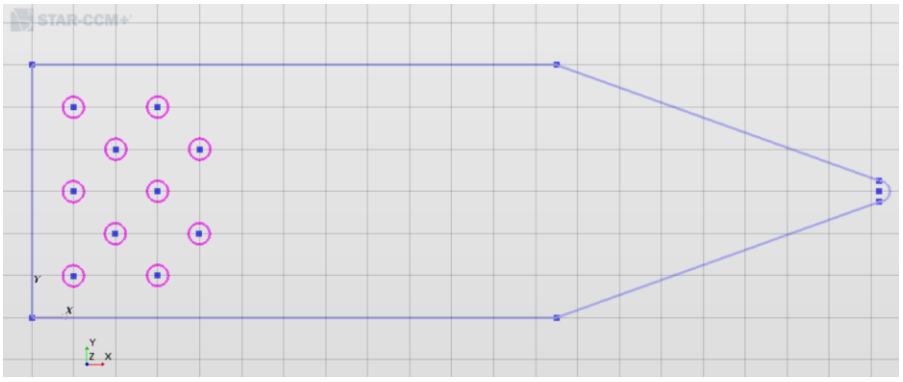
4 m < x ≤ 8 m	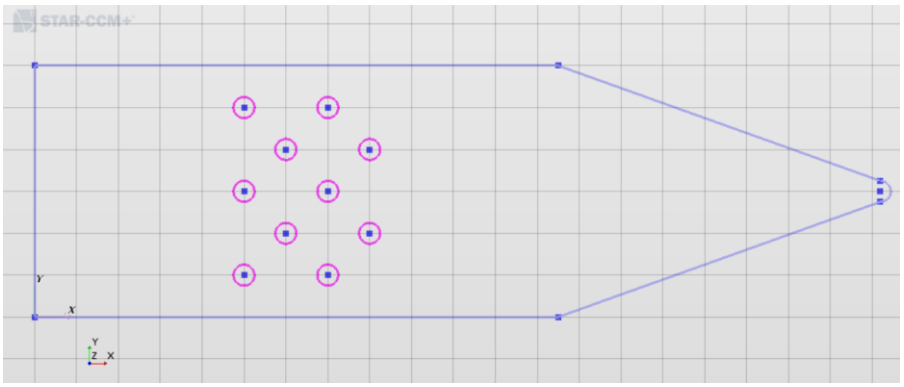
8 m < x ≤ 12 m	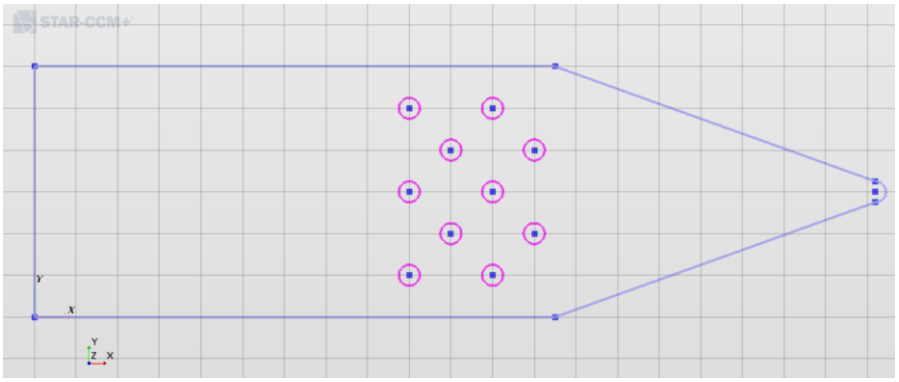
12 m < x ≤ 16 m	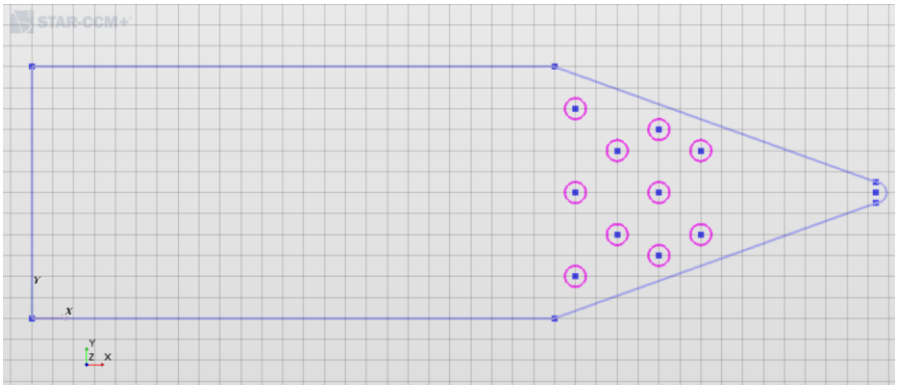

3.9.6 Simulation of Different Chimney Diameters

The investigation of the inclined SCPP with various diameters of the chimney is conducted to identify the possibility of preventing the choked air flow behavior at the chimney's throat. Six configurations of the inclined SCPP are simulated considering different chimney diameters of 0.5 m, 0.6 m, 0.7 m, 0.8 m, 0.9 m, and 1.0 m. As for the constant variables, the solar collector area is fixed at 100 m^2, where the rectangular and trapezium plates have areas of 75 m^2 and 25 m^2, respectively. The rectangular plate has 12.5 m length and 6 m width. The collector is inclined at 15° to the horizontal ground surface. The shell model is employed to define the thicknesses of the transparent cover and the absorber, at 0.005 m and 0.3 m, respectively. The chimney has a total height of 26.85 m. The inlet of the collector is specified as 0.1 m, while its outlet is 1.1 m. 10 numbers of air vents are included into the system, in which each vent has a radius of 0.25 m that leads to a total vent area of 2 m^2. The vents are oriented at 50° with respect to the flat absorber's surface. In this investigation, the positions of the vents are kept constant for all the six different configurations of the inclined SCPP involving various chimney diameters. The vents are designed to spread across nearly the whole area of the concrete absorber. It is expected that when the diameter of the chimney is gradually enlarged from 0.5 m to 1.0 m, the fluid's critical flow behavior can be eliminated.

3.9.7 Simulation of Air Vents' Opening Areas

The areas of the air vents are manipulated between 1 m^2, 2 m^2, 3 m^2, and 4 m^2. The analysis is conducted to identify the effect of the change in the air vents' areas on the air buoyancy and thermal performance of the inclined SCPP. The system now includes a chimney of 1.0 m diameter which has a height of 26.85 m. The chimney is joint at the collector's exit, in which the collector has a total area of 100 m^2. The collector's area of 100 m^2 is divided into two regions containing a rectangular plate of area 75 m^2 and a trapezium plate of area 25 m^2. The rectangular plate has 12.5 m length and 6 m width. The inclination angle of the collector is fixed at 15°. The collector's inlet has a height of 0.1 m while the collector's outlet has a height of 1.1 m. For the collector, the transparent cover has a shell thickness of 0.005 m and the absorber has a shell thickness of 0.3 m. The air vents are installed at 50° orientation angle with respect to the flat surface of the absorber. 10 numbers of air vents are used for each investigation. The diameter and radius of each vent is provided in Table 3.7 to meet the requirement of the total vents area.

Table 3.7: Diameter and Radius of Air Vent for Different Vents Areas

Total Vents Area	Diameter of Each Vent	Radius of Each Vent
1.0 m^2	0.36 m	0.18 m
2.0 m^2	0.50 m	0.25 m
3.0 m^2	0.62 m	0.31 m
4.0 m^2	0.71 m	0.36 m

3.9.8 Simulation of Numbers of Air Vents

In this investigation, the number of air vents is being manipulated to determine the possibility of enhancing the inclined SCPP's performance. The total area of the vents is now fixed at 2 m^2. Therefore, the diameter and radius of each 15° vent is provided in Table 3.8 for the different numbers of air vents. The collector's area is kept constant at 100 m^2, which consists of rectangular and trapezium plates of area 75 m^2 and 25 m^2, respectively. The rectangular plate has a length and width of 12.5 m and 6 m, respectively. The inclination angle of the collector is set at 15°. The collector's inlet is 0.1 m whereas the collector's outlet is 1.1 m. The glass has a shell thickness of 0.005 m while the absorber has a shell thickness of 0.3 m. The diameter of the chimney is 1.0 m. The height of the chimney is 26.85 m.

Table 3.8: Diameter and Radius of Air Vent for Different Number of Vents

Numbers of Air Vents	Diameter of Each Vent	Radius of Each Vent
5	0.71 m	0.36 m
10	0.50 m	0.25 m
15	0.41 m	0.21 m
20	0.36 m	0.18 m

3.9.9 Simulation of Water Thermal Storage

For this case study, the best configuration of the inclined SCPP with underneath air vents is selected for subsequent investigation of the water thermal storage. The manipulated variable in this study is the different volume of water storage, in which the water volume is based on a proportion of the total collector's air volume. The locations of the water energy storage layers and the underneath air vents are shown in Figure 3.9. The length and width of the water storage casing are fixed at 4.4 m and 0.8 m width, respectively. For the water volume which occupies

10 % of the collector's air volume, the depth of the water storage is 0.17 m. For the water volume which occupies 20 % of the collector's air volume, the depth of the water storage is 0.34 m. When the volume of the water occupies more than 20 % of the collector's air volume, the water filled tight casings will restrict the air flow under the transparent cover.

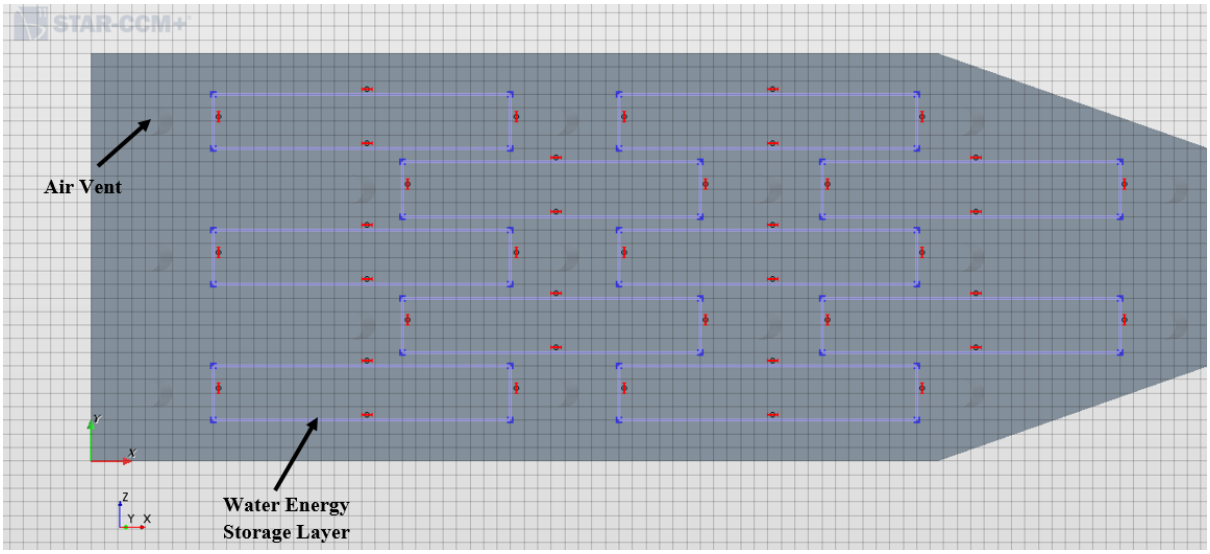

Figure 3.9: Locations of the Water Energy Storage Layer and Air Vents

In this study, the air vent area is 2 m^2. The number of vents is fixed at 15 vents. The radius of each vent is 0.21 m. The vents' angle is 50°. The diameter of the chimney is 1.0 m. For the solar collector, the area of the rectangular region is 75 m^2 while the area of the trapezium region is 25 m^2, which sums up to 100 m^2 collector area. The inclination angle of the collector is 15°. The thickness of the glass is 0.005 m, whereas the thickness of the concrete absorber is 0.3 m. The length and width of the collector's rectangular plate are 12.5 m and 6 m, respectively. The height of the chimney is 26.85 m. The collector's inlet is 0.1 m and the collector's outlet is 1.1 m.

3.9.10 Simulation of Inclined SCPP without Additional Chimney Component (Introduction of 4 Novel Designs)

In this study, four novel designs of the inclined SCPP are introduced. The physical geometries of the four respective designs are simulated to investigate the operation of the inclined SCPP without chimney for 100 m^2 collector. This study is based on the hypothesis that the collector tilt angle creates a height advantage for the buoyancy driven flow of the air. Therefore, the use of the inclined collector has the advantage of acting as chimney and collector in a single unit.

Table 3.9 shows the geometrical representations of the inclined SCPP without additional updraft tower, categorized under Design A, B, C and D.

Table 3.9: Schematics of the 4 Novel Designs and the Top Views of the Designs

Novel Designs	Schematics of the Design and the Location of Turbine Installation	Top View of the Designs and the Vents Locations
Design A	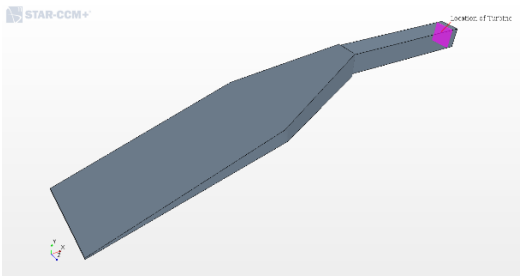	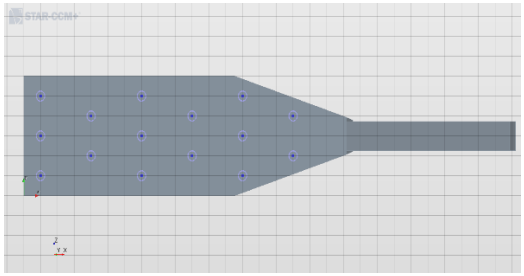
Design B	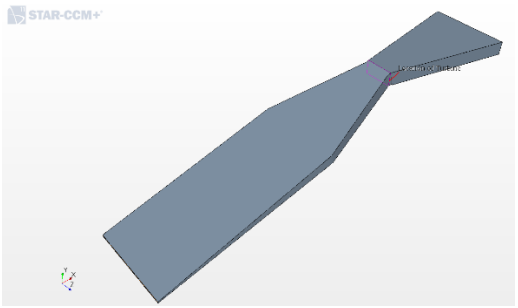	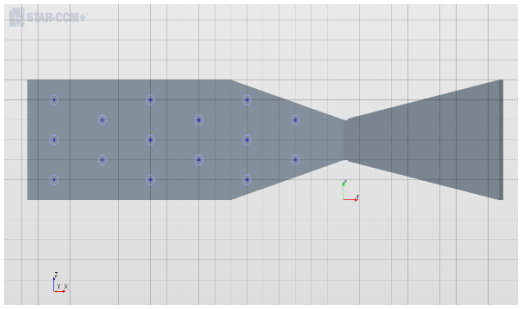
Design C	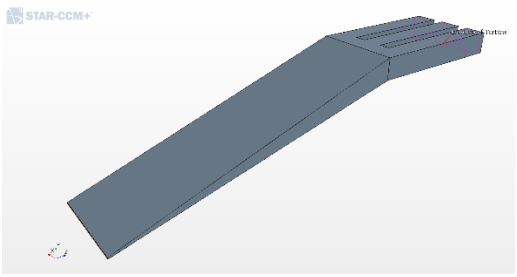	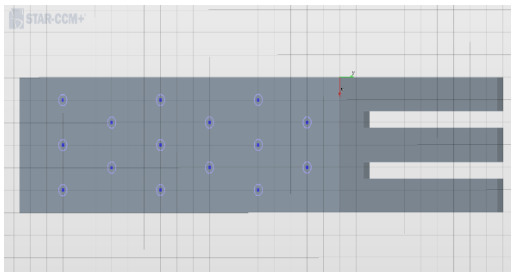
Design D	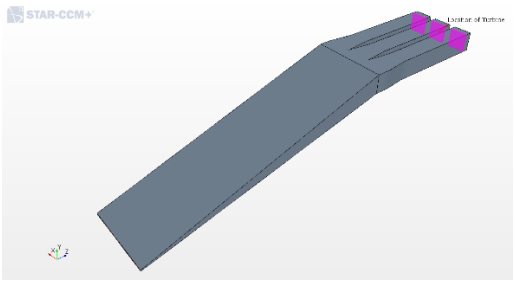	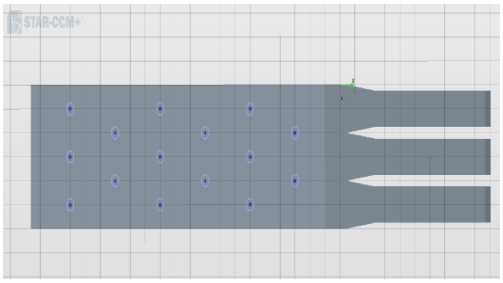

3.10 Summary of Methodology

The Solar Chimney Power Plant (SCPP) basic operation equations and its detailed physics were included in this chapter. In the simulation of the SCPP, the numerical model involved simplifying the geometry and physics of the Manzanares experimental pilot SCPP. The governing equations for the numerical model were solved by using Star-CCM+. The obtained solution would then be compared to the experimental results published in the literature for validation. The model development of the inclined SCPP with and without underneath air vents was also explained in this chapter, which employed similar physics and equations to those of the Manzanares SCPP. Furthermore, the boundary conditions of the simulation model were included in this chapter which described how the heat and energy transfer processes were related to their surroundings. This chapter also explained the case studies and the steps involved in achieving the project's objectives.

Chapter 4
Results and Discussions

4.1 Grid Independence Tests and Validation Results of the CFD Model of Solar Chimney Power Plant in Manzanares

The SCPP simulation model was adapted to the structural dimensions of the Manzanares experimental pilot plant for validation study. The system consisted of a chimney with a height of 195 m and a diameter of 10 m. A circular open-solar-air collector of 122 m radius comprised of the ground and transparent cover. The collector was raised to an average height of 1.85 m above the ground. In the simulation, a 2 m ground thickness was considered. The weather data that was used for the simulation were from the results presented by Haaf (1984) where the solar radiation intensity was 1000 W/m^2 and the ambient temperature 32^{o}C (305K).

4.1.1 Grid Independence Tests of the Manzanares SCPP Computational Domain

The computational domain of the Manzanares experimental SCPP was meshed using four different element sizes. These sizes were defined as coarse mesh with 97,779 elements, medium mesh with 534,473 elements, fine mesh with 1,018,318 elements and finer mesh with 2,489,637 elements, as shown in Figure 4.1, Figure 4.2, Figure 4.3, and Figure 4.4, respectively. According to Nia et al. (2015), the required wall distance Y plus value for the consideration of the boundary layer in a SCPP was 6, due to the low value of freestream velocity inside the system. In this study, considering a low freestream velocity of 1.0 m/s at 325 K, air density of 1.086 kg/m^3, air dynamic viscosity of 0.00001962 kg/m s, collector's reference length of 20 m, and desired y^+ value of 6, the wall spacing is about 0.002 m.

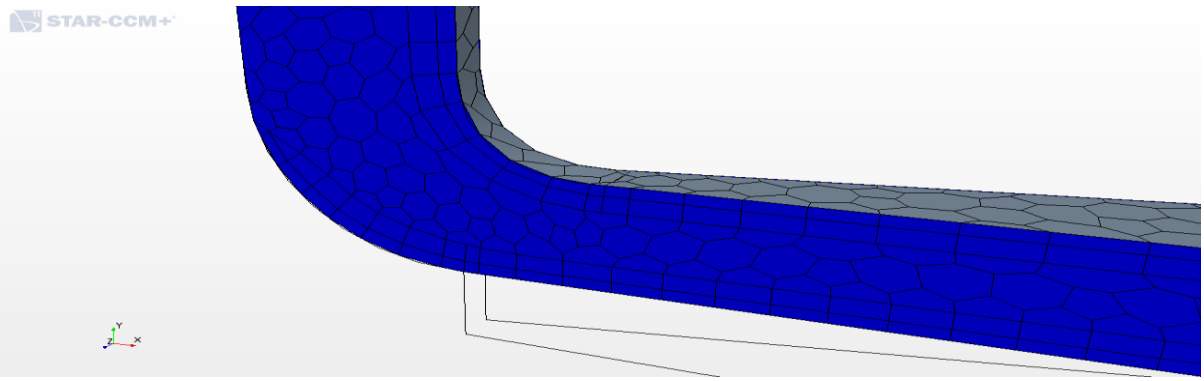

Figure 4.1: Coarse mesh representation showing the collector to chimney transition section

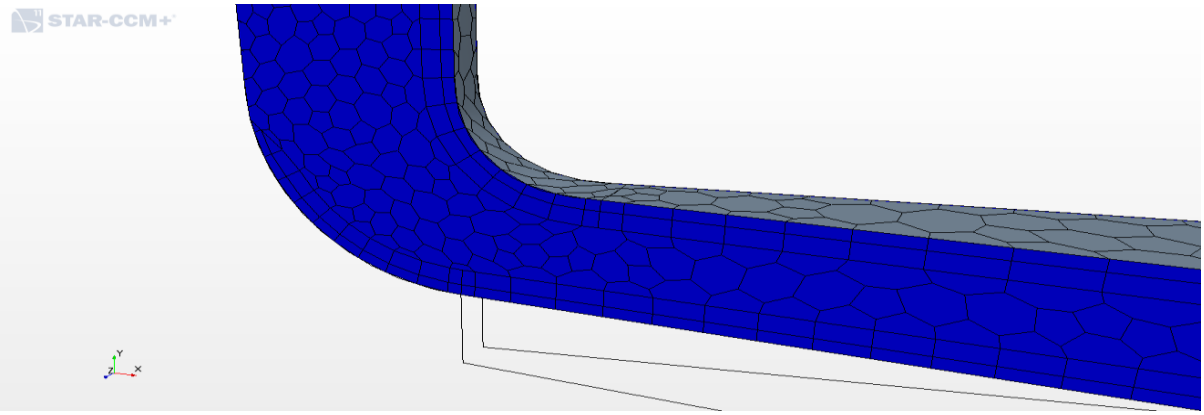

Figure 4.2: Medium mesh representation showing the collector to chimney transition section

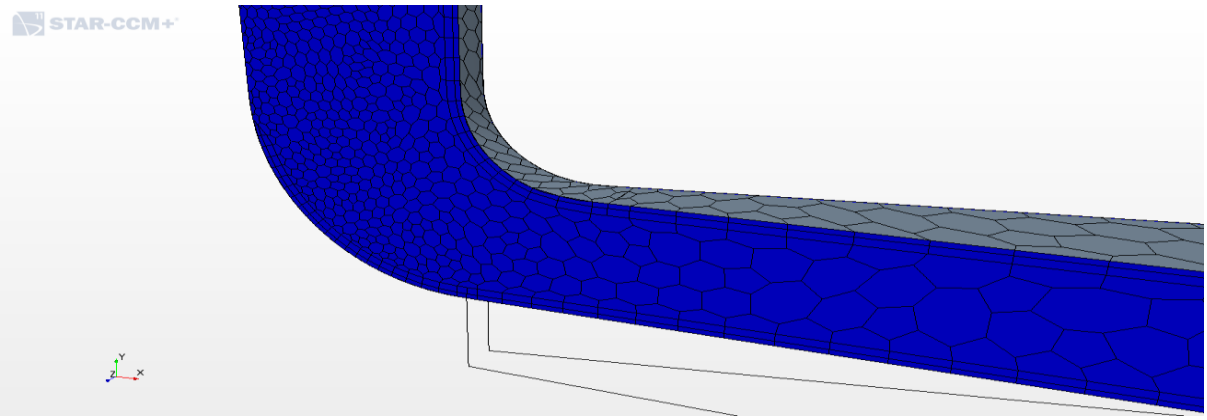

Figure 4.3: Fine mesh representation showing the collector to chimney transition section

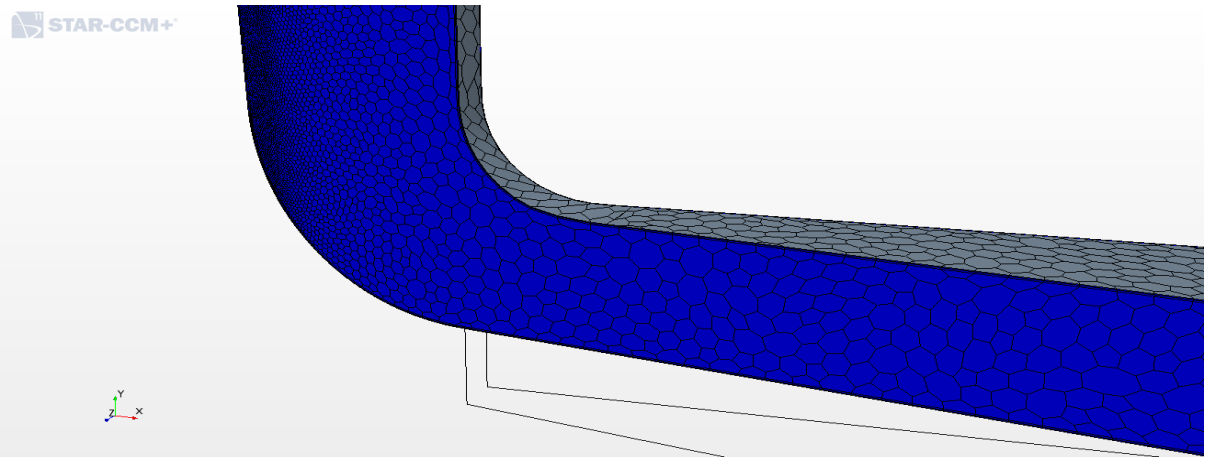

Figure 4.4: Finer mesh representation showing the collector to chimney transition section

Results of the grid independence tests are shown in Table 4.1. The tests considered the grid dependent parameters (temperature and velocity of operating air) using 1000 W/m^2 solar radiation intensity. The error percentage in temperature was found to be above 10% for coarse and medium meshes. Similar observation was found on the velocity output. The use of fine

mesh showed less than 1% difference when compared with the output results for the finer mesh. Considering the time used in the simulation, the fine mesh converged in 6 hours while the finer mesh took over 24 hours to converge and generate results. The fine mesh was employed for the simulation of the Manzanares SCPP at different solar radiation intensities of 1000 W/m^2, 800 W/m^2, 600 W/m^2, 400 W/m^2 and 200 W/m^2 for validation purposes.

Table 4.1: Grid Independence Tests of the Manzanares SCPP (At Solar Radiation Intensity of 1000 W/m2)

Sizes of Elements	Number of Elements	Temp. at Collector's Exit (K)	Temp. at Collector's Exit (^{o}C)	Temp. Diff. Error (%)	Velocity of Air at the Collector's Exit (m/s)	Vel. Diff. Error (%)
Coarse	97,779	318.42	45.42	11.12	5.39	30.54
Medium	534,473	318.75	45.75	10.47	6.56	15.46
Fine	1,018,318	323.94	50.94	0.31	7.71	0.64
Finer	2,489,637	324.1	51.1	-	7.76	-

4.1.2 Validation Results of the CFD Model of Solar Chimney Power Plant

The simulated Manzanares SCPP model results were compared with the published results of experiment on the Manzanares pilot operation reported by Haaf (1984). The experimental results as reported by Haaf (1984) was recorded on the 2nd of September 1982. The experimental results had been the most sought results for validation of numerical studies by most researchers. Furthermore, the simulation results of this study were compared to the simulation results of Guo et al. (2014) who were the first researchers to include the effects of solar radiation by using a radiation model and an additional solar load model in their SCPP simulation. The comparison of the updraft velocity between simulation results and the experimental published data is shown in Figure 4.5. The updraft velocity referred to the air velocity as the air flowed from the collector's outlet into the entrance of the updraft tower. In Figure 4.5, both simulation results were observed to be consistent with the experimental data on velocity of air in the system. The simulation model of this project was slightly higher than the experimental results on the updraft velocity for low solar radiation intensity cases. This was attributed to the assumption of uniform heat transfer at the absorber which in reality varied along the collector radius. In the morning, when the solar radiation intensity was low, the collector's air temperature was higher than that of the transparent cover. There was a transfer of heat from the air to the transparent cover. This resulted in a relatively lower collector's air

temperature in the experimental model of the SCPP. Consequently, the updraft velocity of the experimental data would be lower when the solar radiation intensity was low. During afternoon or evening, when the solar radiation intensity was high, the transparent cover temperature was higher than the collector's air temperature. Transfer of heat from the collector's air to the transparent cover did not occur. Therefore, at a higher solar radiation intensity, the simulation model of this project predicted well with the experimental published data.

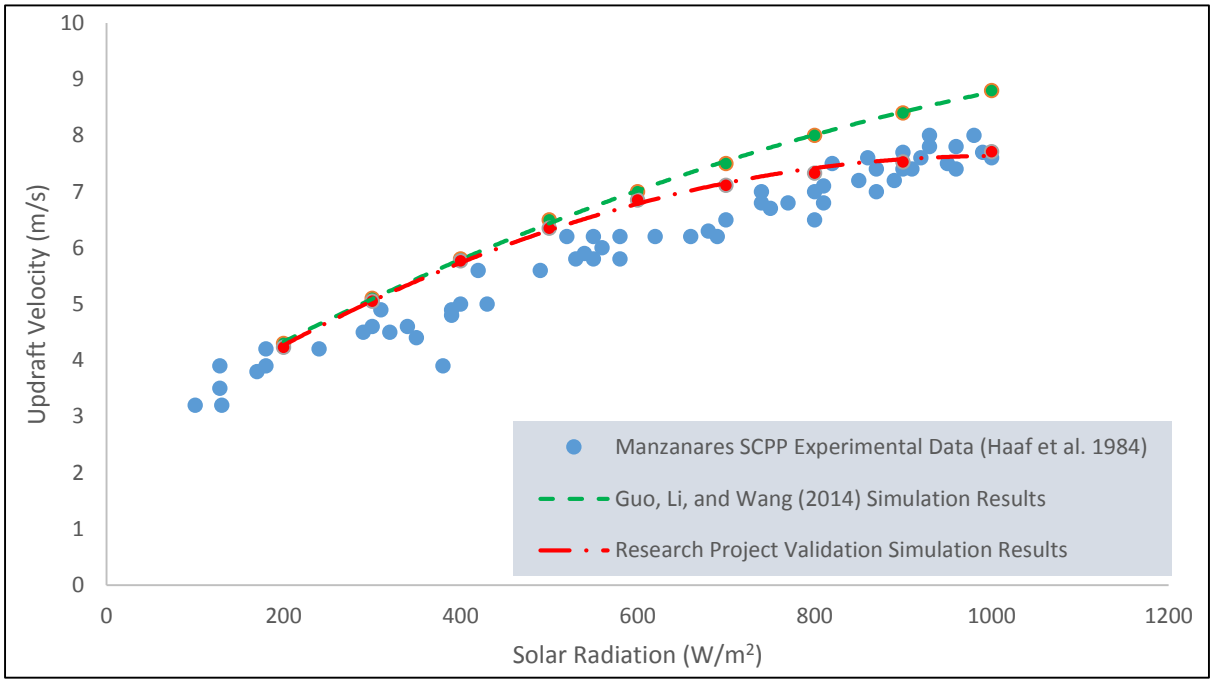

Figure 4.5: Comparison of Updraft Velocity between Simulation Results and Experimental Data

Moreover, the actual experimental model considered the effects of dust. In the morning, the dust was at a lower temperature and the dust was heavier due to the absorption of moisture. The dust accumulated on the transparent cover and partially blocked the solar radiation. In the afternoon and evening, the dust was at a higher temperature and the dust became lighter due to the evaporation of the moisture content. The dust was then removed by wind. This increased the transparent cover's transmissivity and allowed more solar radiation to transmit through the transparent cover. There was no data on collector component temperatures from published experimental results of the Manzanares pilot plant. The present work simulation results were compared to the results of Guo et al. (2014) for the operating fluid (air) temperature as shown in Figure 4.6. Both data were in agreement to one another with slight difference in temperature at the various solar radiation intensities.

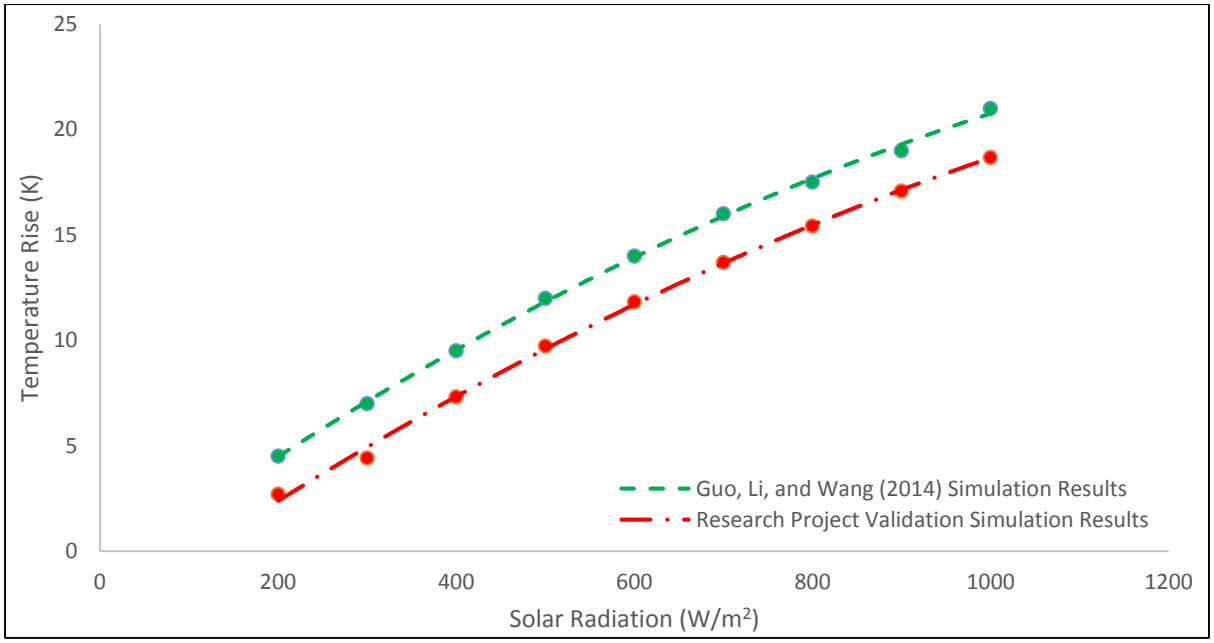

Figure 4.6: Comparison of Collector's Fluid Temperature Rise between Simulation Results

Furthermore, the results on the velocity of air at the fully-developed flow region in the chimney was 15 m/s from a cross-section average velocity analysis at 1000 W/m^2. The velocity vector for the buoyant air is shown in Figure 4.7. The temperature contour for the air at the connection between the collector and the chimney is shown in Figure 4.8. Figure 4.9 shows the temperature contour for the air flowing from inlet through the chimney with a temperature difference of about 20 K at 1000 W/m^2. These results were consistent with the data obtained from the experimental results of Haaf (1984) and also the simulation published results by Sangi et al. (2011). Therefore, the numerical simulation model of the SCPP in this study, which was developed by using Star-CCM+, proved to be reliable for adoption into the development of other models of SCPP. The physics and governing equations employed in the validation model were used to model the inclined SCPP in this research.

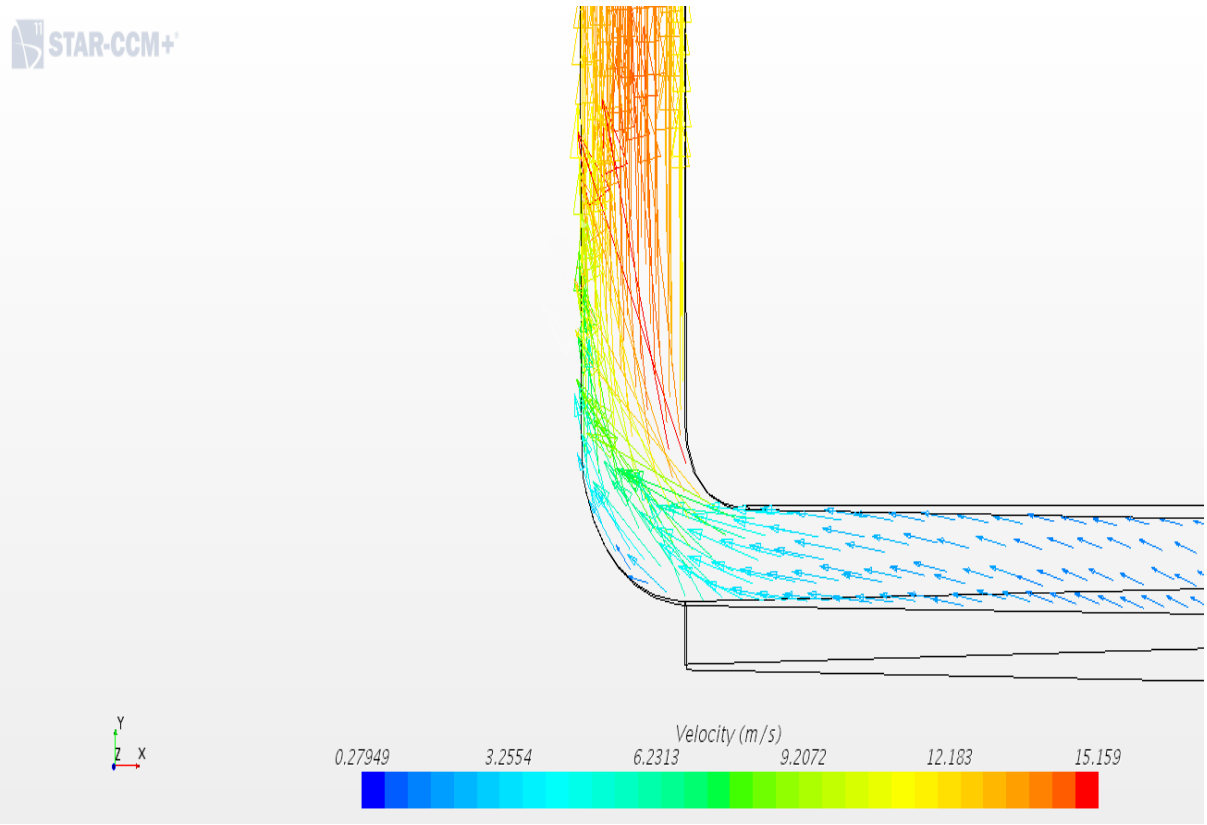

Figure 4.7: Velocity of air at the region of a fully developed flow inside chimney was 15 m/s

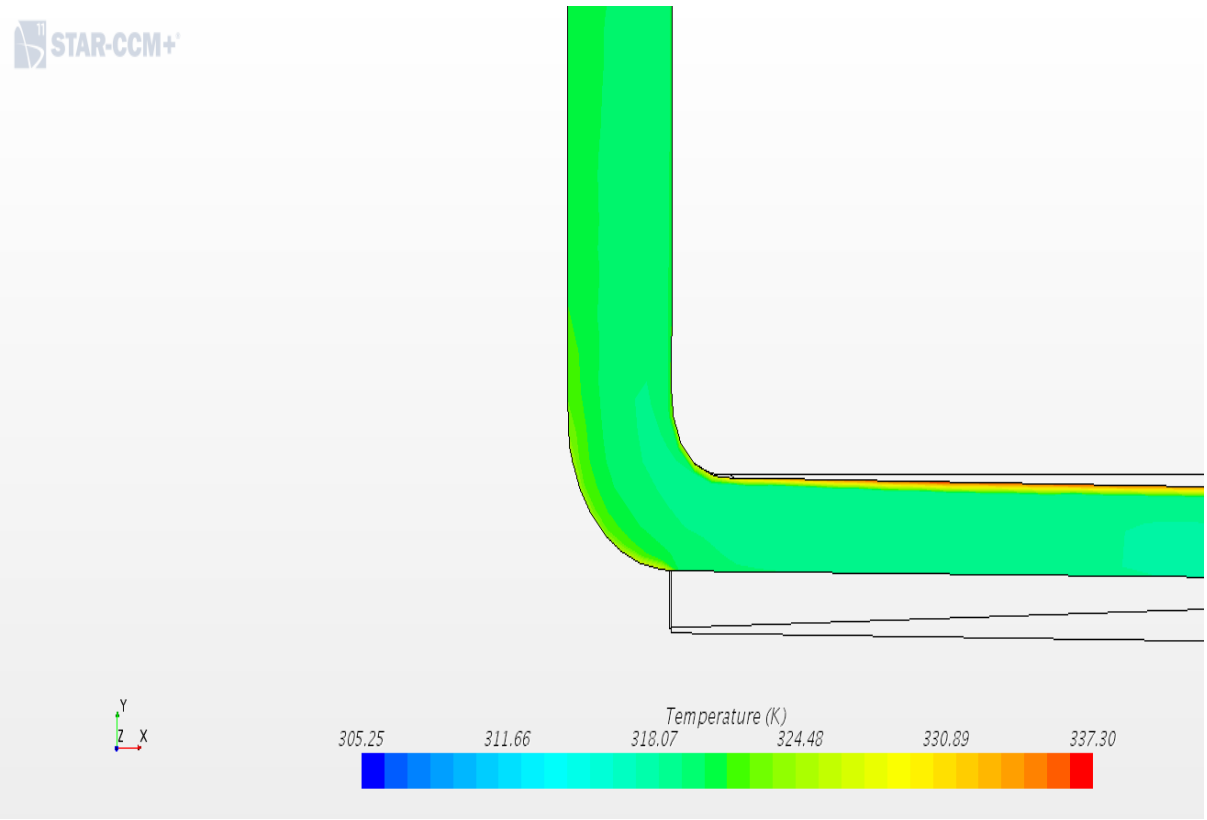

Figure 4.8: Temperature of air at the collector to chimney transition section

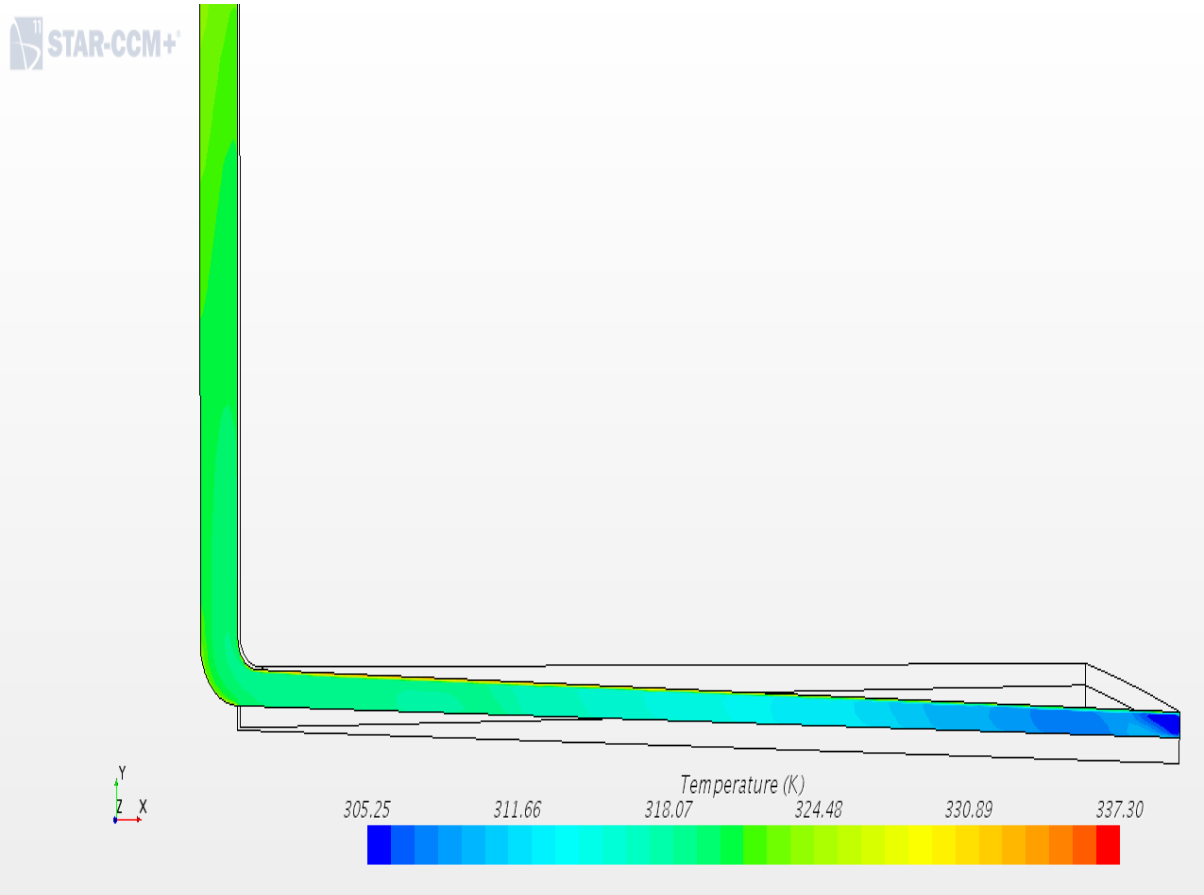

Figure 4.9: Temperature distribution along the complete radius of the solar collector

4.2 Grid Independence Tests Results of the Inclined SCPP

For the inclined SCPP model which was the focus of this research, the reference geometry used for the grid evaluation test involved a solar collector tilted at 15° to the horizontal ground surface. For the grid independence study, the solar collector consisted of a rectangular plate and trapezoidal surface integrated in one length. The rectangular plate had 5 m length and 15 m width making a surface area of 75 m^2. The trapezoidal plate had base width of 15 m connected to the rectangular plate and exit base width of 0.5 m. The length between the bases was 3.2 m making an area of 25 m^2 for the trapezoidal plate. Therefore, the total area of the solar collector was 100 m^2. The collector had the same inlet and outlet height of 0.5 m. The chimney height was fixed at 20 m. The transparent cover had a thickness of 0.005 m and the absorber's thickness was 0.3 m. Solar radiation data in Miri, Sarawak, was used as inputs data for the boundary conditions of the inclined SCPP model. Figure 4.10, Figure 4.11, Figure 4.12, and Figure 4.13 show the schematics of the coarse, medium, fine and finer grids, respectively.

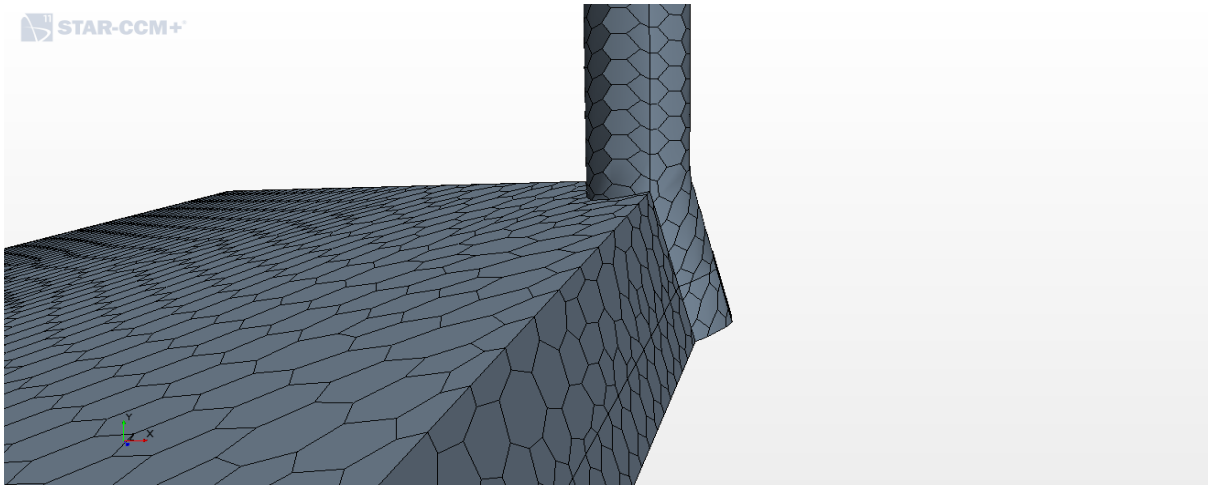

Figure 4.10: Coarse mesh of the inclined SCPP model

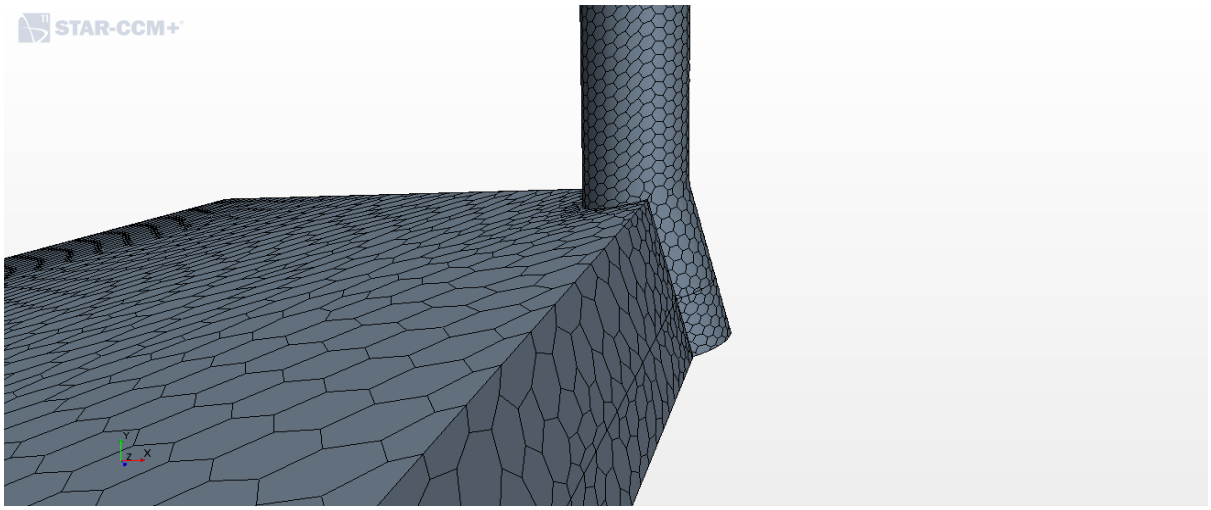

Figure 4.11: Medium mesh of the inclined SCPP model

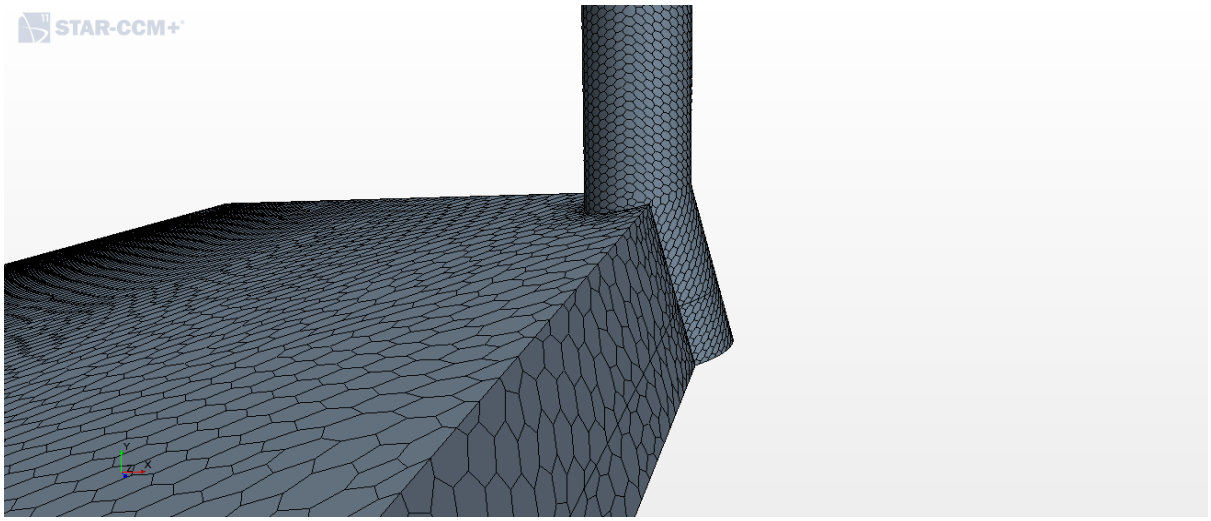

Figure 4.12: Fine mesh of the inclined SCPP model

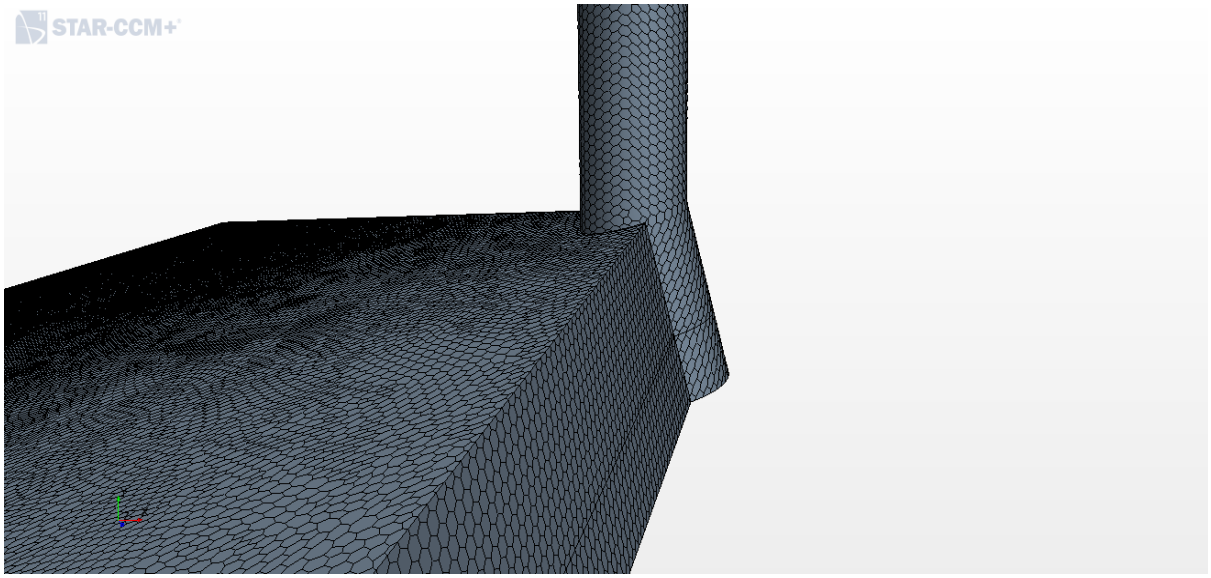

Figure 4.13: Finer mesh of the inclined SCPP model

The simulation was conducted using 1000 W/m^2 solar radiation intensity. The effect of grid sizes on the results of the dependent variables (temperature and velocity) were analyzed for air at the collector's exit. The results of the grid independence study are shown in Table 4.2. From these results, it was determined that the inclined SCPP model meshed by the coarse grids had higher percentage of error when compared to the model with finer grids. On the other hand, the use of medium and fine grids for the model led to approximate results to those of the finer grids. Hence, the medium mesh with 454,149 number of elements could give satisfactory and reliable results. This medium grid size was also selected to reduce the computation time during the simulation process.

Table 4.2: Results of the grid independence test for the inclined SCPP model

Sizes of Elements	**Number of Elements**	**Collector Exit Temp. (K)**	**Collector Exit Temp. at (°C)**	**Temp. Error (%)**	**Collector Exit Air Velocity (m/s)**	**Velocity Error (%)**
Coarse	58,860	329.997	56.997	2.70	3.967	2.11
Medium	454,149	328.929	55.929	0.77	3.916	0.80
Fine	735,288	328.898	55.898	0.72	3.911	0.67
Finer	1,449,050	328.501	55.501	-	3.885	-

4.3 The Effect of Collector Absorber Geometry on Collector Energy Transfer

In this section, the geometries employed in the development of the inclined solar chimney power plant and the energy transfer at the various geometry are discussed.

4.3.1 Geometrical Models Dimension Analyses for Heat Transfer Investigation

The main objective of this research was to develop a new design of an inclined solar chimney power plant for performance enhancement. The collector area was made constant at 100 m^2 for this study. The shape of the collector might have significant effect on the system operation with regards to rate of heat transfer. Thus, the current research investigated different configurations of length and width dimensions of the collector absorber with focus on the heat transfer and air velocity in the system. With reference to geometrical analyses presented in Section 3.9.1, the width and length of the collector were varied creating different geometries for the study. The collector had two major shapes integrated together which were rectangular and trapezoidal shapes. The rectangular plate had 75 m^2 area. The trapezoidal plate had 25 m^2 area. The volume of air in the solar collector was fixed at 50 m^3. The solar collector had constant inlet and outlet heights of 0.5 m. The inclination angle of the collector with respect to the horizontal ground was 15°. The concrete absorber and the transparent cover thicknesses were 0.3 m and 0.005 m, respectively. Solar radiation intensity of 1000 W/m^2 was used for the simulation. The length and width of the rectangular plate were varied which resulted in 12 different types of cases. The collector for the different cases were partitioned into four parts to determine the temperature at every 15 m^3 volume along the collector air channel.

4.3.2 Results Analysis of Energy Transfer in the Various Geometrical Models

4.3.2.1 Collector Absorber Temperature Analysis for the Various Geometrical Models

The results of the study for the temperature at the collector absorber considering the various cases are presented in Figure 4.14. The results showed the temperatures at every 15 m^3 partition from the collector inlet. The results showed that Case 1D, Case 1E, and Case 1F had highest average absorber temperatures. Moreover, these three cases observed the highest temperatures at the fourth partition of the absorber, which represented the collector exit/chimney base. The high values of the absorber temperatures revealed that Case 1D, Case 1E, and Case 1F were within the optimal ratios of the length and width configurations for the absorber. Absorber

temperature is an important factor in the process of generating air in motion in the solar collector. It causes the temperature difference between the working fluid and the ambient air.

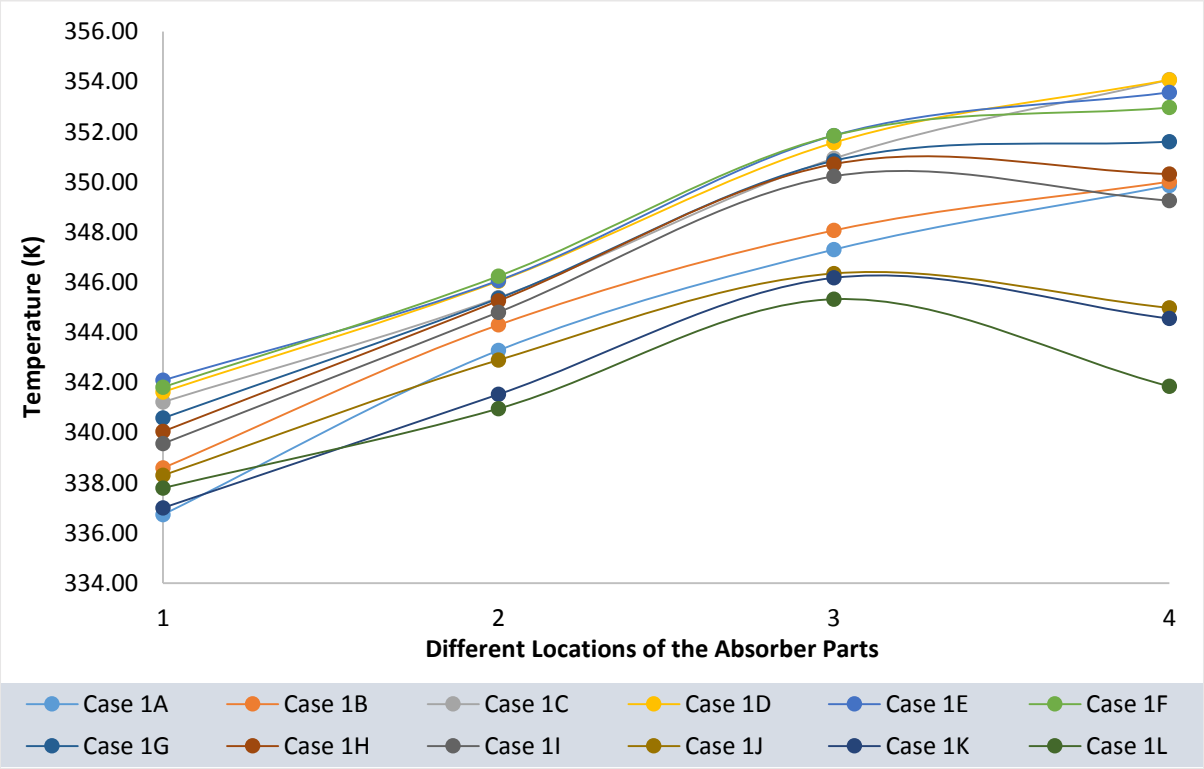

Figure 4.14: Comparison of temperature versus different locations of the absorber

4.3.2.2 Collector Cover Temperature Analysis for the Various Geometrical Models

The collector absorber temperature had effect on the collector cover as a result of re-radiation. The re-radiation heat transfer from the absorber to the transparent cover often reflected on the high temperature observed at the transparent cover. Considering the partitioning used in the study, Figure 4.15 shows the temperatures of the transparent cover for different cases of the collector configuration. The transparent cover temperatures for Case 1D, Case 1E, and Case 1F also had shown moderately high value compared to other cases. At the fourth partition of the transparent cover, which referred to the canopy area near the chimney, Case 1E was found to have a higher transparent cover temperature than Case 1F. This indicated the possibilities of higher thermal losses to the ambient from the transparent cover. Furthermore, it was apparent from Figure 4.14 and Figure 4.15 that Case 1J, Case 1K, and Case 1L had the lowest average temperatures at the absorber and the transparent cover components. It should be noted that these three cases represented the configurations where the absorbers had longer lengths in comparison to their widths.

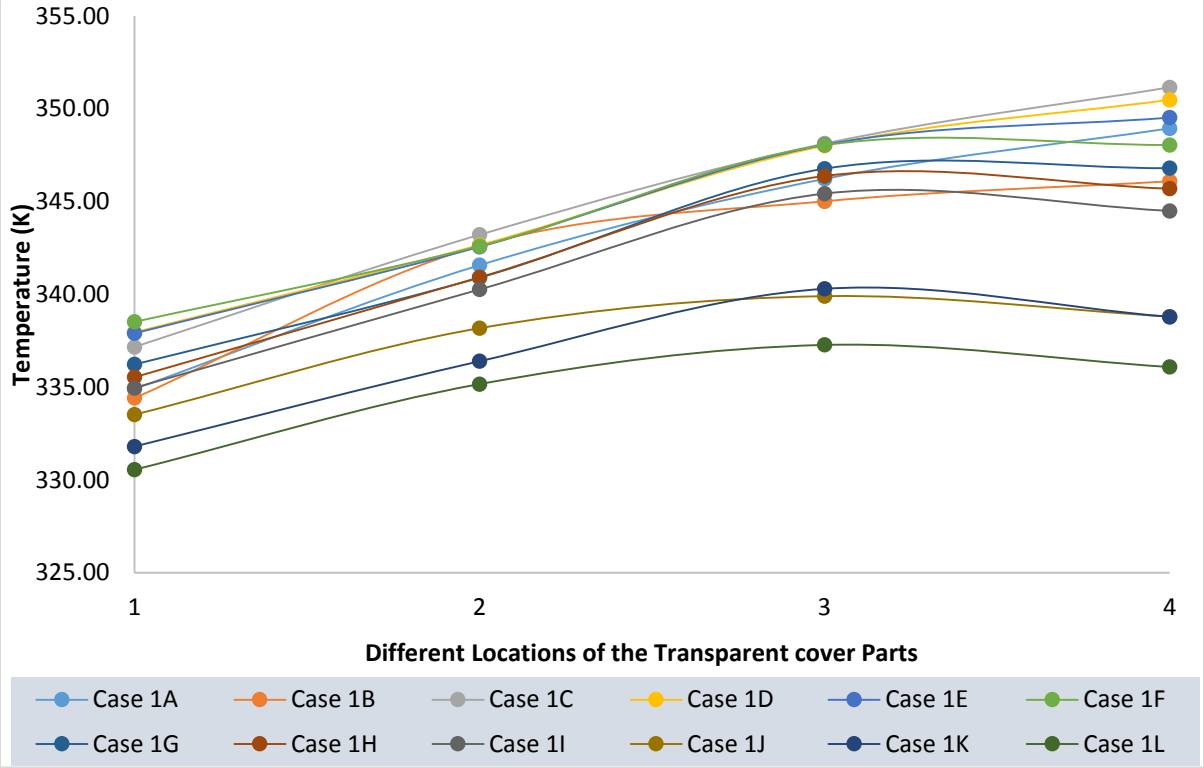

Figure 4.15: Temperature versus different locations of the transparent cover parts

As can be seen from Figure 4.14 and Figure 4.15, the trends in the temperature changes along the different partitions of the absorber and the transparent cover followed a similar pattern for Case 1J, 1K and 1L. From the first to the third partitions, the temperatures increased significantly before the values started to reduce up to the fourth partition. When there was an increased length of the collector, while the collector was being inclined at a fixed angle of 15°, the collector exit gained a height advantage for chimney installation. In a situation where the inclined length became excessively long with small width, there was reduced temperature at the absorber and the cover as can be seen in Cases 1J, 1K and 1L. At optimum length and width of the absorber (without having the absorber's length and width being excessively long), the temperatures of the absorber and transparent cover were found to be high and also maintained consistent temperature increase along the collector flow direction as can be seen in the Cases 1E and 1F.

4.3.2.3 Collector Air Temperature Analysis for the Various Geometrical Models

A closer inspection of the collector's air temperature is presented in Figure 4.16. The results showed that the air temperature for the various model were close to each other except for Case 1A. In Case 1A, it was observed that the air temperature was considerably higher than the air

temperatures in the other models. This was attributed to the heated air being trapped in the collector/greenhouse for a longer duration of time leading to higher convective heat transfer from the absorber to the air. The cause of the residence time linked to the long width against the short length which had low streamline flow channel and the buoyant air experienced circulation compared to other cases. For instance, in Case 1A, multiple airflow vectors experienced difficulties to converge from a long 30 m width to a short chimney inlet width of 0.5 m. This caused pressure losses at the collector-to-chimney transition region due to the restriction at the chimney air-flow cross section. Therefore, the air particles stayed longer in the solar collector and received a higher amount of heat from the absorber.

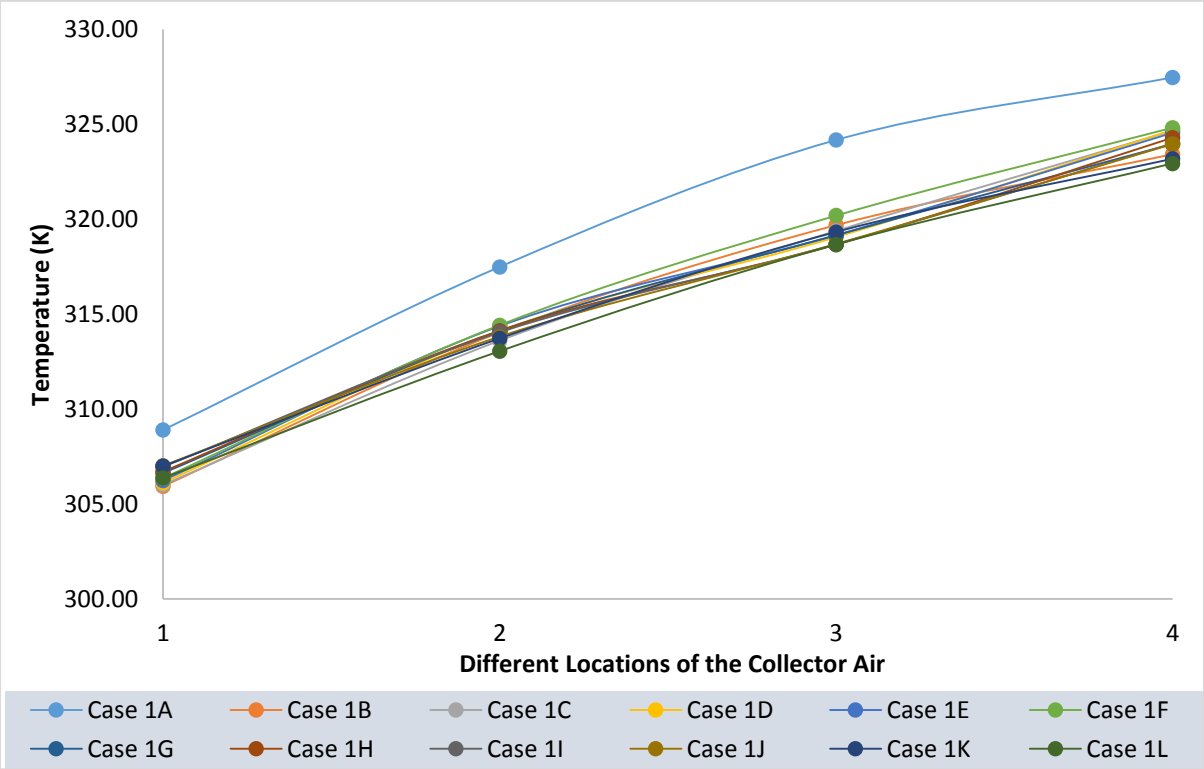

Figure 4.16: Temperature versus different locations of the collector's air

4.3.3 Results of Air Flow in the Various Geometrical Models

4.3.3.1 Collector Air Velocities Analysis for the Various Geometrical Models

The analysis of the air flow in the various models further buttresses the effect of the geometrical dimensions on the energy transfer of the models. The air velocities for the different geometrical models are presented as shown in Figure 4.17. The system air velocity was found to increase as the length of the collector increased ranging from Case 1A to Case 1F and dropped from

Case 1G to Case 1L. In Figure 4.17 it was also observed that Case 1E and Case 1F predicted the highest air velocity at 4.401 m/s and 4.416 m/s, respectively. These results demonstrated that both Cases 1E and 1F were within the optimum dimension ratios which ensured higher air velocities in the collector. Geometrical configurations in these cases induced higher rates of heat energy removal from the transparent cover and the collector absorber.

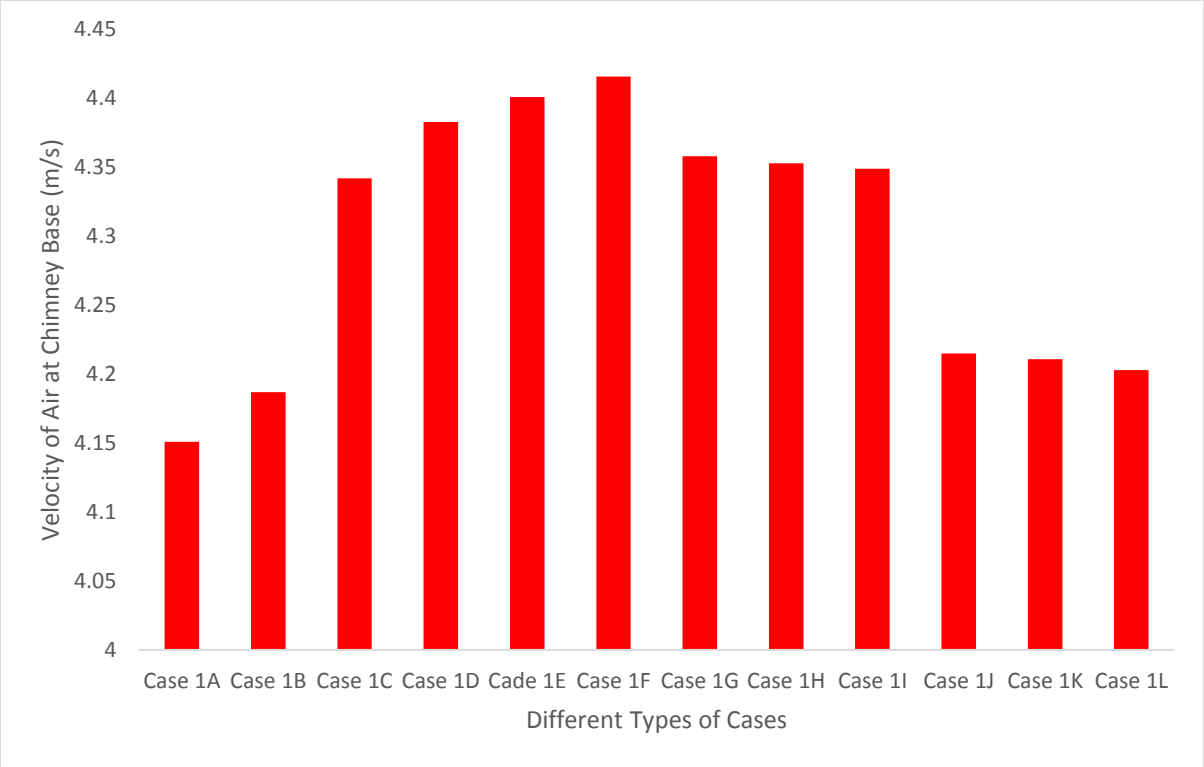

Figure 4.17: Velocity of air at the chimney base for all 12 cases

For Case 1A, there was a constriction on the airflow at the collector-to-chimney junction. The constricted channel flow led to the heated air being trapped inside the solar collector. This caused high thermal loss to the ambient through the cover. At the same time, the occurrence of air circulation/reversed flow was observed in Case 1A, as depicted by Figure 4.18. The reversed flow of air happened due to the low driving force generated in the system.

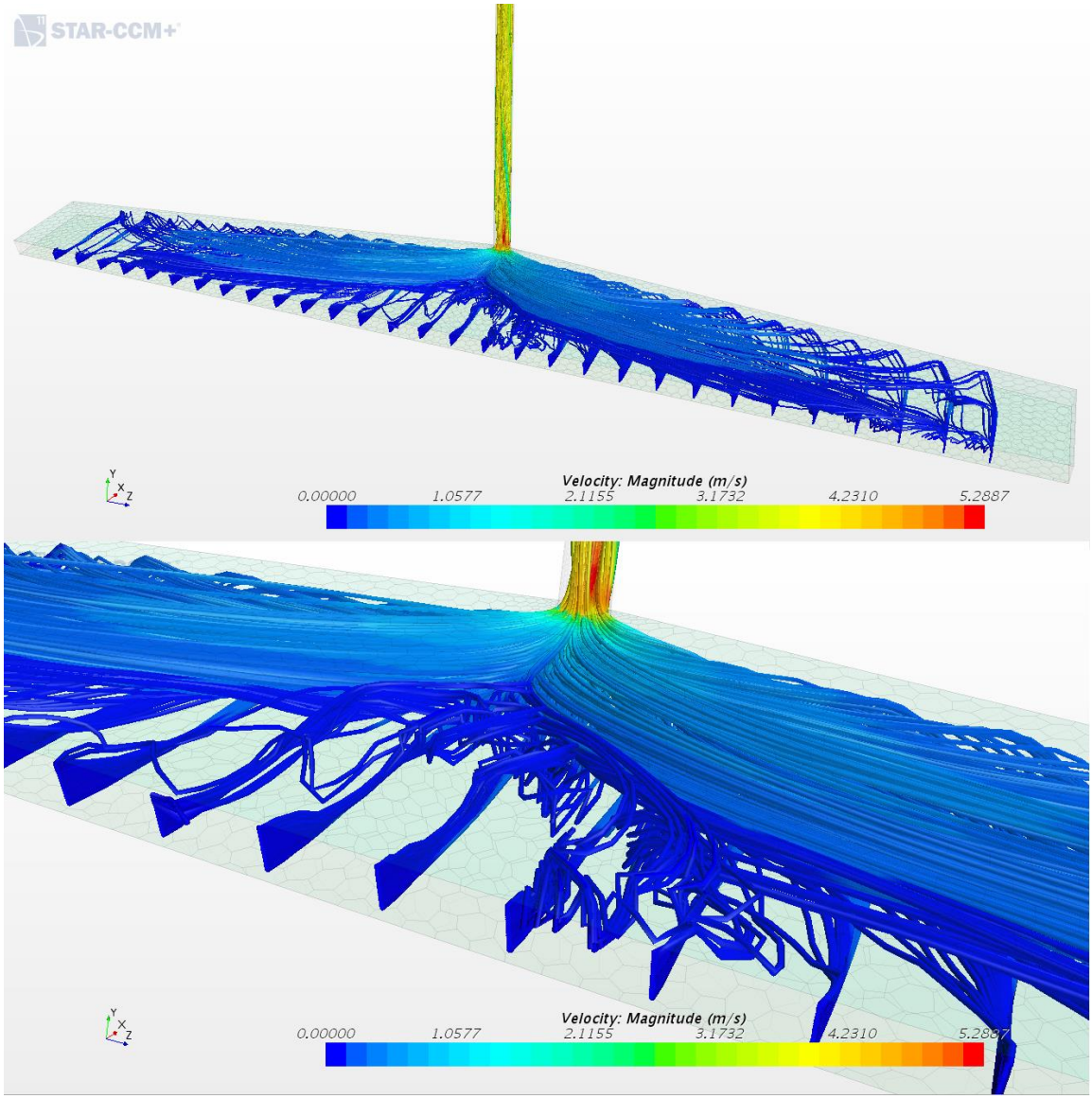

Figure 4.18: Velocity streamlines showing reversed air flow in Case 1A

On the other hand, the flow reversal phenomenon did not occur in the other models/cases. In Case 1L, which involved a long solar collector with a short width, the velocity streamlines in Figure 4.19 showed continuous air flow stream from the collector's inlet to the chimney's inlet. This further proved that the collector tilt angle and the increased length of the collector created a height advantage for the buoyancy driven flow of the air. From Figure 4.19, it was also important to note that the peak velocity occurred at the base of the chimney. This indicated that the air property at the base of the chimney was an important factor to determine the system's performance. Although the area of the trapezoidal streamlined plate was kept constant at 25 m^2, there existed a threshold limit for the effective length between the parallel sides of the trapezoidal area. If the length threshold was reached, the air flow started losing heat to the surroundings.

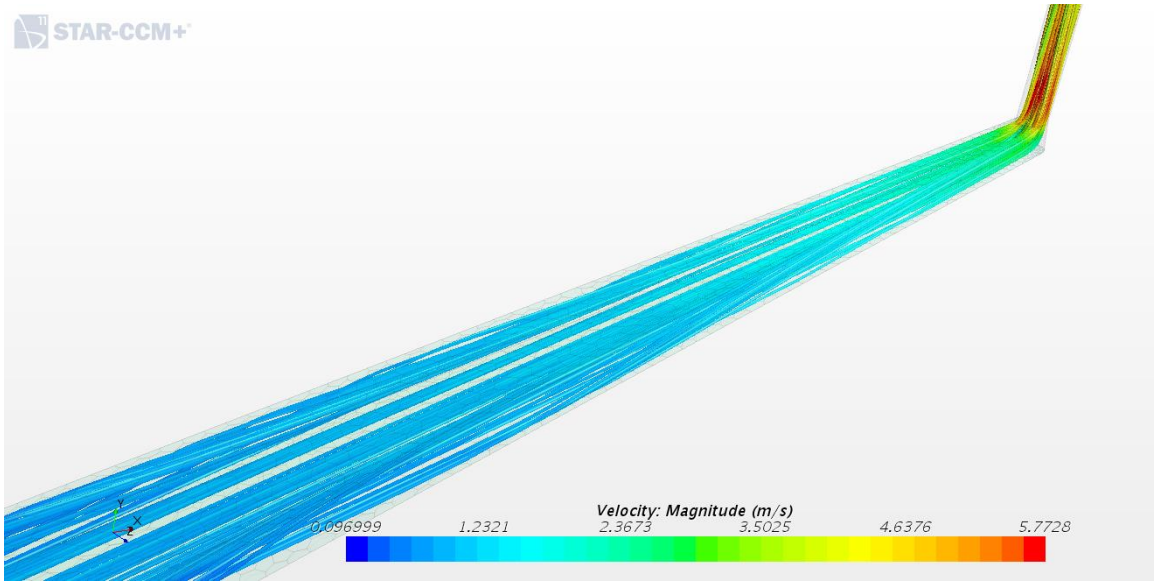

Figure 4.19: Velocity streamline for Case 1L

The flow stream was also observed to show no reverse flow for other cases such as can be seen at the near optimum length represented in Case 1E. Figure 4.20 reports the velocity magnitudes of the air flow in the system for Case 1E with no flow circulation or reversal at the collector.

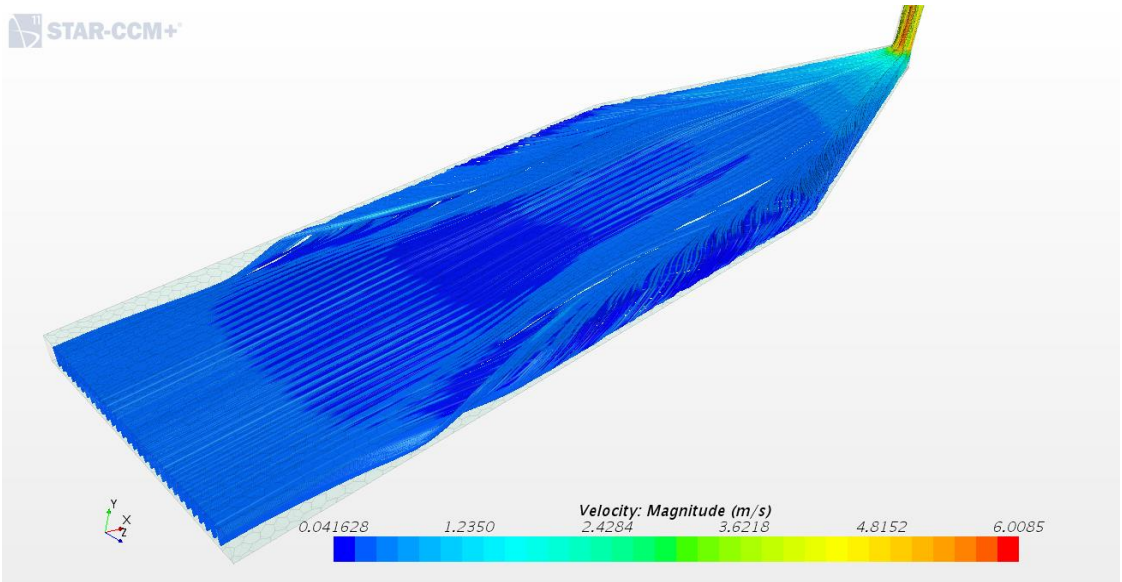

Figure 4.20: Velocity streamlines for Case 1E

4.3.3.2 Collector Air Mass Flow Rate Analysis for the Various Geometrical Models

With respect to the various geometrical models, the average air temperature at the base of the chimney (cross-sectional area average) was employed in determining the air density. The mass flow rate was determined considering the collector exit air velocity. The results of the air mass

flow rates for the various geometrical models is presented in Figure 4.21. The results showed Case 1E and Case 1F with highest mass flow rate in comparison to other cases. For Case 1E and Case 1F, the mass flow rate generated was 0.92 kg/s.

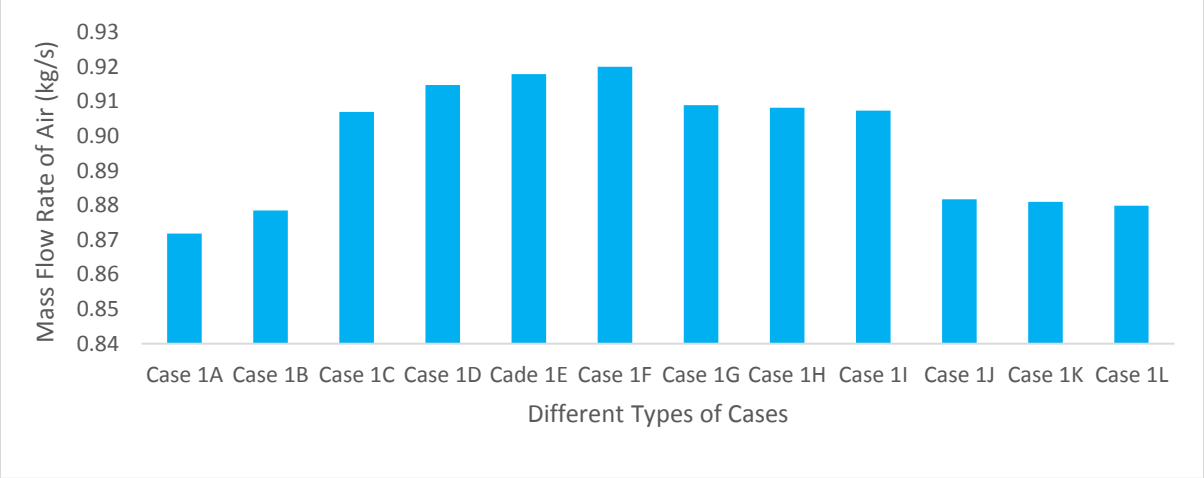

Figure 4.21: Mass flow rate of air for different types of cases

4.3.3.3 System Power Output Analysis for the Various Geometrical Models

For the various geometrical models, the possible electrical power output was evaluated using Equation 3.47 with consideration of the turbine efficiency at 70%. The results as shown in Figure 4.22 depicts that Case 1E and Case 1F produced the highest electrical power output rated at 6.22 W and 6.28 W, respectively.

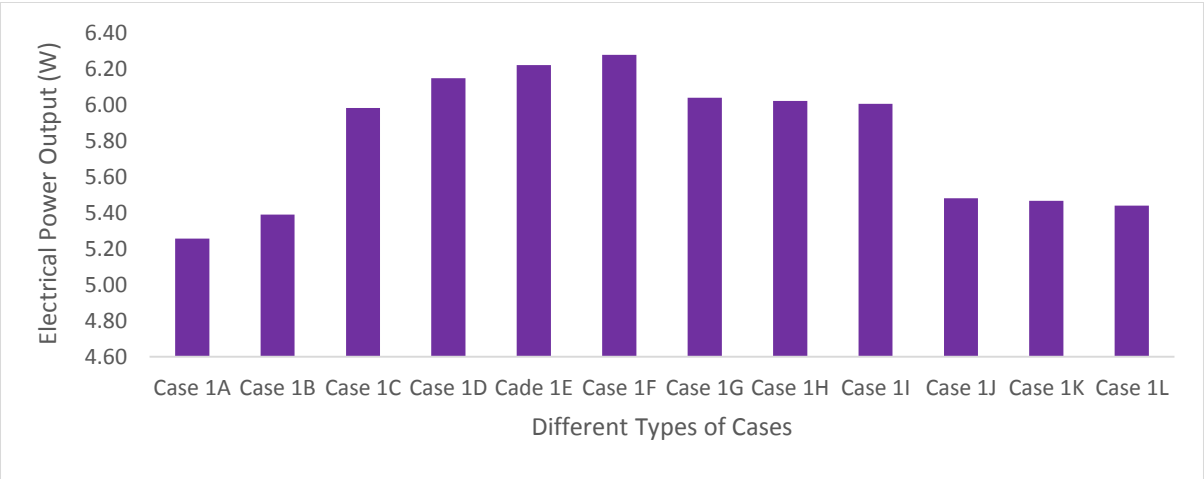

Figure 4.22: Electrical power output for different types of cases

4.3.3.4 Collector Efficiency Analysis for the Various Geometrical Models

The analysis of the collector efficiency was important to factor in thermal losses into the performance of the collector. The analysis of the collector efficiency is presented in Figure 4.23. The results showed that Cases 1E and 1F had about 21.2% and 21.6% efficiency respectively. Therefore, considering that the absorber temperature in Case 1E was higher and there existed opportunities for further enhancement, this was the deciding factor to select Case 1E as the reference geometry in this research study.

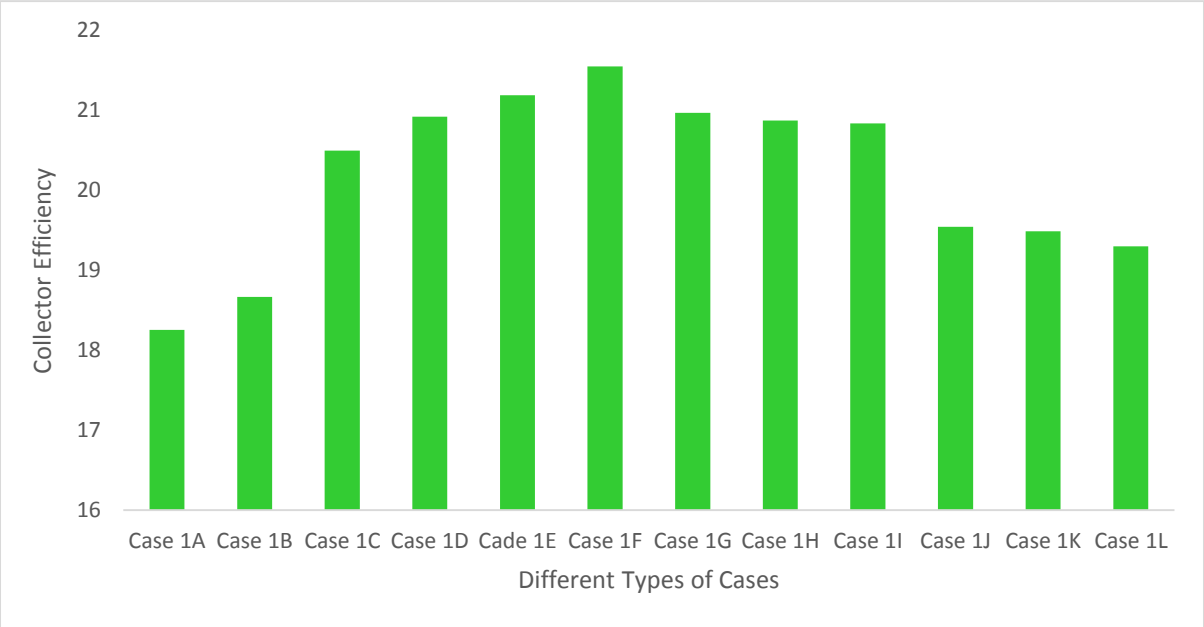

Figure 4.23: Collector efficiency for different types of cases

4.4 Effect of Canopy Profile on the Performance of the Inclined Solar Chimney Power Plant

The results of the temperature and air velocities of the various geometrical models of inclined SCPP presented in Section 4.3 showed that the inclined SCPP with collector component described as Case 1E performed best. In Case 1E, the absorber temperature showed potentials for further thermal energy recovery. Hence, Case 1E geometrical model was investigated further for possible enhancement. The model was developed such that the gap between the absorber and the transparent cover remained constant from inlet to exit of the collector. Moreover, the air volume was varied to determine the air volume that was most appropriate for 100 m^2 solar collector absorber surface. With the determination of the optimum air volume, a variation in the collector's inlet gap and the outlet height was studied at constant air volume to

determine the best configuration for buoyancy enhancement. The different geometrical configurations for the varied inlet and outlet heights of the system were described in Section 3.9.2 with explanation of the manipulated and constant variables used in this investigation. The schematics of the geometries which were used in the numerical study of the canopy profiles were also provided.

4.4.1 Effect of Air Volume on Buoyancy in the Incline Solar Collector of the System

4.4.1.1 Velocity of Air at Chimney Base for Case 1E at Different Air Volume

The study on the air flow velocity measured at the collector exit/chimney base was conducted to determine the relationship between the air volume and buoyancy. The velocities of the air at different air volume deduced from the investigation are presented in Figure 4.24. The results are presented with respect to different solar radiation intensities of 200 W/m^2, 400 W/m^2, 600 W/m^2, 800 W/m^2 and 1000 W/m^2. The results showed that when the volume of air was increased from 30 m^3 to 60 m^3, the air velocity at the chimney base increased significantly. When the air volume was further increased from 60 m^3 to 70 m^3 for the flat canopy profile, the velocity of air at the chimney base observed a significant drop. The results showed that the air volume had a direct impact on the air velocity. It was found that higher heat removal occurred at the absorber as the air volume increased but when the air volume was in excess, the available energy from the collector was not enough to excite the internal energy in the air to higher velocity. The higher volume reduced the temperature of the absorber, and it will reduce the re-radiation from the absorber to the transparent cover. As a result, most of the thermal energy from the absorber was transferred by the air creating buoyancy to drive the air into the chimney. The results showed that for the 100 m^2 absorber investigated with varying air volume, the 60 m^3 volume was optimum which had inlet to outlet height of 0.6 m between absorber and transparent cover. The 60 m^3 air volume generated 4.43 m/s at the chimney base when the solar radiation intensity was 1000W/m^2. Furthermore, this result showed a satisfactory agreement with the numerical investigation by Ghorbani et al. (2015). It was reported by Ghorbani et al. (2015) that when the collector's air volume was increased to a great extent, the velocity of air at the collector's exit started to reduce. This was because at low internal energy of air, the buoyancy force was low leading to recirculating flow instead of flowing to the chimney.

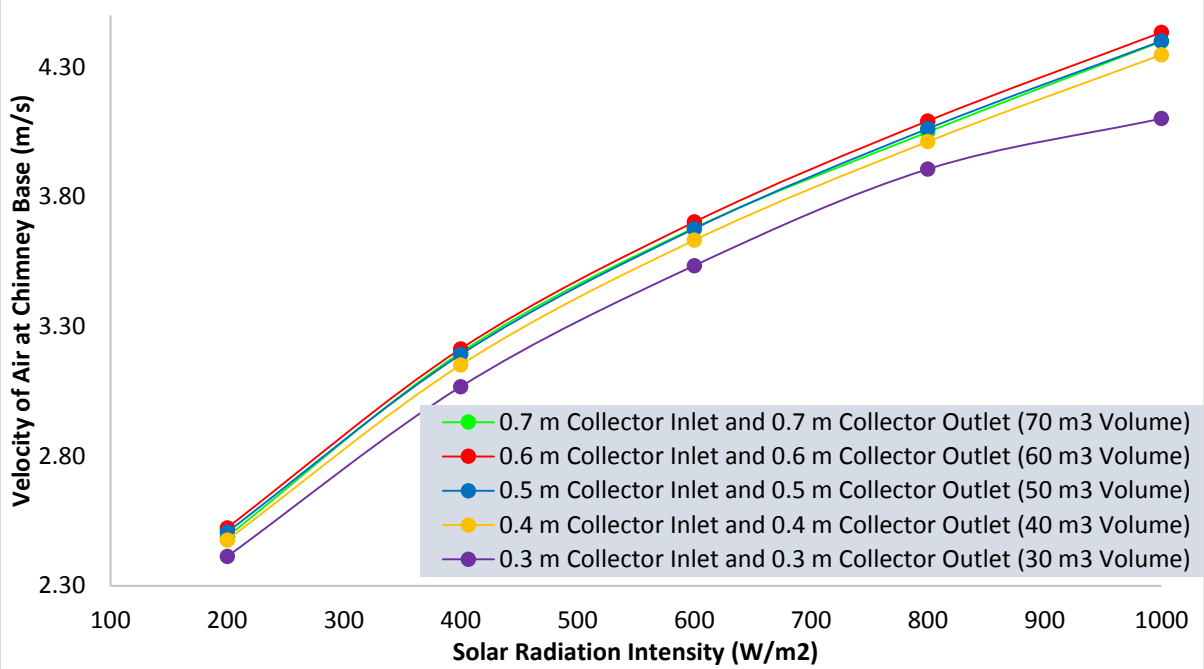

Figure 4.24: Velocity of air at the chimney base against the solar radiation intensity for different air volumes

4.4.1.2 Velocity of Air at Chimney Base for Case 1E at Optimum Air Volume (60 m^3)

The results of the varied air volume showed that the optimum air volume for 100 m^2 concrete absorber used in this study was 60 m^3. This configuration generated the highest air velocity of 4.43 m/s at 1000 W/m^2 solar radiation. Further investigations were conducted for the geometrical dimension of Case 1E with air volume of 60 m^3. The inlet and the outlet gaps/heights of the solar collector were varied to determine the best configuration for enhanced velocity and power output. The investigation was conducted for six configurations and the results of the air velocity at the base of the chimney with respect to different solar radiation intensities are presented in Figure 4.25. The results showed that the best configuration was when the transparent cover was raised 0.1 m at the collector inlet (inlet height) and the gap at the collector exit was 1.1 m, thus obtaining maximum air velocity. A combination of 0.1 m collector inlet height and 1.1 m collector outlet height at 1000 W/m^2 generated 4.61 m/s which was higher than the 4.43 m/s air velocity generated from the flat canopy profile of same air volume under same boundary conditions. The electrical power output at this combination was 7.13 W, which was a 12.1 % improvement over the flat collector's roof. Moreover, when the collector's inlet height was reduced from 0.6 m to 0.1 m, the air velocity increased. This suggested that flow inlet area had a significant influence on the heat transfer rate. The flow

inlet area determined the amount of air which flowed into the collector at a given time. This affected the rate of heat transfer considering that larger inlet height induced large inflow of ambient air per unit time. This air would require sometime to gain heat from the absorber, thus leading to air circulation and high residence time in the collector.

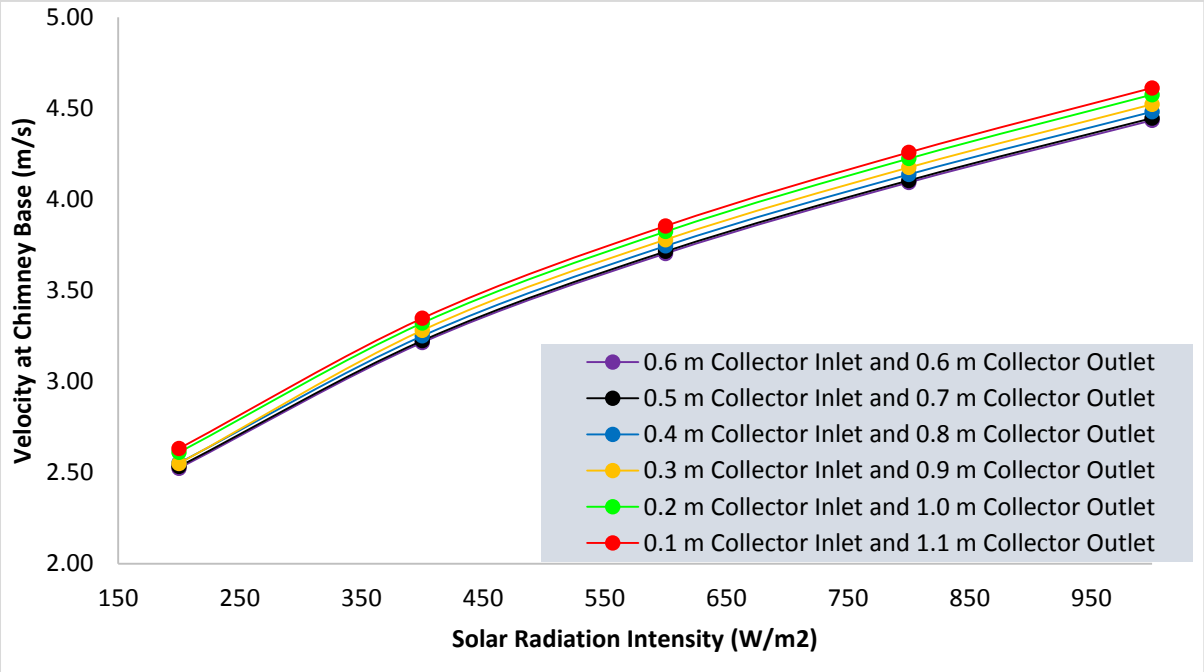

Figure 4.25: Velocity of air at chimney base against the solar radiation intensity for different collector inlet and outlet heights combinations (60 m3 Volume)

The low inlet height was found to be important as it only allowed the admittance of air based on the thermal energy in the collector region which induced suction of air from ambient into the greenhouse. The induced suction which led to the inflow of ambient air into the greenhouse made it easier for the air in the system to be evenly heated up, thereby reduced the air density and enhanced buoyancy driven flow based on the Boussinesq approximation. The results obtained from the graph in Figure 4.25 were consistent with research report of Patel et al. (2014) which inferred that a small collector opening led to higher values of air velocities at higher values of collector's fluid mass flow rate at the chimney base. The rate of heat transfer was higher for the smaller collector's inlet height, which created a higher amount of air updraft in the chimney. Hence, more fresh air entered the SCPP collector component and the mass flow rate of fluid significantly increased.

4.4.1.3 Air Mass Flow Rate at Chimney Base for Case 1E at Optimum Air Volume (60 m^3)

The effect of temperature and air velocity at the chimney base was very significant when the mass flow rate was computed. The results of the air mass flow rate is shown in Figure 4.26. The result indicated the configuration with inlet height of 0.1 m and outlet height of 1.1 m had highest mass flow rate of air at the collector's exit at the various solar radiation intensities. This was because the air had less restriction when it flowed by buoyancy to the chimney at divergent mode.

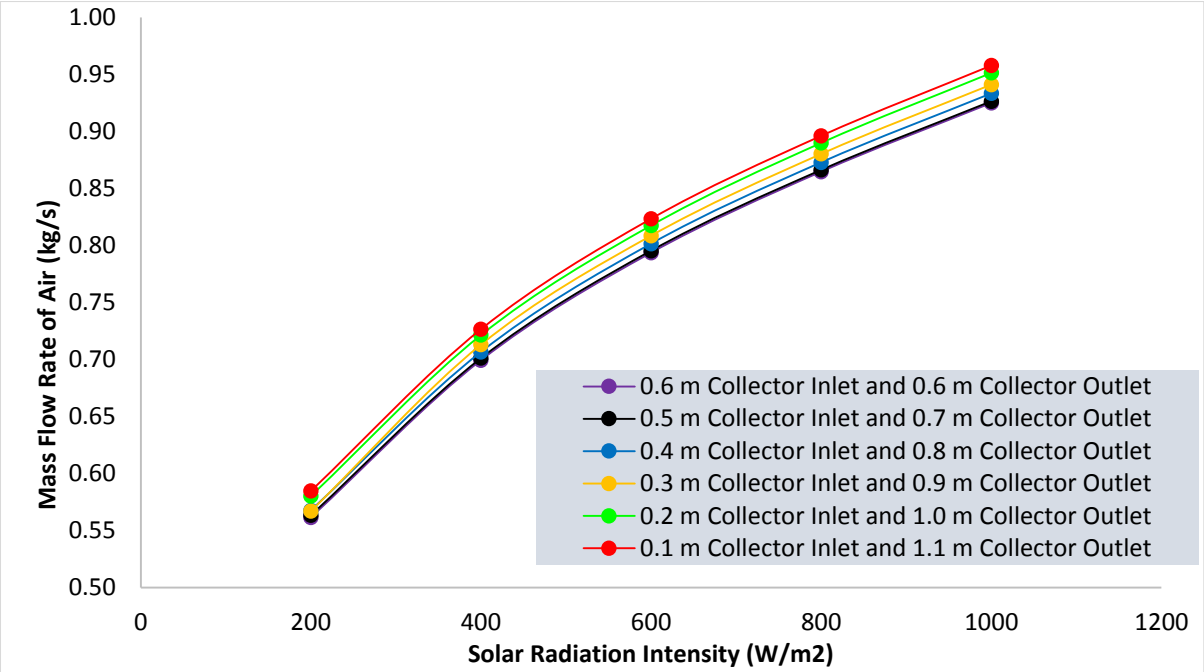

Figure 4.26: Mass flow rate of air versus solar radiation intensity for different collector's inlet and outlet heights

The results of the air mass flow rates were in line with the study conducted by Gholamalizadeh et al. (2016), in which they discovered that the collector's roof inclination caused an increased mass flow rate of air through the system. Similarly, the results from Figure 4.26 were consistent with the experimental observation of the SCPP investigation conducted by Ghalamchi et al. (2016), whereby they determined that the smallest inlet height of the solar collector caused the air mass flow rate through the system to increase. From their experimental study, they reported that the rate of heat transfer was high when the collector involved a smaller inlet height. It was also claimed that the heated collector's fluid had a minor interaction with the surrounding air for the smaller inlet opening. These collectively resulted in the higher mass flow rate of air when the collector was sloped with a small inlet height.

4.4.1.4 Electrical Power Output for Case 1E at Optimum Air Volume (60 m^3)

The comparison of the electrical power outputs for the different sloped canopy profiles at different solar radiation intensity is presented in Figure 4.27. As previously stated, the sloped profile at 0.1 m collector inlet height and 1.1 m collector outlet height resulted in the highest electrical power output, which was rated at 7.13 W at 1000 W/m^2. This sloped canopy profile achieved a 12.1 % improvement in comparison to the conventional flat canopy which only resulted in a total electrical power output of 6.36 W. As the mass flow rate and the velocity of air at the collector's exit were increased with the inclination of the transparent cover, the air power to the turbine was increased too. Therefore, a higher electrical power output was produced by the turbine-generator. These results further supported the idea of Cottam et al. (2016) in which they suggested that the outlet height of the solar collector should be sufficiently high to achieve a higher electrical power output. The large outlet height of the collector was proven to provide a maximum kinetic energy to the air particles flowing through the collector-to-chimney junction. On top of that, the results of the electricity power generation in Figure 4.27 were in agreement with Ghorbani et al. (2015)'s findings which showed that the electricity production increased as the roof slope steepened. These findings were likely to be related to the fact that when the height of the solar collector was increased towards the updraft tower, it served to guide the heated collector air up the chimney. As a consequence, the heated air flowed more easily across the collector-to-chimney transition region. These observations were similar to those of the fluid flow in piping elbows and bends, whereby there is less pipe friction loss when the pipes and bends are designed to redirect the flow in a smooth manner.

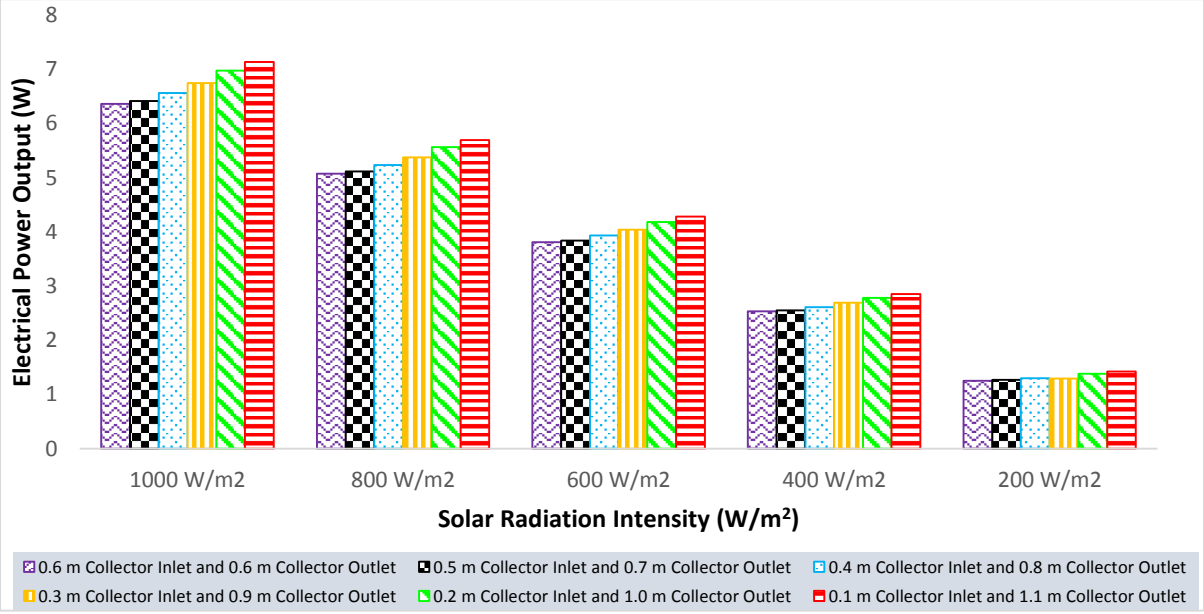

Figure 4.27: Electrical power output for different sloped canopy profiles

4.4.2 Effect of Air Volume on Heat Transfer in the Incline Solar Collector of the System

The inclined solar collector of 100 m^2 absorber and transparent cover areas represented as Case 1E was investigated with five different air volumes in the greenhouse and compared. The air volumes investigated were consisted of 30 m^3, 40 m^3, 50 m^3, 60 m^3 and 70 m^3. The analysis of the collector component temperatures and the air temperatures with the energy transfer to the ambient are presented in subsections below.

4.4.2.1 Collector Component Temperatures for Case 1E at Different Air Volume

The effect of air volume on collector components average temperatures were investigated. Figure 4.28 shows the temperatures of the absorber components operating at different air volumes. It was observed that absorber temperature was highest when the air volume in the greenhouse was 30 m^3. This indicated the possibility for the occurrence of higher re-radiation heat transfer from the absorber to the transparent cover. With the increase in the air volume from 30 m^3 to 70 m^3, the temperatures of the absorber were found to reduce. These results showed that as the air volume increased, more heat was removed from the absorber thereby reducing the absorber temperature and consequently the re-radiation heat transfer to the cover.

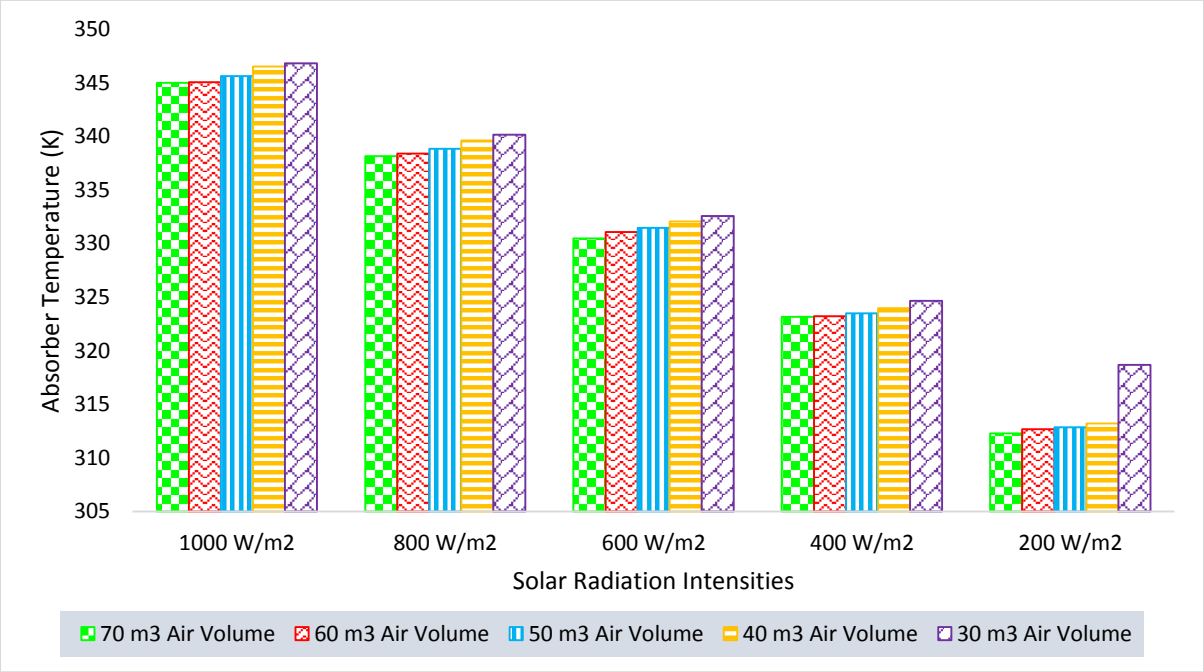

Figure 4.28: Absorber Temperature against Solar Radiation Intensity at Different Air Volumes (Flat Collector Profile)

The air volume was also observed to affect the temperature of the transparent cover as can be seen on the temperature plot at different solar radiation intensities as presented in Figure 4.29. The results showed that when the air volume increased, the temperature of the transparent cover dropped. This was attributed to the reduced re-radiation heat transfer from the absorber to the cover. It was found that at 30 m^3 air volume, the transparent cover temperature was highest considering different solar radiation intensities. This result further proved that there was a higher re-radiation heat transfer from the absorber to the transparent cover in the case involving the 30 m^3 air volume, which caused the transparent cover temperature to be higher in comparison to other cases. Section 4.4.2.3 discusses the thermal loss to the ambient from the transparent cover for Case 1E involving different air volumes.

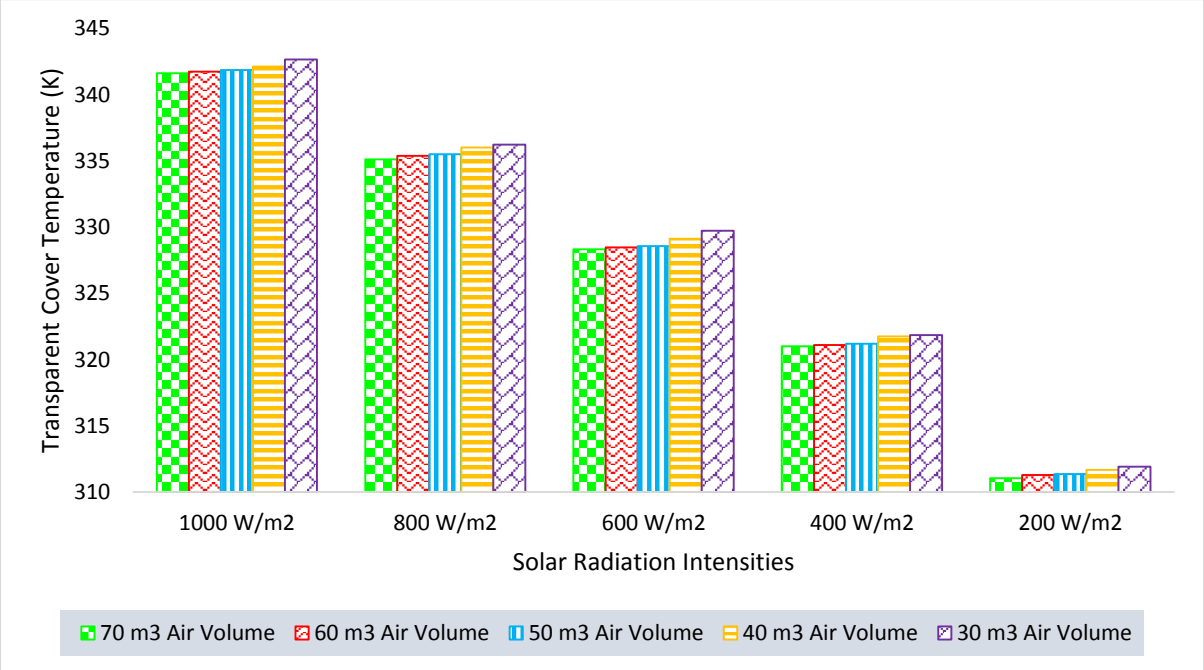

Figure 4.29: Transparent Cover Temperature against the Solar Radiation Intensity at Different Air Volumes (Flat Collector Profile)

The air temperature in the collector was also investigated to see their variations at different air volume for the Case 1E system. The results of the air temperature is presented in Figure 4.30. The air temperature was observed to reduce with increase in air volume. A study on the air velocity and mass flow rate as presented in Section 4.4.1 showed that in excess air as in the case of the 70 m^3 air volume, the buoyancy dropped. This was because the heat generated by the absorber was insufficient to excite the internal energy of all the air particles in the greenhouse. This caused recirculation in some parts of the collector leading to reduced buoyancy and air velocity at the chimney. The result showed that when the air volume was

increased from 60 m^3 to 70 m^3, the performance of the system deteriorated as can be seen from Figure 4.24.

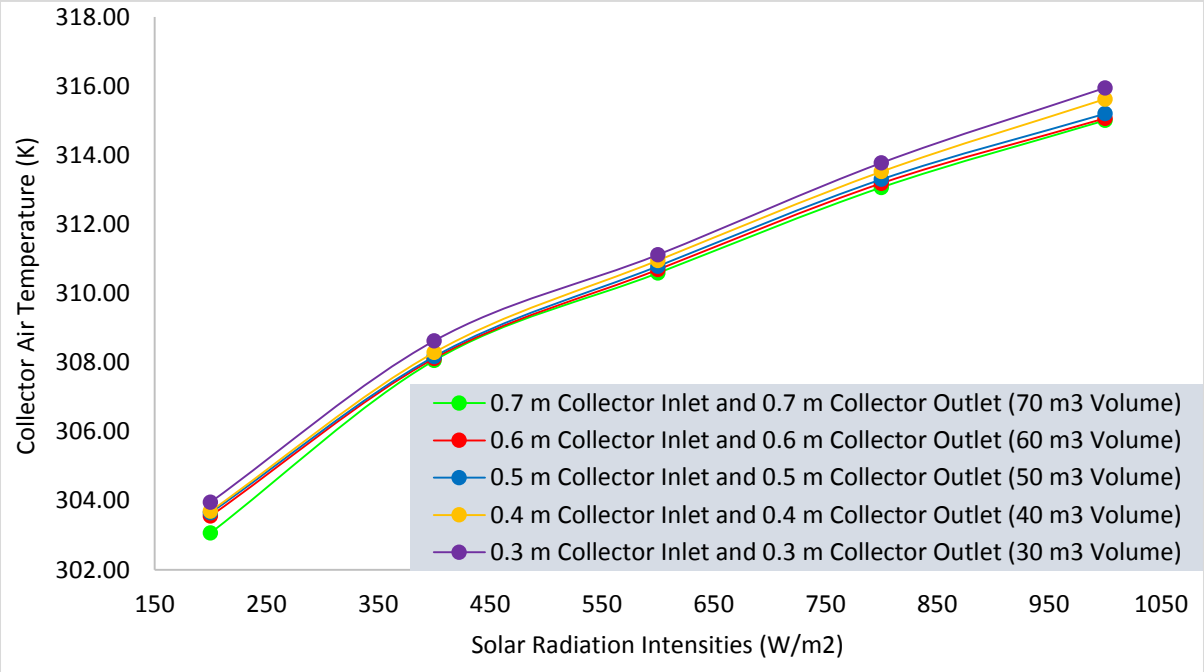

Figure 4.30: Collector Air Temperature against Solar Radiation Intensity at Different Air Volumes

4.4.2.2 Collector Component Temperatures for Case 1E at Optimum Air Volume (60 m^3)

The temperature of the collector components for various configurations of Case 1E was analyzed where the air volume was maintained at 60 m^3. The results of the absorber temperature at varying solar radiation intensities is reported in Figure 4.31. It was evident that the absorber temperature was highest when the gap between the absorber and the cover remained constant at 0.6 m. As the collector's inlet height was reduced while the collector's outlet height was gradually increased, there was a reduction in the average temperatures of the absorbers. Figure 4.31 shows that at 0.1 m collector's inlet height and 1.1 m collector's outlet height, the absorber temperature showed considerable temperature difference to other configurations and indicated lowest temperature among all the configuration. This was important in reducing re-radiation heat transfer to the cover even as the velocity increased.

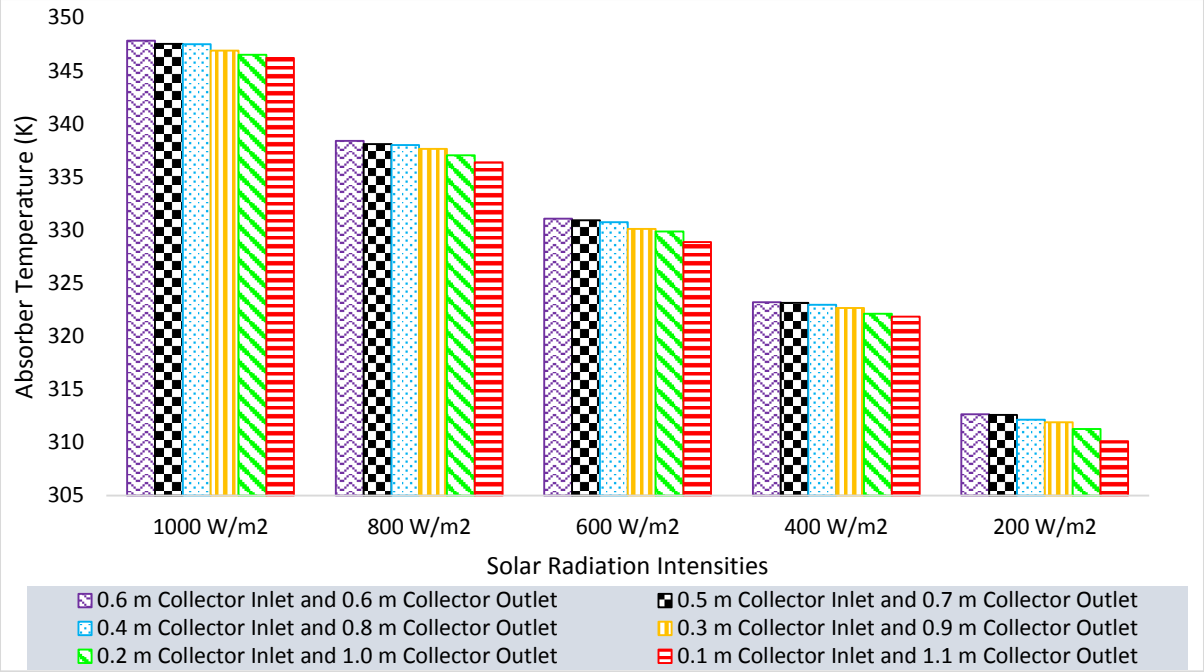

Figure 4.31: Absorber Temperatures against the Solar Radiation Intensity at Different Collector's Inclination

The absorber temperatures above had a significant effect on the corresponding transparent cover temperatures. For instance, a high temperature of the absorber would lead to increase in the transparent cover's temperature. Cover temperature analysis is presented in Figure 4.32. It was observed that the collector configuration having constant inlet and outlet height of 0.6 m showed highest transparent cover average temperatures at different solar radiation intensities. On the other hand, when the collector was inclined at 0.1 m inlet height and 1.1 m outlet height, the transparent cover average temperature was observed to be the lowest. These results proved that the transparent cover's inclination could improve the system's performance by reducing the temperatures of the transparent cover which would consequently reduce the thermal losses to the ambient. The effect of the collector's inclination profile on the thermal loss reduction at the transparent cover component is discussed in Section 4.4.2.4.

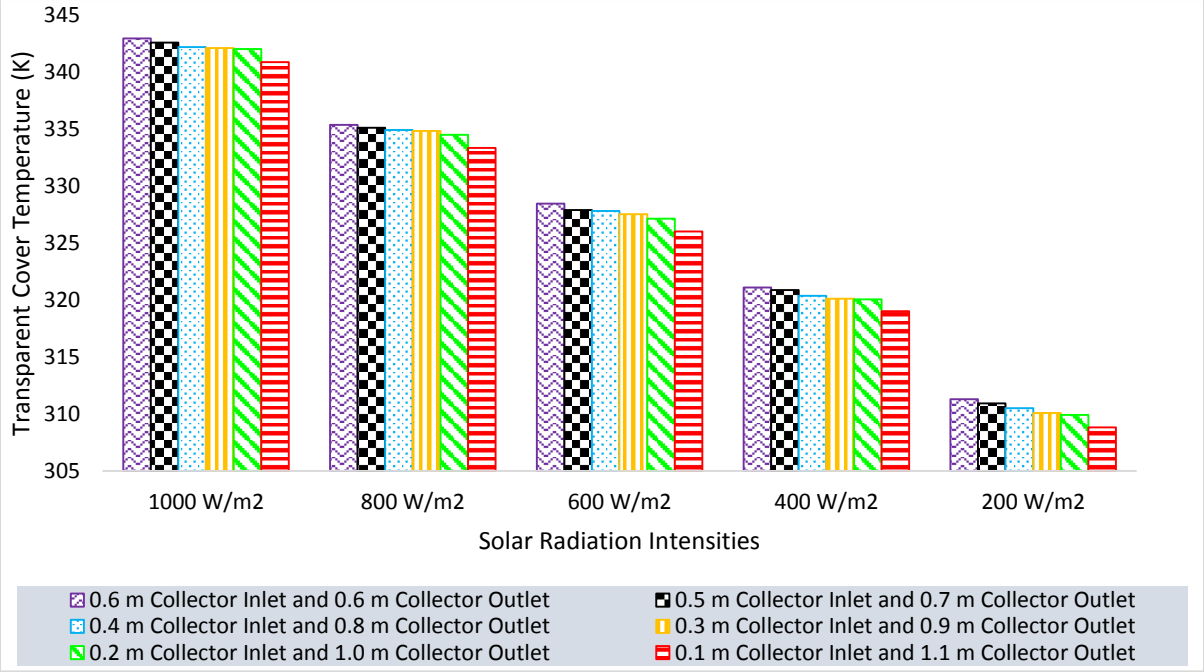

Figure 4.32: Transparent cover Temperature against the Solar Radiation Intensity at Different Collector's Inclination

4.4.2.3 Thermal Loss to the Ambient for Case 1E at Different Air Volume

The thermal losses from the cover of the collector were investigated without considering the effect of wind. The results of the investigation are reported in Figure 4.33. In this figure, when the air volume of the solar collector was 30 m^3, there was a higher thermal loss from the transparent cover to the ambient. This was indicated by the high values of radiation heat transfer loss coefficients from the transparent cover. These results further support the justification provided in the previous Section 4.4.2.1 that a low volume of collector's air led to significant heat transfer by radiation from the absorber to the transparent cover, which consequently resulted in a thermal loss to the ambient. Figure 4.33 also shows that as the air volume was increased from 30 m^3 to 70 m^3, the thermal loss coefficient from the transparent cover component to the ambient was reduced. Considering the effect of temperature difference between the cover and the ambient for the various air volume, 30 m^3 air volume configuration will lose more heat from the cover to the ambient by radiation.

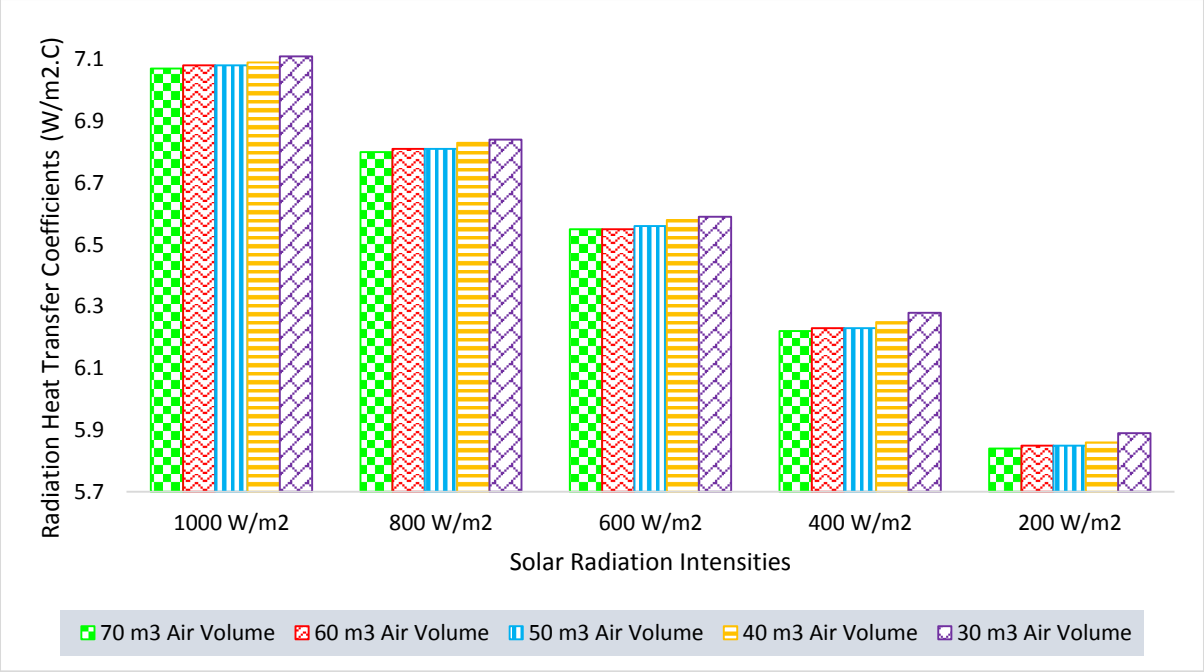

Figure 4.33: Radiation Heat Transfer Loss Coefficients from the Transparent cover to Ambient at Different Solar Radiation Intensities

4.4.2.4 Thermal Loss to the Ambient for Case 1E at Optimum Air Volume ($60m^3$)

The thermal losses from the transparent cover to the ambient were also investigated considering different transparent cover's inclination at the optimum air volume of 60 m^3. When the solar collector had uniform inlet and outlet heights 0.6 m (flat canopy roof), higher thermal losses from the cover to the ambient occurred, as shown in Figure 4.34. In the flat canopy roof system, as the air approached the streamlined region of the collector, the air temperature became too high which led to a higher re-radiation. However, when the transparent cover roof was inclined, the re-radiation dropped. It was evident in Figure 4.34 that when the roof was inclined by reducing the inlet gap to 0.1 m and increasing the exit gap to 1.1 m, the radiation heat transfer loss coefficients from the transparent cover to the ambient were significantly reduced. This was due to the larger gap between the absorber and the transparent cover in the sloped canopy roof system. The gap here referred to the effective cross-sectional area of the air flow channel. When the gap gradually increased as the roof was being inclined, the radiation heat transfer reduced and the air removed higher amount of heat from the streamlined region of the absorber.

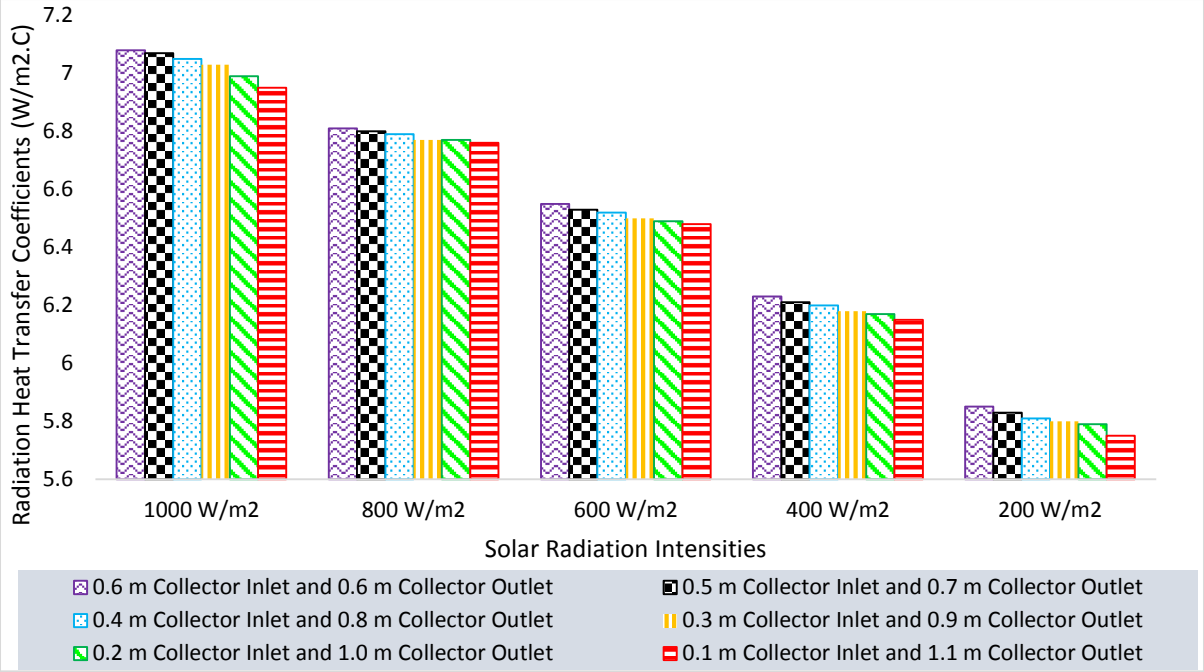

Figure 4.34: Radiation Heat Transfer Loss Coefficients from the Transparent cover to the Ambient at Different Collector's Inclination

4.4.3 Collector Efficiency Analysis at Various Canopy Profile

The analysis of the collector efficiency was conducted for the various air volume discussed in previous sections. With respect to the optimum air volume determined in the study for the collector area of 100 m^2, the efficiency of the collector was also analyzed for the different configuration of Case 1E.

4.4.3.1 Collector Efficiency Analysis at Different Air Volume

The efficiency of the collector was evaluated considering the collector component temperatures and the useful energy generated from the various air volume investigated. The results of the collector efficiencies at different air volume is reported in Figure 4.35. The results showed that the collector with 60 m^3 air volume had the best collector efficiency while the collector with a low air volume of 30 m^3 showed lowest efficiency. It can be inferred that lower air volume led to higher thermal loss which resulted to low collector efficiency. Similarly, extreme high air volume reduced the collector efficiency as well. The simulation helped in determining the optimum air volume that gives highest collector efficiency.

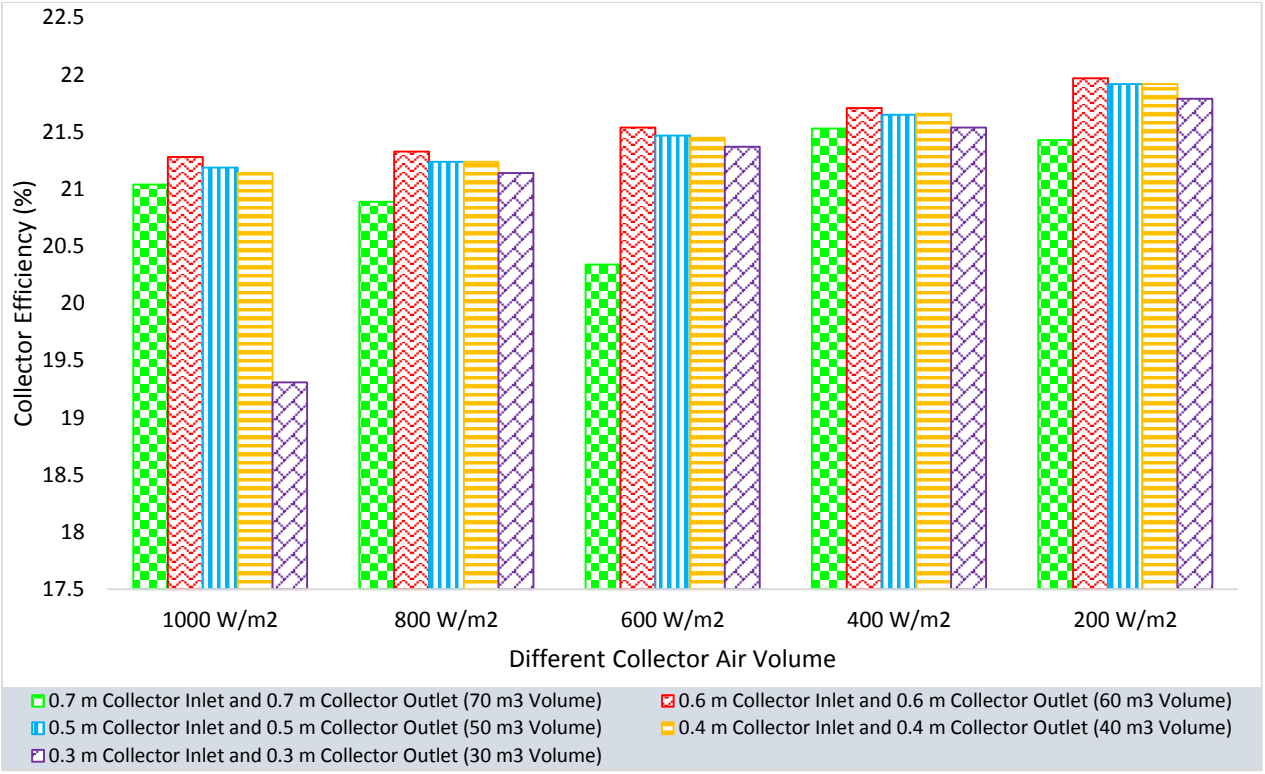

Figure 4.35: Collector Efficiency at Different Solar Radiation Intensities for Different Collector Air Volumes

4.4.3.2 Collector Efficiency Analysis for Optimum Air Volume with Varied Configurations

The steepest collector with 0.1 m collector's inlet height and 1.1 m collector's outlet height has the highest efficiencies at different solar radiation intensities, as compared to the collector of 0.6 m constant gap between absorber and transparent cover which shows lowest efficiencies as can be observed from Figure 4.36. Therefore, the collector with its transparent cover roof being inclined at 0.1 m inlet height and 1.1 m outlet height was selected as the reference geometry for other numerical investigations.

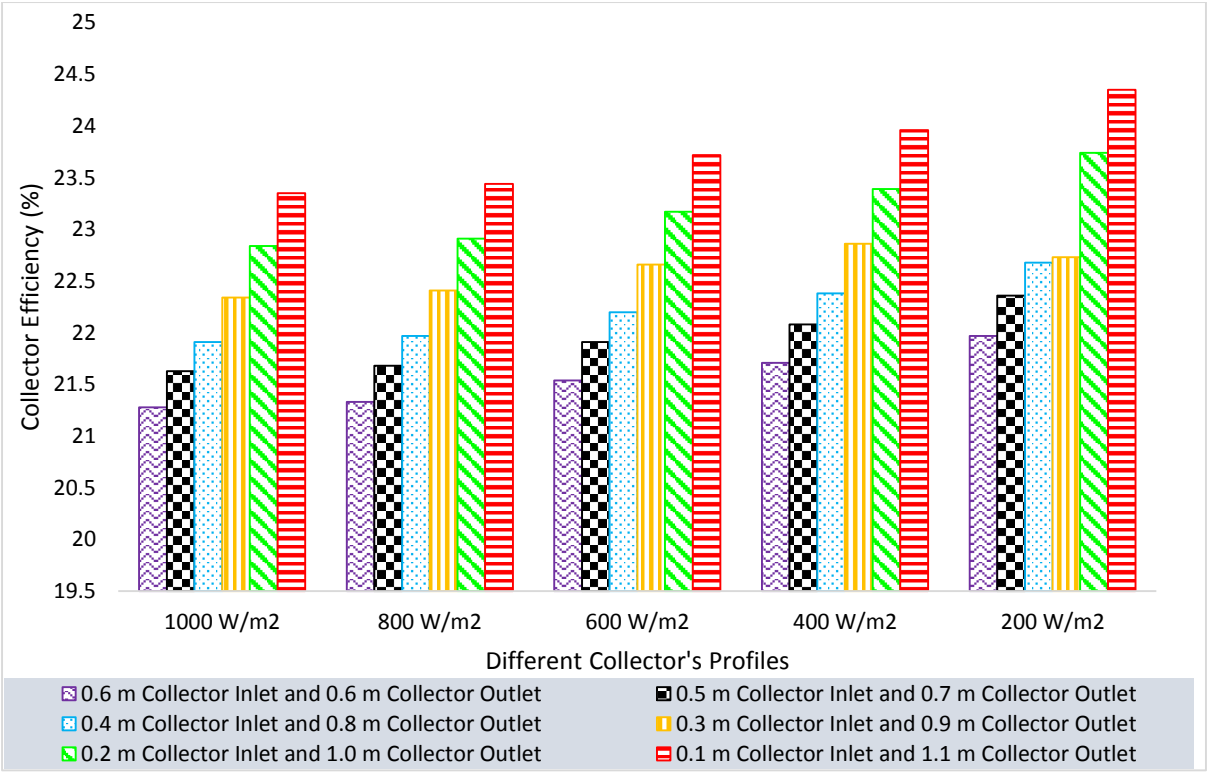

Figure 4.36: Collector's efficiency for different sloped canopy profiles

4.5 Influence of the Concrete Thicknesses on Inclined SCPP Collector Performance

The effect of concrete absorber thickness on collector performance of the inclined SCPP was investigated. The investigation was conducted with focus on thermal storage of the absorber for extended operation of the plant. This investigation was carried out to achieve the research objective which aimed to identify the absorber thickness suitable for enhancement of collector thermal energy storage. In the simulation of the absorber's thermal storage effect, the major parameters included the absorber thickness and available solar radiation while considering other constant variables, as presented in Section 3.9.3. Sub-sections 4.5.1 and 4.5.2 present the results of the influences of the concrete thicknesses on the air buoyancy in the inclined SCPP and the temperature field of the absorbers with different absorber thicknesses respectively. The potential capacities of the concrete absorber for thermal storage will also be described.

4.5.1 Effect of Concrete Thicknesses on Buoyancy in the Inclined SCPP

The effect of concrete thickness was investigated to determine the optimum thickness suitable for a 100 m^2 inclined collector area for the inclined SCPP. The results are analyzed as shown below considering the buoyant air velocity, mass flow rate and collector efficiency.

4.5.1.1 Velocity of Air at the Chimney Base at Different Concrete Absorber Thicknesses

The buoyant air velocity at the chimney base for the same collector area and chimney height was analyzed considering the different absorber thicknesses. The simulation results of buoyant air velocity at the base of the chimney is shown in Figure 4.37 for different concrete thicknesses under different solar radiation intensities considered from 200 W/m^2 to 1000 W/m^2. In consideration of the different solar radiation intensities, the results showed that the air velocity at the base of the chimney slightly increased when the absorber's thickness was increased from 0.1 m to 0.3 m. No significant changes in the air velocity were noticed when the thickness of the absorber was 0.4 m and above. These findings, while preliminary, suggested that there was a higher heat loss occurring through the back of the concrete absorber when its thickness was lower than 0.3 m. The occurrence of heat losses through the back of the concrete resulted in a reduced useful energy in the buoyant air within the greenhouse. At low absorber thickness considering the size of collector in this investigation, there was decrease in thermal resistance of the absorber. This led to significant thermal energy transfer by conduction from the absorber surface through the absorber thickness to the back which in-turns led to convective thermal loss to the ambient and radiation to the surrounding ground. Consequently, with the reduced useful energy in the greenhouse at low absorber thickness, the buoyancy of the air heated in the collector was affected which caused a reduction in the air velocity at the chimney's base.

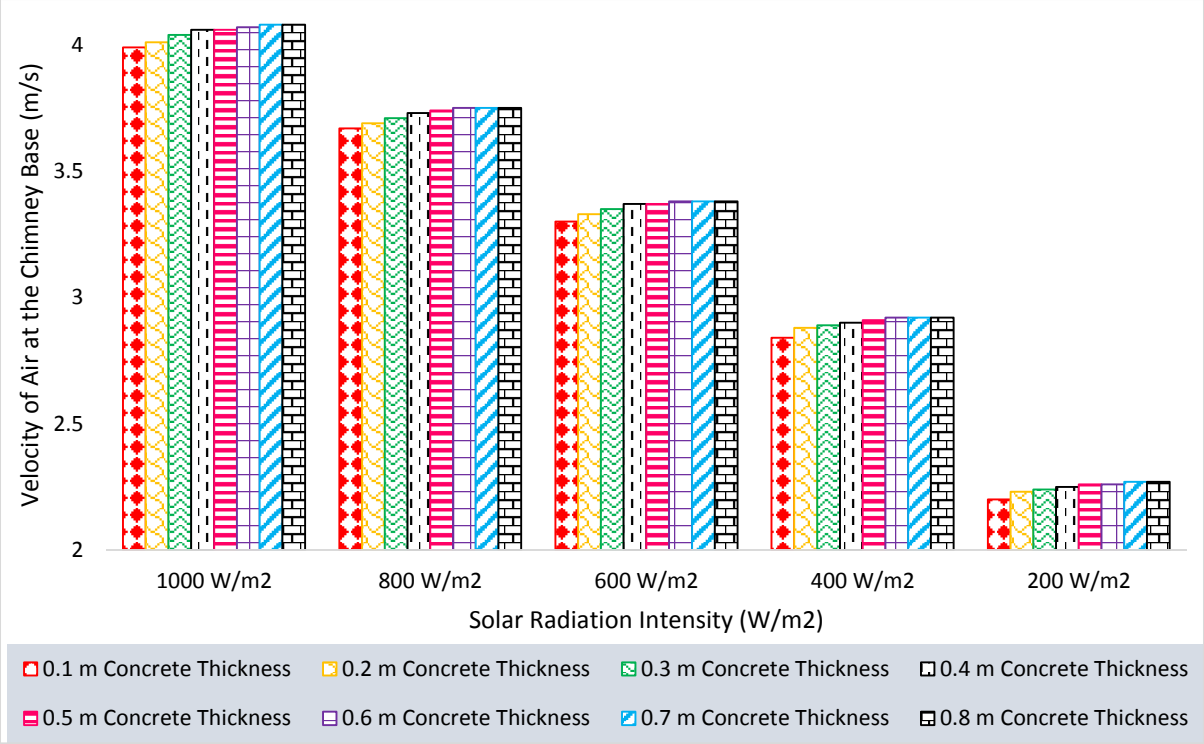

Figure 4.37: Velocity of Air at the Chimney Base against Solar Radiation Intensity at Different Concrete Thicknesses

Another important finding from Figure 4.37 was that the computational models (considering the absorber thicknesses in the range between 0.4 m and 0.8 m) predicted almost similar air velocity at the chimney's inlet. This result indicated that the concrete thicknesses of 0.4 m and above were sufficiently deep to restrict the thermal energy losses from the back to the ambient. This led to a higher heat energy gained at the absorber and consequently higher velocity at the chimney base. The higher thickness of the concrete allowed the bottom surface of the absorber to continually adjust to the condition and temperature of the ambient in line with the solar radiation intensity. This led to reduced thermal losses from the back of the absorber to the surrounding. A detail discussion on the thermal storage and thermal performance is presented in Section 4.5.2.

4.5.1.2 Mass Flow Rate of Air at Chimney Base at Different Concrete Absorber Thicknesses

The results of the evaluated mass flow rate of air at the base of the chimney with respect to different solar radiation intensities and varying concrete thicknesses are presented in Figure 4.38. The mass flow rate of air was calculated based on the air velocity magnitudes reported in Figure 4.37, using Equation 3.39. The result as presented in Figure 4.38 showed significant

increase in mass flow rate of air at the base of the chimney considering the concrete absorber thickness of 0.1 m to 0.3 m. On the other hand, the air mass flow rate was virtually constant when the thickness of the concrete was higher than 0.3 m considering the various solar radiation intensities.

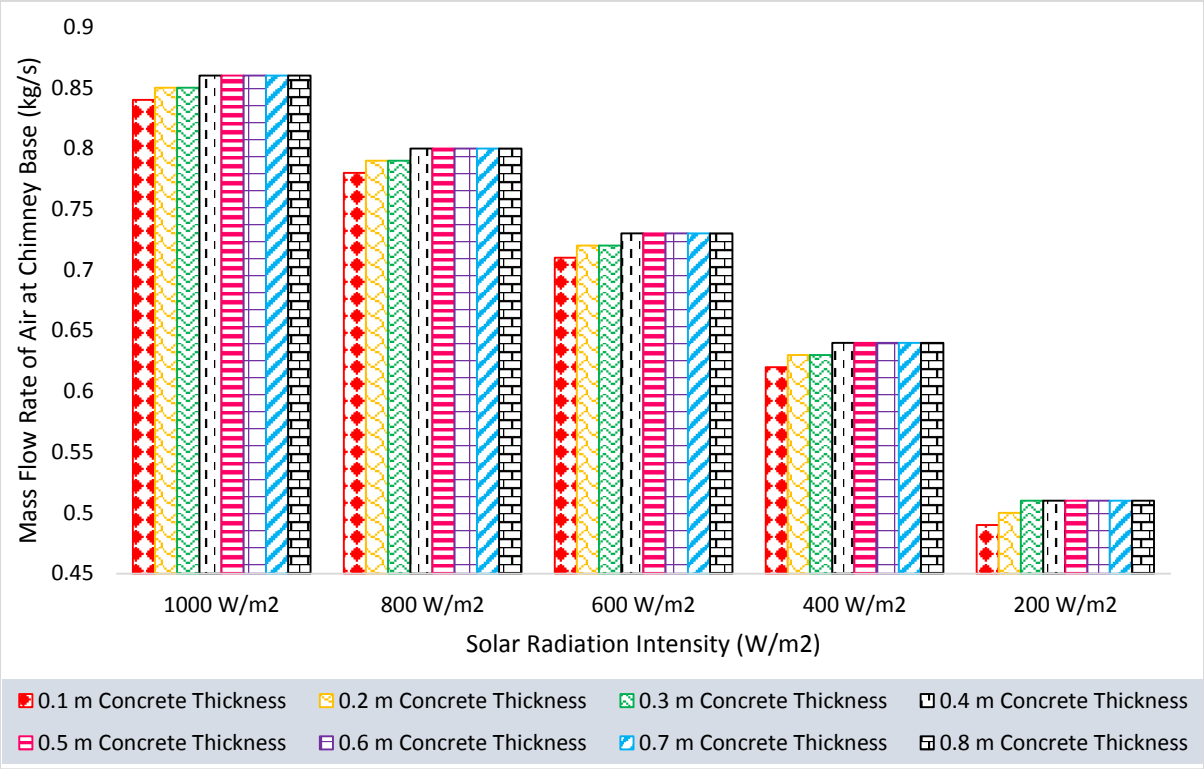

Figure 4.38: Mass Flow Rate of Air at the Chimney Base against the Solar Radiation Intensity at Different Concrete Thicknesses

4.5.1.3 Electrical Power Output of the Inclined SCPP with the Consideration of Different Concrete Thicknesses

The potential electrical power outputs of the inclined SCPP at different concrete absorber thickness are presented in Figure 4.39, with respect to different solar radiation intensities. The electrical power output at the chimney base was evaluated using Equation 3.47 where the turbine efficiency is assumed at 70% considering the report of Fluri (2008) of shrouded vertical axis wind turbine efficiency range from 66% to over 80%. At lower solar radiation intensities below 400 W/m^2, the power output showed less significant difference for the different concrete absorber thickness. This was because the thermal loss at this point was low for the lower thicknesses. Above 400 W/m^2, it was observed that the concrete absorber thickness of 0.1 m resulted in the lowest electrical power output and significant changes across the thickness of

0.1 m to 0.4 m. This was also associated to the explanation that the low thickness of the concrete caused a higher heat exchange with the surrounding ambient which reduced the useful heat energy gain by the working fluid inside the solar collector.

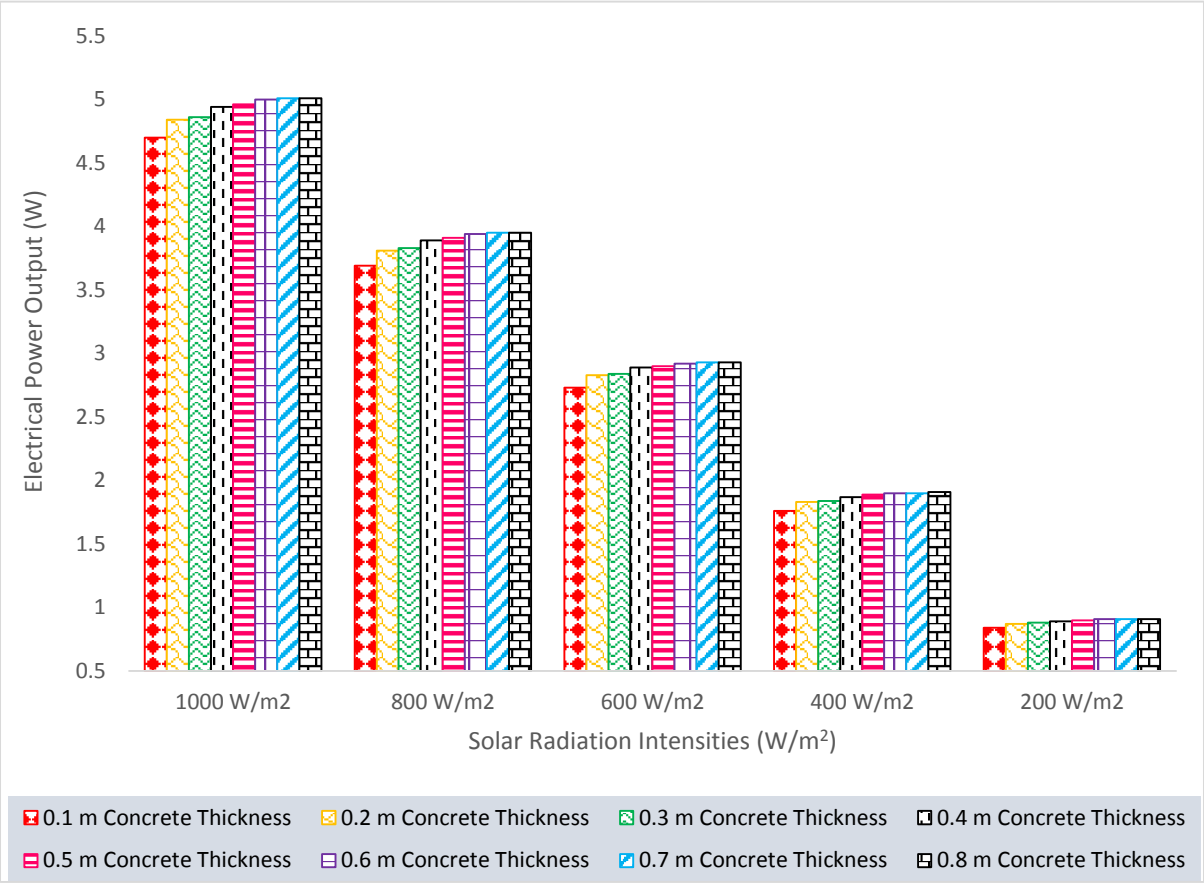

Figure 4.39: Electrical Power Output against the Solar Radiation Intensity at Different Concrete Thicknesses

4.5.2 Effect of Concrete Thicknesses on the Absorber's Temperature Field and Thermal Storage

This section presents the temperature variations at different solar radiation intensities and concrete thicknesses. The temperature variations also help in determining the thermal energy stored in the concrete. The results analyses are presented in the following sub-sections.

4.5.2.1 Effect of Concrete Thicknesses on the Absorber's Temperature Field

The analysis of the average temperatures of the top and bottom surfaces of the concrete absorber at various solar radiation were conducted for the 100 m^2 collector absorber

considering different concrete thicknesses, as shown in Figure 4.40 and Figure 4.41, respectively.

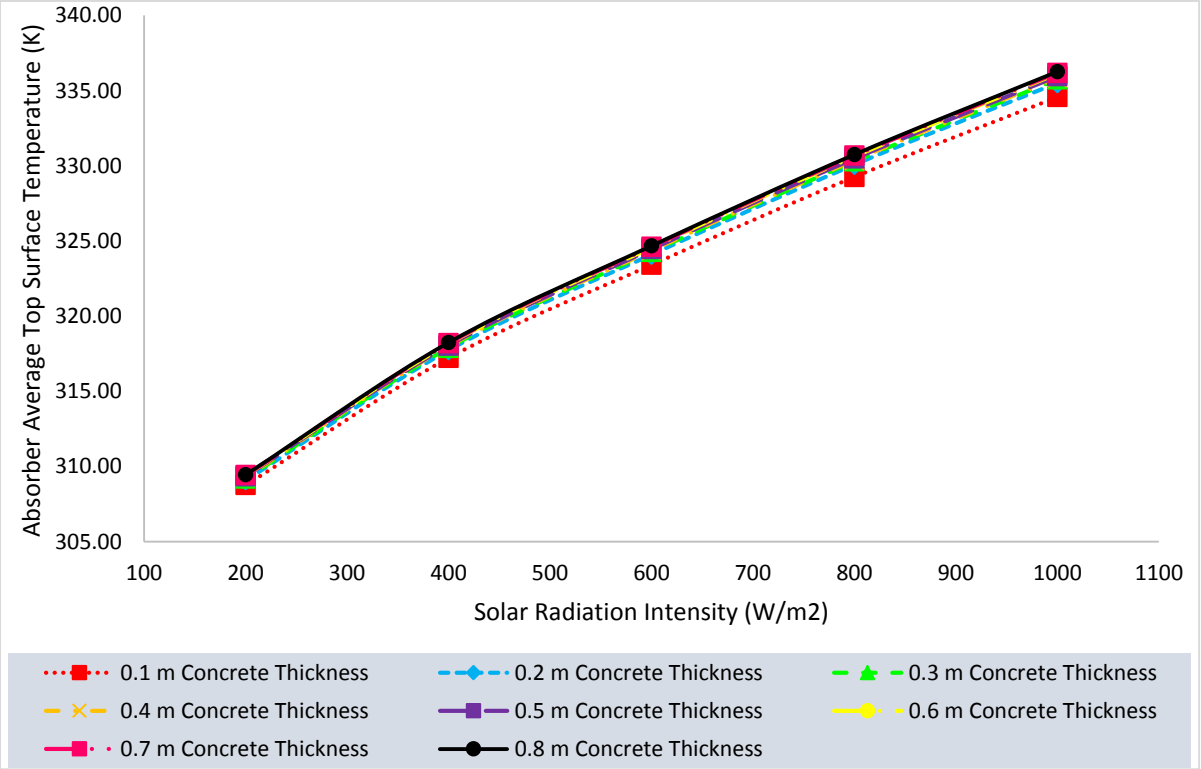

Figure 4.40: Absorber Average Top Surface Temperature for Different Concrete Thicknesses

Figure 4.40 reveals that the thickness of the absorber influences the temperature of the surface. This is because as the concrete absorber thickness increases, there is reduced thermal loss which consequently increases the energy stored in the absorber. This is evident in the results of the temperature of the back of the concrete absorber as shown in Figure 4.41. In Figure 4.41, the temperature difference for the different absorber thicknesses showed higher variation as compared to the temperature difference observed at the absorber's surface in Figure 4.40. A consideration of the absorber thickness from 0.3 m and above indicated less significant temperature differences at various solar radiation intensity were observed at both the top and back surface of the concrete absorber.

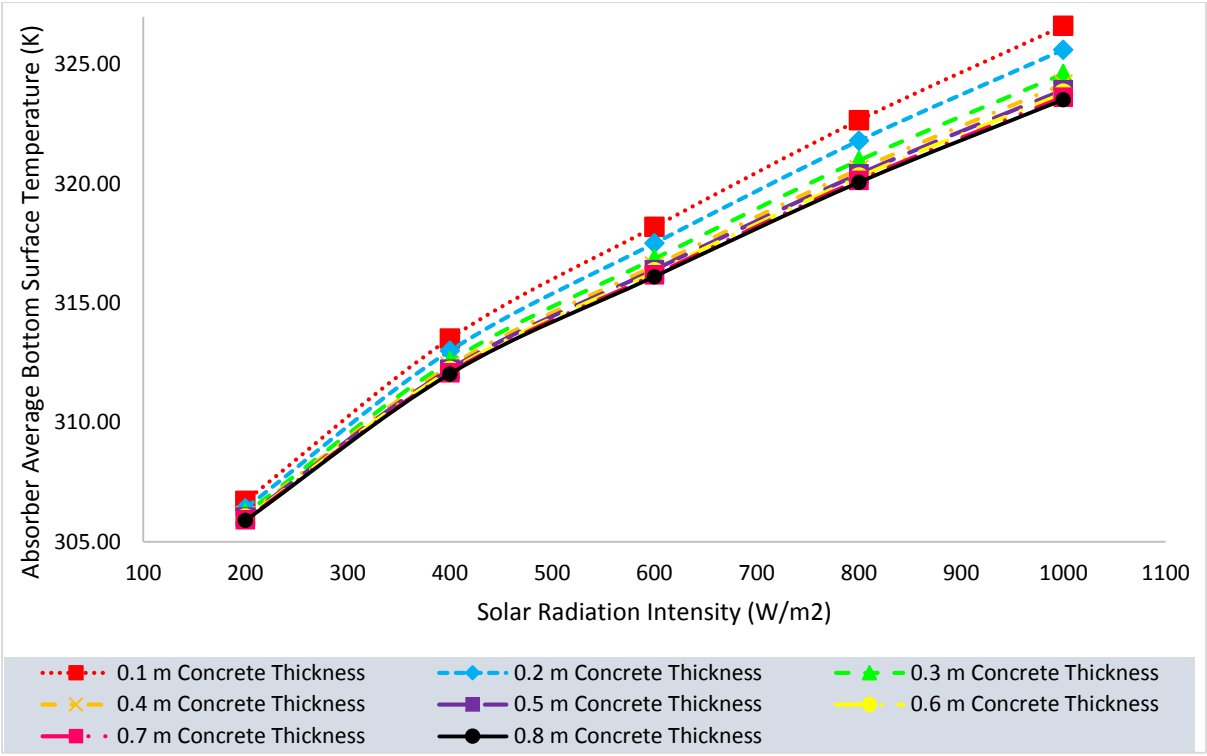

Figure 4.41: Absorber Bottom Surface Temperature for Different Concrete Thicknesses

A clear visualization of the impact of the concrete absorber thickness can be seen from the temperature difference between the absorber surface and the temperature of the absorber's back as presented in Figure 4.42. The results as presented in Figure 4.42 revealed that there was increase temperature differences between the bottom and top surfaces of the absorber with respect to absorber thickness from 0.1 m to 0.3 m but showed less significant variation above 0.3 m concrete thickness, the temperature differences between the absorber's bottom and top surfaces did not increase but remained nearly constant. These findings raised important implications for describing the thermal storage capabilities of the concrete material, in relation to the concrete's thicknesses.

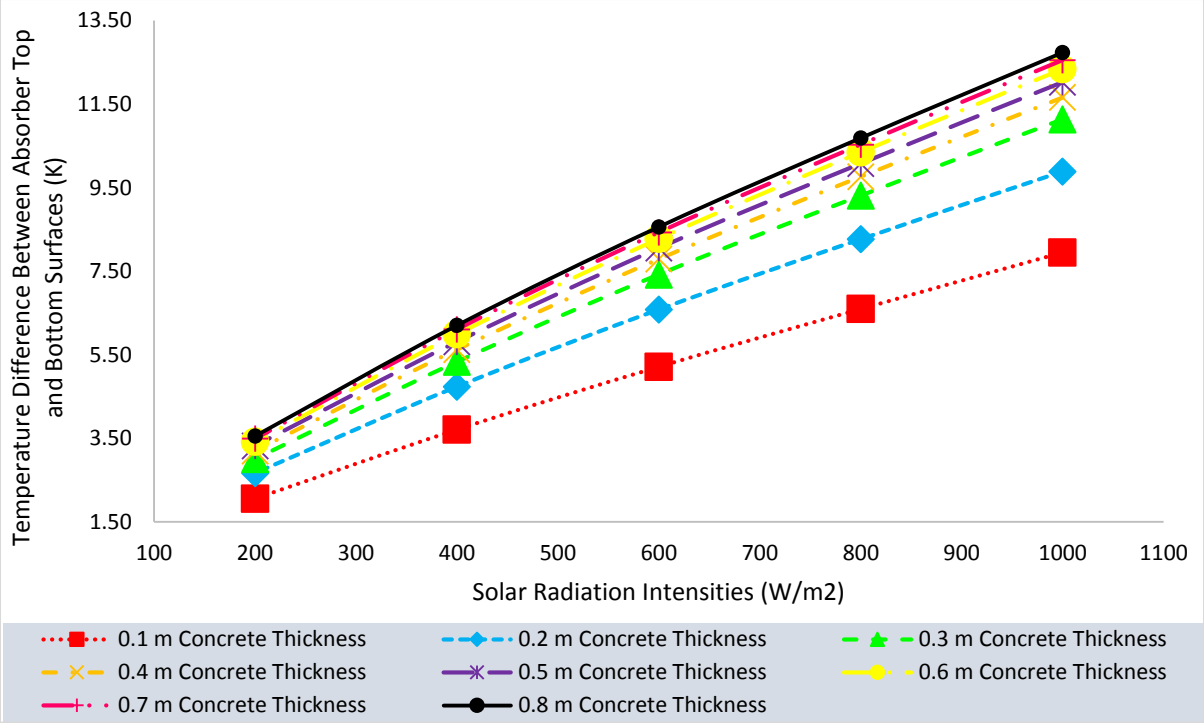

Figure 4.42: Average Temperature Differences between Absorber Top and Bottom Surfaces for Different Concrete Thicknesses

At 0.1 m concrete thickness, there was small temperature difference between the absorber's top surfaces and the back surface temperature while with increase in absorber thickness, there were significant increase in temperature difference between the top surface and the back of the concrete absorber. The low temperature difference in the 0.1 m thickness indicated possibilities for higher thermal losses through the back of the absorber to the surroundings. The findings from this investigation showed that higher thickness of the concrete provided resistance to conduction heat transfer from the absorber's top surface through the concrete absorber thickness to the back surface, thus allows for heat storage for possible extended operation of the plant at low solar radiation and night time in the inclined SCPP.

4.5.2.2 Stored Thermal Energy in the Concrete Absorber with Respect to Thickness

The effect of thickness of the absorber on temperature variation across the collector absorber as presented in 4.5.2.1 indicates that the temperature difference contributed to thermal loss and possible energy storage. In view of the above, a visualization of the temperature contour obtained by the CFD simulations for the various concrete thicknesses in Appendix A. The figures showed the flow of the heat from the absorber's top surface to the back surface. It was

observed that the bottom layers of the absorber with thickness of 0.3 m and above had lower temperatures difference between the back and the ambient and shows reduced trend of heat transfer to the ambient as compared to 0.1 m and 0.2 m absorber. As the thermal loss to the ambient through the back of the absorber was minimized, the concrete was capable to store the excess heat at various solar radiation intensities which could be used for continuous operation of the plant during less sunny time and night.

The analysis of the energy storage in the different absorber thickness is presented in Figure 4.43 considering Equation 3.41. The results show that the inclined SCPP with 0.1 m concrete thickness resulted in the lowest heat energy stored while the thermal storage capacity increased with increase in absorber thickness.

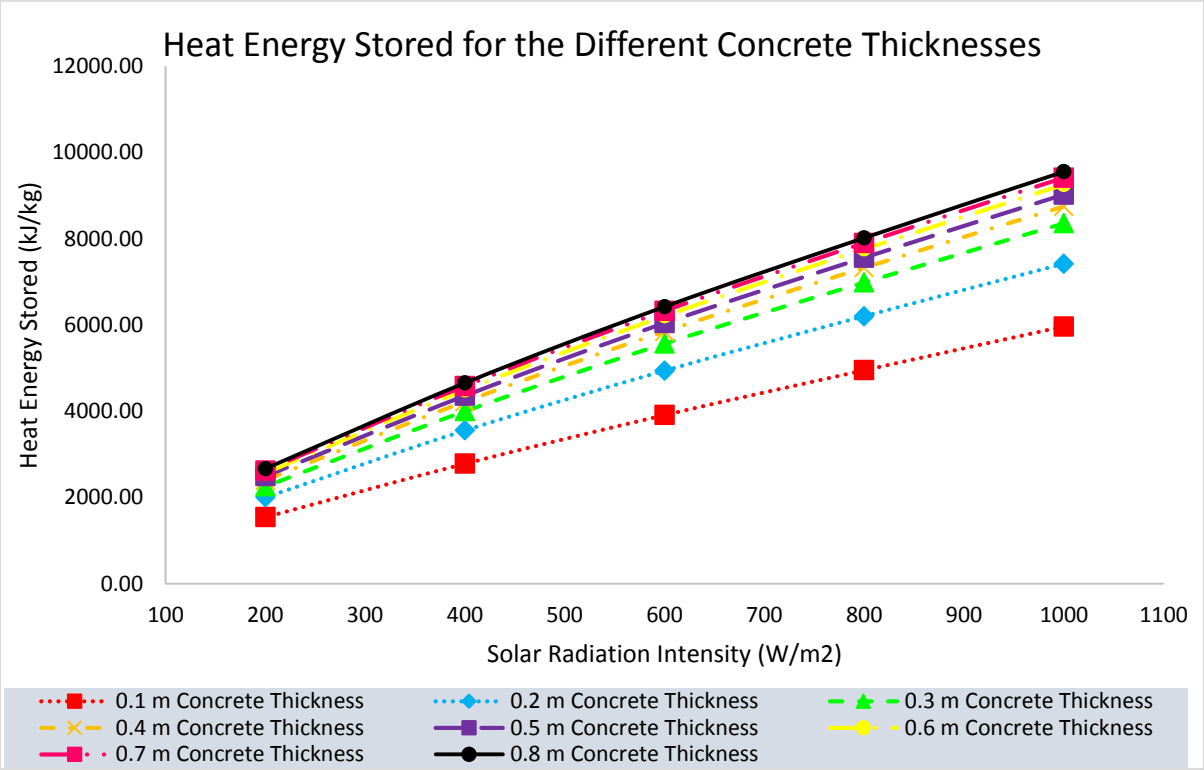

Figure 4.43: Heat Energy Stored for the Different Concrete Thicknesses

4.5.2.3 Thermal Losses through the Back of the Concrete Absorber with Respect to Thickness

The collector's thermal losses through the back surface of the concrete absorber were analyzed in this section. Figure 4.44 presents the results obtained for the convective heat losses through the absorber's back to the ambient. In this study, it is found that the convective heat losses to the ambient were the highest considering the low absorber thickness of 0.1 m. Similarly, the

use of 0.1 m absorber thickness led to the highest radiation heat transfer loss coefficients through the absorber's back surface to the surrounding ground, as shown in Figure 4.45. The results also indicate that both convective and radiation heat transfer losses through the back of the concrete absorber were reduced with higher absorber thicknesses.

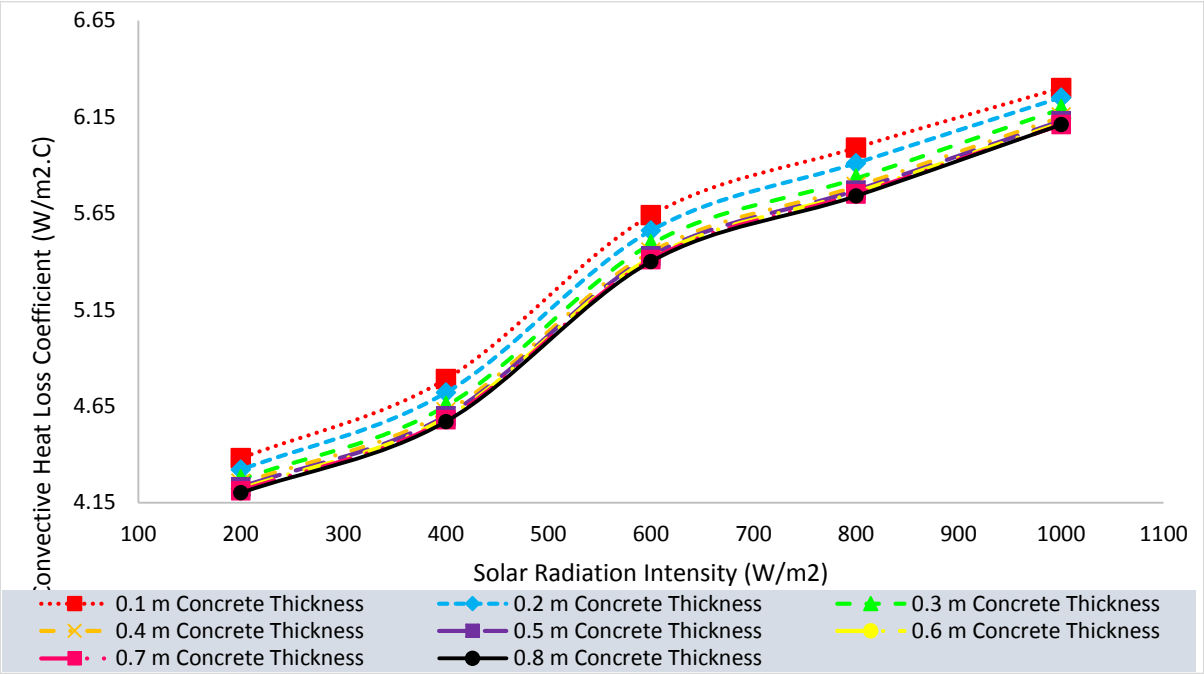

Figure 4.44: Convective Heat Loss Coefficients for Different Absorber Thicknesses

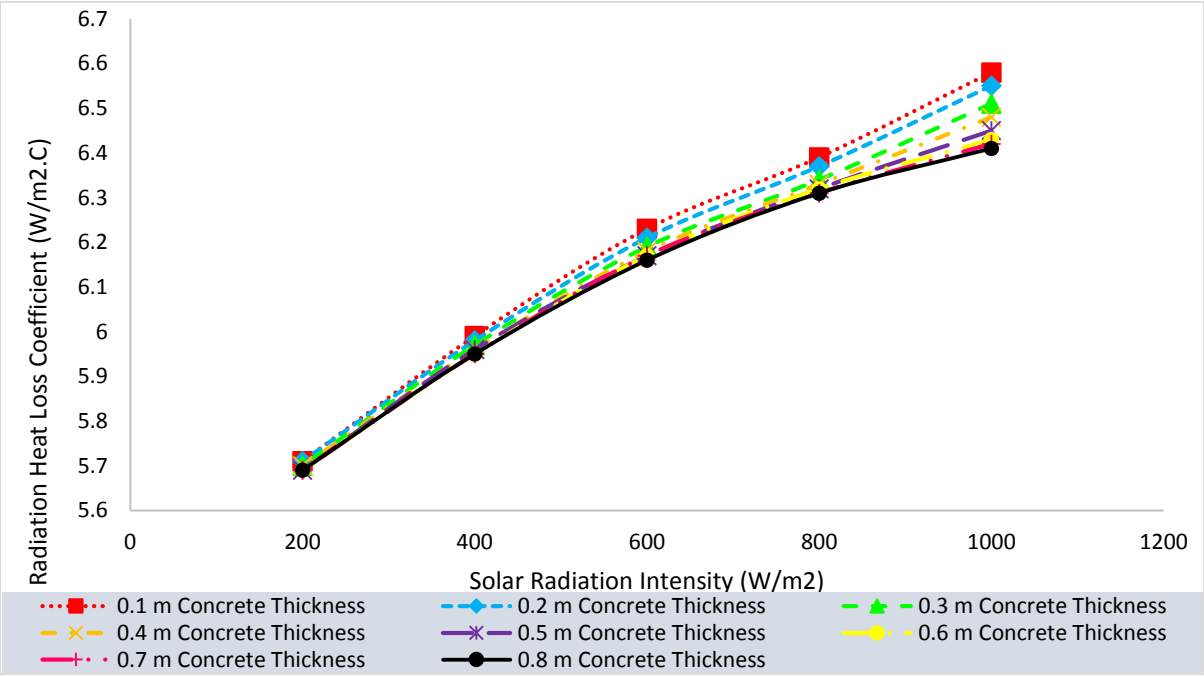

Figure 4.45: Radiation Heat Loss Coefficients for Different Absorber Thicknesses

4.5.2.4 Collector Efficiency of the Inclined SCPP with the Consideration of Different Concrete Thicknesses

The results of the collector efficiency as presented in Figure 4.46 showed that lower absorber thickness degrades the solar collector efficiency. The collector efficiency was evaluated using Equation 3.40. In Figure 4.46, it was apparent that the collector efficiencies were approximately equal between the 0.3 m and 0.4 m concrete thicknesses, ranging from 15.5 % efficiency at 200 W/m^2 to 16.3 % efficiency at 1000 W/m^2 solar radiation intensity. It was also found that at higher concrete absorber thicknesses, the collector efficiencies remained constant at 15.8 % and 16.6 % for the solar radiation intensities between 200 W/m^2 and 1000 W/m^2, respectively. However, it should be noted that a high absorber thickness is at the expense of higher investment cost for the plant construction.

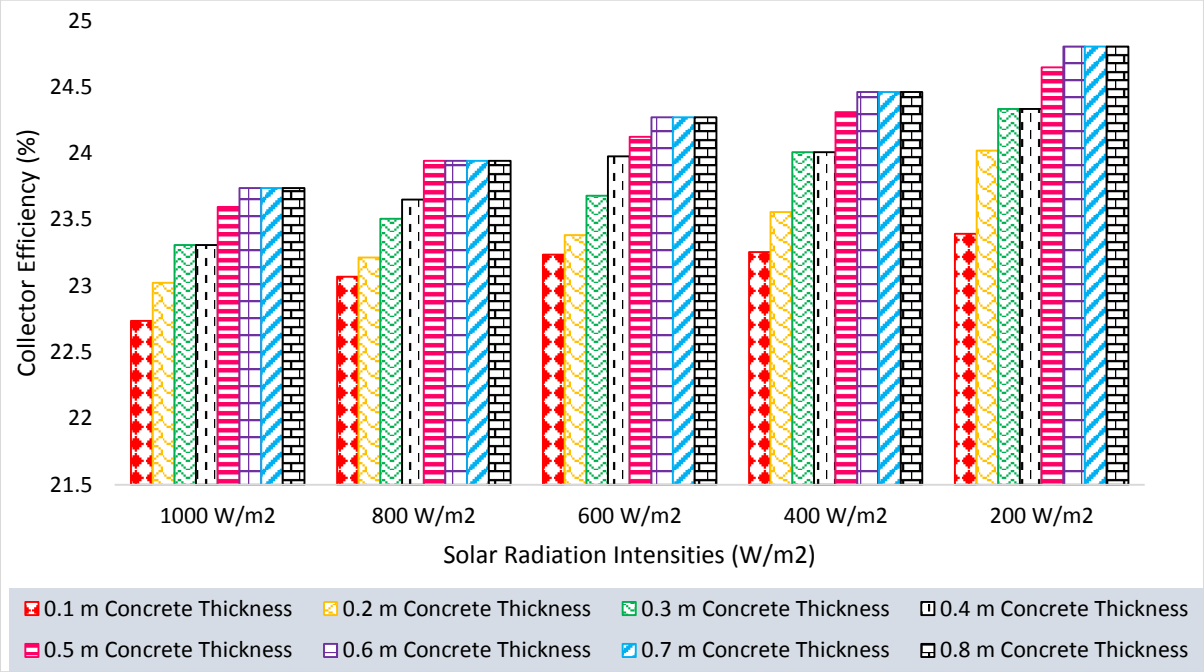

Figure 4.46: Collector Efficiency versus Solar Radiation Intensities for Different Concrete Thicknesses

For the results presented in the sections below, the decision for the concrete absorber thickness was based on the performance as presented in Section 4.5.

4.6 Introduction of Underneath Air-Vents to the Inclined SCPP

The model employed in further investigation on the impact of air-vents on the inclined SCPP is detailed in Section 3.9.3. The system was integrated with underneath air-vents of 10°, 50°

and 90° orientation angles and evenly distributed across the collector absorber. The results of the air velocity is presented in Figure 4.47. The result showed degradation in the air velocity as compared to the case without air vents. In furtherance to this investigation, preliminary studies on the location of the vents were conducted which inferred that the best location for the vents in the configuration described above as detailed in Section 3.9.3 is at the locations near the inlet within 25% of the air-flow channel length (Vents located between 0 m to 4 m along the collector's length). As shown in Figure 4.47, the air velocity for the system with the air-vents located between 0 m to 4 m from the inlet of the collector showed higher output.

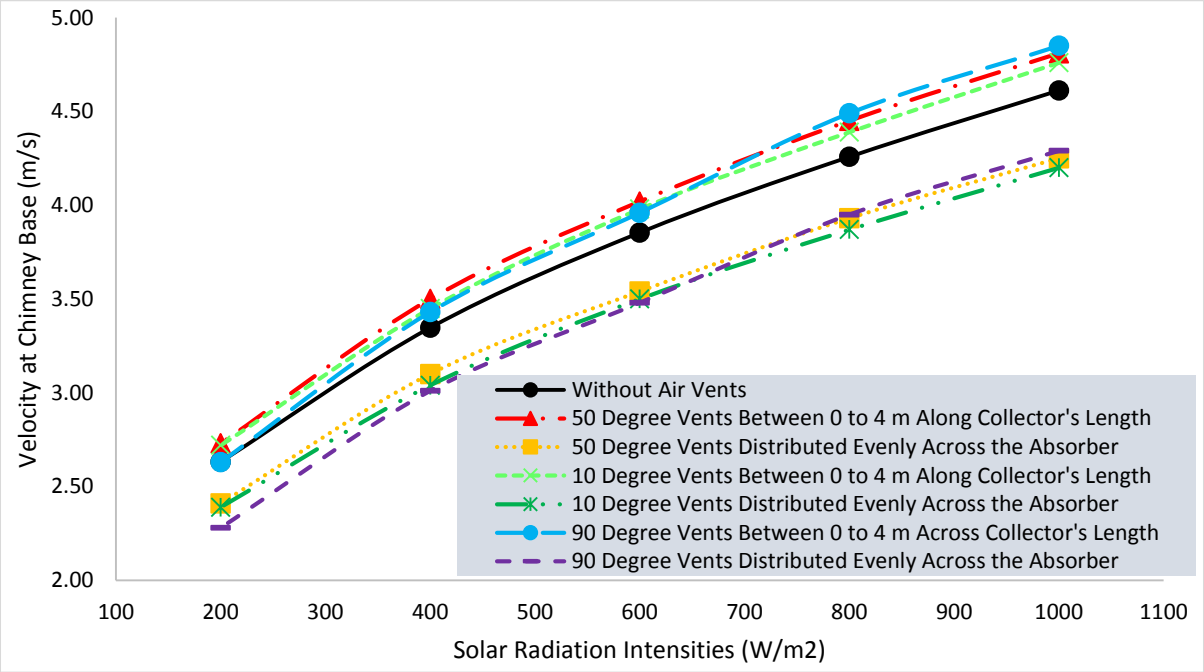

Figure 4.47: Air Velocity at the Chimney Base for the Inclined SCPP Air-Vents Orientations

The next study is based on the system with its air-vents located at 0 m to 4 m from the inlet of the collector along the air-flow channel aimed at determining the best air-vent orientation for the system. Detail studies on the location of the vents for this model is presented in Section 4.8.

4.7 Effect of the Installation of underneath Air Vents with Varying Angles on the Inclined SCPP's Performance

In Section 4.5, the air velocities, temperature field, thermal energy storage capacity and thermal losses from the absorber of inclined SCPP under different absorber thicknesses were discussed. The model with concrete absorber thickness of 0.3 m was selected for further studies for the 100 m^2 collector, 26.85 m high chimney of 0.5 m chimney diameter as described in Section

3.9.4. The investigation on the use of underneath air-vents considers the effect of vent angle on the performance of the system and the effect of air vents on the absorber's thermal storage capacity.

4.7.1 Effect of the Air Vents with Varying Orientation Angles on Air Buoyancy

The effect of air vent on air buoyancy, mass flow rate and possible power output of the system was investigated. The analysis and the results discussions are presented in subsections below.

4.7.1.1 Velocity of Air at the Chimney Base at Different Orientation Angles of the Vents

With reference to the model described in Section 3.9.4 which this results are based on, it was observed that the inclusion of underneath air-vents to the solar collector absorber, there was significant increase in the air velocity at the chimney base as shown in Figure 4.48. With the inclusion of the underneath air-vents, air velocity was enhanced at different solar radiation intensity of 200 W/m^2 to 1000 W/m^2. For example, at a high solar radiation intensity of 1000 W/m^2, the air velocity at the chimney base of the inclined SCPP without air vents was 4.61 m/s whereas the inclined SCPP with 80° and 90° vents predicted the highest air velocity of 4.85 m/s at the chimney base. On the other hand, at a low solar radiation intensity of 200 W/m^2, the inclined SCPP without vents estimated 2.63 m/s while the inclined SCPP with 50° vents predicted the highest air velocity of 2.73 m/s. These results verified the hypothesis that the air vents could enhance the collector performance and consequently improve the air buoyancy in the inclined SCPP.

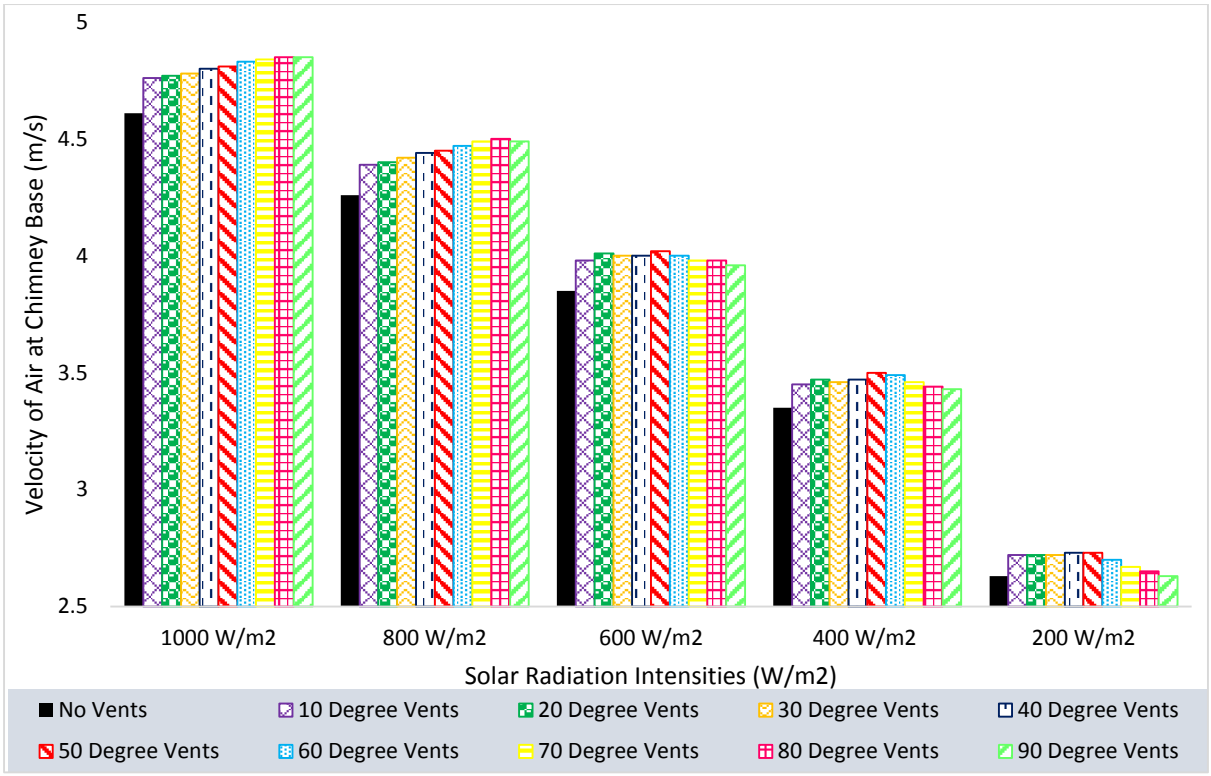

Figure 4.48: Velocity of Air at the Chimney Base for the Inclined SCPP with Different Orientation Angles of Vents

The driving force for the influx of air through the underneath air-vents is the increase in temperature of the absorber. With the influx of lower temperature air into the solar collector through the air vents, higher amount of heat is removed from the absorber and converted to useful energy in the buoyant air and consequently increases the mass flow rate of air at the chimney base. The increase in temperature of the buoyant air contributed to the drop in air density as well as increase the air velocity. Considering Bernoulli principle, higher velocity of air corresponded to lower air pressure inside the chimney. Meanwhile, the low ambient temperature and low ambient air velocity caused a higher air pressure on the outside of the system. This created larger pressure and density differences between the buoyant air exiting the chimney and the surrounding atmospheric air at the top of the chimney. With increase in air mass flow rate and air velocity induced by the inclusion of the underneath air-vents, the driving force in the inclined SCPP tends to overcome the pressure buildup over the chimney outlet and enhance power output of the plant.

Considering the angle of the vents, it can be observed from Figure 4.48 that below 600 W/m^2 solar radiation intensity, the higher inclined angles of 60^o to 90^o showed less enhancement but at higher solar radiation intensity of 800 W/m^2 and 1000 W/m^2, the velocity of air at the chimney base increased with increase in vent-angle. On average, the highest air velocity was

recorded at 50° vent-angle. The velocity vectors of the air flow near the vents at different angles are presented in Appendix B. The results showed that the higher vent-angles (60^o to 90^o) shows higher influx at higher solar radiation intensity but with less air near the absorber surface leading to air circulation near the air vent location. This air circulation could explain the performance degradation of the inclined SCPP with higher vent-angle when the system was subjected to lower solar radiation intensities. On the other hand, at lower vent-angles (10^o to 50^o), the velocity vectors showed the air path closer to the absorber surface which explains why higher air velocity was observed at the chimney base at lower solar radiation intensity at these lower vent-angles.

4.7.1.2 Mass Flow Rate of Air at Chimney Base at Different Vents Orientation Angles

The air mass flow rate at the chimney base considering the air velocities presented in Figure 4.48 was computed as and presented in Figure 4.49. The result as can be seen shows that the system without air vents has the lowest air mass flow rates at the base of the chimney. In line with one of the research objectives which aimed to improve the performance of the inclined SCPP through the use of vents, these results proved that the inclusion of underneath air vents at the collector absorber increased the air mass flow available to the turbine. The introduction of air vents induced additional air stream into the collector which increase the air mass flow rate and improve the plant's performance. As can be seen from the Figure 4.49, at solar radiation intensities of 200 W/m^2, 400 W/m^2 and 600 W/m^2, the inclined SCPP with 50° vents showed the highest air mass flow rates at 0.61 kg/s, 0.77 kg/s and 0.87 kg/s, respectively. Meanwhile, at a high solar radiation intensity of 1000 W/m^2, the highest air mass flow rate was obtained through the use of vents with the orientation angles between 60° and 90°. The system installed with 50° vents could still result in an almost equivalent air mass flow rate to those of the previously mentioned systems. Therefore, the underneath air vents oriented at 50° with respect to the horizontal surface of the absorber was determined to be the best orientation angle for optimum air mass flow rates output considering all solar radiation intensities.

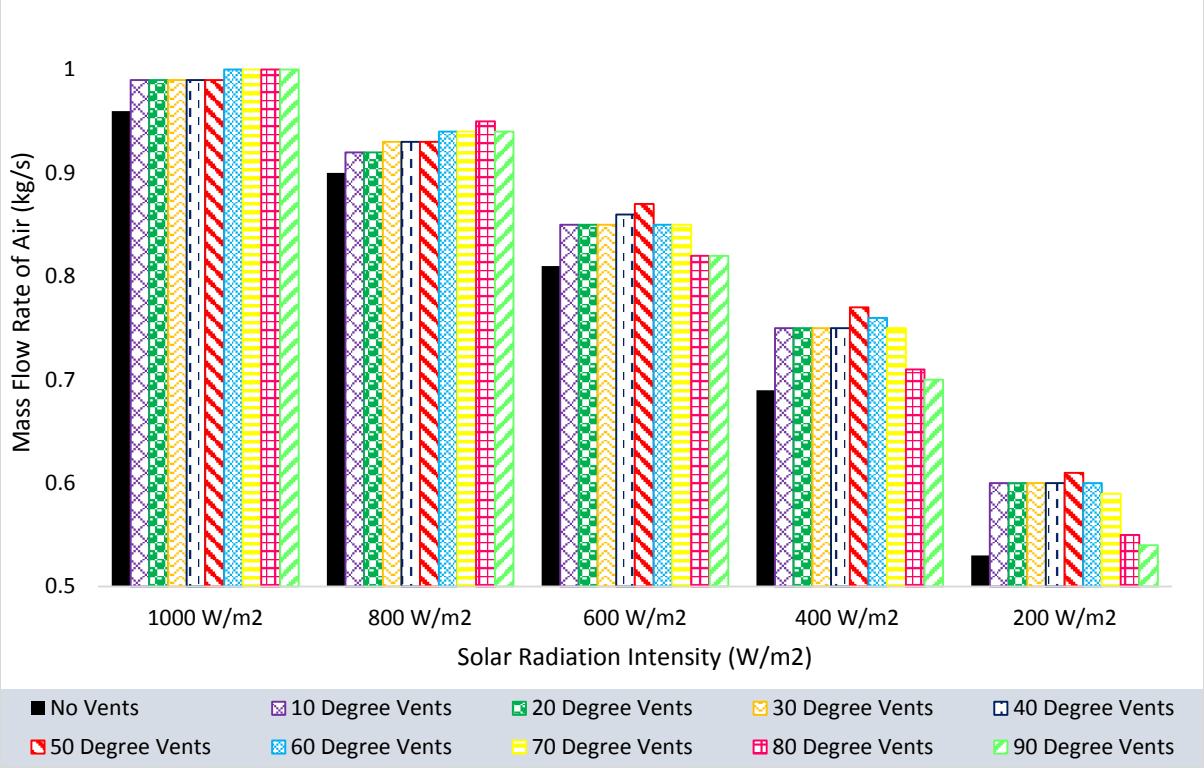

Figure 4.49: Mass Flow Rate of Air at the Chimney Base for Different Vents Angles

4.7.1.3 Electrical Power Outputs of the Inclined SCPP with Vents of Varying Orientation Angles

The results of the evaluation of the electrical power output for the inclined SCPP considering various vent-angles (10^o to 90^o) is presented in Figure 4.50. The results showed significant higher outputs than the system without vents. At 1000 W/m^2 solar radiation intensity, the inclined SCPP without vents produced only 7.13 W, whereas the system installed with 80° and 90° vents resulted in the highest electrical power output of 8.22 W (15.3% improvement). Similarly, at 1000 W/m^2, the inclined SCPP with 50° vents could produce a reasonably high electrical power output rated at 8.05 W (13% improvement). At lower solar radiation intensities from 200 W/m^2 to 600 W/m^2, the inclined SCPP with 50° vents produced the highest electrical power outputs which led to approximately 13.6 % improvement in comparison to the system without air vents while for the entire range of solar radiation from 200W/m^2 to 1000 W/m^2, an improvement of about 13% was achieved. These results showed that when the vents were oriented at 50° with respect to the absorber surface, the system could produce satisfactory electrical power outputs at different solar radiation intensities. These results also proved that the use of underneath air vents in a low cost inclined SCPP will help improve the power generation from renewable solar energy that can be possibly connected to the grid.

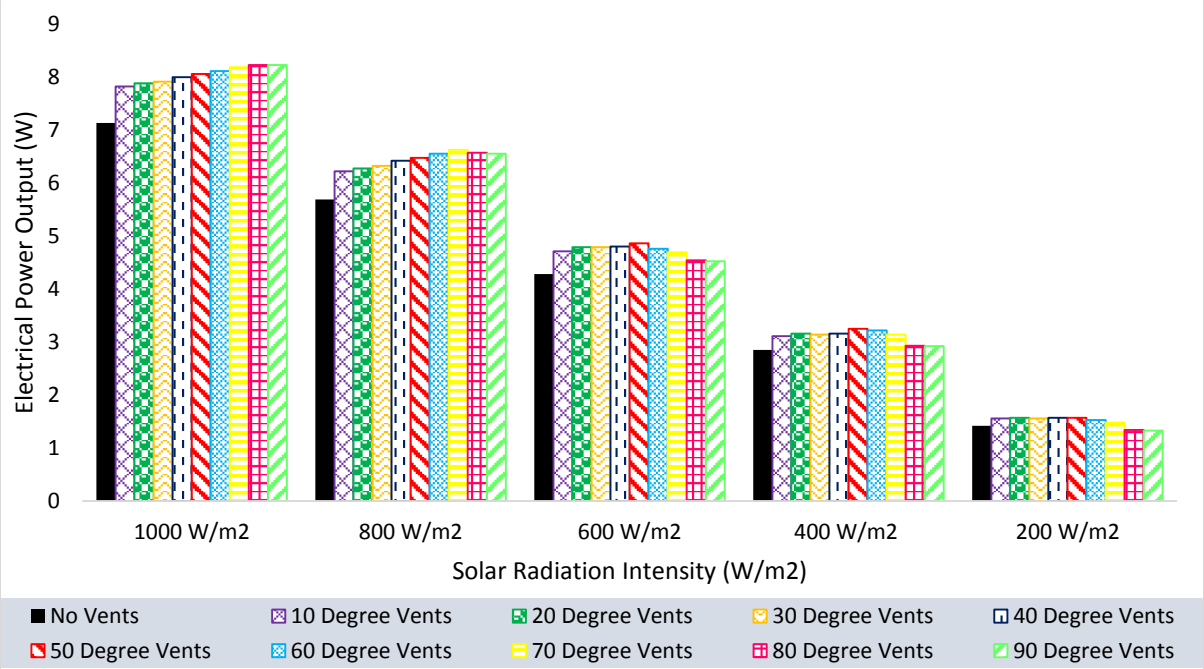

Figure 4.50: Electrical Power Output of the Inclined SCPP with Vents of Different Angles

4.7.1.4 Collector Efficiencies of the Inclined SCPP with the Inclusion of Additional Air Vents of Varying Orientation Angles

The effect of the vent-angles on the efficiency of the collector was evaluated as presented in Figure 4.51. The result shows that the collector efficiencies were lowest for the inclined SCPP system without air vents at different solar radiation intensities. At solar radiation intensity of 1000 W/m^2, the collector efficiency for the system without vents was only 23.35 % while the system with 90° oriented vents showed the highest collector efficiency at 27.37 %. However, at lower solar radiation intensities, the collector efficiency of the inclined SCPP with 90° oriented vents decreased. The possible cause of the drop in efficiency is associated to the air flow circulation observed in the system equipped with 90° oriented vents. The collector efficiency was found to be best with 50^o oriented air-vents at low to moderate solar radiation intensities which is majorly the solar radiation intensity range in Malaysia. Even at higher solar radiation intensity of 800 W/m^2 and 1000 W/m^2, the collector efficiency was reasonably higher than the system without air vents. At 200 W/m^2, 400 W/m^2 and 600 W/m^2 solar irradiance, the inclined SCPP with 50° oriented air-vents showed 26.87 %, 27.03 % and 27.08 % collector efficiencies, respectively. The average collector efficiencies considering the solar radiation intensities showed 12.3% improvement in comparison to the system without air vents. Overall,

the findings of the current study suggested that, with the inclusion of air vents, the collector efficiencies of the inclined SCPP was enhanced through improved air mass flow in the system.

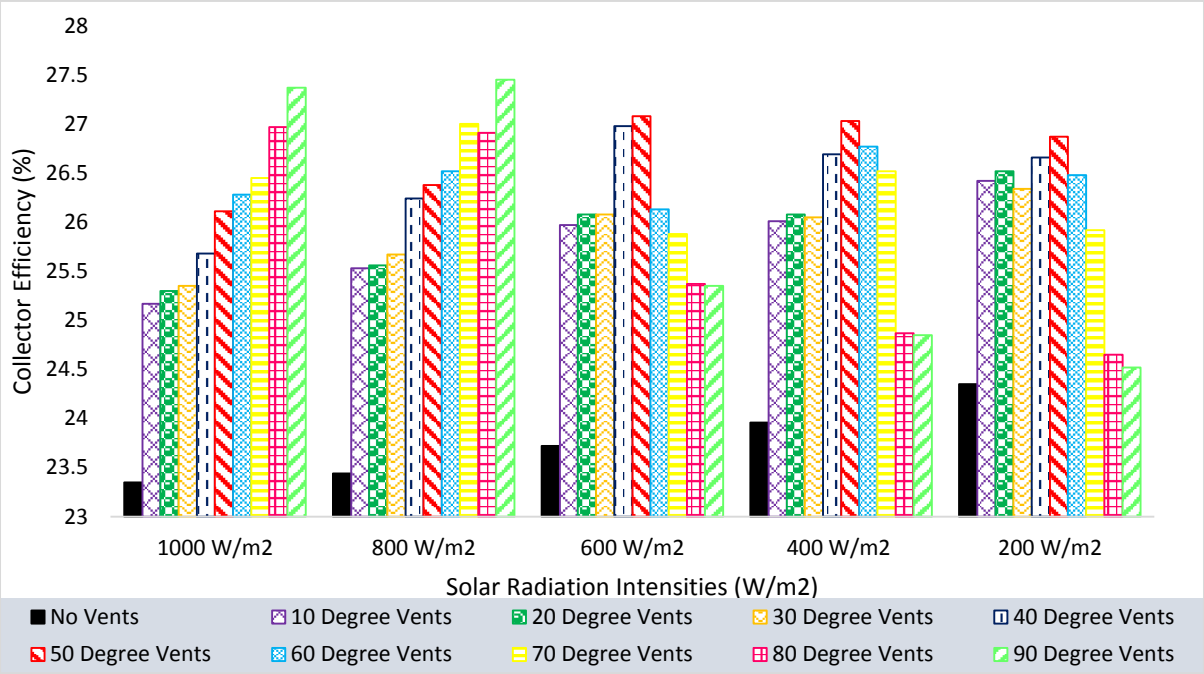

Figure 4.51: Collector Efficiency of the Inclined SCPP with Air Vents at Various Angles

4.7.2 Results Analysis of Collector Components' Temperatures and Thermal Energy Transfer within the Inclined SCPP

The analysis of the collector components' temperatures and the energy loss to the ambient through the cover of the collector are described in this section.

4.7.2.1 Collector Absorber Temperature Analysis for the Inclined SCPP

The collector absorber average temperature for the absorber without air-vents and the absorbers with different air-vent-angles were evaluated. The results in Figure 4.52 show the average temperatures of the absorber for the model without air-vents, 10^{o} oriented air-vent model, 50^{o} oriented air-vents model and 90^{o} oriented air-vents model. Figure 4.52 showed that the inclined SCPP without air vents has highest average absorber temperatures across all solar radiation intensities from 200 W/m^2 to 1000 W/m^2. On the other hand, the models with air-vents indicated reduced absorber temperature which can be attributed to the increase in air volume resulting from the air influx through the vents. The effect of the vent-angles is evident as shown in Figure 4.52 where the 50^{o} oriented air vent model displayed lowest absorber plate

temperature. This is because there is higher heat removal from the absorber by the air considering that the air flow near the absorber as presented in Appendix B, Figure B.5. This reduced the average temperature of the absorber.

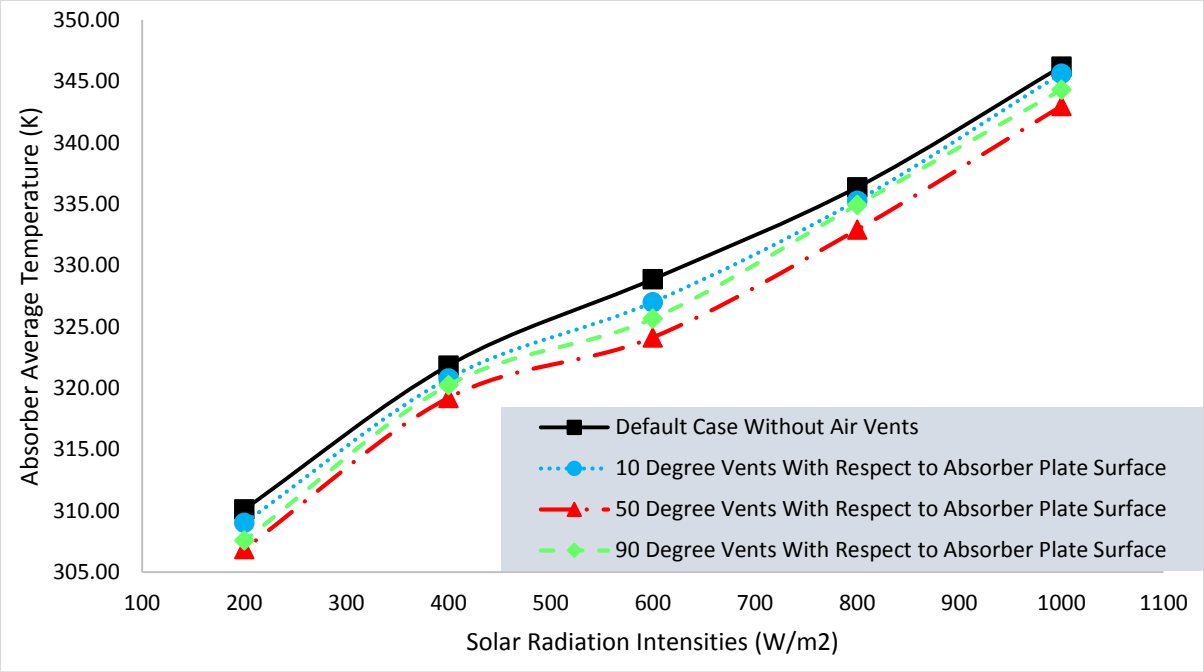

Figure 4.52: Absorber Temperatures for the Inclined SCPP with and without Vents

Moreover, Figure 4.52 showed that the inclined SCPP with 10° and 90° vents had higher absorber temperatures in comparison to the inclined SCPP with 50° vents. For the air vents orientation angle of 90°, less air flow was observed near the collector absorber while the air flow at that point was characterized of circulation flow thus less heat removal from the absorber as can be observed in the velocity vectors presented in Appendix B, Figure B.9. For the case of the system with 10° vents, as the vents were sloped at 10° with respect to the flat absorber surface, the slant position of the vents caused low influx of air from ambient into the greenhouse, thus less air volume to remove heat from the absorber.

4.7.2.2 Collector Cover Temperature Analysis for the Inclined SCPP

The results obtained for the average temperatures of the collector cover of the inclined SCPP for the models with and without air-vents are presented in Figure 4.53. The figure compares the results for three models with air-vent-angles 10º, 50º and 90º with the model without air-vents. The results revealed that the default system without the installation of air-vents was characterized of high average temperature of transparent cover as compared to the models with air-vents. The inclusion of underneath air vents at the collector absorber induced influx of lower

temperature air from the ambient through the vents into the greenhouse, thus increased convective heat removal from the absorber by the air and reduced radiation heat transfer from the absorber to the cover. This caused a reduction in the average temperatures of the transparent cover and also less thermal loss to the ambient from the cover.

The effect of the vents' orientation angles on the temperatures of the transparent cover showed that the 50° vent angle displayed lowest cover temperature at different solar radiation intensities. These results can be explained by using the velocity vector diagram in Figure B.5. The velocity vectors showed that the air particles flowing into the greenhouse from the 50° vent homogenously mixed with the buoyant hot air in the greenhouse and assume same flow pattern and direction with the buoyant air from the point of entrance. As the hot air particles in the greenhouse were evenly mixed with the induced cold air particles from the ambient, a lower temperature of the transparent cover was observed in the inclined SCPP with 50° vents. In the configurations where the vents were oriented at 10° and 90° angles, the transparent cover resulted in higher temperatures in comparison with the 50° oriented air-vent model. As can be seen in Section 4.7.2.1, the absorber temperatures for the system with 10° and 90° vents were higher in comparison to the system with 50° vents, which prompted the increase in the transparent cover temperatures.

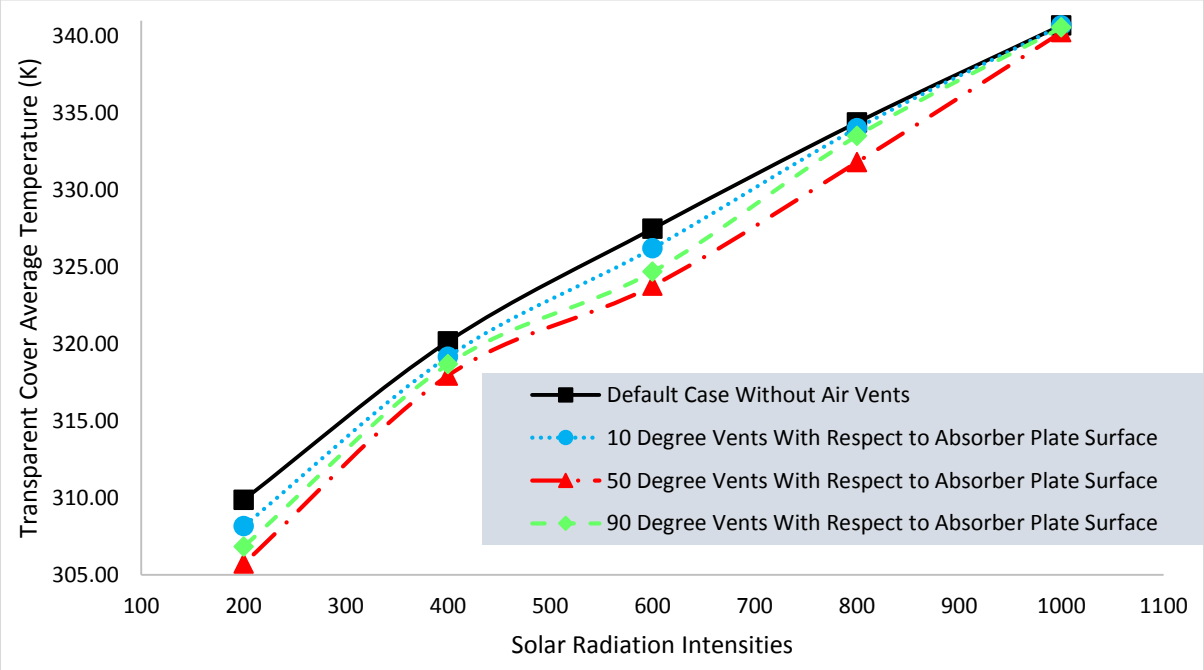

Figure 4.53: Transparent Cover Average Temperature for the Inclined SCPP with and without Vents of Varying Angles

4.7.2.3 Thermal Losses to the Ambient for the Transparent Cover of Inclined SCPP

The effect of the varying average temperatures of the cover at different air-vent angles were evaluated along with the case of the model without air-vents. The results as shown in Figure 4.54 showed the radiation heat transfer coefficient variation considering the radiation effect between the cover and the sky. Similarly, the convective heat transfer coefficient from the cover to the ambient is presented in Figure 4.55 under no wind condition following natural convective heat transfer effect due to temperature difference between the cover and the ambient. In Figure 4.54, it was observed that without the inclusion of the underneath air-vents, the system was characterized of higher radiation thermal loss from the transparent cover to the ambient. On the other hand, the inclined SCPP with underneath air-vents showed lower value of radiation heat transfer coefficients from the transparent cover to the ambient.

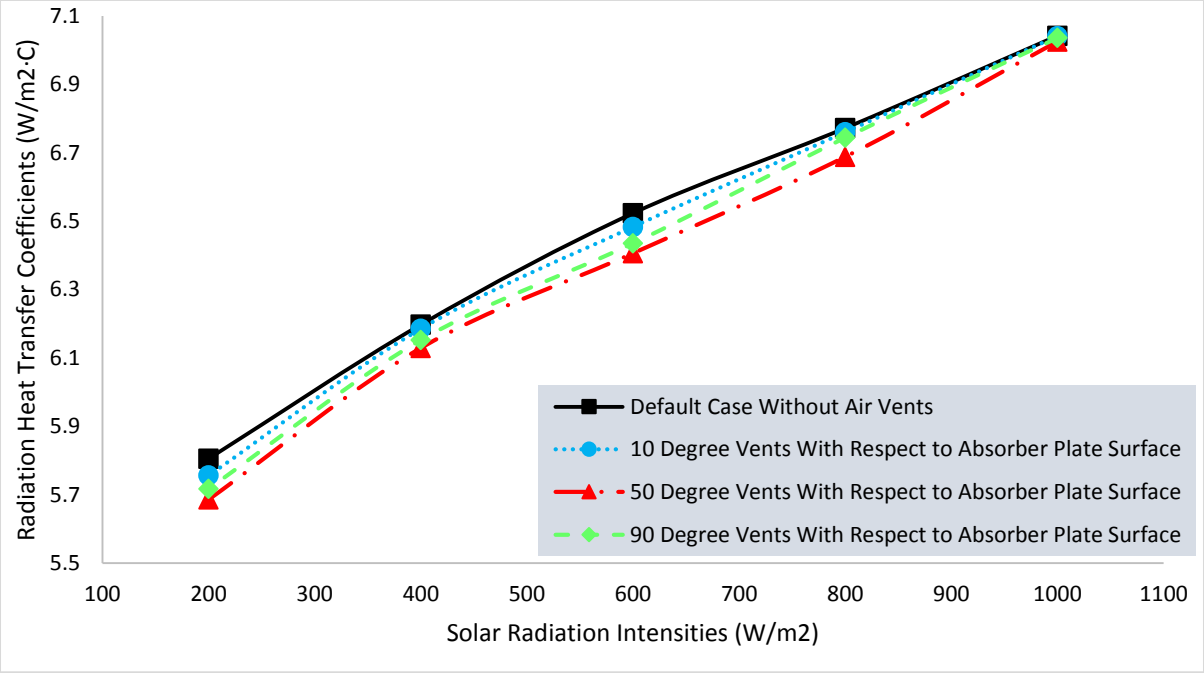

Figure 4.54: Radiation Heat Transfer Loss Coefficients from Cover to Ambient for the Inclined SCPP with and without Air-Vents

Similarly, considering Figure 4.55, it was also observed that the convective heat transfer coefficient of the model without inclusion of air-vents was higher than the models with air-vents. The model with 50^{o} oriented air-vents showed the least convective heat transfer coefficient due to the low cover temperature.

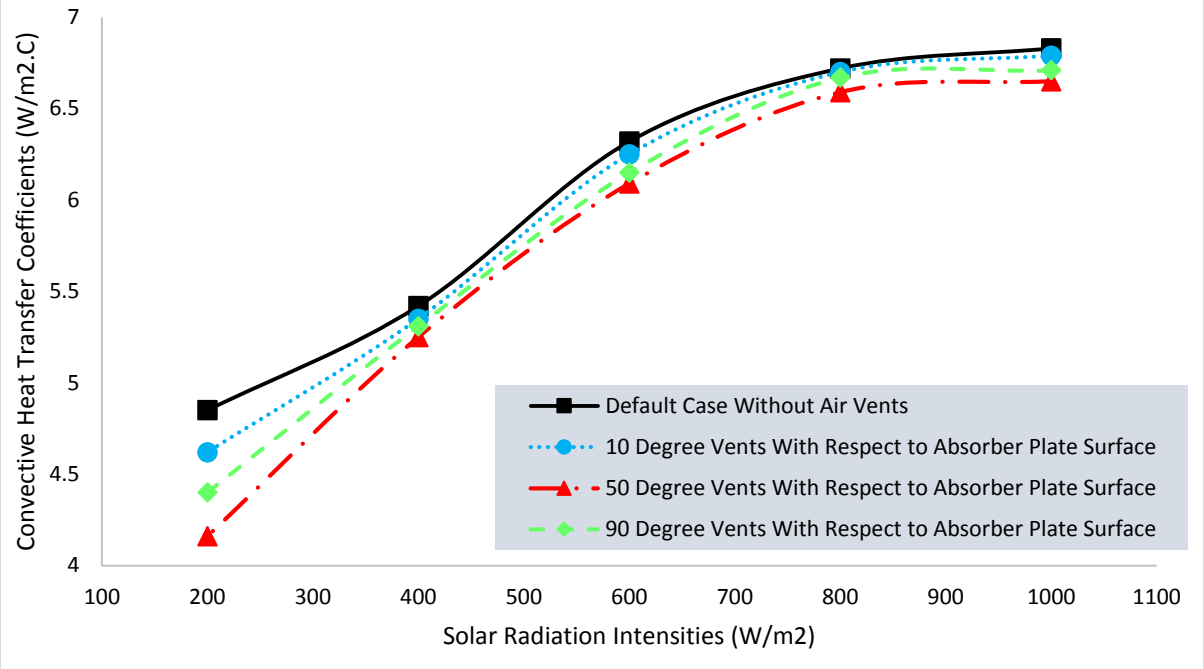

Figure 4.55: Convective Heat Transfer Loss Coefficients from Cover to Ambient for the Inclined SCPP with and without Air-Vents

The analysis above reflects the reason why the power output in the system with 50^{o} oriented air-vents was highest. This is because the thermal energy gained by the absorber was recovered by the buoyant air and the guided influx of cold air from the vents as useful energy for power generation. These results proved the hypothesis of this research that the underneath air-vents integrated to an inclined SCPP can be utilized to reduce thermal losses in the solar collector and enhance the driving force of the buoyant air.

4.8 Effects of the Different Positions of the Air Vents in the Solar Collector

The flow behavior of the hot buoyant air in the solar collector was investigated by changing the positions of the vents in the solar collector absorber. The effects of the variation in the air vents' positions on the inclined SCPP's performance was studied. As indicated in the previous section, the vents angle of 50° showed best configuration to minimize the thermal losses from the transparent cover to the ambient, thus, the 50° oriented air-vents was used to model the system for further investigation. Section 3.9.5 presented the description of the manipulated and constant variables employed in the investigation of the air-vents positions.

4.8.1 Influence of the Air Vents' Locations on Air Buoyancy

In line with the standard model described in Section 3.9.3 which has 0.5 m chimney diameter, the investigation was carried out to see the best location for the air-vents. This section presents the finding on the varying position of the air-vents in the inclined SCPP. The effect on velocity, pressure, power output and thermal loss is presented in the subsections.

4.8.1.1 Velocity of Air at the Chimney Base for Different Air-Vents' Positions

The air velocity magnitudes recorded at the base of the chimney with respect to the different air vents' positions are presented in Figure 4.56. Considering the base model, the results showed that when the air vents were located at 0 to 4 m position along the air-flow length of the solar collector, the output velocities were highest considering solar radiation intensities from 200 W/m^2 to 1000 W/m^2. When the vents were evenly distributed across the entire absorber area or located further from the collector's inlet (after 4 m from the inlet) and nearer to the chimney inlet, the air velocities at the base of the chimney significant drops. For example, when the vents were situated at 12 m to 16 m partition of the solar collector, the output velocities were lowest as shown in Figure 4.56. The visual presentation of the air velocity vectors at the various locations are presented in Appendix C.

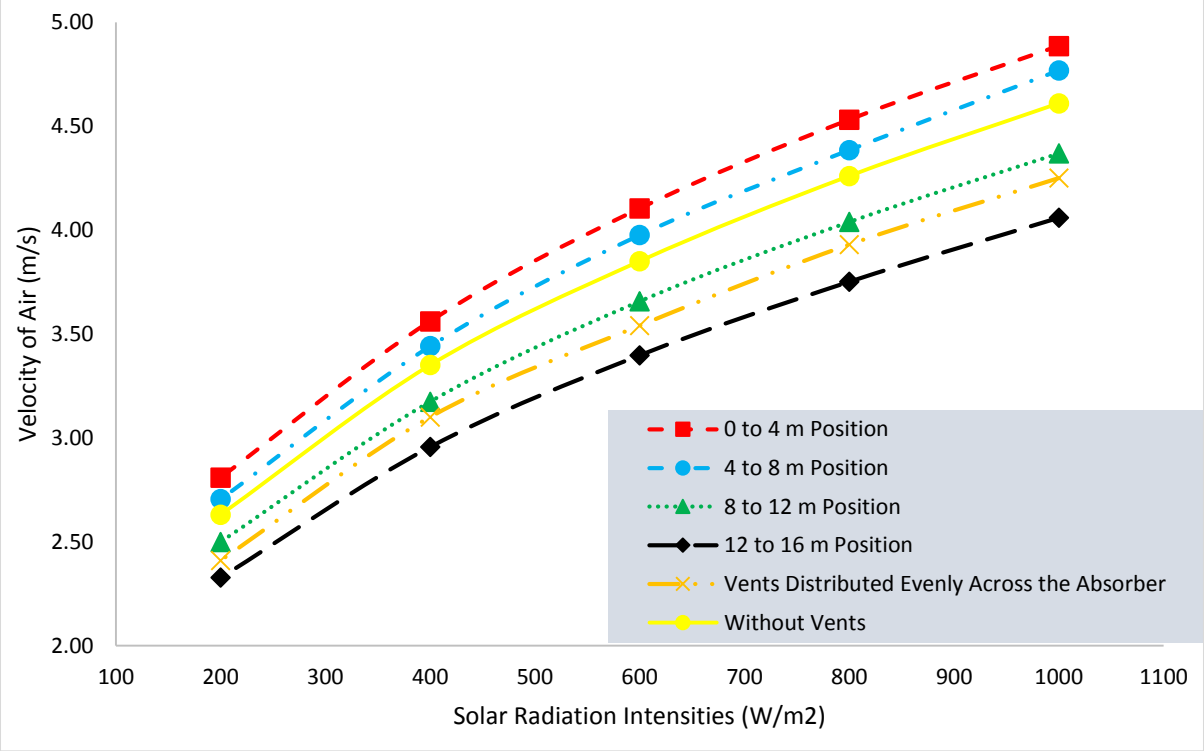

Figure 4.56: Velocity of Air at the Chimney Base for Different Vents' Positions

4.8.1.2 Gauge Pressure of Air with respect to Various Air Vents Positions

Figure 4.57 showed the system's air gauge pressure evaluated from plains drawn at the air flow channel along the length of the collector from its inlet to chimney base. The pressure difference between the ambient air and the system air is a major driving force for the buoyant air in the chimney. Thus at low gauge pressure, the air velocity dropped.

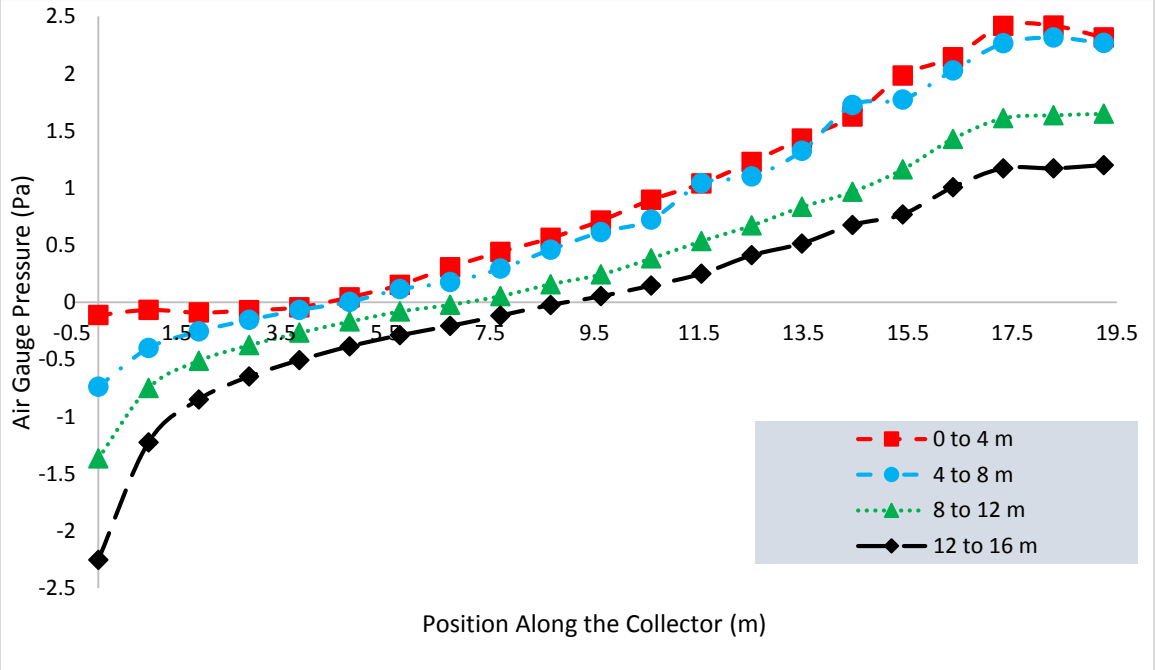

Figure 4.57: System's Air Gauge Pressure Measured along the Length of the Collector

To explain the situation that occurred at chimney base as shown in the graph of Figure 4.57, when the vents are installed at higher locations nearer to the chimney, higher influx of air will occur which leads to choke at the chimney base and consequently creates pressure buildup which restricts air flow.

4.8.1.3 Mass Flow Rate of Air at the Chimney Base for Different Air Vents Positions

The air mass flow rates in Figure 4.58 were determined based on the average air velocities recorded at the base of the chimney. As indicated in the previous Section 4.8.1.1, the inclined SCPP with air vents being installed between 0 to 4 m positions in the collector generated the highest air velocities and consequently, produced the highest air mass flow rates at the chimney base. When the vents were located further away from the collector's inlet and nearer to the chimney's entrance, the air mass flow rates at the chimney base were observed to decrease.

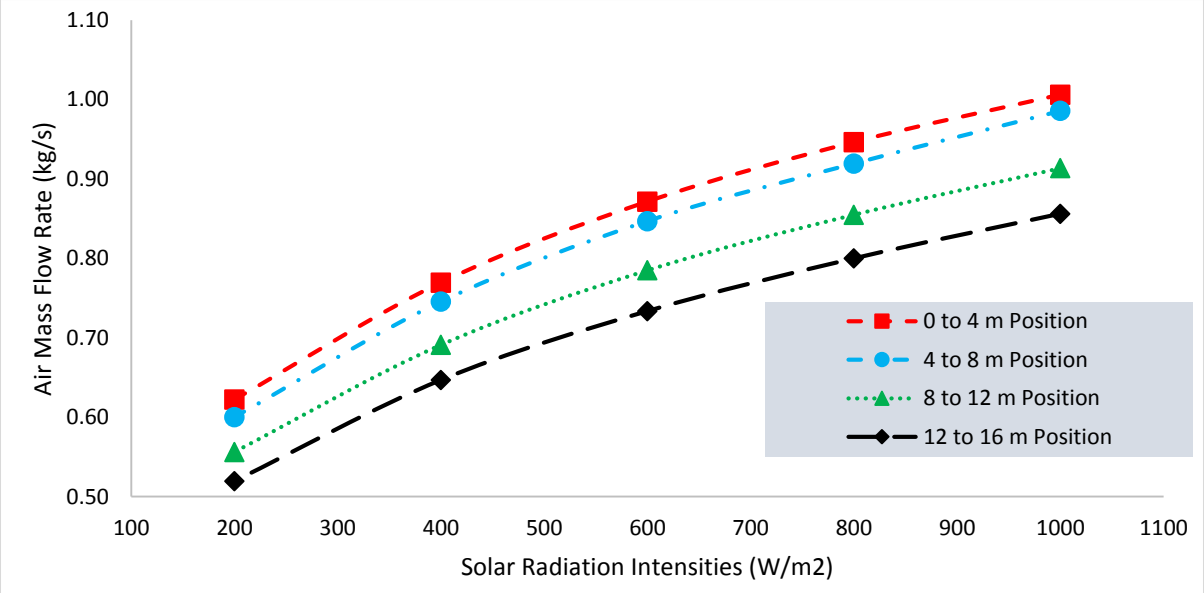

Figure 4.58: Mass Flow Rate of Air at the Chimney Base for Different Positions of the Vents

4.8.1.4 Electrical Power Outputs of the Inclined SCPP Considering Different Air Vents' Positions

The electrical power output of an inclined SCPP depends on the power in the buoyant air and the efficiency of the turbine. Considering the mass velocities presented in Figure 4.56, the air power was determined using Equation 3.44. The electrical power output obtained from the various configurations are presented in Figure 4.59 showing the system with the air-vents near to the collector inlet with higher power output.

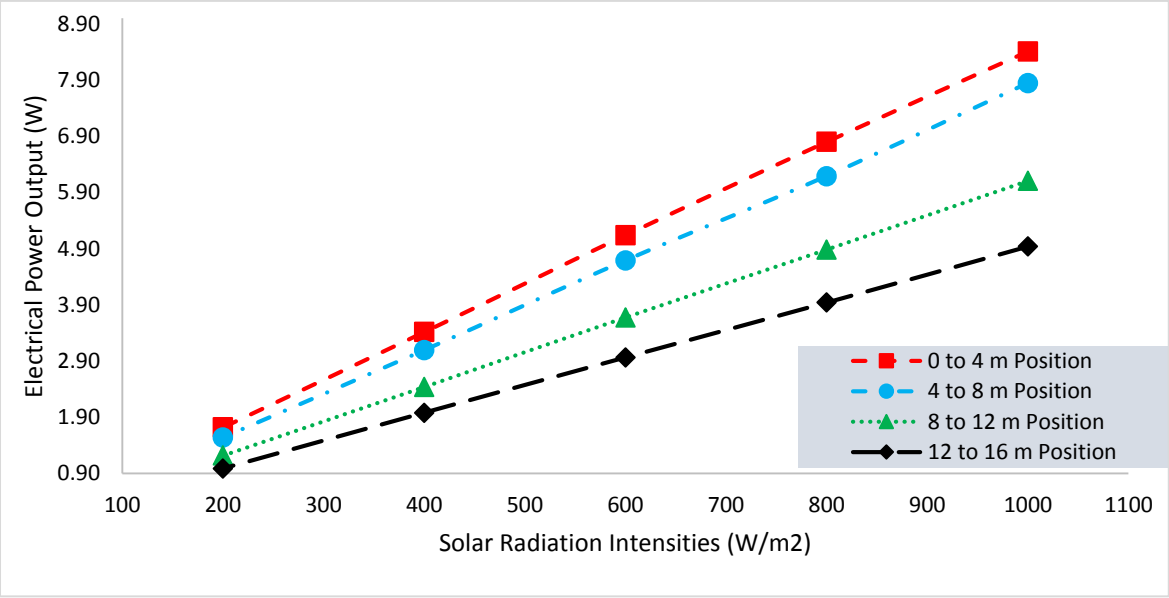

Figure 4.59: Electrical Power Outputs of the Inclined SCPP Considering Different Positions of the Air Vents

4.8.2 Thermal Field Analysis of the Collector Components of Inclined SCPP at Different Vents' Positions

Considering the collector, this section presents the effect of the vent locations on the components temperatures and the thermal losses through the cover.

4.8.2.1 Collector Absorber Temperatures for the Inclined SCPP with Vents at Various Positions

The collector absorber average temperatures for the inclined collector with vents located at various locations are presented in Figure 4.60. The results showed that the absorber average temperature was lowest for the model with the air-vents between 0 to 4 m along the collector's length. On the other hand, the systems with vents situated at 4 m to 8 m, 8 m to 12 m, and 12 m to 16 m along the collector's length indicated higher absorber temperature which might be associated to the loss of air flow through the vents. Similarly, the nearer the vents to the chimney, the absorber will experience higher temperature because the absorber surface area before the vents already gained higher temperature in excess which the less volume of air at that location could not utilize optimally, thus increased the absorber temperature. This increase in temperature also reflect on the cover temperature showing the effect of re-radiation from the absorber to the cover.

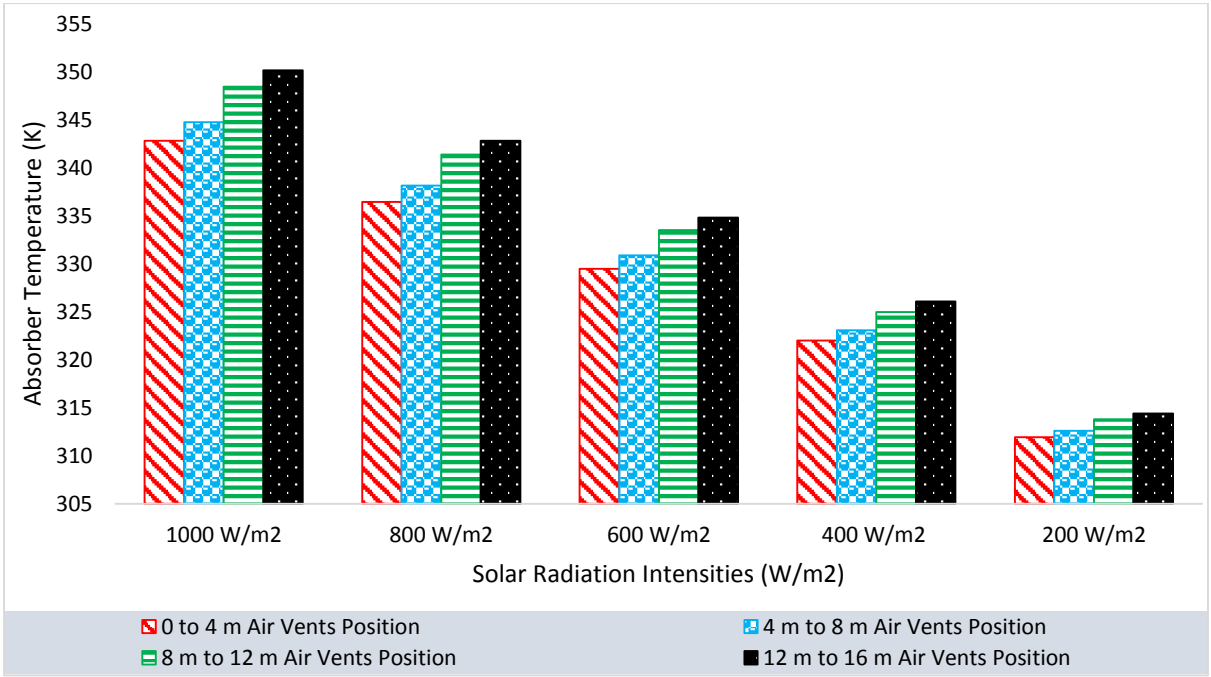

Figure 4.60: Absorber Temperatures for Different Positions of the Air Vents

4.8.2.2 Temperatures Analysis for Collector Transparent Cover of Inclined SCPP with Vents at Various Positions

Based on the discussion in Section 4.8.2.1, it was determined that the absorber temperatures were the lowest when the air vents were installed between 0 to 4 m away from the collector's inlet. The variation in the absorber temperatures for the various models are evident on the variations of the cover temperatures as can be seen in Figure 4.61. The system with air-vents between 0 to 4 m showed the least cover temperature while the cover average temperature continues to gradually increase as the location of the vents are adjusted towards the chimney location. The gradual increase in average transparent cover temperatures leads to higher thermal losses to the ambient.

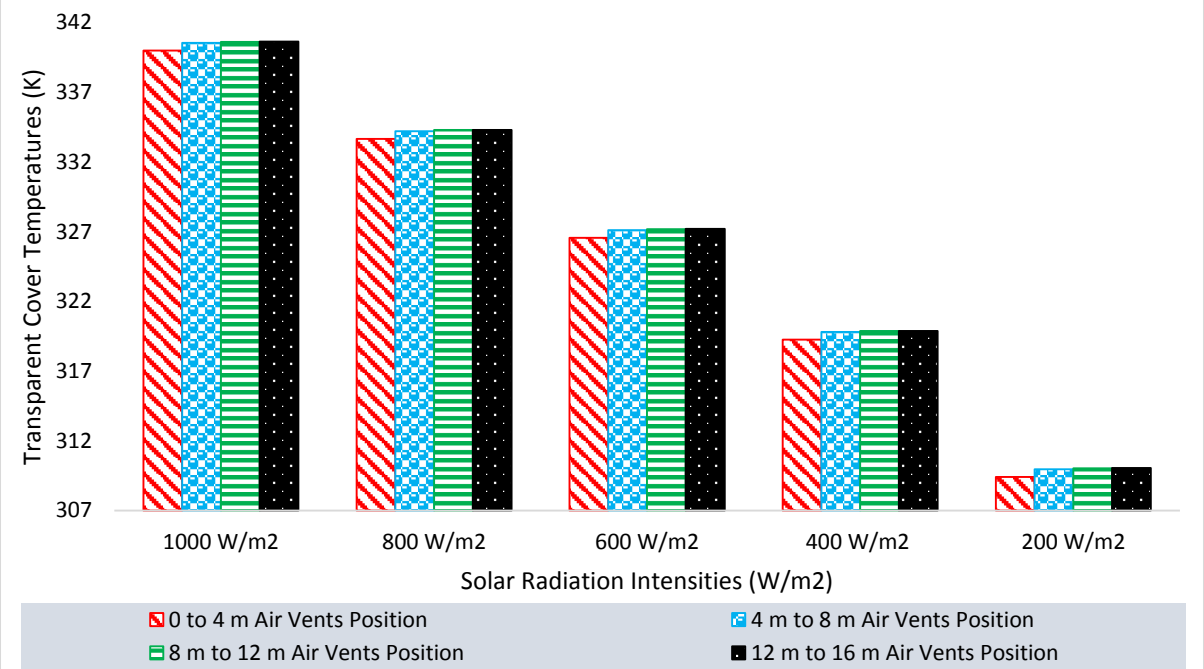

Figure 4.61: Transparent Cover Temperatures for the Different Vents' Positions

4.8.2.3 Useful Energy Gain and Buoyant Air Average Temperatures in the Collector of Inclined SCPP with Vents at Various Positions

The air temperatures in the collector are plotted in Figure 4.62. The results show that when the vents were installed between 0 to 4 m away from the collector's inlet, the system observed highest collector's buoyant air temperatures. As the vents were moved further from the inlet of the collector, the buoyant air temperatures were found to reduce. In Figure 4.63, the useful energy gain of the buoyant air in the greenhouse is presented for the systems equipped with vents located at different positions. With respect to the vents located between 0 to 4 m along

the collector's length, the useful energy gained was highest. This result was determined due lower thermal losses by radiation to the ambient, therefore, the collector's air was able to obtain higher useful energy.

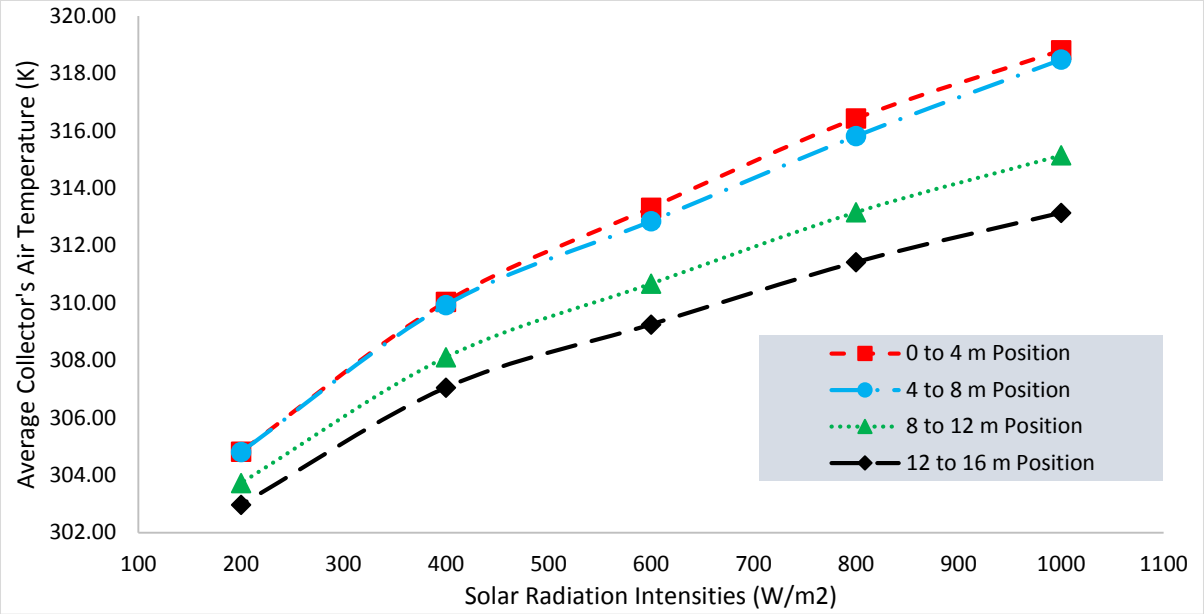

Figure 4.62: Average Temperatures of Buoyant Air in the Greenhouse for the Different Vents' Positions

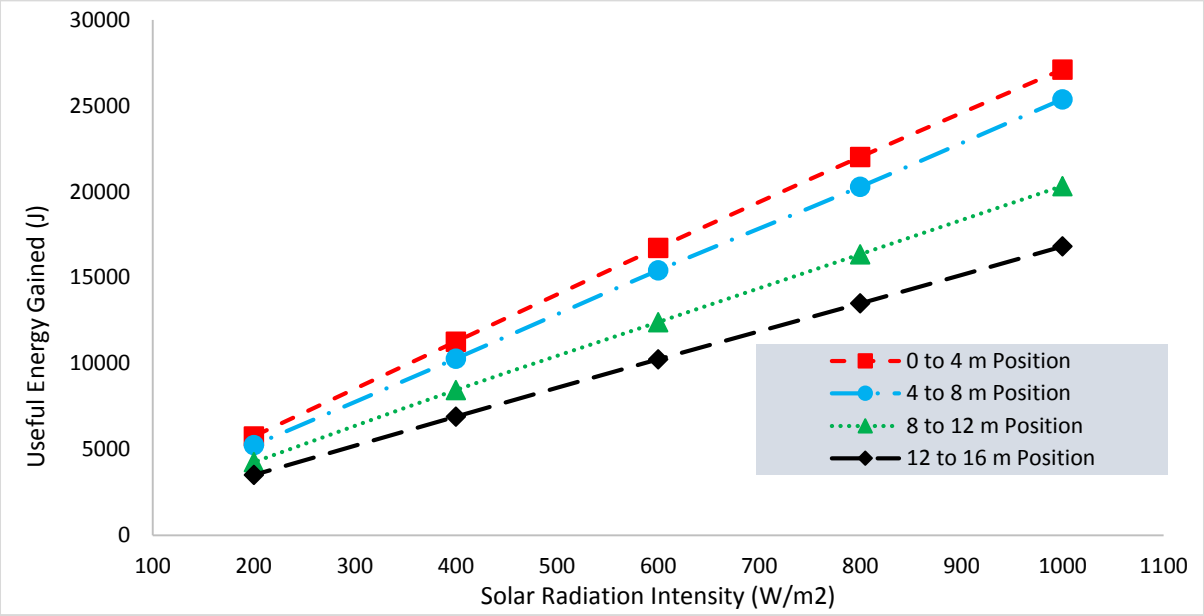

Figure 4.63: Useful Energy Gain of Buoyant Air in the Greenhouse for the Different Vents' Positions

4.8.2.4 Thermal Losses to the Ambient Through the Transparent Cover of the Collector for the Inclined SCPP with Vents at Various Positions

The thermal losses from the cover to the ambient are evaluated considering the radiation thermal loses and convective thermal losses under no wind conditions. The radiation heat transfer loss coefficients for the various models are presented in Figure 4.64 while the convective thermal loss coefficients are presented in Figure 4.65. The inclined SCPP with vents located between 0 to 4 m along the collector's length present the lowest radiation heat transfer loss coefficients from the transparent cover to the ambient. Due to the lower thermal losses by radiation to the ambient, this system was able to result in a higher useful energy gain by the collector's air. The reversed flow of air at the collector region led to reduced mass flow rate of air in the system for models with air vents at 4 m to 8 m, 8 m to 12 m, and 12 m to 16 m thereby created insufficient air volume in the greenhouse, thus, leading the increase thermal loss. This is because the absorber temperature was significantly increase contributing the increase heat transfer from the absorber to the cover and consequently to the ambient.

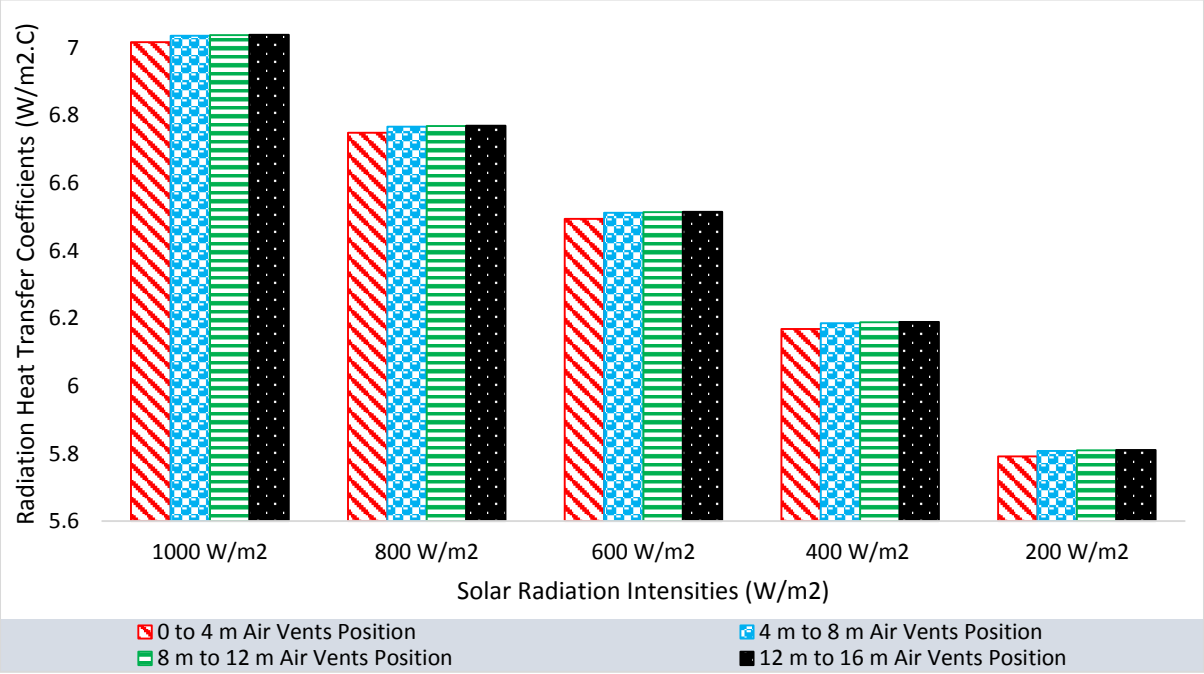

Figure 4.64: Radiation Heat Transfer Loss Coefficients from the Transparent Cover to the Ambient Considering the Inclined SCPP with Various Vents' Positions

The increase in temperature of the cover also contributed to the increase convective heat transfer loss coefficient as shown in Figure 4.65.

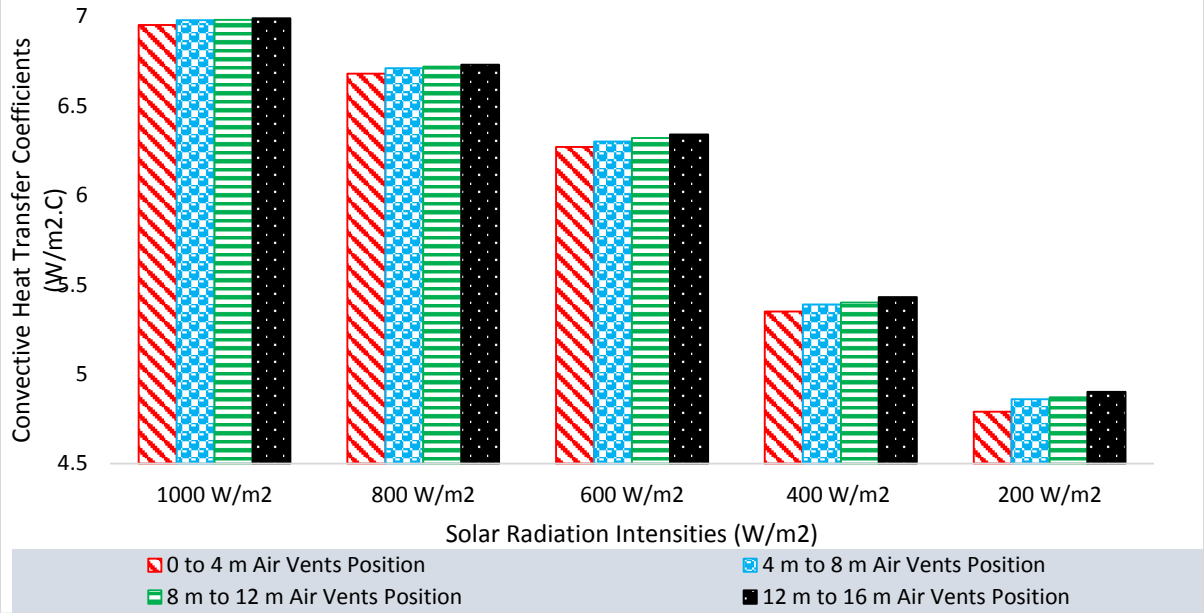

Figure 4.65: Convection Heat Transfer Loss Coefficients from the Transparent Cover to the Ambient Considering the Inclined SCPP with Various Vents' Positions under no Wind Condition

4.8.3 Collector Efficiencies of the Inclined SCPP with Vents at Various Positions

The results of the collector efficiency for the system with different air vents showed that the model with the air-vents between 0 to 4 m has best efficiency among the investigated model as shown in Figure 4.66.

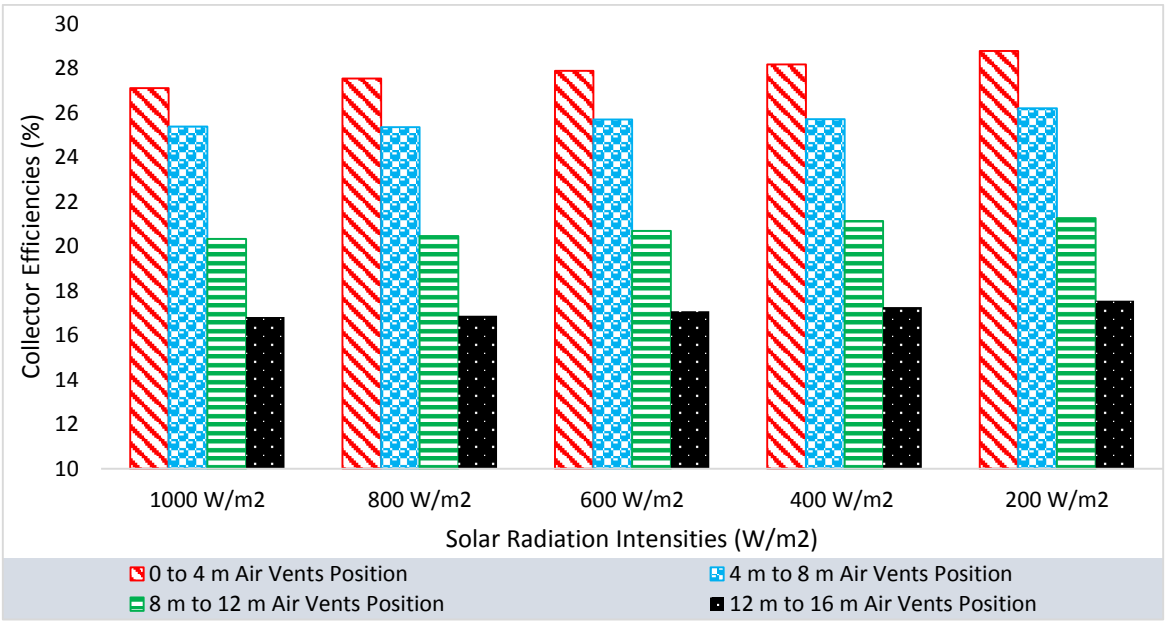

Figure 4.66: Collector Efficiencies of the Inclined SCPP with Vents at Various Positions

4.9 Influence of Chimney Diameters on the Performance of the Inclined SCPP with Underneath Air Vents

In this study, the performance of the inclined SCPP with underneath air vents was evaluated by manipulating the diameter of the chimney while the air-vents were evenly distributed across the surface of the absorber. It was determined in the previous Section 4.8 that the system's air experienced choke effect at the base of the chimney (throat) when the chimney had a small diameter of 0.5 m. By enlarging the diameter of the chimney, the critical flow behavior (reverse flow through the vents) of the fluid at the chimney's throat was resolved. The complete description of the manipulated and constant variables used in this investigation were provided in Section 3.9.6.

4.9.1 Effect of the Chimney Diameters Variation on the Air Buoyancy

The buoyant air was investigated under various chimney diameters to determine the diameter where the reverse flow will be eliminated and suitable for the system with air vents. The analysis presented in the subsections below include the velocity, mass flow rate and power output. The diameters considered in this investigation are 0.5 m, 0.6 m, 0.7 m, 0.8 m, 0.9 m and 1.0 m while the chimney height remained constant.

4.9.1.1 Velocity of Air at the Chimney Base for Different Chimney Diameters

With respect to the varied diameters, the velocity at the chimney base were evaluated from the simulation data. The results of the average air velocity at the base of the chimney are presented in Figure 4.67 with respect the different chimney diameter. Considering velocity, the inclined SCPP with 0.5 m chimney diameter produced the highest air velocity at the base of the chimney. As the diameter of the chimney was gradually enlarged from 0.5 m to 1.0 m, the air velocity at the chimney base was observed to reduce at the various solar radiation intensities. These results were consistent with the principle of fluid continuity where the effect of the chimney cross sectional which indicated that the cross-sectional area of the flow channel was inversely proportional to the air flow velocity.

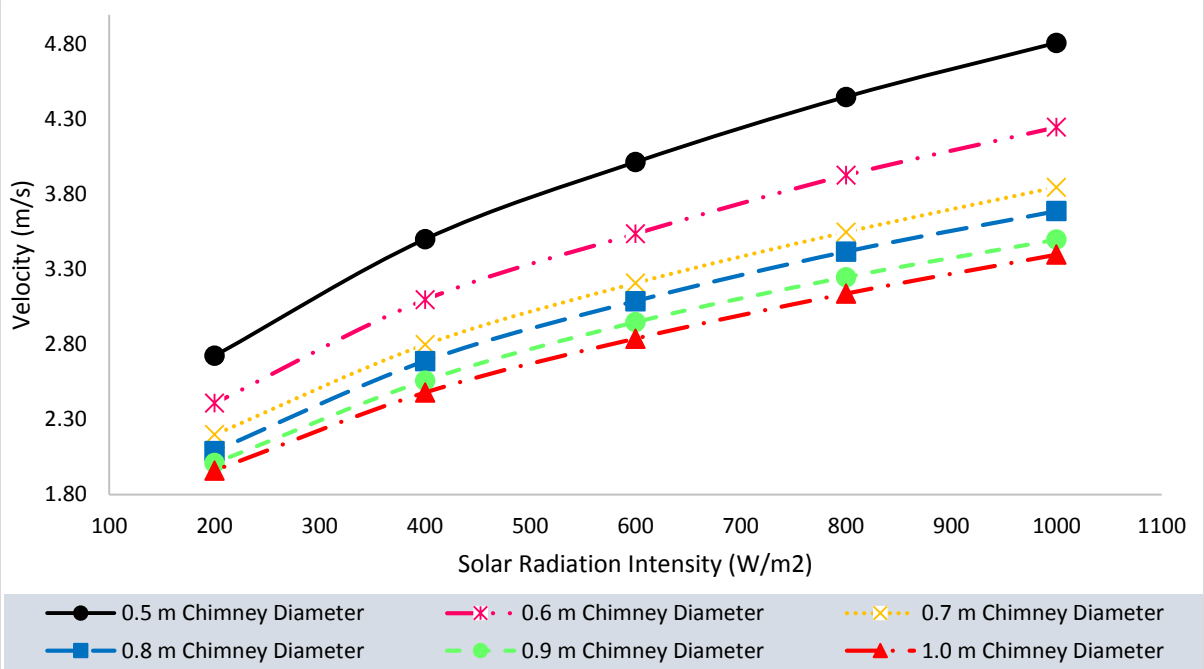

Figure 4.67: Velocity of Air at the Chimney Base for the Inclined SCPP with Different Chimney Diameters

With the chimney of 0.5 m diameter, the air in the collector experienced choked at the throat of the chimney which led to reverse flow in the air such that some of the air exited the collector through the underneath air-vents. The increase in the chimney diameter was observed to reduce the volume of air that exits through the vents. In Appendix D is the detailed velocity vector diagrams of air velocity profile at the vent location for 0.5 m, 0.6 m, 0.7 m, 0.8 m, 0.9 m and 1.0 m chimney diameters are respectively represented by Figure D.1, Figure D.2, Figure D.3, Figure D.4, Figure D.5 and Figure D.6. Considering the results as presented in Appendix D, the reverse flow was eliminated at 1.0 m chimney diameter as can be seen from the velocity vector diagram presented in Figure D.6.

4.9.1.2 Gauge Pressure of Air at Different Points in the Greenhouse

The gauge pressures of the system air from the inlet to the chimney base of the greenhouse section is considered on average with respect to locations along the collector's length as shown in Figure 4.68. The air pressure was observed to reduce with increase in chimney diameter which in turns reflected in the drop in the buoyant air velocity. This gradual increase in the chimney diameter gradually eliminated the choke experienced 0.5 m diameter chimney as reported in previous sections. At 1.0 m chimney diameter, the chimney's cross-sectional area

was sufficiently large to allow the heated air to flow through without any restriction, thus no reverse flow was experienced at the underneath air-vents.

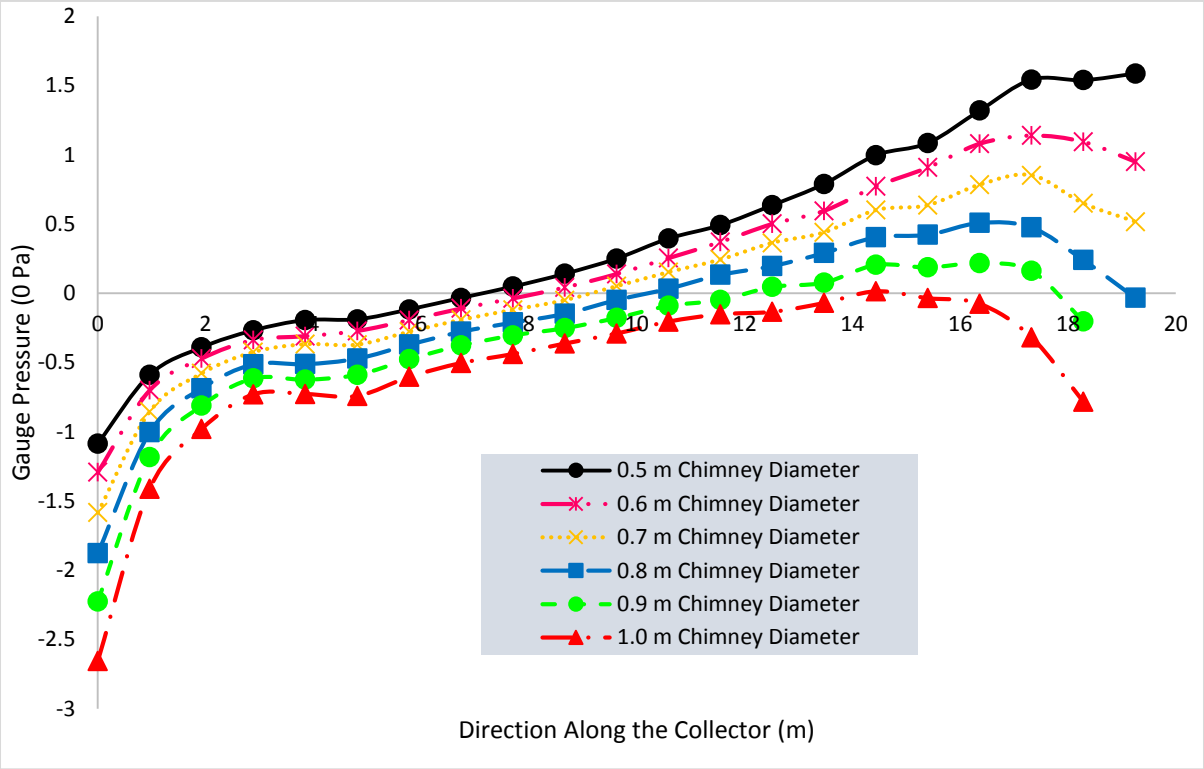

Figure 4.68: Gauge Pressure of System Air along the Collector's Length

4.9.1.3 Mass Flow Rate of Air at the Chimney Base for Different Chimney Diameters

In consideration of the various chimney diameters investigated, the air mass flow rates measured at the base of the chimney were evaluated and presented in Figure 4.69. The inclined SCPP with a larger chimney diameter of 1.0 m for the 100 m2 inclined collector showed highest air mass flow rate at various solar radiation intensities, despite having lower air velocity in comparison to other systems involving smaller chimney diameters. The effect of the collector exit cross-sectional area (chimney base cross-sectional area) is a propelling factor in the mass flow rate as supported by Equation 3.39, thus infers that the chimney's cross-sectional area played dominant role towards the system's air mass flow rate enhancement when the diameter is at optimum.

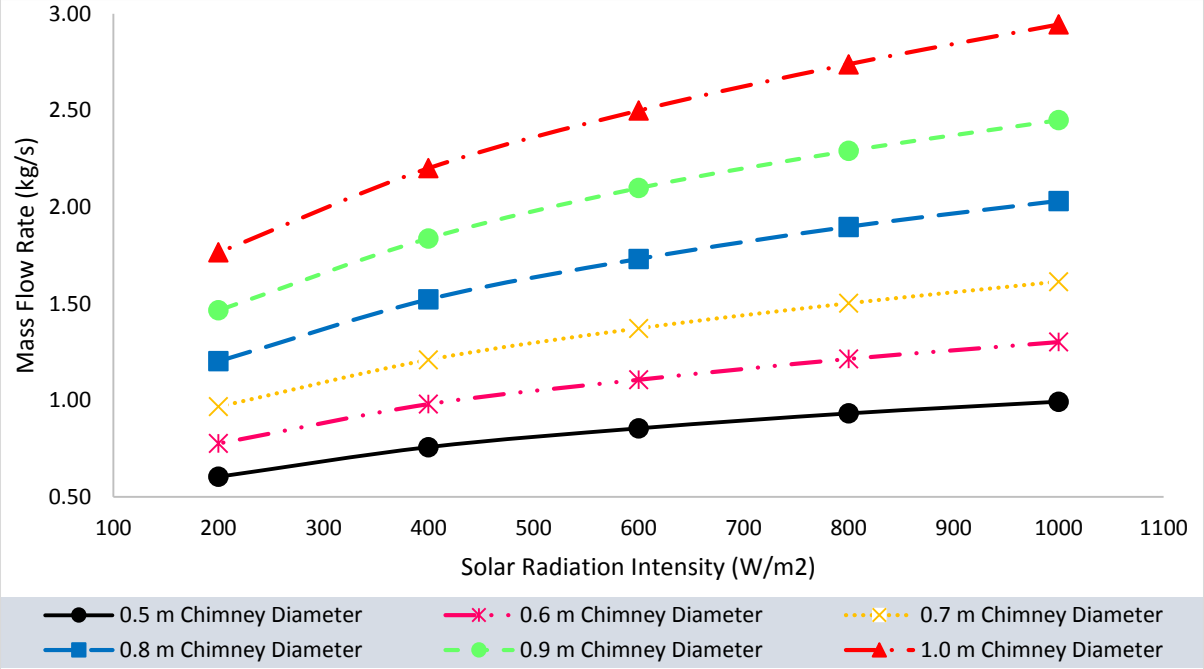

Figure 4.69: Mass Flow Rate of Air at the Chimney Base for the Inclined SCPP of Different Chimney Diameters

4.9.1.4 Electrical Power Outputs of the Inclined SCPP with Chimneys of Different Diameters

The electrical power outputs represented by Equation 3.47, for the various chimney diameters were evaluated considering the effect of pressure using Equation 3.43, air power as represented in Equation 3.44 and turbine efficiency of 70% following the report of (Fluri 2008). In consideration of different chimney diameters, Figure 4.70 shows the results of the electrical power output of the inclined SCPP where the system with 1.0 m chimney diameter was observed to show the highest power output considering the solar radiation intensities of 200 W/m^2 to 1000 W/m^2. In the previous section 4.9.1.3, it was determined that the system with 1.0 m chimney diameter resulted in the highest air mass flow rates at the collector's exit which also influenced the air power available to the turbine and consequently, the produced the highest electrical power output. When the inclined SCPP consisted of a 0.5 m diameter chimney, the electrical power output was only 8.05 W at 1000 W/m^2. As the chimney's diameter was enlarged to 1.0 m, the electrical power output was increased to 11.91 W which showed a 48 % performance improvement.

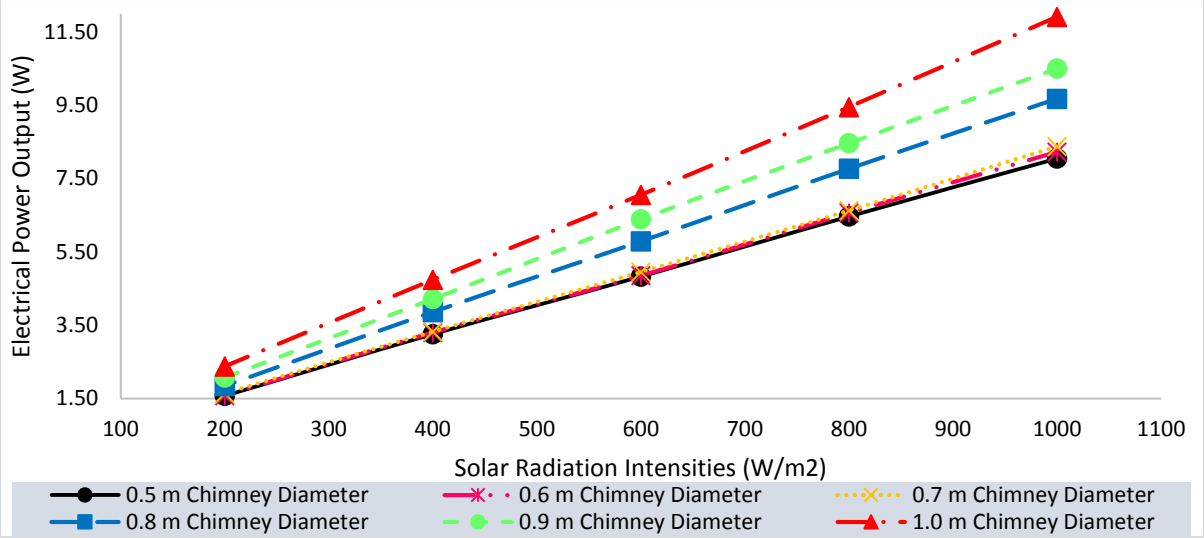

Figure 4.70: Electrical Power Outputs of the Inclined SCPP with Different Chimney Diameters

4.9.1.5 Collector Efficiencies of the Inclined SCPP with Chimneys of Different Diameters

The collector efficiencies were observed to increase when the diameter of the chimney was enlarged from 0.5 m to 1.0 m, as shown in Figure 4.71. At a large chimney diameter of 1.0 m, the air-vents performed effectively, thus the reverse air flow was eliminated at the vents locations. The increase in the chimney diameter eliminated the choke as well, thus there was no restriction to the buoyant air at the chimney base and influx air from the air-vents. As a result, there was a continuous flow of air from the collector's inlet and the air vents' inlets into the updraft tower.

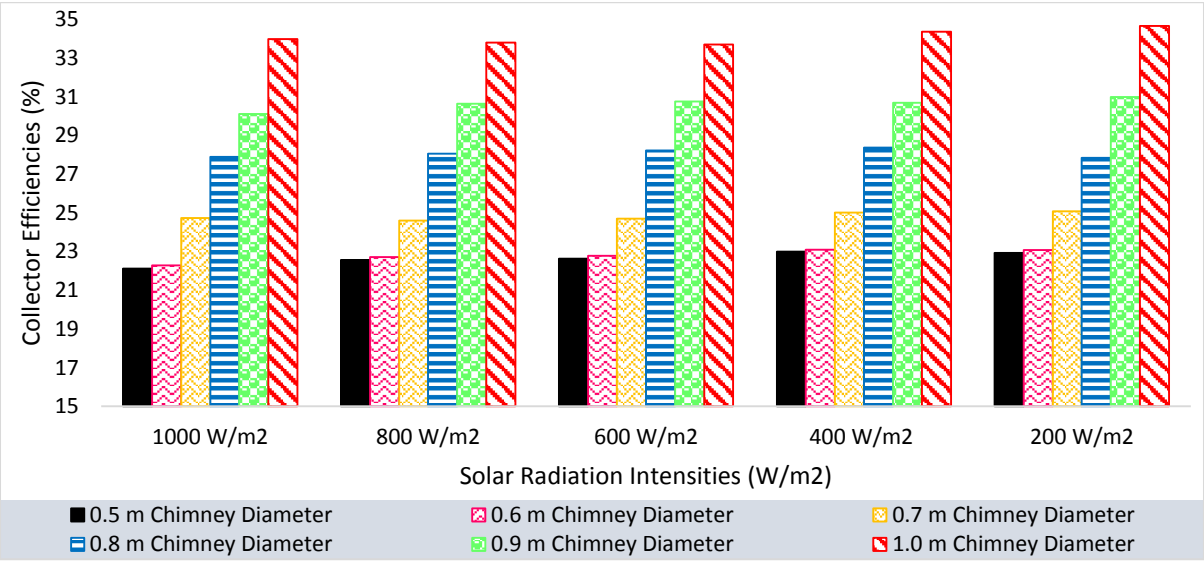

Figure 4.71: Collector Efficiencies of the Inclined SCPP with Different Chimney Diameters

4.9.2 Effect of the Chimney Diameter Variations on the System's Thermal Losses

This section presents the collector components average temperatures, buoyant air average temperature and the thermal loss from the cover to the ambient through radiation and convection under no wind conditions. The subsections present the different conditions.

4.9.2.1 Collector Components Temperature Analysis of the Inclined SCPP with Chimney of Different Diameters

In Figure 4.72, as the diameter of the chimney was increased from 0.5 m to 1.0 m, it was observed that there was a reduction in the average temperature of the absorber. This result showed that increase in the chimney diameter reduced the resident time of the air in the collector as a result of choke. With the elimination of the choke at the chimney base, the buoyant hot air leaves the system easily and make room for influx of colder air from the surrounding through the underneath air-vents into the greenhouse. The influx of colder air into the greenhouse increases heat removal from the collector's absorber leading to reduced thermal loss from the absorber to the cover and consequently to the ambient through the cover. The effect of the heat removal from the collector absorber can be seen on the reduction of the absorber's average temperature as shown in Figure 4.72 were the model with 1.0 m chimney diameter experienced the lowest absorber temperature across the various solar radiation intensities and more evident with increase in solar radiation intensity. The lower temperature of the absorber was remarkable for the sole purpose of minimizing the re-radiation heat transfer from the absorber to the transparent cover.

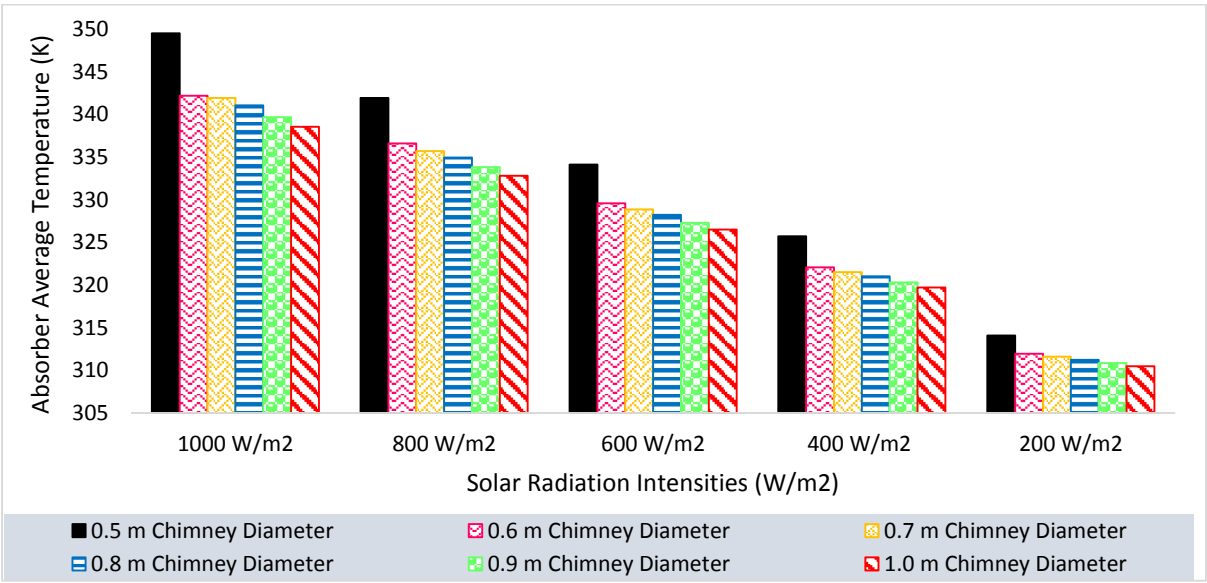

Figure 4.72: Absorber Temperature for the Inclined SCPP with Different Chimney Diameters

The reduction in the average temperature of the absorber had a significant effect on the transparent cover's temperature. When the chimney's diameter was increased from 0.5 m to 1.0 m, the lower absorber's temperature caused a lower re-radiation heat transfer to the transparent cover. As a consequence, the transparent cover's temperature was observed to decrease, which can be seen in Figure 4.73.

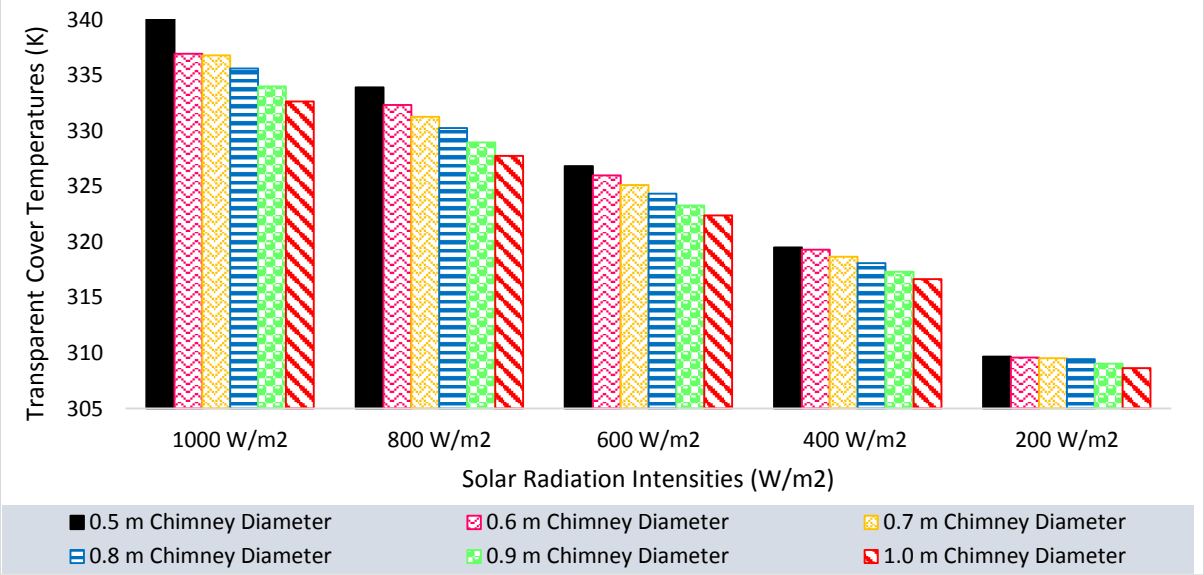

Figure 4.73: Cover Temperatures for the Inclined SCPP with Different Chimney Diameters

The lower temperature of the transparent cover was a positive outcome which denoted minimized thermal radiation losses from the transparent cover to the ambient. The solar energy received by the absorber which was converted to heat were used to generate higher amount of useful energy in the buoyant as the thermal losses associated to the transparent cover was reduced. A representation of the temperature contours for the transparent cover when the system was investigated without air-vents and cases when it was investigated with air-vents under different chimney diameters are presented in Appendix E. It was observed that the increase in chimney diameter to 1.0 m and the inclusion of the air-vents reduced the average temperature of the cover showing multiple patches of lower temperature region on the transparent cover, as can be seen in Figure E.*2*. This observation proved that the transparent cover's average temperature could be lowered through the optimization of the chimney's cross-sectional area and the use of additional air vents.

The collector's air temperature was plotted in Figure 4.74. The results showed that when the vents were found to be working effectively in the inclined SCPP with 1.0 m diameter chimney, the average collector's air temperature decreased. The inflow of lower temperature air into the

system through the underneath air vents and the elimination of resident time for the buoyant air caused a reduction of the temperature of the collector's air. This reduced the re-radiation from the absorber to the transparent cover as much air now competes for the heat at the absorber thereby recovering the thermal energy into useful energy. Overall, the thermal losses to the surrounding was minimized.

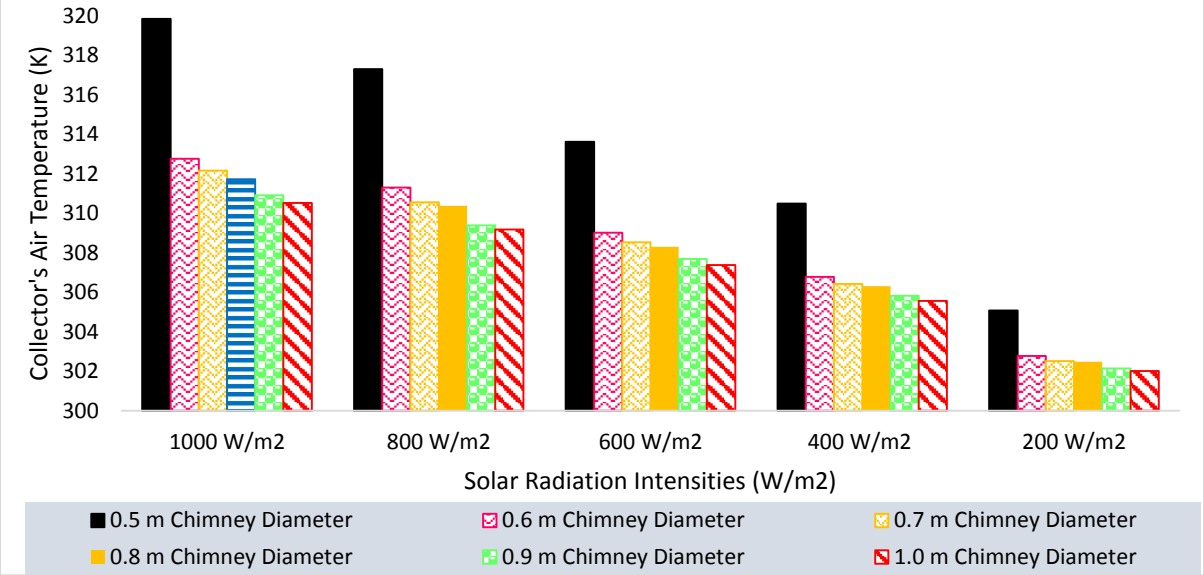

Figure 4.74: Collector's Air Average Temperatures for the Inclined SCPP with Different Chimney Diameters

4.9.2.2 Heat Transfer Loss Analysis at the Collector with Respect to Different Chimney Diameters of Inclined SCPP

The thermal energy transfers at the collector are reported in this part of the report. The thermal energy transfer coefficient by re-radiation from the collector absorber to the collector cover is presented in Figure 4.75. The results as can be seen showed that with increase in the chimney diameter which eliminated the reverse flow at the air-vents, the re-radiation heat transfer coefficient dropped as compare to the cases where the system with smaller chimney diameter.

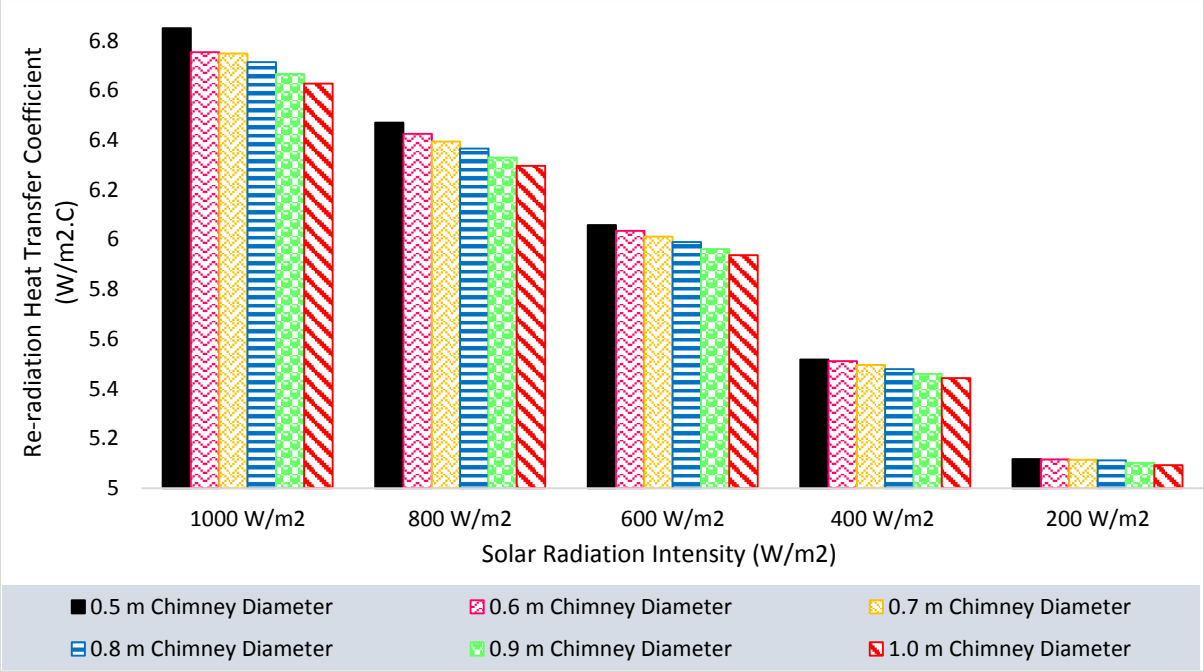

Figure 4.75: Re-radiation Heat Transfer Coefficients from the Absorber to the Transparent Cover of the Inclined SCPP at Different Chimney Diameters

The effect of the reduced re-radiation as in the case of 1.0 m diameter chimney, which was presented in Figure 4.73 showing reduction on temperature of the transparent cover, the analysis of the thermal loss by convection and radiation to the ambient were evaluated. The radiation heat transfer loss coefficient from the transparent cover of the solar collector was analyzed and presented in Figure 4.76 with respect to different inclined SCPP configurations involving various chimney diameters. The results showed that the inclined SCPP with 0.5 m diameter chimney estimated the highest radiation heat transfer loss coefficients from the transparent cover to the ambient. In other words, the system with 0.5 m diameter chimney was determined to have the highest thermal losses from the collector's roof to the ambient while the system having 1.0 m chimney diameter displayed lowest radiation heat transfer coefficient from the cover to the sky.

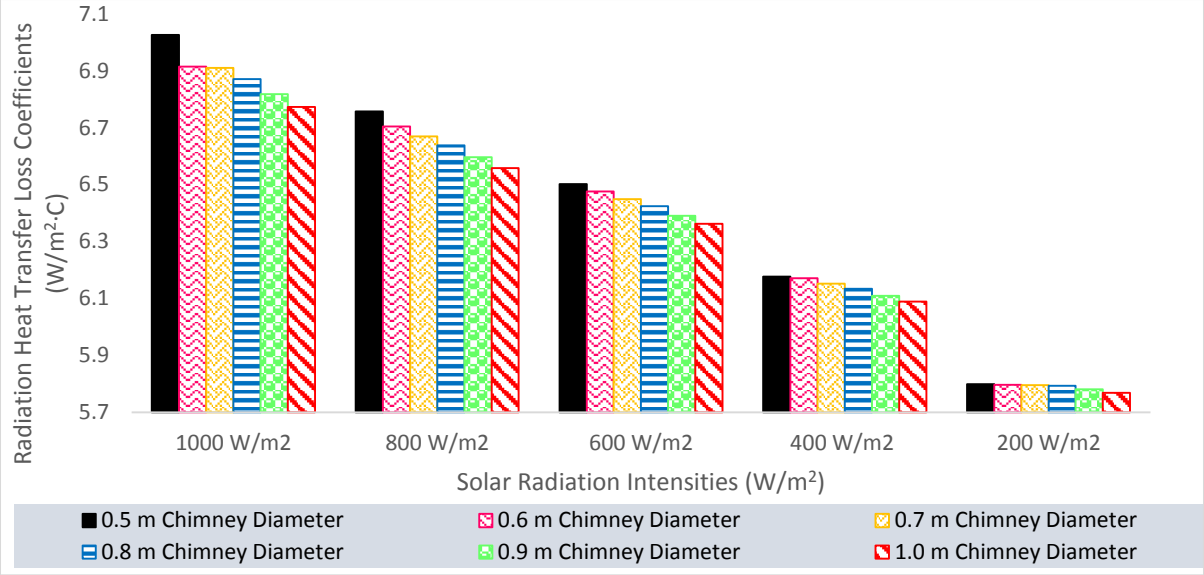

Figure 4.76: Radiation Heat Transfer Loss Coefficients from the Transparent Cover to the Ambient Considering Inclined SCPP of Different Chimney Diameters

The study also evaluated the convective heat transfer loss coefficient from the transparent cover to the ambient under no wind condition. The results of the convective heat transfer loss coefficients from the cover to the ambient at the different chimney diameter are presented in Figure 4.77. The results as presented in Figure 4.77 showed that the inclined SCPP with 1.0 m diameter chimney presented the lowest convection heat transfer loss coefficients from the transparent cover to the ambient. A reduction in the system's thermal losses through the use of 1.0 m diameter chimney increased the performance of the system.

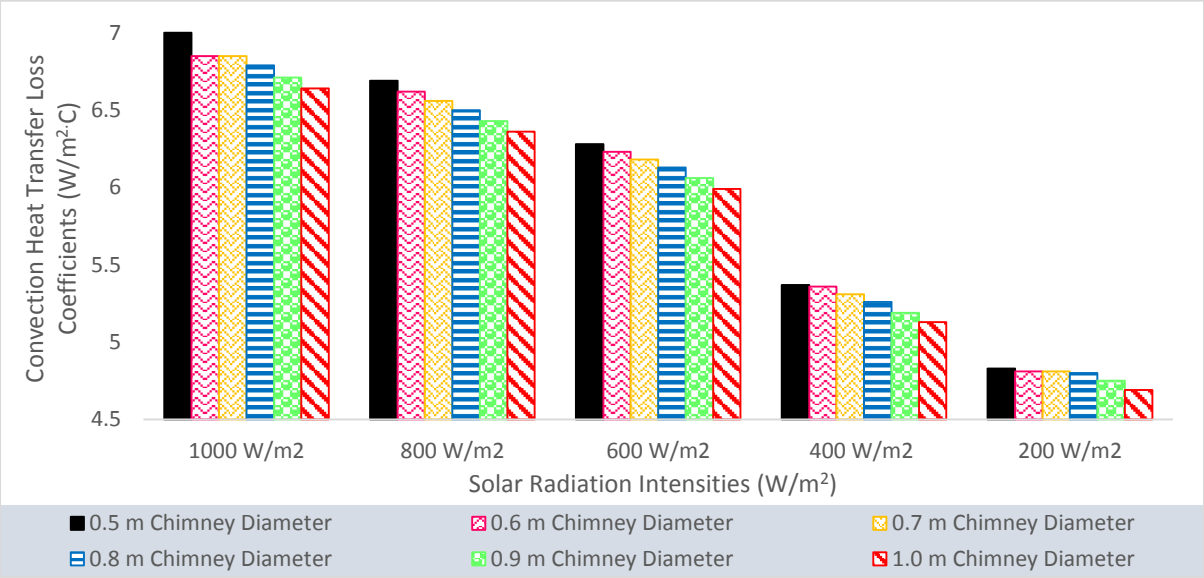

Figure 4.77: Convection Heat Transfer Loss Coefficients from the Transparent Cover of the Collector of Inclined SCPP to the Ambient at Different Chimney Diameters

4.10 Influence of the Change in the Vents' Area on the Performance of the Inclined SCPP

In this study, the area of the vents was manipulated to determine its effect on the plant's performance. The manipulated and fixed variables involved in the investigation of the vents' areas were detailed in Section 3.9.7.

4.10.1 Effect of Changing the Vents' Total Area on the Air Buoyancy

The effect of the total area and number of the air-vents were investigated considering the air velocity, air mass flow rate, and electrical power output. Detail results on the investigations are presented in the subsections below.

4.10.1.1 Velocity of Air at the Chimney Base for the Inclined SCPP with Different Vents' Area

The air-vents area was varied between 1 m^2 area and 4 m^2 area for the 100 m^2 collector absorber area. The results of the air velocity as evaluated from the simulation are presented in Figure 4.78. The results showed that when the air-vents area was varied from 1.0 m^2 to 2.0 m^2, there was a significant increase in the air velocity measured at the base of the chimney. A further increase in the vents' area from 2.0 m^2 to 3.0 m^2 did not cause much changes to the air velocity at the chimney base, particularly when the solar radiation intensity was between 200 W/m^2 to 800 W/m^2. Furthermore, Figure 4.78 revealed that the air velocity reduced when the vents' area was increased to 4.0 m^2. Increasing the air vents' area over a certain limit resulted in the reduction of air velocity because excess air was introduced from the vents with less heat energy to increase the fluid's energy to buoyancy. With excess air influx to the greenhouse through the vents, the absorbed thermal energy by the absorber was insufficient to ignite the internal energy of the whole air volume in the greenhouse thus leading to circulation and increase in resident time of the system air and lead to stagnation of the air flow at lower solar radiation intensity. Following the investigations on the total area of the vents, 2 m^2 was considered most effective for both low and high solar radiation intensities. Analysis of the number of vents was based on the 2 m^2 air-vents total inlet area.

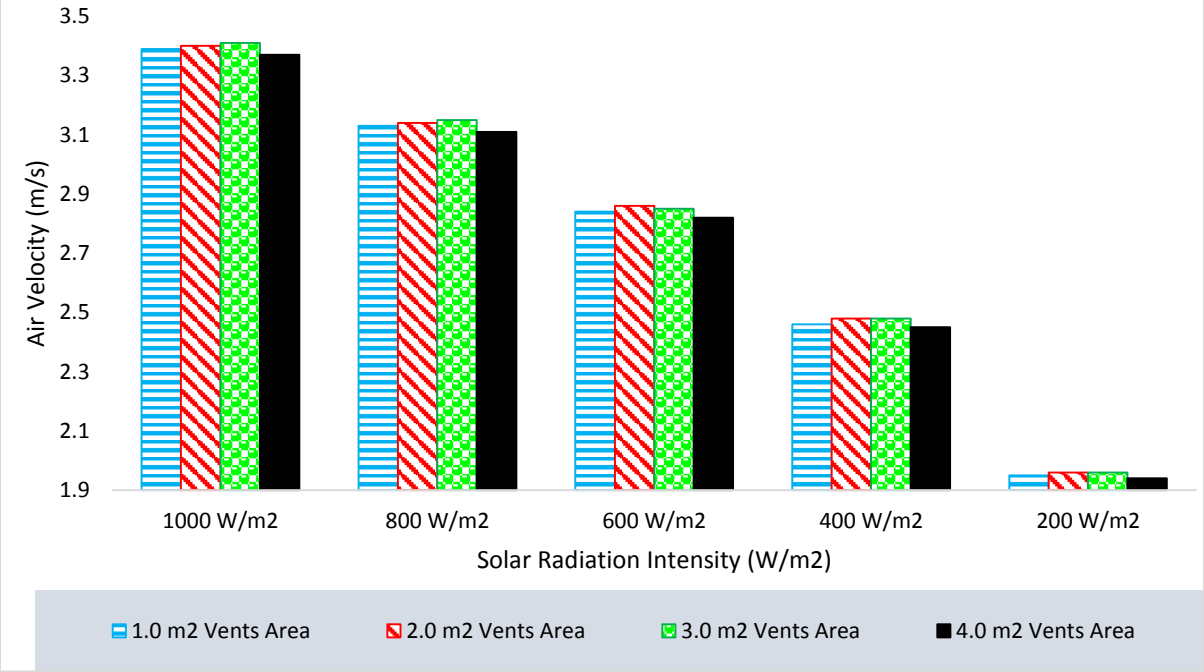

Figure 4.78: Air Velocity at the Chimney Base for the SCPP with Various Vents' Area

4.10.1.2 Mass Flow Rate of Air at the Chimney Base for the Inclined SCPP with Different Total Areas of Air-Vents

Considering the air velocity evaluated at the chimney base and reported in Figure 4.78, the air mass flow rates for the different total area of the air-vents were evaluated considering the various air temperature recorded at the chimney base. The mass flow rate are presented in Figure 4.79, which indicates clearly the increasing trend air mass flow rate with increase in the total vents area of 1.0 m^2 to 3.0 m^2 but drops at 4.0 m^2 total surface area of the air-vents. It can be seen that for lower solar radiation intensity, the 2.0 m^2 area showed better performance but slight decreased below the result of the 3.0 m^2 surface area from about 600 W/m^2. However, it was found that at solar radiation intensity of 400 W/m^2, both 2.0 m^2 and 3.0 m^2 vents areas predicted similar air mass flow rate at the base of the chimney. Considering all solar radiation intensities from 200 W/m^2 to 1000 W/m^2, Figure 4.79 showed that the inclined SCPP with 4.0 m^2 vents' area resulted in the system's performance degradation. The area of the air-vent to the collector was decided for 2.0 m^2 as the percentage increase in mass flow rate of 3.0 m^2 was only 0.165% above the mass flow rate of the 2.0m^2 area output. It is important to note that 1.0 m^2 area is 1% of the total collector area but in the 3.0 m^2 vent area which is 1.0 m^2 higher than the 2.0 m^2 vent area could only improve the mass flow rate by 0.165%. Utilizing this 1.0 m2 area for thermal storage will generate higher energy during low solar radiation time and night period and enhance operation thus 2.0m^2 was employed for other investigations.

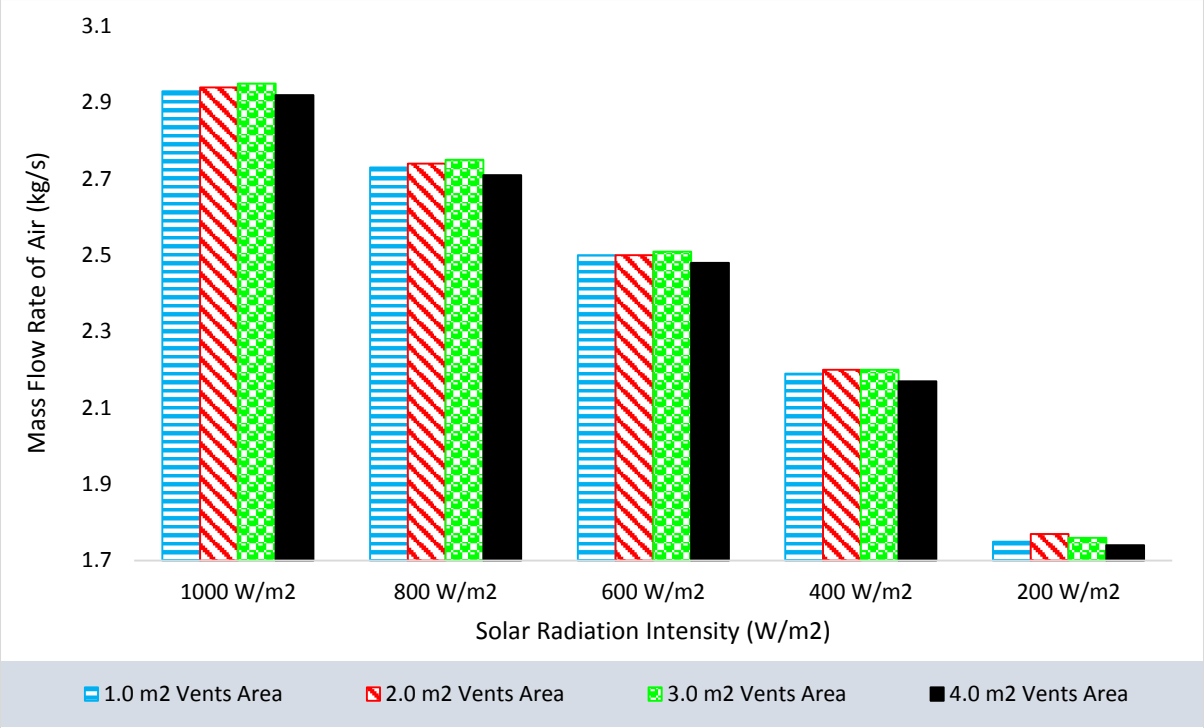

Figure 4.79: Mass Flow Rate of Air at the Chimney Base for the Inclined SCPP with Various Air Ventilations Areas

4.10.1.3 Electrical Power Output of the Inclined SCPP with Different Vents' Area

The analysis of the effect of varied air-vents area in the inclined SCPP on electrical power output are presented in Figure 4.80 at different solar radiation intensity. At 1000 W/m^2, 800 W/m^2, and 600 W/m^2 solar radiation intensity, the inclined SCPP equipped with air vents of 3.0 m^2 area estimated the highest electrical power output rated at 12.01 W, 9.52 W and 7.11 W, respectively. Moreover, the system's electrical power output was determined to increase with the expansion of the vents' area from 1.0 m^2 to 3.0 m^2. However, at 400 W/m^2 and 200 W/m^2 solar radiation intensity, the inclined SCPP equipped with vents of 3.0 m^2 area predicted a slightly lower electrical power output in comparison to the system with vents of 2.0 m^2 area. In Figure 4.80, it was noticeable that the inclined SCPP with vents of 4.0 m^2 area produced the lowest electrical power output.

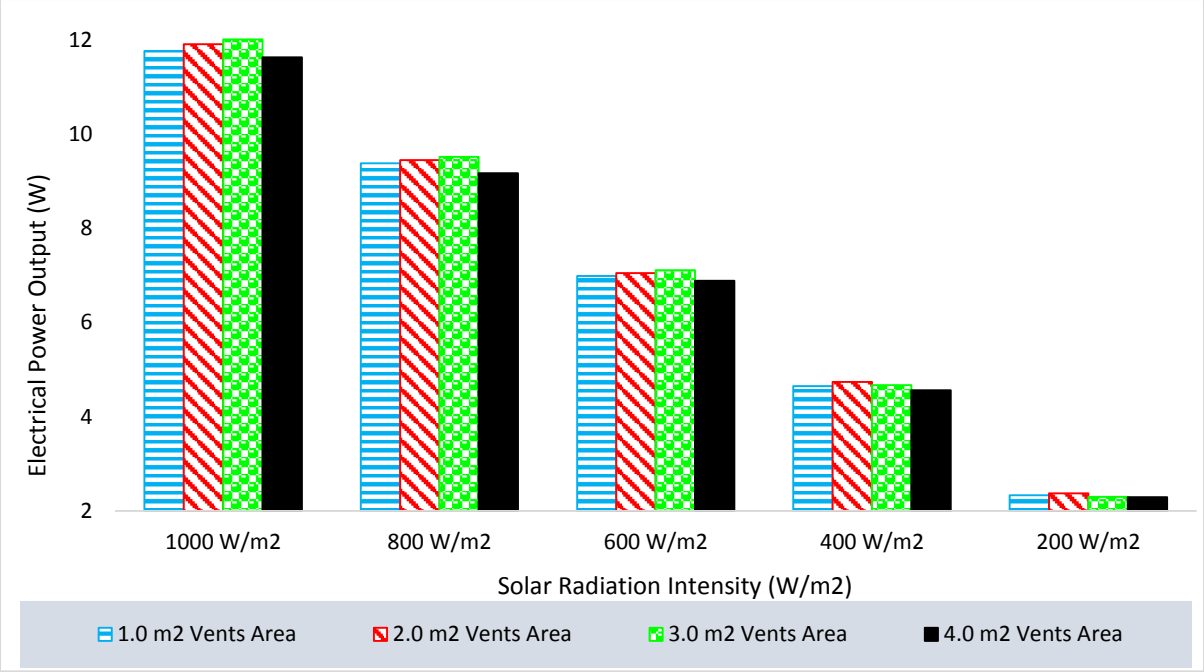

Figure 4.80: Electrical Power Output of the Inclined SCPP with Various Air Vents Area

4.10.2 Effect of Varying Number of Vents on the Air Buoyancy

Analysis on the effect of changing the total number of air vents in the inclined SCPP system was investigated in which the explanation on the manipulated and constant variables was provided in Section 3.9.8. The air-vents total surface area used for this investigation was 2.0 m^2 as justified in previous sections.

4.10.2.1 Air velocities at the Chimney Base for the Inclined SCPP with Different Number of Vents

With the consideration of the 2 m^2 air-vents total inlet area following the results presented in Figure 4.78, different numbers of vents were investigated to determine the optimum numbers of vents for the 100 m^2 collector area. The results of the varied numbers of air-vents are presented in Figure 4.81. It was observed that air velocity increase with increase in number of vents from 5 air-vents to 15 air-vents. This is because the higher number of vents provides opportunity for ambient air from different location behind the absorber to gain access into the greenhouse. On the other hand, lower number of air-vents led to increase in influx from each individual inlet but with low energy distribution to increase the buoyancy at the point of entrances. A higher number of vents led to a reduced inlet flow area at each vent, however, this configuration had the advantage to distribute the vents evenly across the absorber and also

offers the influx air the opportunity to gain energy faster from the surrounding absorber heat. Moreover, with successive increases from 15 to 20 vents, no significant difference in the air velocity between the two configurations was evident. For this research, there is requirement to install water storage tanks on the absorber surface which the surface area is an important factor. Thus further investigations were based on the 15 air-vents.

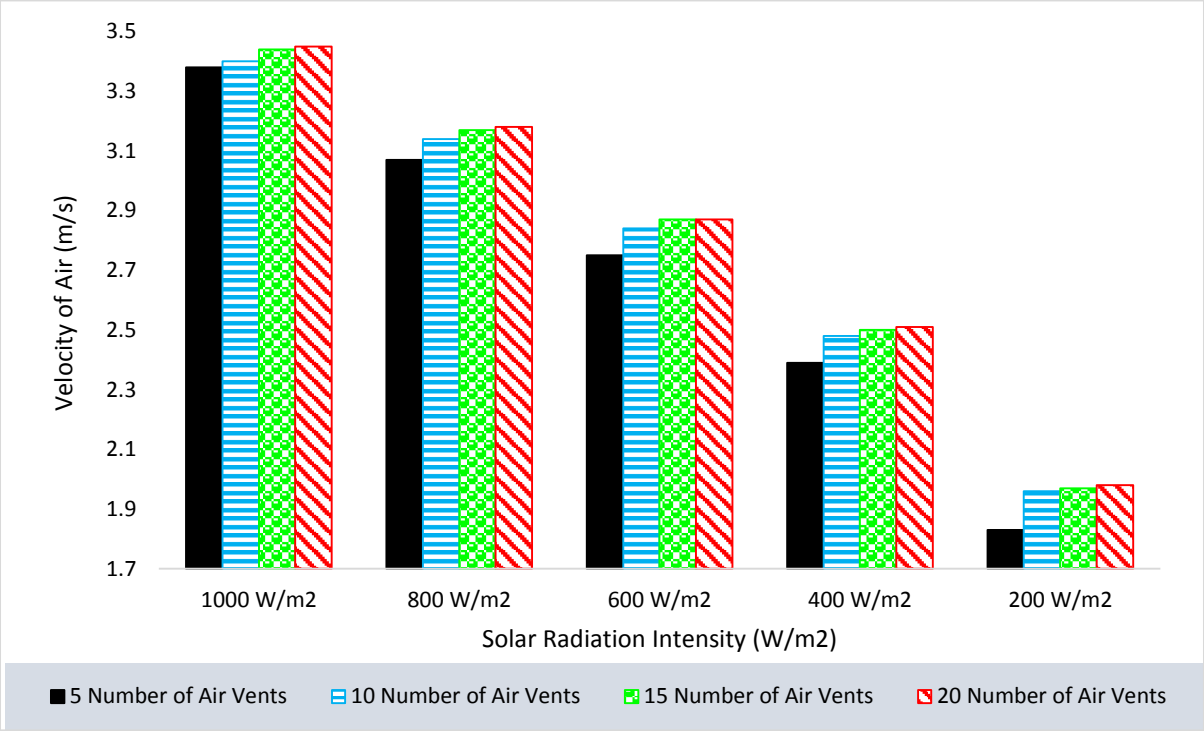

Figure 4.81: Air Velocity at the Chimney Base for the Inclined SCPP with Different Number *of Air Vents*

4.10.2.2 Air Mass Flow Rate at the Chimney Base for the Inclined SCPP with Different Number of Vents

From the data in Figure 4.82, there was a significant increase in the air mass flow rate when the total number of vents was increased from 5 to 15. These results proved that the installation of a higher number of air vents yielded better performance as the vents could be spread evenly across the surface area of the concrete absorber. With a lower number of air vents, the vents could only be concentrated in a specific region. On the other hand, with a higher number of air vents, the system acquired the flexibility to distribute the vents at various points and regions on the collector's absorber. As the mass flow rate of air increased at every point of installation of the vents, higher number of vents led to increased air mass flow rate.

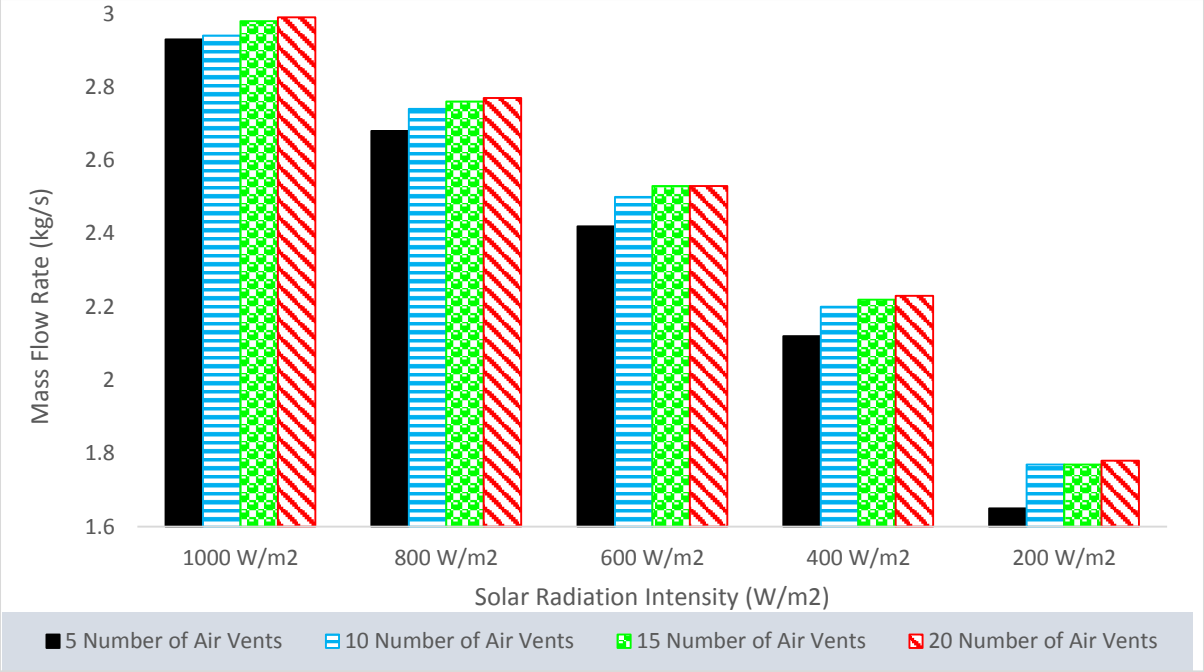

Figure 4.82: Mass Flow Rate of Air at the Chimney Base for the Inclined SCPP with Different Number of Air Vents

4.10.2.3 Electrical Power Output of the Inclined SCPP with Different Number of Vents

In Figure 4.83, the effect of changing the total number of air vents on the electrical power output of the inclined SCPP was determined. At all solar radiation intensities of 1000 W/m^2 to 200 W/m^2, the electrical power output of the system increased with higher number of air vents. At 1000 W/m^2, the inclined SCPP with 5 number of air vents produced the lowest electrical power output rated at 11.72 W, whereas the system with 20 number of air vents produced the highest electrical power output of 12.44 W. There was about 6.14 % improvement on the power output considering 5 air-vents in comparison with 20 air-vents of equal total surface area at 1000 W/m^2. Furthermore, it was also observed that there was only a minor cumulative improvement of 0.88% to the electrical power output when the total number of vents was increased from 15 to 20 vents across all the solar radiation intensity.

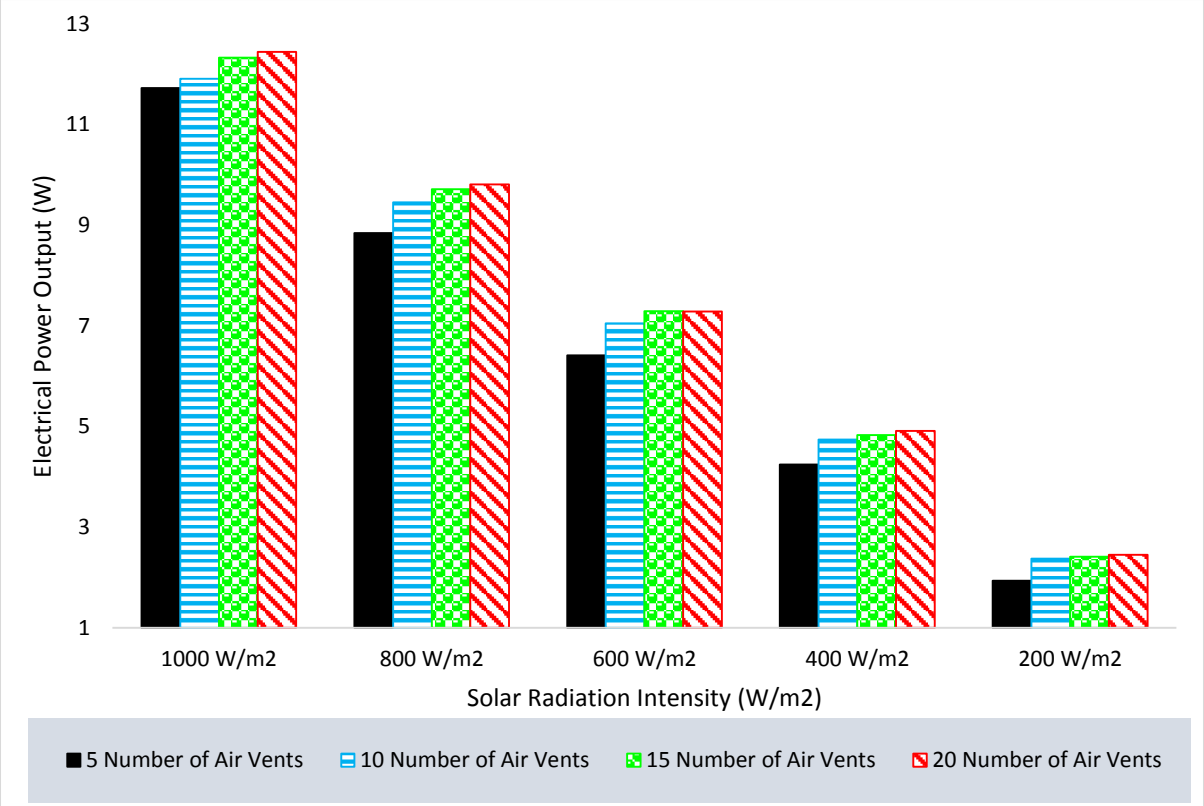

Figure 4.83: Electrical Power Output of the Inclined SCPP with Different Number of Vents

4.10.3 Effect of Varied Vents' Total Area on the Temperatures of the Collector Components and the Associated Thermal Losses

The temperatures of the collector components and the thermal losses were evaluated in relation to the total surface area of the air-vents. Similarly, the collector efficiencies were evaluated for the different air-vents area. Detail of the findings are presented in the subsections below.

4.10.3.1 Collector Components' Temperatures for the Inclined SCPP with Different Vents' Areas

Figure 4.84 presented the absorber's average temperatures obtained from the simulation of the inclined SCPP equipped with air vents of different areas. The results showed that as the area of the vents was expanded from 1.0 m^2 to 4.0 m^2, the absorber's average temperatures were found to decrease. With respect to a smaller vent's area of 1.0 m^2, the high absorber's temperature indicated higher re-radiation heat transfer occurring from the absorber to the transparent cover. Considering the vents' areas of 2.0 m^2 and 3.0 m^2, the absorber's average temperatures were gradually reduced as a result of the higher volume of air entering the collector through the larger air vents. The influx of the higher volume of lower temperature air

into the collector was able to remove a substantial amount of heat from the absorber. It was also evident from Figure 4.84 that there was a significant drop in the absorber's average temperatures when the area of the vents was increased to 4.0 m^2. Based on the previous Section 4.10.1 which reported that the use of 4.0 m^2 vents' area resulted in an excess volume of air entering the collector, the result of the absorber temperature presented below showed that the absorber temperature was least and possess less heat energy to increase the fluid's energy to buoyancy, thereby leading to circulation.

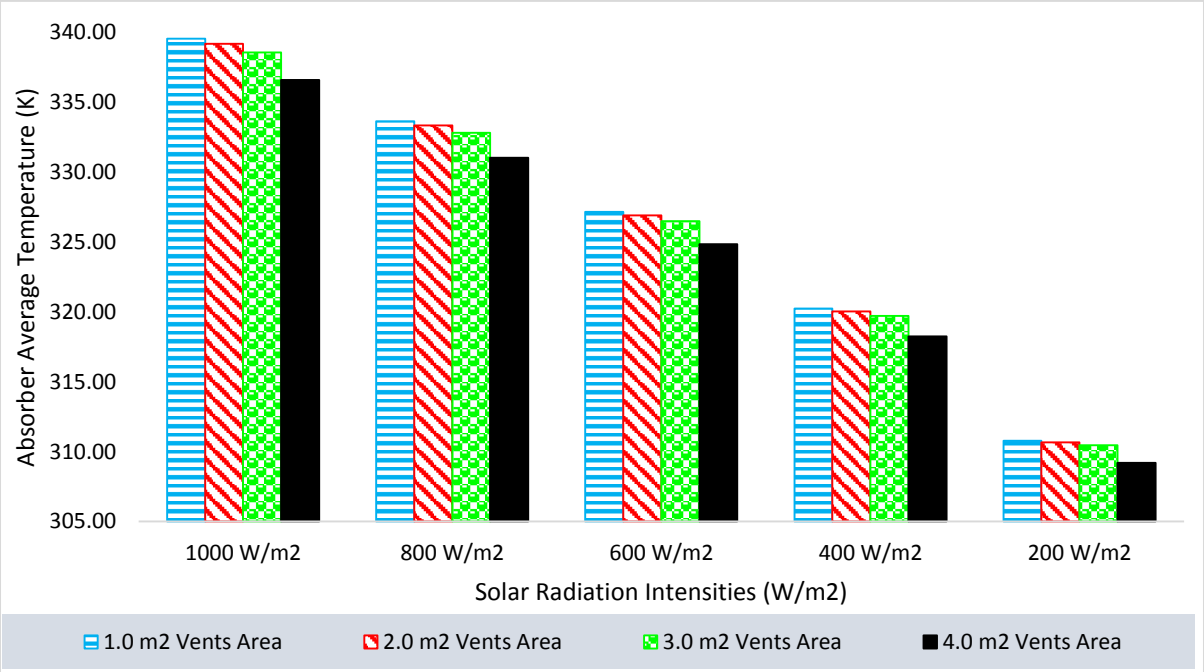

Figure 4.84: Absorber's Temperatures for the Inclined SCPP with Different Vents Areas

In Figure 4.85, the transparent cover's average temperatures were also found to decrease when the area of the vents was expanded from 1.0 m^2 to 4.0 m^2. For the case involving a small vents' area of 1.0 m^2, the higher re-radiation heat transfer occurring from the absorber to the transparent cover caused the transparent cover's temperature to increase. On the other hand, the inclined SCPP equipped with underneath air vents of 2.0 m^2, 3.0 m^2 and 4.0 m^2 area observed a reduction of the transparent cover's average temperatures. The variation in the cover temperature indicates different ranges of thermal loss to the ambient from the cover. Detail on the thermal loss is presented in Section 4.10.3.2.

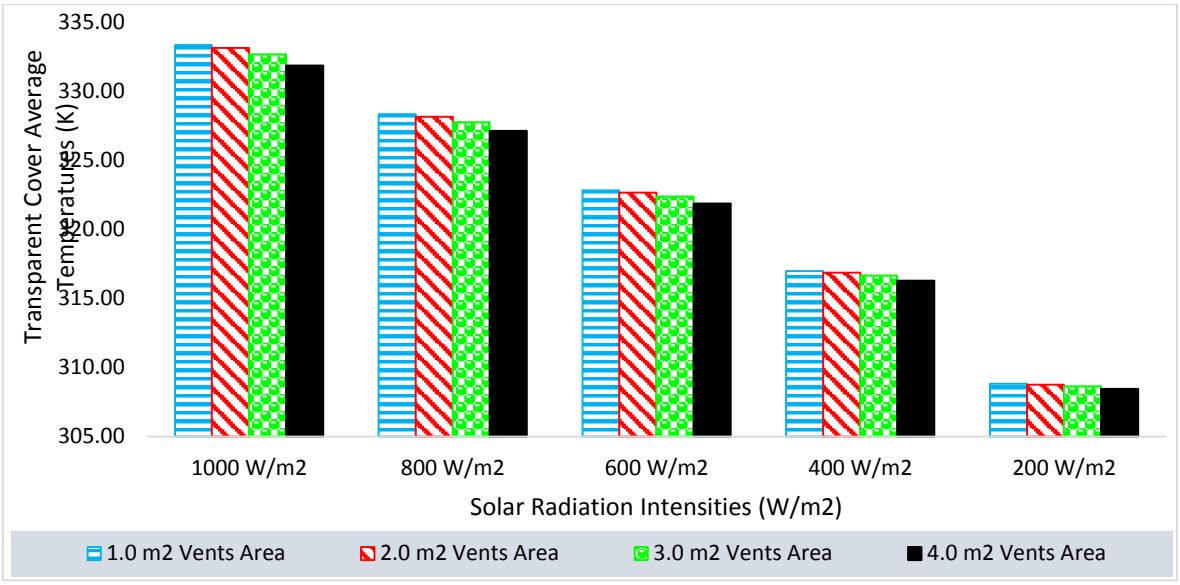

Figure 4.85: Transparent Cover Average Temperatures for the Inclined SCPP with Different Vents' Areas

4.10.3.2 Thermal Losses Analysis for the Inclined SCPP with Different Vents' Areas

The heat transfer coefficients by convection and radiation from the cover to the ambient were evaluated and reported in Figure 4.86 and Figure 4.87 respectively. The reduced temperature of the cover with increase total surface area of the air-vents was observed to reduce the heat transfer coefficient of the cover to the ambient as shown in Figure 4.86.

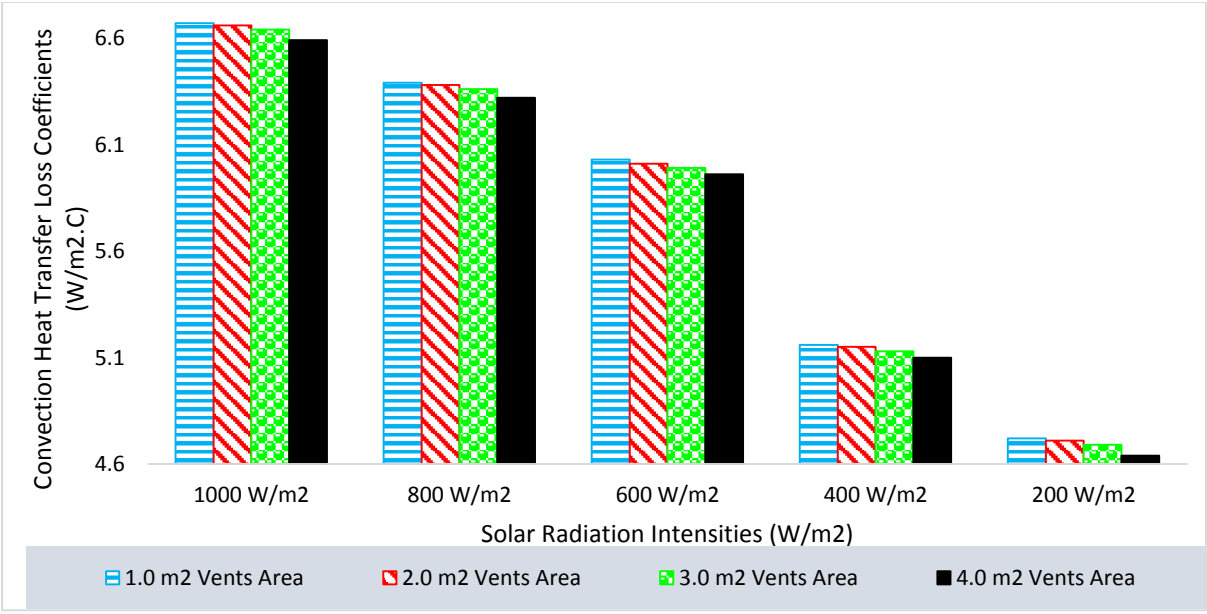

Figure 4.86: Convection Heat Transfer Loss Coefficients from the Transparent Cover to the Ambient for the Inclined SCPP with Different Vents' Areas

The radiation heat transfer coefficients for the different air-vents areas are analyzed and reported in Figure 4.87 and it showed that the radiation heat transfer loss coefficients from the transparent cover to the ambient reduced when the area of the air vents was increased from 1.0 m^2 to 4.0 m^2. With the expansion of the vents' area, the system generated a higher volume of air into the collector which removed the heat from the absorber and the transparent cover. Consequently, the effective removal of heat from the transparent cover resulted in a lower transparent cover's average temperature and lower thermal losses to the ambient.

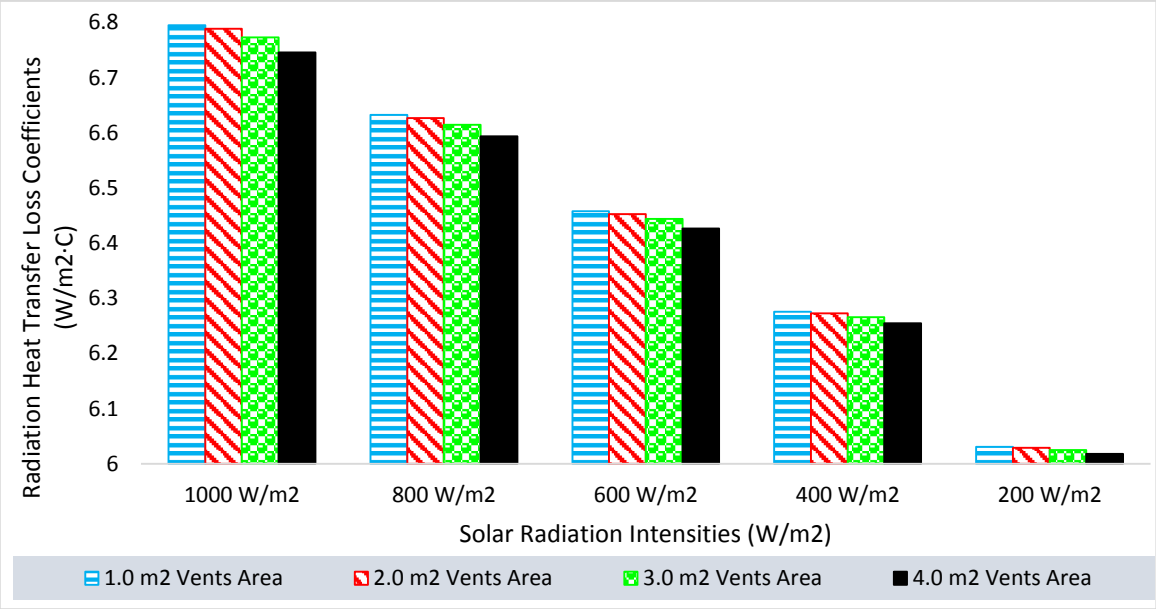

Figure 4.87: Radiation Heat Transfer Loss Coefficients from the Transparent Cover to the Ambient for the Inclined SCPP with Different Vents' Areas

4.10.3.3 Collector Efficiencies of the Inclined SCPP with Different Vents' Areas

As can be seen from the plot in Figure 4.88, the efficiency of the collector was increased when the air vents' area was expanded from 1.0 m^2 to 3.0 m^2, with respect to the solar radiation intensities between 600 W/m^2 and 1000 W/m^2. However, as the solar radiation intensities were reduced to the range in between 200 W/m^2 and 400 W/m^2, the inclined SCPP with vents of 3.0 m^2 area observed lower collector efficiencies in comparison to the system with vents of 2.0 m^2 area. For instance, the system equipped with air vents of 2.0 m^2 area was able to produce relatively high collector efficiencies at all solar radiation intensities. The results also indicated that the use of the air vents with 2.0 m^2 total area led to remarkable improvement to the collector efficiencies when the solar irradiance was low. Moreover, Figure 4.88 revealed that the collector efficiency observed a drastic drop when the area of the air vents was further expanded

to 4.0 m^2. This finding suggested that the additional flow of air into the collector through the vents of 4.0 m^2 area was in excess. As a result, the heat energy generated by the absorber became insufficient to excite the air particles which caused the system to experience air circulation and reduced buoyancy.

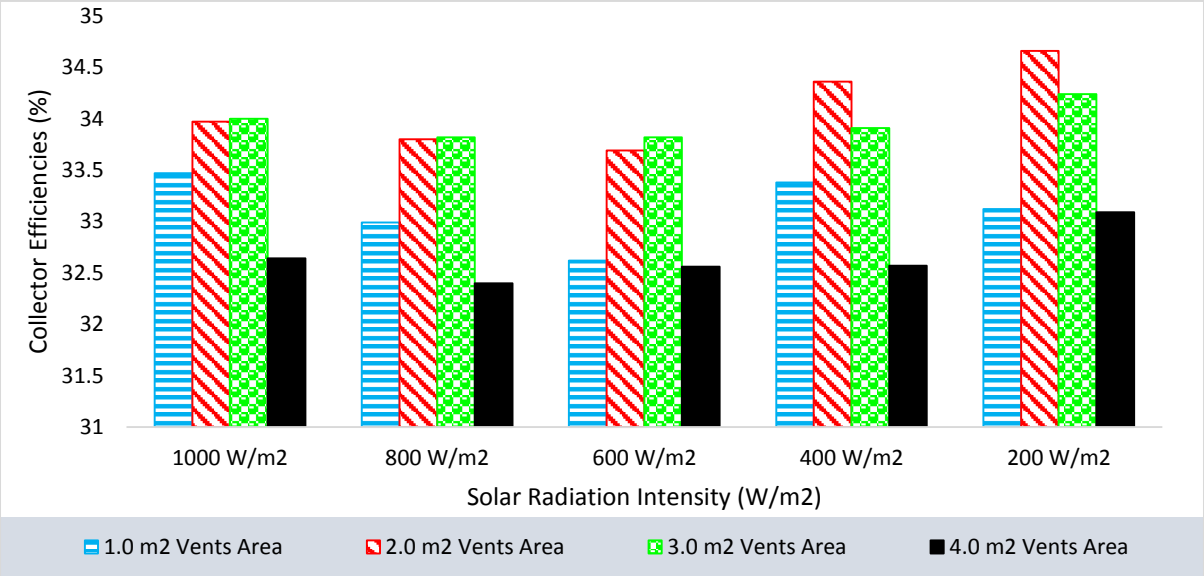

Figure 4.88: Collector Efficiencies of the Inclined SCPP with Different Vents' Areas

4.10.4 Effect of Varying the Number of Vents on the Collector Components' Temperatures and Thermal Losses

The temperatures of the collector components and the thermal losses were evaluated in relation to the different numbers of air-vents using the 2.0 m^2 air-vents inlet surface area as the base vent-area. Similarly, the collector efficiency were evaluated for the different model with varied number of air-vents. Detail of the findings are presented in the subsections below.

4.10.4.1 Collector Components' Temperatures for the Inclined SCPP with Varied Number of Air-Vents

In the investigation of the effect of varying the total number of air vents, Figure 4.89 showed that the absorber's average temperatures were reduced when the collector was installed with a more number of vents considering 5 to 20 air-vents. The inclined collector with a higher number of air-vents generated higher air mass flow rate into the system through the vents. As a consequence, the heat removal from the absorber was increased. This reduced the temperature

of the absorber as well as reduced the re-radiation heat transfer occurring from the absorber to the transparent cover.

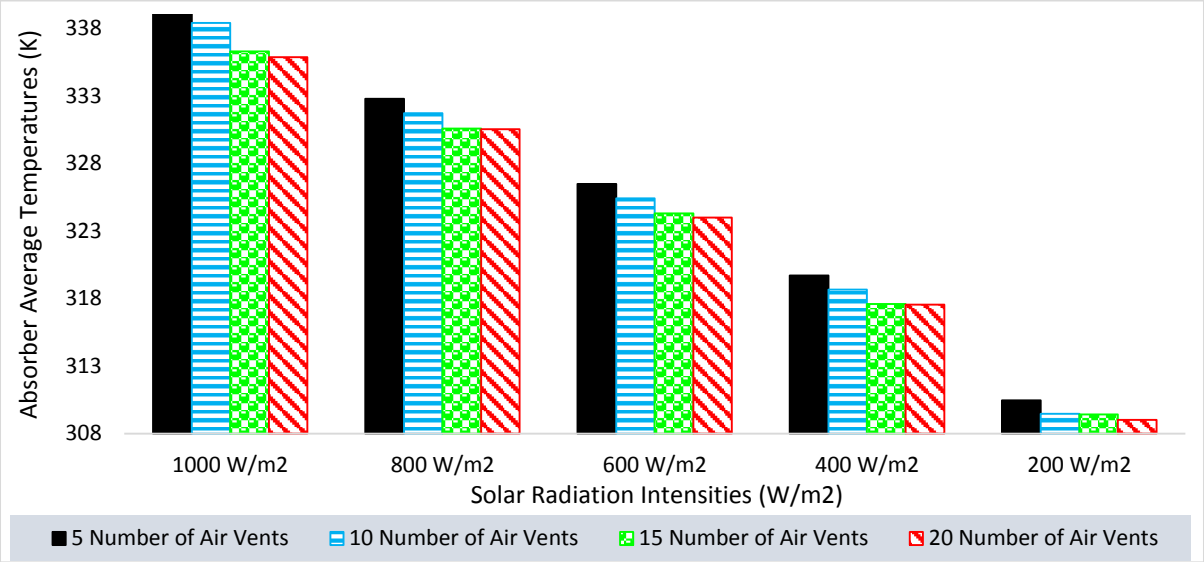

Figure 4.89: Absorber Temperatures for the Inclined SCPP with Different Number of Vents

In line with the reduced temperature of the absorber, it was also observed from the analysis of the transparent cover temperature that the number of air-vents has influence on the temperature of the transparent cover as shown in Figure 4.90. The transparent cover's average temperatures were found to decrease with the installation of higher number of air vents ranging from 5 to 20 vents. This result suggested that there was a lower thermal loss associated to the collector when the system is designed with higher number of air vents. In the case where the inclined collector was installed with few number of vents, the area of each vent was larger (considering that the total area of the vents was fixed at 2.0 m^2 in this study). Therefore, the vents transferred the ambient fluid into the collector in a bulk which took a longer time for the incoming fluid from the vent to diffuse evenly across the greenhouse/air flow channel, thus longer period is required to lower the temperature of the transparent cover.

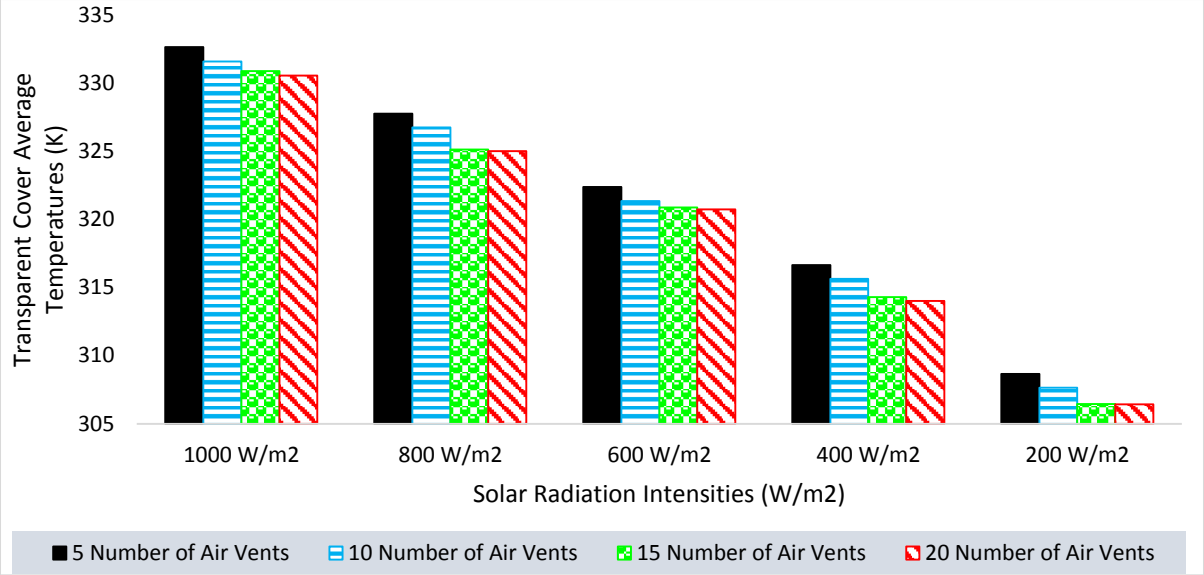

Figure 4.90: Cover Temperatures for the Inclined SCPP with Different Number of Vents

4.10.4.2 Thermal Losses Analysis for the Inclined SCPP with Varied Number of Air Vents

With respect to the inclined SCPP with different number of air vents, the convective heat transfer loss coefficients are presented in Figure 4.91 at various solar radiation intensities. The results indicated that the convective thermal losses from the cover to the ambient reduced with higher numbers of air-vents at the collector's absorber. Under no wind condition, the convection heat transfer from a surface is mainly induced naturally and as such the lower the temperature of the cover the lover the heat transfer loss coefficient as seen in Figure 4.91.

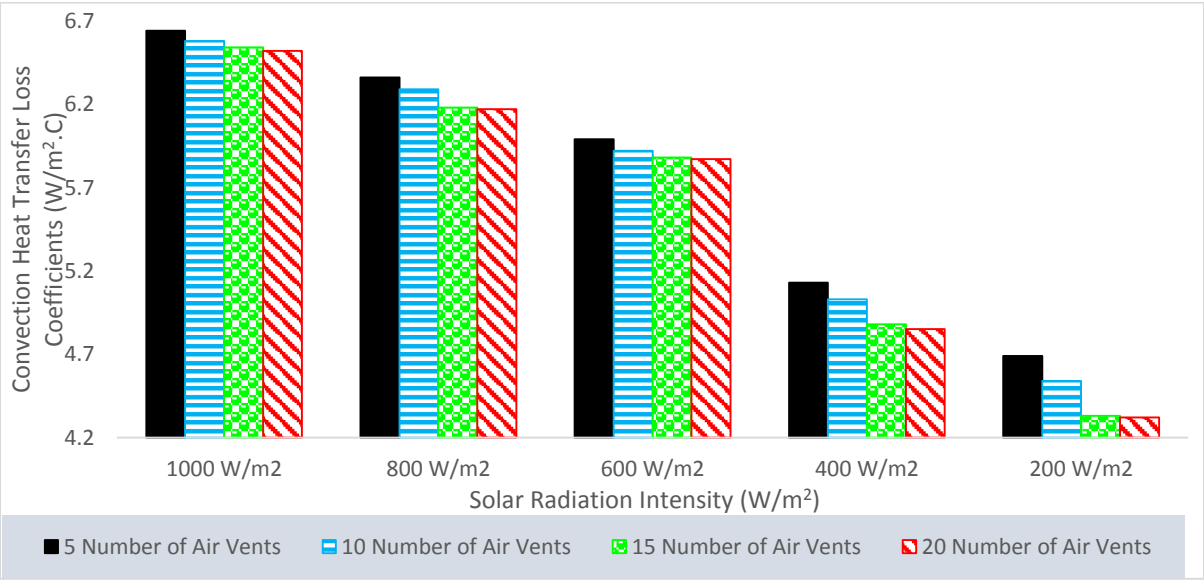

Figure 4.91: Convection Heat Transfer Loss Coefficient from the Cover to the Ambient for Different Number of Vents

The analysis of the thermal loss from the cover to the sky by radiation focusing on the radiation heat transfer loss coefficient revealed reduction in radiation heat transfer loss coefficients for the model with installed higher number of air-vents as compared to the model with less number of air-vents as can be seen from Figure 4.92. This is due to the reduced temperature of the transparent cover as discussed in previous sections which resulted the lower thermal loss from the cover to the ambient by convection and radiation. Thus, the useful energy gained by the collector's air was increased proving that inclined SCPP equipped with a higher number of air vents could improve energy output as well as minimized the collector's thermal losses.

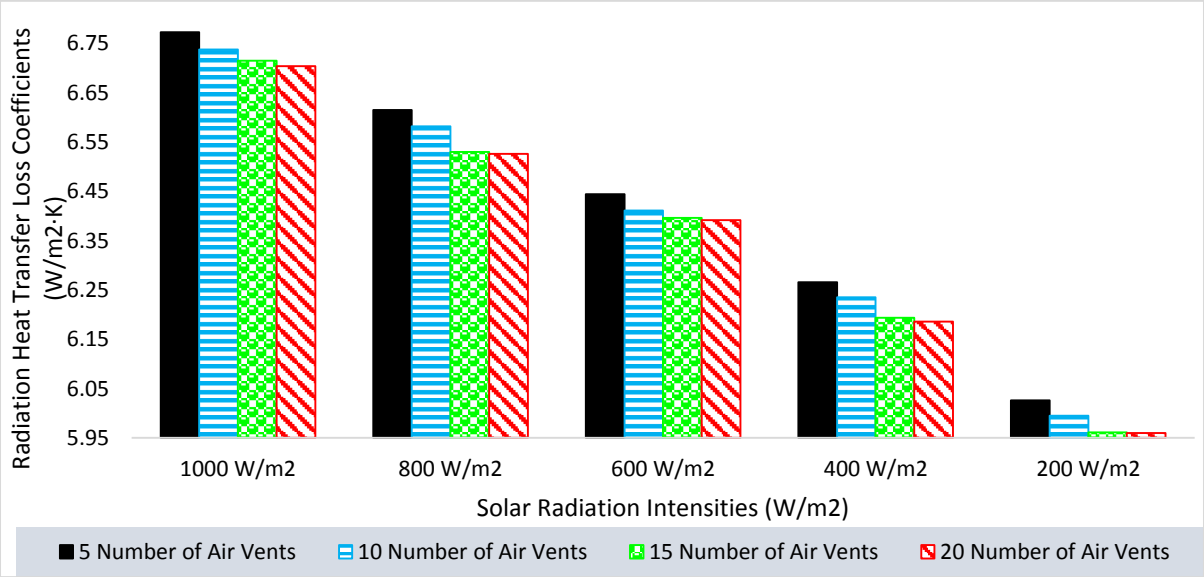

Figure 4.92: Radiation Heat Transfer Loss Coefficients from the Transparent Cover to the Ambient for the Inclined SCPP with Different Number of Air Vents

4.10.4.3 Collector Efficiencies of the Inclined SCPP with Varying Number of Air Vents

The analysis of the efficiencies of the models with different numbers of air-vents are presented in Figure 4.93 and can be observed that the efficiencies of the collector increased with the higher number of air vents ranging from 5 to 15 vents. This result was evident considering all solar radiation intensities from 200 W/m^2 to 1000 W/m^2. The limitation of using a lower number of underneath air vents in the collector was due to design restriction where the position of the vents had to be constrained in a certain location. On the other hand, the use of a higher number of vents allowed for more design flexibility in which the vents were evenly distributed across the absorber. Based on the results of Figure 4.93, it was also determined that there was only a slight increase to the collector efficiencies when the number of vents was increased from 15 to 20 vents.

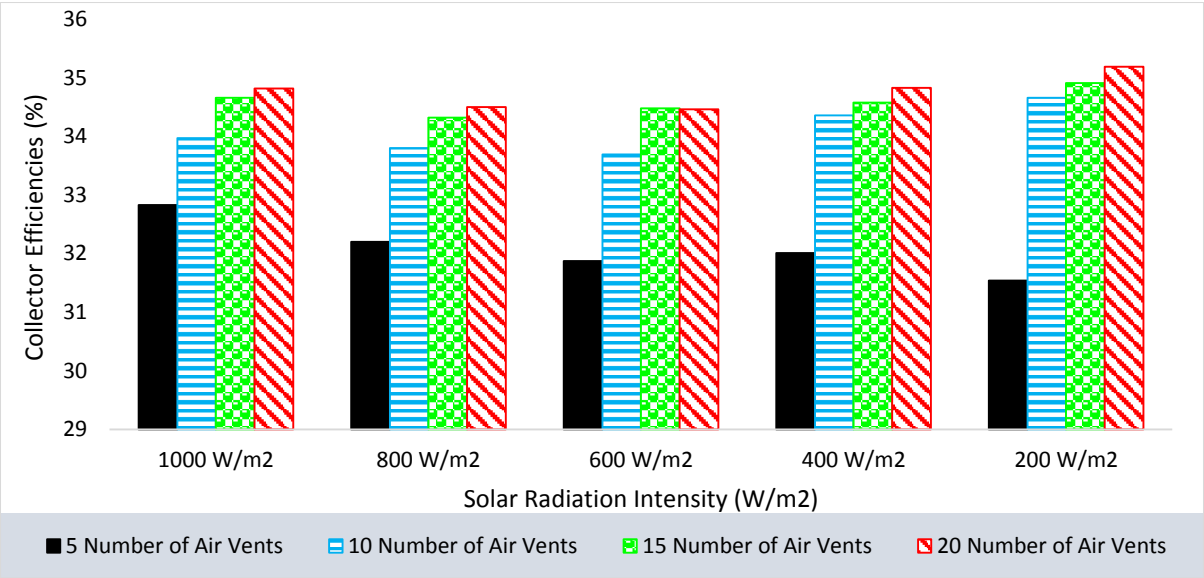

Figure 4.93: Collector Efficiencies for the Inclined SCPP with Different Number of Vents

4.11 Inclined SCPP Model Comparison Based on Performance Enhancement

Following the analysis in previous sections, Figure 4.94 showed the analysis for the electrical power output of three inclined SCPP models for comparison based on performances output. The three models selected are as follows:

i. The inclined SCPP having 100 m^2 collector area (12 m by 6 m rectangular surface and a trapezoidal extension of 8 m length with bases of 6.0 m connected to the rectangular area and 1.0 m at the chimney) of collector inlet height 0.1 m and collector exit/chimney connection height 1.1 m where the absorber was integrated with 15 underneath air-vents. The chimney component has a diameter of 1.0 m and height of 26.85 m cylindrical in shape while the turbine was considered with 70% efficiency.
ii. Inclined SCPP as described in i. above but without air-vents integrated.
iii. The inclined SCPP having 100 m^2 collector area (12.5 m by 6 m rectangular surface and a trapezoidal extension of 7.7 m length with bases of 6.0 m connected to the rectangular area and 0.5 m at the chimney) of collector inlet height 0.1 m and collector exit/chimney connection height 1.1 m with no underneath air-vents integrated to the absorber. The chimney component has a diameter of 0.5 m and height of 26.85 m of cylindrical shape while the turbine was considered with 70% efficiency.

The results of the electrical power output show remarkable improvement when the model was integrated with underneath air-vents in comparison to the inclined SCPP without air-vents. The electrical power output of the system with underneath air-vent (i. above) showed

about 60% increase in electrical power as compared to the model without vents (ii. above) which has similar geometrical dimensions.

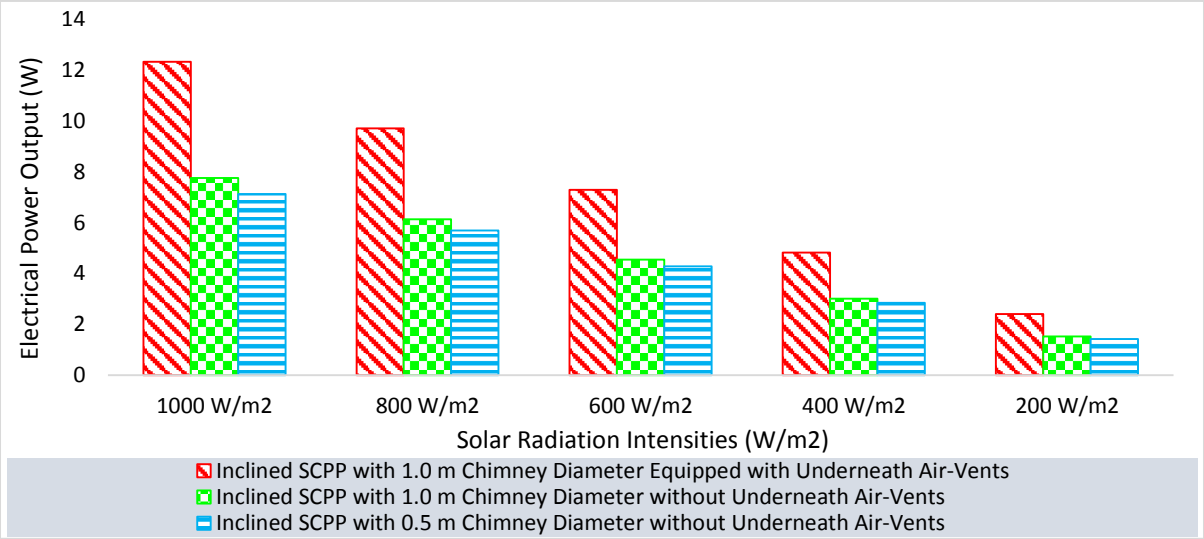

Figure 4.94: Electrical Power Output Comparison for the Inclined SCPP Models

Furthermore, the total plant efficiencies for the different inclined SCPP models were evaluated using Equation 3.49 and the results presented in Figure 4.95. The results showed that the inclined SCPP equipped with underneath air-vents led to highest system efficiencies. The average plant efficiency for the system equipped with underneath air-vents was 0.0121% for the hours of sunshine while model ii. and iii. described above were at an average of 0.0076% and 0.0071% total performance efficiency respectively. The percentage improvement with respect to these total plant efficiencies are presented in Figure 4.96, in which the inclined SCPP (0.5 m diameter chimney) without underneath air-vents was selected as the reference base case.

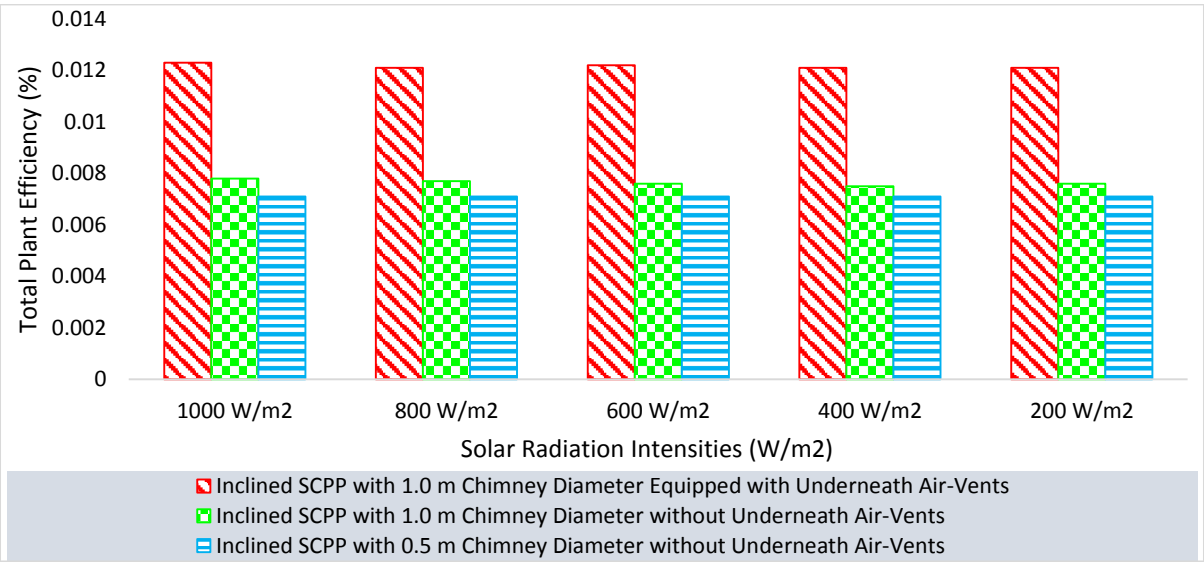

Figure 4.95: Total Plant Efficiency for the Inclined SCPP Models

The comparison of the results show that there was approximately 9.86 % performance improvement when the chimney diameter was enlarged from 0.5 m to 1.0 m, considering 1000 W/m^2 solar radiation intensity. With the inclusion of underneath air-vents in the inclined SCPP of 1.0 m diameter chimney, the system showed 73.2 % performance enhancement in comparison to the inclined SCPP of 0.5 m diameter chimney without air-vents.

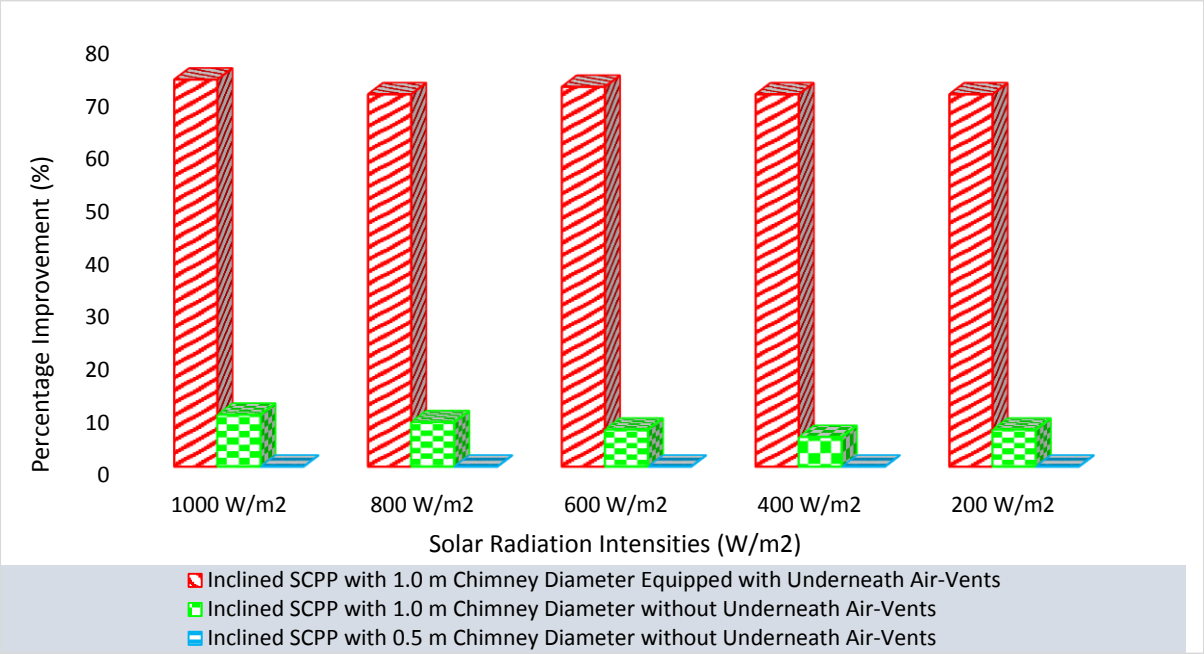

Figure 4.96: Percentage Improvement with respect to the Total Plant Efficiency for the Inclined SCPP Models

4.12 Water Thermal Storage Analysis of the Inclined SCPP

In previous sections, this study has focused on determining the performance of the inclined SCPP focusing on solar radiation intensity without consideration of the effect of stored energy in the absorber. In this section, the study investigated the system with water filled tight storage facility. The model selected for this investigation is the Inclined SCPP with 0.3 m absorber thickness, 20 m length and 6 m width having collector air-inlet height of 0.1 m and collector air-exit height of 1.1m (representing 60 m^3 air volume). At the collector exit, the system has extended cylindrical chimney of 26.85 m height of 1.0 m diameter. At the collector absorber, the system has 15 underneath air-vents inclined designed to incline at 50^o to the absorber surface to allow influx of ambient air into the system. The total surface area of the 15 air vents sums to 2.0 m^2. The manipulated and constant variables involved in this investigation of the above system integration with water storage facility are provided in Section 3.9.9. This study

was carried out to determine the effects of the installation of water storage on the inclined SCPP's operation during full day operation (hours of sunshine and night operations). Subsections to this section report the performance of the system with water filled tight storage facility on buoyancy, power output, thermal loses and extended operations.

4.12.1 Effect of Water Thermal Storage on the Air Buoyancy

The investigation looks at air velocity, air mass flow rate, power output when the system is integrated with water storage facilities. The analysis considers the plant operation from sunrise through the night operations.

4.12.1.1 Velocity of Air at the Chimney Base for the Inclined SCPP with and without Water Thermal Storage

In this section, the study used the solar calculator in the Star CCM+ considering a specific day (10/06/2017) to generate the solar radiation which is the input energy to the system. The Solar radiation data used for this study is presented in the secondary axis of the plot in Figure 4.97. The average air velocity at the chimney base of the inclined SCPP was generated from the simulation for the cases when the system was integrated with and without water thermal storage facility. For the system with thermal storage facility, the volume of the water storage was based on proportion of the total air volume space of the greenhouse. The results of the analysis are presented in Figure 4.97 considering the different solar radiation intensity from sunrise to sunset and the stored energy for extended operation in the night (hours of the day from 7 a.m. in the morning until 12 a.m. midnight). In Figure 4.97, it was determined that the inclined SCPP without water storage estimated a higher air velocity at the chimney base between 7 a.m. to 1 p.m. On the other hand, at the same duration of time from 7 a.m. to 1 p.m., the system with water storage predicted lower air velocity output. These results were consistent with the experimental investigation of the SCPP with water energy storage layer by Ahmed et al. (2017), whereby the air velocity in the day time was found to be lower water bags were installed in the collector in comparison to operation of same system in the absence of water bags. This was because the energy gained by the collector has some components stored as thermal energy was in the water storage medium, which reduced the heat transfer from the absorber to the working fluid particularly from morning to noon. As a result, the energy gained by the collector's air was lowered and the system with water storage observed lower air velocity.

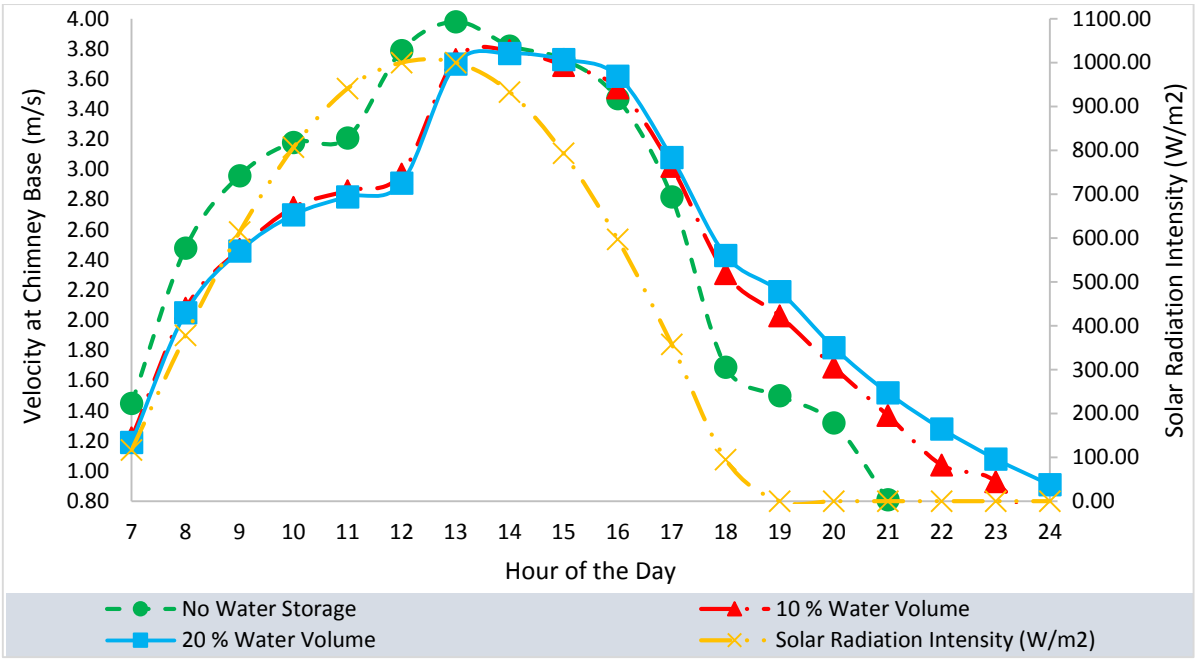

Figure 4.97: Velocity of air at the chimney base for the inclined SCPP with and without water thermal storage

Figure 4.97 showed that the inclined SCPP without water storage estimated lower air velocity in comparison to the system with water storage from 3 p.m. till midnight. In the afternoon, when the solar radiation intensity gradually reduces, the water storage medium starts releasing its heat energy to heat up the air in the greenhouse. As a consequence, the energy gained by the collector's air increased and the system with water storage observed higher air velocity. Between 6 p.m. and 8 p.m., when the solar radiation intensity was approaching 0 W/m^2, the inclined SCPP without water storage could still operate through the stored energy release but got exhausted by 9.00 pm. As for the inclined SCPP with water thermal storage, the system operated until midnight before the energy stored in the water became completely exhausted.

4.12.1.2 Mass Flow Rate of Air at the Chimney Base for the Inclined SCPP with and without Water Thermal Storage

In Figure 4.98, the air mass flow rates were plotted against the different hours of the day, with respect to the inclined SCPP with and without water storage. The investigation found that the use of the water storage led to a reduced air mass flow rate during the day, between 7 a.m. and 1 p.m. which is commensurate with the velocity generated. With the installation of the thermal energy storage, the heat was being stored in the water storage medium. As a consequence, less heat was supplied by the absorber which resulted in a small driving force of the system air and lower air mass flow rate at the base of the chimney.

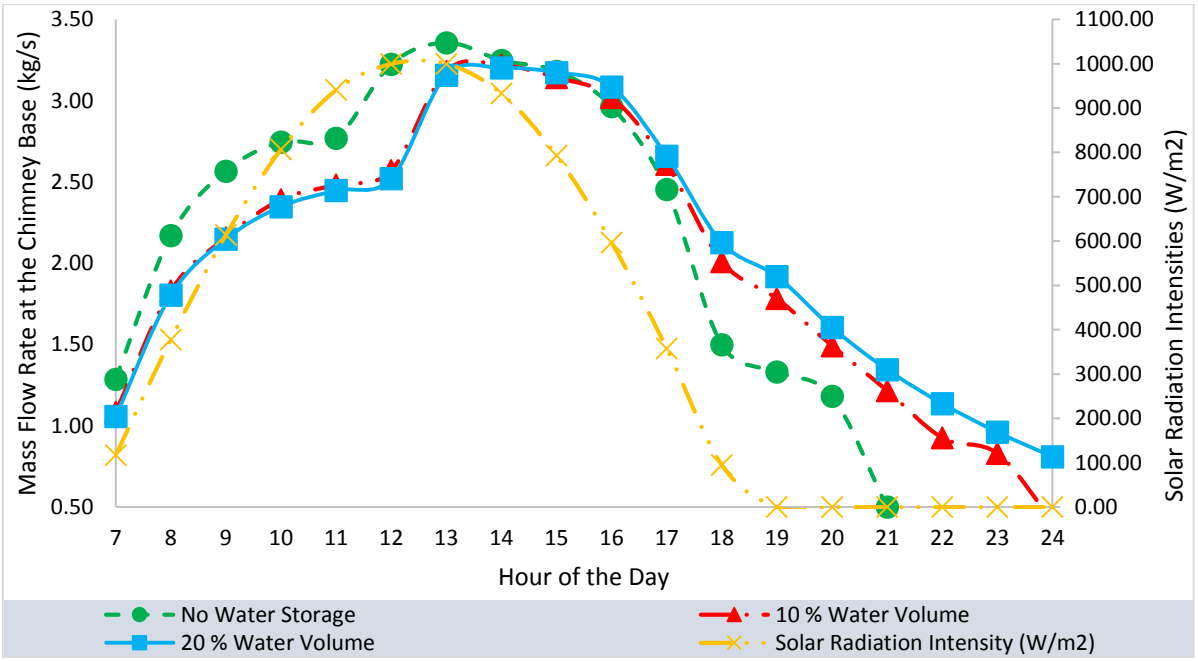

Figure 4.98: Mass flow rate of air at the chimney base for the inclined SCPP with and without water storage medium

However, the results obtained from the simulation of the inclined SCPP between 1 p.m. and 6 p.m. showed an opposite trend. The system equipped with water thermal storage was able to produce higher air mass flow rate at the exit of the collector. This result was attributed to the high water temperature under the influence of higher solar irradiation during the solar noon. At these hours, the hot water storage released its heat to the collector's air, which resulted in a higher air buoyancy and mass flow rate.

4.12.1.3 Electrical Power Output of the Inclined SCPP with and without Water Storage

Figure 4.99 showed that the electrical power output during the day correlated closely with the solar radiation intensity for the inclined SCPP without additional water storage. The results identified that the inclined SCPP without water storage was able to generate electricity after 6 p.m., whereby the solar radiation intensity was approaching 0 W/m^2. By 9 p.m. in the night, the energy stored in the concrete absorber was fully exhausted. These results proved that with an optimum concrete absorber thickness, the thermal loss to the ambient through the back of the absorber was minimized. The concrete was capable to store the excess heat during the day and released the heat into the collector at night. There was still an updraft during the night, in which the inclined SCPP without water storage could operate during some hours of the night at reduced electrical power output.

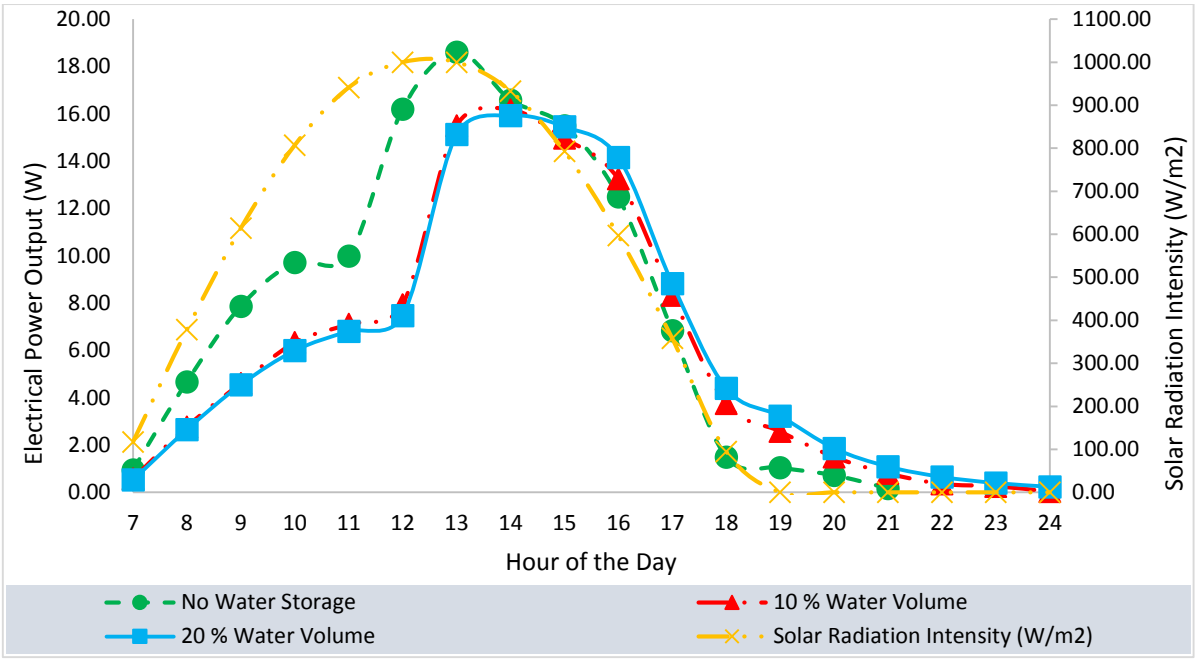

Figure 4.99: Electrical power output of the inclined SCPP with and without water storage

The system installed with water storage produced a higher electrical power output at night time without solar insolation. Furthermore, there was a longer duration of electrical power generation until 12 a.m. midnight with the presence of water storage medium. At night, when the air in the collector started to cool down, the water inside the storage casing released the heat that it stored during the day. The current investigation found that an increase in the volume of the water storage system led to an increased power generation during the night, however, electrical power output during the day was reduced. This result was observed because the additional water storage placed under the collector's transparent cover absorbed part of the radiated energy during the day and released it into the collector at night.

4.12.2 Effect of Water Thermal Storage on the Collector's Components Temperature

This section looks at the thermal fields and the associated losses from the collector through the components and also evaluate the collector efficiencies at various operating conditions from sunrise to the night operations.

4.12.2.1 Absorber Temperature for the Inclined SCPP with and without Water Storage

The average temperatures of the absorber were evaluated considering the case of the inclined SCPP without water storage, 10% greenhouse as storage and 20% of Greenhouse as storage. The results are presented in Figure 4.100 which on the secondary axis, the input solar radiation

used for the simulation is presented for clarity. The results showed that the concrete without thermal storage has the highest absorber temperature from sun rise in the specific day till about 3.00 pm in the afternoon. On the other hand, the average absorber temperature was reduced when water storage medium was integrated into the model as the water gained and stored most of the energy due to its higher specific heat capacity than concrete. The higher heat capacity of water caused the water to absorb and store more heat before it increased in temperature.

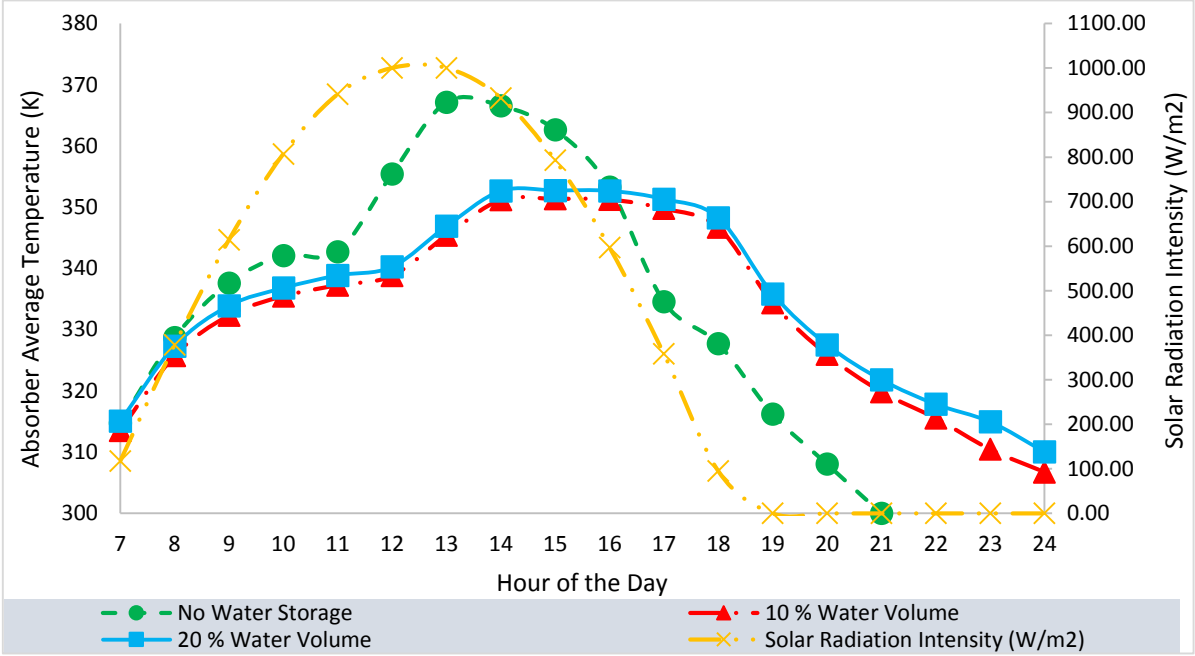

Figure 4.100: Absorber average temperature for the inclined SCPP with and without additional water storage system

By afternoon both the concrete absorber and the water storage medium was observed to have higher average surface temperatures than the hours before noon showing that the surfaces gained and stored some energy. These stored energy was gradually released towards sunset up to night period but the water storage medium released the heat energy at a slower rate in comparison to concrete considering the temperature gradient observed in the two scenarios. In this investigation, the energy stored in the concrete was exhausted by 9 p.m. whereas the energy stored in the water was fully consumed by 12 a.m. midnight.

4.12.2.2 Transparent Cover Temperature for the Inclined SCPP with and without Water Storage

The results of the transparent cover temperature for the different models showed as presented in Figure 4.101 that during the period between 7 a.m. and 1 p.m., the transparent cover

temperature was found to reduce with the installation of the water storage system. At these hours, heat was stored in the water energy storage because of its relatively higher specific heat capacity.

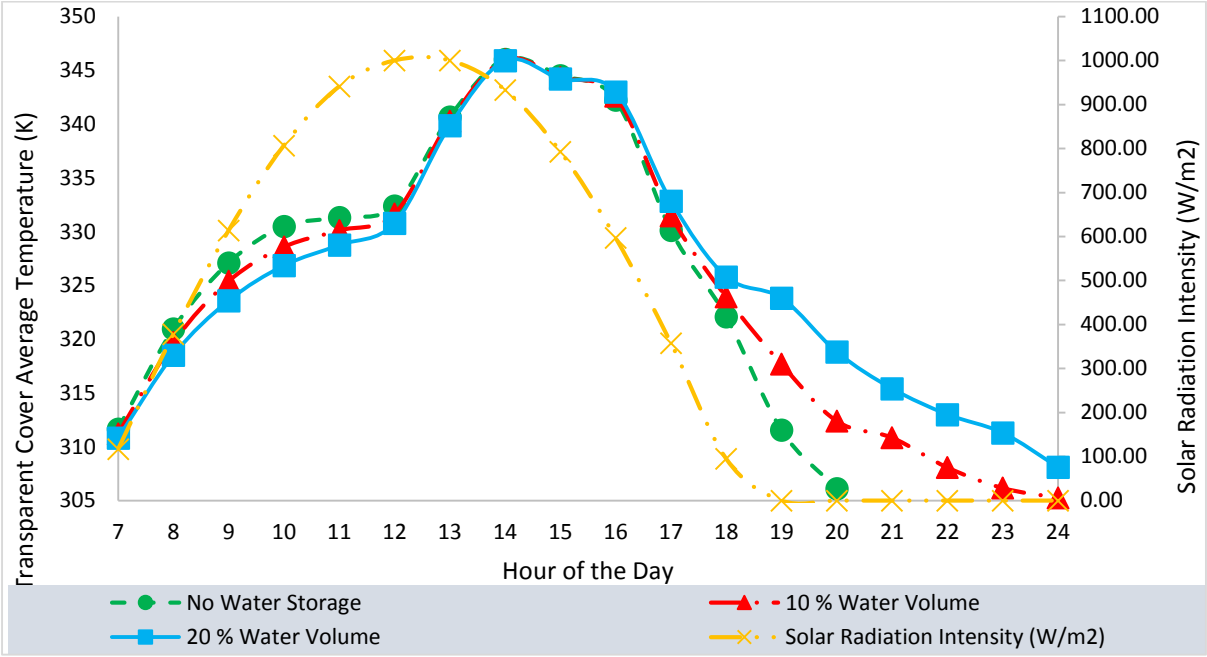

Figure 4.101: Transparent cover average temperature for the inclined SCPP with and without water energy storage layer

The thermal energy stored in the water reduced the re-radiation heat transfer from the absorber to the transparent cover, which led to a reduction in the temperature of the transparent cover. Between 1 p.m. and 4 p.m., the transparent cover temperatures for all three systems (no water storage, 10 % water volume, 20 % water volume) were approximately equal. At 5 p.m. onwards, the transparent cover temperatures for the inclined SCPP with water storage were higher than that of the system without water storage, due to the release of heat energy from the water during the night.

4.12.2.3 Collector's Air Temperature for the Inclined SCPP with and without Water Storage

With respect to the different hours of the day, the collector's air temperatures are presented in Figure 4.102 for the inclined SCPP with and without water storage tanks. The results indicate that the collector's air temperature for the system without water storage produced highest air temperature in the period between 7 a.m. and 1 p.m. With the presence of water storage tanks of 10 % and 20 % water volumes, the collector's air temperatures were observed to reduce

between 7 a.m. and 1 p.m. At these hours, the lower temperatures of the collector's air were attributed to the heat energy being stored inside the water medium. At 2 p.m. onwards, the inclined SCPP with 20 % water volume showed highest collector's air temperature due to the release of heat from the water storage tanks.

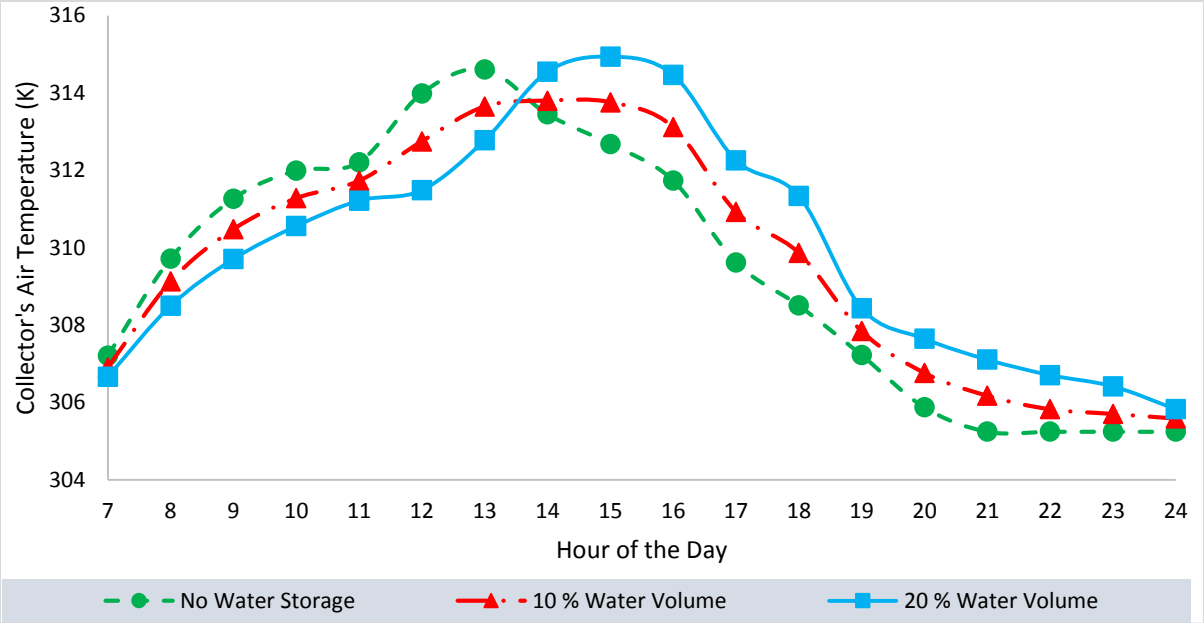

Figure 4.102: Collector's Air Temperature for the Inclined SCPP with and without Water Thermal Storage

4.12.2.4 Collector Efficiencies for the Inclined SCPP with and without Water Storage

Figure 4.103 presented the collector efficiencies for the inclined SCPP recorded at different hours of the day, with respect to the systems with and without water storage. From 7 a.m. until 10 a.m. in the morning, it was evident from the plot that the collector efficiencies for all three systems (no water storage, 10 % water volume, 20 % water volume) were found to reduce. As the solar radiation intensity showed a drastic increase from 117 W/m^2 to 807 W/m^2 between 7 a.m. and 10 a.m., the concentration of heat in the collector prompted higher thermal losses from the collector cover to the ambient leading to reduction in the collector efficiencies. However, as the solar radiation intensity increased from 807 W/m^2 to 1000 W/m^2 in the period between 10 a.m. and 1 p.m., the collector efficiencies for all three systems were observed to increase. During the day, the solar radiation intensities between these hours were the highest and the collector's air gained relatively higher useful energy, although the thermal losses still occurred. From 3 p.m. to sunset, when the solar radiation intensities approached 0 W/m^2, the inclined SCPP with water storage resulted in higher collector efficiencies, as compared to the system

without storage. When the system-air starts to cool down, the water released its heat energy to continuously produce an updraft in the system. It is worth to note that the collector efficiencies for all three systems with and without water thermal storage produced considerably high collector efficiencies at lower solar radiation intensities. This result is attributed to the fact that the collector efficiency is improved as irradiation or the rise in temperature decreases (Schlaich 1995). The greenhouse collector experiences a minimized thermal loss at lower solar irradiation.

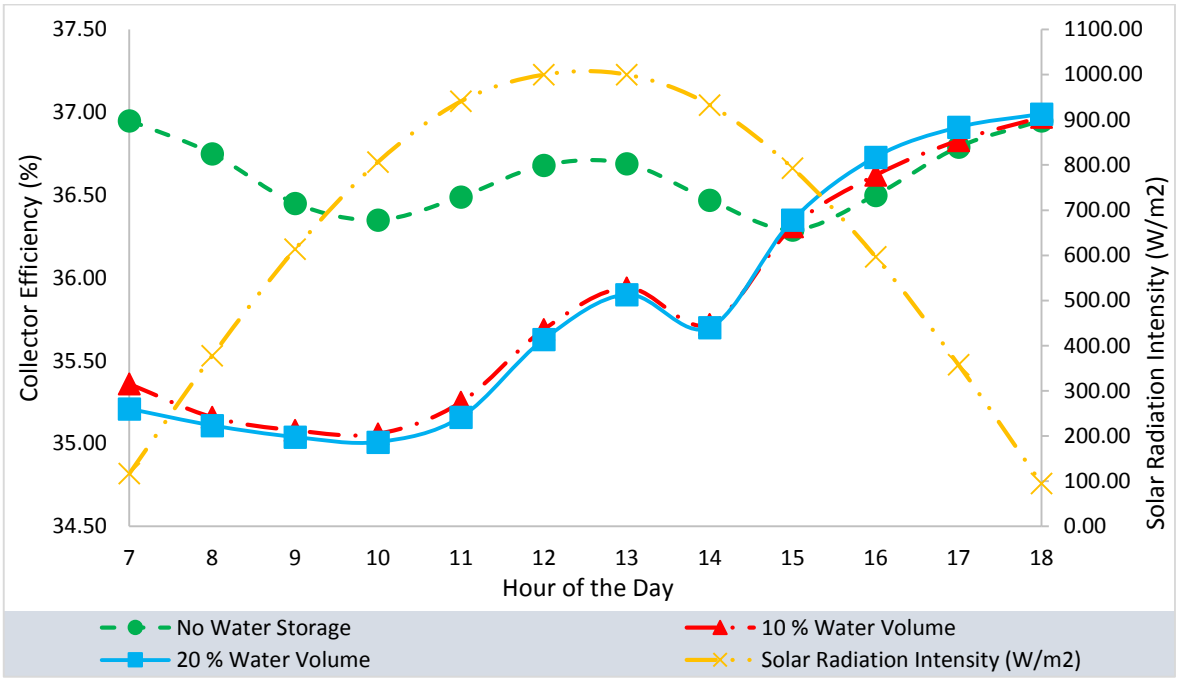

Figure 4.103: Collector efficiencies for the inclined SCPP with and without water storage

4.13 Analysis of Inclined SCPP without Chimney Component

The detail of the numerical investigation procedure of four novel designs of the inclined SCPP without chimney was presented in Section 3.9.10. The schematic representations of the four novel designs were provided for a clearer understanding of the models' geometries. Design A consisted of an inclined collector integrated with a horizontal tube. Design B combined an inclined collector with a horizontal divergent section. Design C consisted of an inclined collector merged with three horizontal tubes. Design D involved an inclined collector integrated with converging guide walls and three horizontal tubes.

4.13.1 Velocity of Air at the Collector's Outlet for the Novel Designs of the Inclined SCPP without Updraft Tower

As shown in Figure 4.104, the collector outlet velocities recorded for the different design showed that Design B has the highest air velocity. This result was attributed to the narrow air flow channel at the junction connecting the inclined collector and the horizontal divergent section. Based on the theory of the mass conservation, the significant reduction in the cross-sectional area of the air flow channel caused increase velocity.

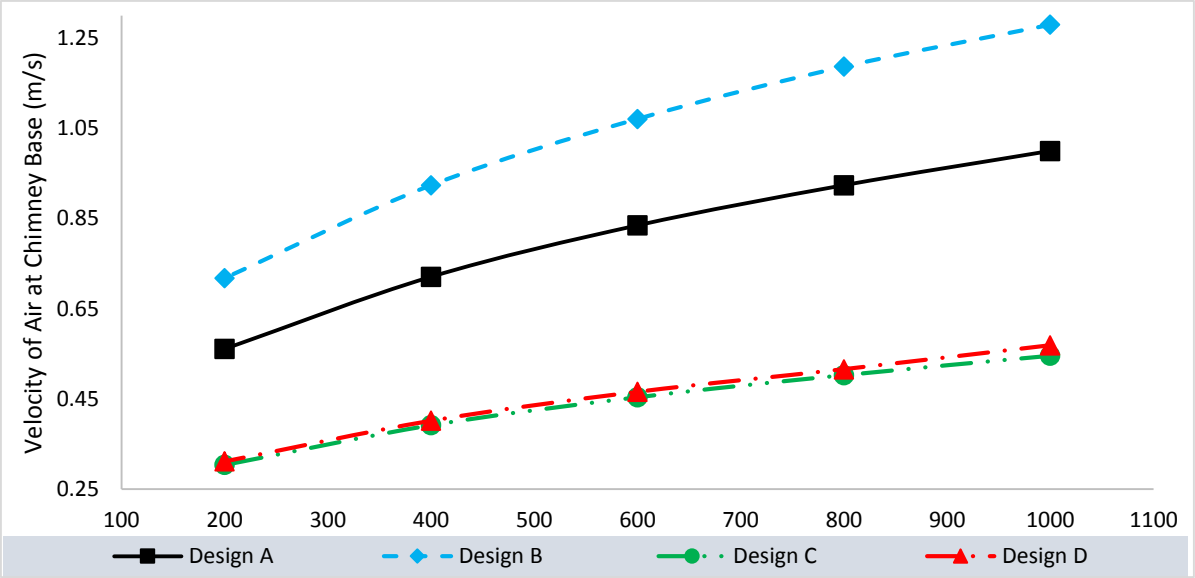

Figure 4.104: Velocity of Air at the Collector's Outlet for the Inclined SCPP without Additional Chimney

In Figure 4.104, it was apparent that both Design C and Design D predicted low air velocity at the collector's outlet/exit. This was due to the fact that the collector used in Design C and Design D had the exit width dimension same as the inlet width dimension of 1:1 ratio as against Design A and Design B which has their exit width to inlet in the ratio of 1:6. The area ratio of exit to air flow inlets (inlet and air-vents) area of Design C and Design D were 33:13 as compared to the Design A and Design B which had exit to air flow inlets (inlet and air-vents) area ratio of 11:26. Design C and Design D involved the integration of an inclined collector with three separate horizontal tubes instead of a single tube. The three separate horizontal tubes permit the installation of three individual turbines. Furthermore, Design D observed slightly higher air velocities at the collector's outlet than Design C due to the use of the converging guide walls in Design D which allowed the air flow to travel smoothly in regular paths into the separate horizontal tubes. Visual flow streamlines of the different models are presented in Appendix F.

4.13.2 Mass Flow Rate of Air at the Collector's Outlet for the Novel Designs of the Inclined SCPP without Updraft Tower

Figure 4.105 shows the air mass flow rate evaluated from simulation at the collector's outlet for the inclined SCPP designs without additional chimney component. Design C and Design D were found to produce higher air mass flow rate in comparison to Design A and Design B. These results obtained for Design C and Design D show the impact of the exit area on the mass air flow rate. The air mass flow rate yielded in both designs were higher when compared to Design A and Design B which only permitted the installation of a single turbine.

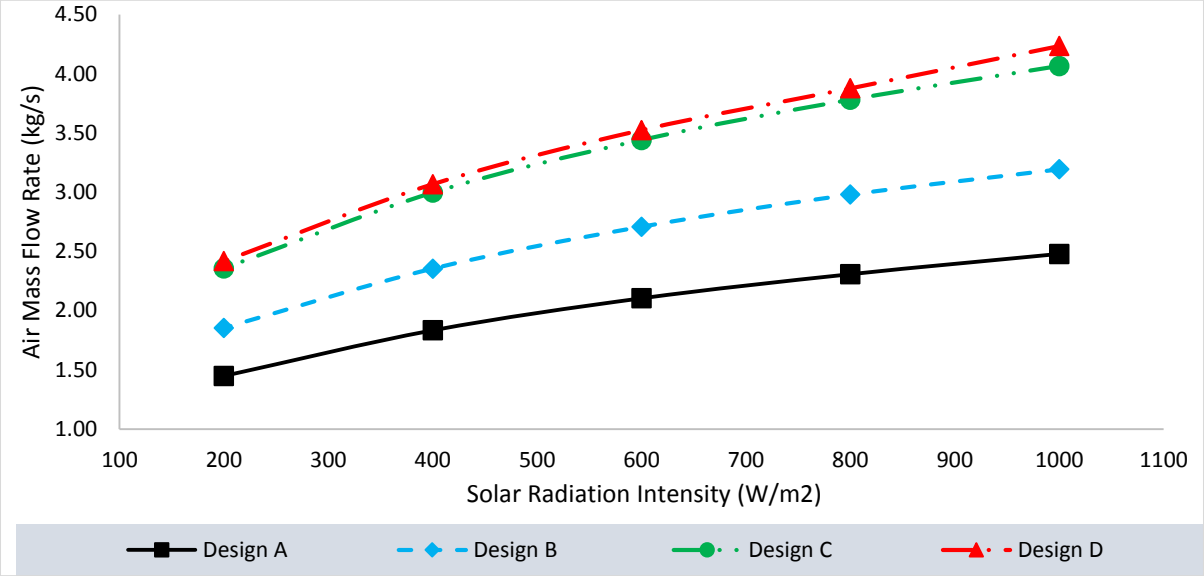

Figure 4.105: Mass Flow Rate of Air at the Collector's Outlet for the Inclined SCPP without Additional Chimney Component

4.13.3 Electrical Power Output of the Inclined SCPP without Updraft Tower

The inclined SCPP with no chimney installed was still able to generate electricity. Figure 4.106 shows the electrical power output of all four novel designs of the inclined SCPP without additional chimney component. It was determined that Design D produced the highest electrical power output. Owing to highest air mass flow rate yielded by Design D, the electrical power output was the highest with remarkable performance improvement in comparison to other designs. Design D involved an inclined collector integrated with converging guide walls which assisted the air flow from the greenhouse to the separate flow channels for electrical energy conversion using the turbine.

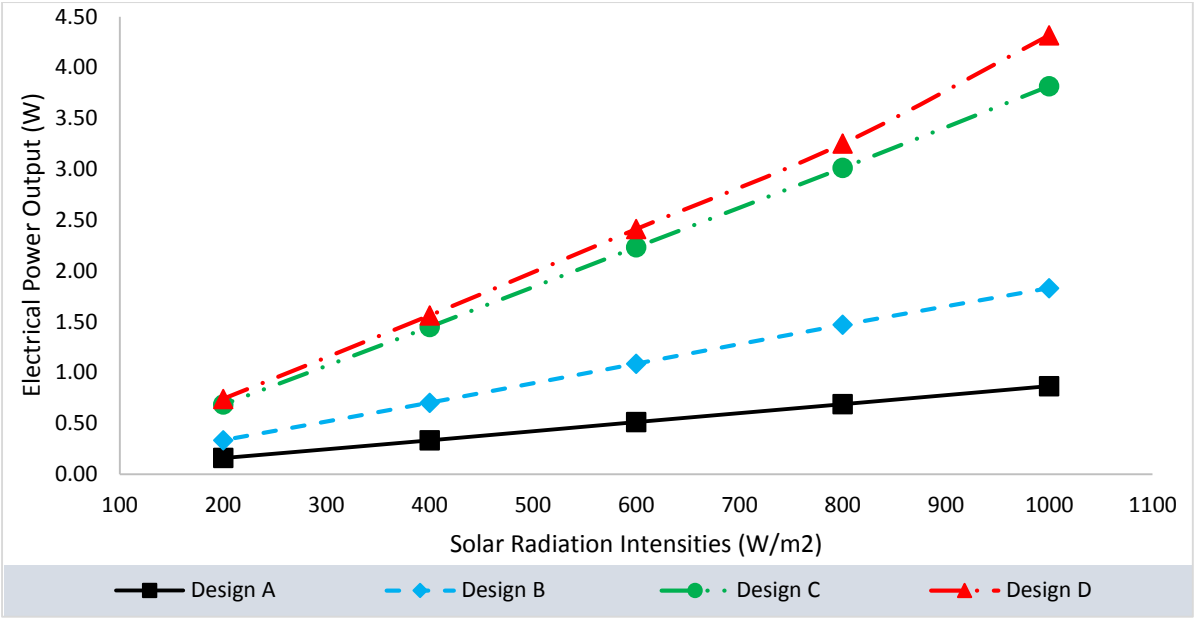

Figure 4.106: Electrical Power Output for the Inclined SCPP without Additional Chimney

4.13.4 Collector Efficiency for the Inclined SCPP without Updraft Tower

Figure 4.107 shows the collector efficiency of the four novel designs involving the inclined SCPP without additional chimney component. Design D was observed to produce the highest collector efficiency. The results shown in Figure 4.107 also proved that the inclined collectors in Design C and Design D were able to function effectively as a chimney and a collector, removing the need for an additional updraft tower. The use of inclined collector integrated with horizontal tubes and converging guide walls had the advantage of acting as chimney and collector, as the tilt angle of the inclined collector created a height advantage for the buoyancy driven flow of the air. By increasing the length of the collector, this model, Design D, can be commercialized for mountainous areas where the mountain can be used for the installation of the turbine and support for the collector exit.

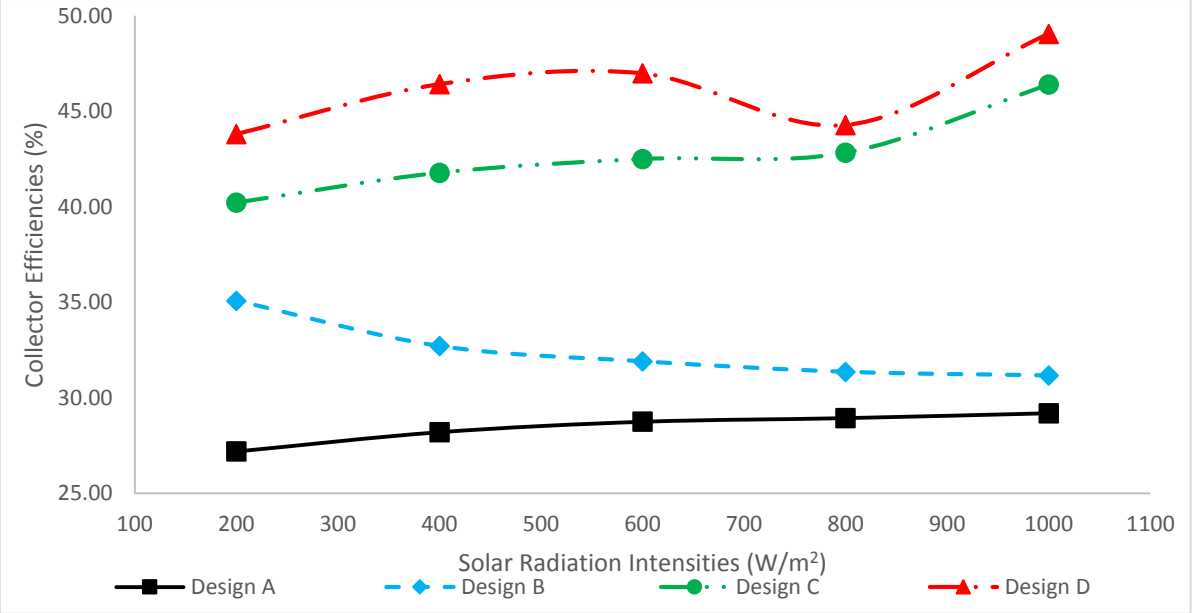

Figure 4.107: Collector Efficiency for the Inclined SCPP without Additional Chimney

4.13.5 Comparison of the Performance of Inclined SCPP with and without Additional Chimney and Underneath Air-Vents

Comparison of the electrical power output of the various models of the inclined SCPP with and without air-vents is presented in Figure 4.108. Considering the different solar radiation intensities from 200 W/m^2 to 1000 W/m^2, all designs equipped with underneath air-vents showed higher electrical power output in comparison to the systems without air-vents. The comparison between the total plant efficiency for Design A, Design B, Design C and Design D with and without air-vents is presented in Figure 4.109. The results show that the total system efficiency was significantly increased with the use of underneath air-vents. The results are further supported by the comparison of the performance improvement with respect to the total plant efficiency, as shown in Figure 4.110, where the systems without air-vents were selected as the reference cases. At 1000 W/m^2 solar radiation intensity, Design A, Design B, Design C and Design D with air-vents observed 102.33 %, 226.79 %, 97.93 % and 104.75 % performance improvement respectively in comparison to the systems without air-vents.

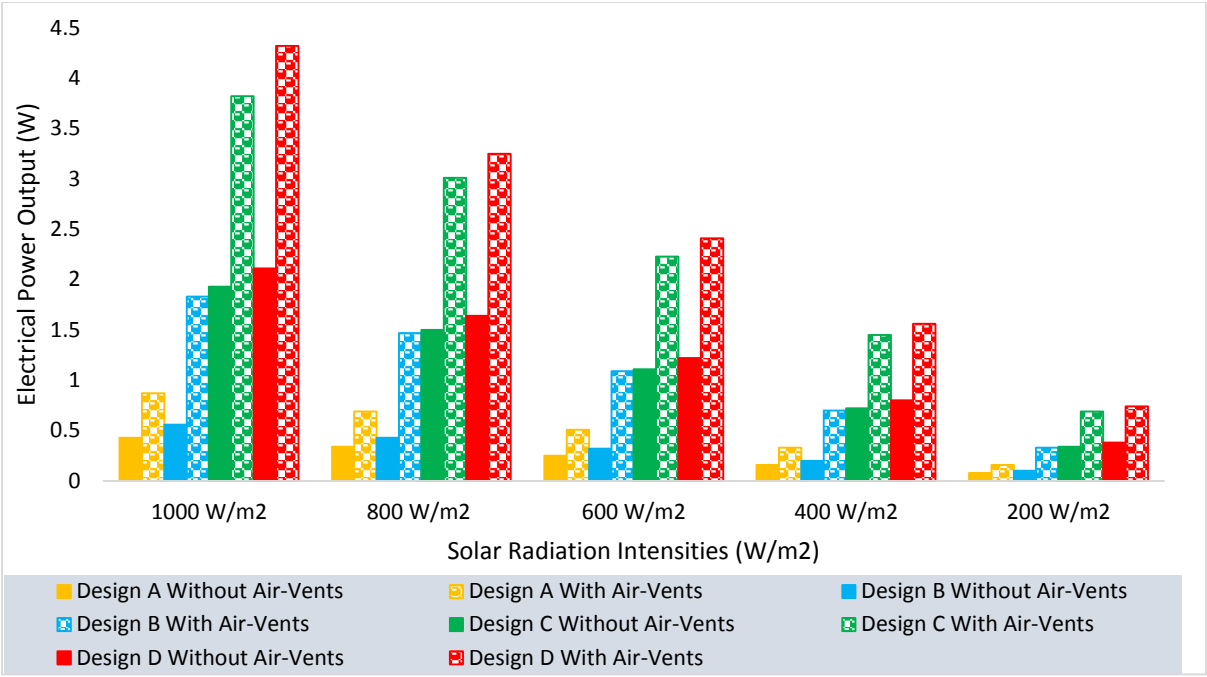

Figure 4.108: Electrical Power Output of the Novel Designs of Inclined SCPP with and without Air-Vents

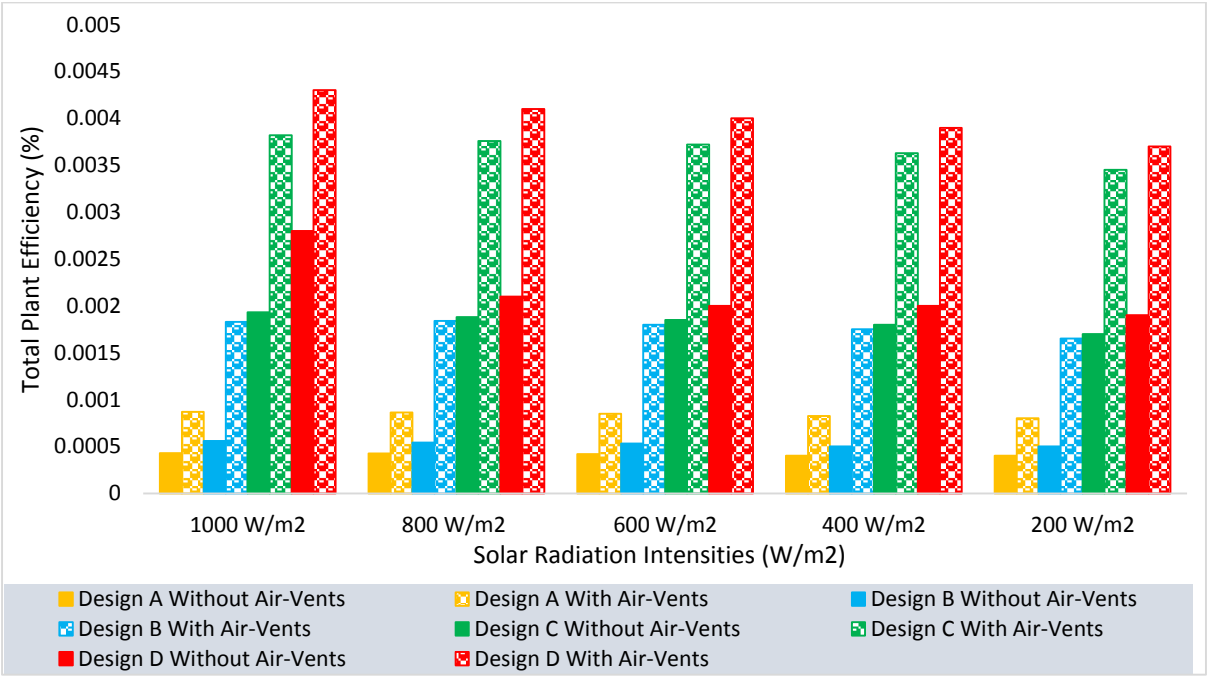

Figure 4.109: Total Plant Efficiency for the Novel Designs of the Inclined SCPP with and without Air-vents

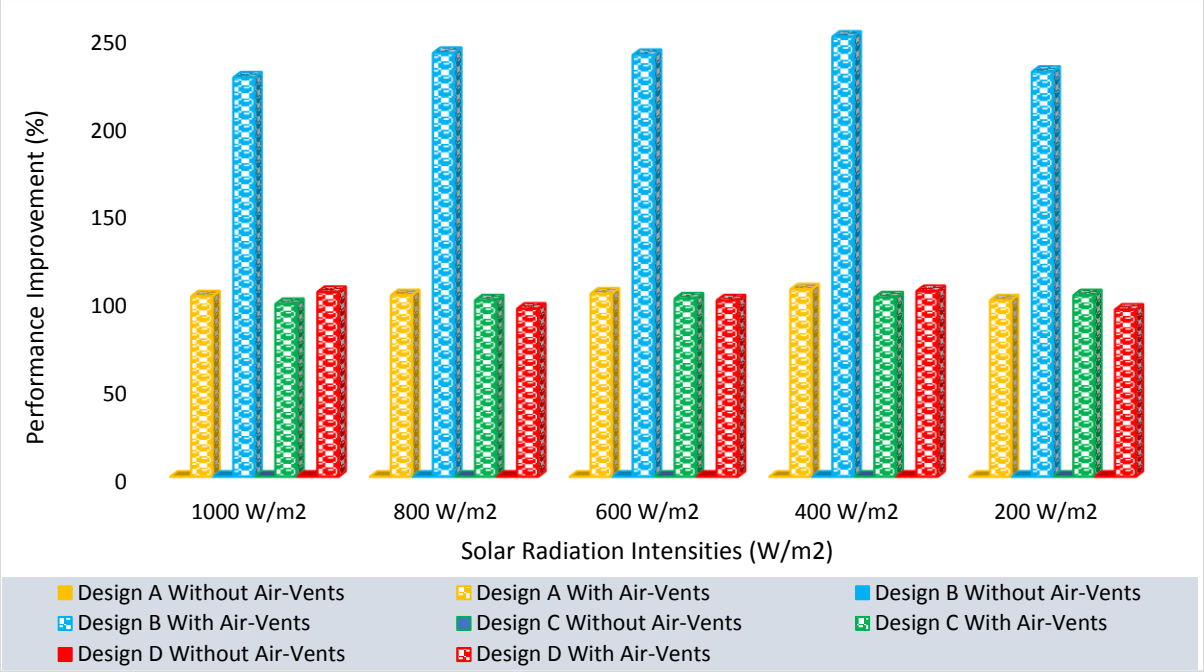

Figure 4.110: Performance Improvement with respect to the Total Plant Efficiency

In this research, it was determined that the inclined SCPP with 15 number of underneath air-vents produced the best system performance. The best model of the inclined SCPP was also characterized by a 100 m^2 solar collector, 26.85 m high chimney, and 1.0 m diameter chimney. The performance of this model was compared with the inclined SCPP without additional chimney component, with respect to the electrical power output as presented in Figure 4.111. The comparison showed that the inclined SCPP with underneath air-vents and chimney produced higher electrical power output than the system without additional chimney component. Moreover, it was found that the system without additional chimney tower could produce approximately one third of the output obtained from the system with a chimney. The inclined SCPP without additional chimney component was a reliable system to generate electricity at various solar radiation intensities despite its lower electrical power generation. As the system operated without a chimney, the investment cost of the inclined SCPP would be significantly reduced considering the high cost of tall chimney tower. Furthermore, the system employed sloped collector with the turbine staged at the collector's exit, thus, allowing easy maintenance of the turbine when required. In addition to that, the construction of tall chimney prompted engineering structural challenges.

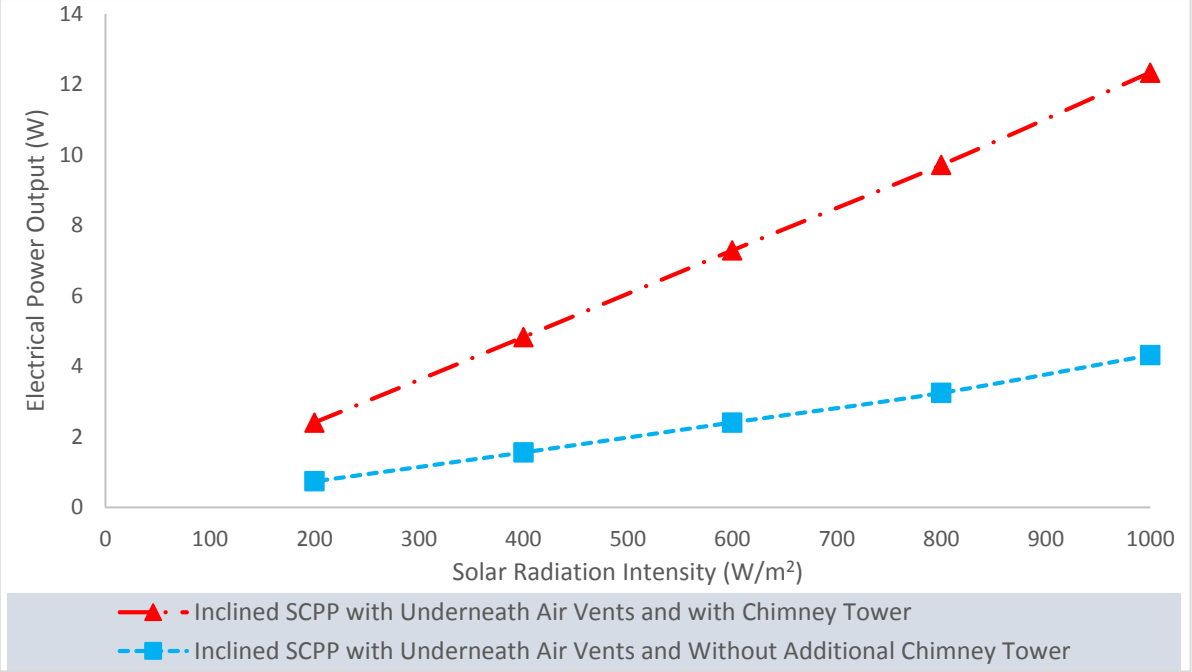

Figure 4.111: Comparison of the Electrical Power Output of the Inclined SCPP with and without Additional Chimney Component

Chapter 5
Conclusion

This chapter presents the conclusion of the findings from the completed research objectives. The conclusions are presented with respect to the objectives.

The findings from the effect of collector absorber geometry on collector air flow and thermal performance can be concluded as follows:

- When the collector absorber's rectangular plate had 12.5 m length and 6 m width, the collector was within the optimum dimension ratios which produced higher air velocities, mass flow rate and air power at the chimney base.
- When the collector's width was longer than the collector length, there was a loss in air power. This was due to air recirculation in the collector region which caused kinetic energy and thermal energy losses.
- It was revealed that when the absorber had extreme longer length in comparison to its width, the average temperatures of the absorber and the transparent cover were excessively reduced. As a consequence, less amount of heat was transferred to the system air which led to a reduction in the useful energy gained by the air.

The study on the air volume at the collector and the variants of the inlet and outlet gap/height between the absorber and the transparent cover revealed the following:

- A higher collector's air volume led to higher heat removal at the absorber but when the air volume was in excess, the available energy in the air was not sufficient to excite the internal energy in the air to higher velocity. This led to recirculation of air at the collector, thus both kinetic and thermal energy losses occurred.
- The investigation on the effect of canopy profile on the performance of the inclined solar chimney power plant had shown that the best configuration was for the transparent cover raised 0.1 m at the collector inlet and 1.1 m at collector outlet, which resulted in maximum air velocity at the chimney base.

The investigation on the influence of the concrete thicknesses on the inclined SCPP collector performance revealed that:

- At low concrete absorber thickness, there was decrease in thermal resistance of the absorber leading to significant thermal energy transfer by conduction from the absorber surface through the absorber thickness to the back. Consequently, convective thermal loss occurred to the ambient and radiation thermal loss to the surrounding ground was increased.
- Higher thickness of the concrete provided resistance to conduction heat transfer from the absorber's top surface through the concrete absorber thickness to the back surface, thus allows for heat storage for possible extended operation of the plant at low solar radiation and night time in the inclined SCPP.

The investigation on the introduction of underneath air-vents with varied orientation angles to the inclined SCPP revealed the following:

- With the inclusion of the underneath air-vents, air velocity and mass flow rate at the chimney base was enhanced. The electrical power output of the inclined SCPP was significantly increased with the use of the underneath air-vents.
- Considering the angle of the vents, the highest air velocity was recorded at 50° vent-angle on average.
- The collector efficiencies were lowest for the inclined SCPP system without air vents at different solar radiation intensities. The collector efficiency was found to be highest with 50° oriented air-vents at low to moderate solar radiation intensities which is majorly the solar radiation intensity range in Malaysia.
- The study determined that without the inclusion of the underneath air-vents, the system was characterized of higher radiation thermal loss from the transparent cover to the ambient. The inclined SCPP with underneath air-vents showed lower value of radiation heat transfer loss coefficients from the transparent cover to the ambient.

The study on the effects of the different positions of the air vents in the solar collector concludes the following:

- For the cases in which the vents were evenly distributed across the entire absorber area or located further from the collector's inlet (after 4 m from the inlet) and nearer to the chimney inlet, the air velocities at the base of the chimney significant dropped.

- When the vents were installed at higher locations nearer to the chimney, higher influx of air occurred which led to choke at the chimney base. This created pressure buildup which restricted air flow.

The analysis on the influence of chimney diameters on the performance of the inclined SCPP with underneath air vents is concluded as shown below:

- The use of 0.5 m diameter chimney caused the air in the collector to experience choked at the throat of the chimney. This led to reverse flow in the air such that some of the air exited the collector through the underneath air-vents.
- The increase in the chimney diameter gradually eliminated the choke air flow at the throat of the chimney. At 1.0 m chimney diameter, the chimney's cross-sectional area was sufficiently large to allow the heated air to flow through without any restriction, thus no reverse flow was experienced at the underneath air-vents.

The investigation on the effect of the change in the vents area and numbers on the performance of the inclined SCPP has the following conclusions:

- Increasing the air vents' area over a certain limit resulted in collector's performance degradation. This was because excess air was introduced from the vents with less heat energy to increase the fluid's energy to buoyancy.
- The use of higher number of air-vents was found to increase the collector's performance. Higher number of air-vents offered the influx air the opportunity to gain energy faster from the surrounding absorber heat.

The investigation on the effect of water thermal storage on the inclined SCPP performance is concluded below:

- An increase in the volume of the water storage tanks led to an increased power generation during the night, however, output power during the day was reduced.

The analysis of inclined SCPP without chimney component concludes the following:

- The inclined collectors were found to function effectively as a chimney and a collector.
- It was found that the system without additional chimney tower could produce approximately one third of the output obtained from the system with a chimney.

Recommendation for Future Work

Considering the scope of this work, the research methods and techniques used in this study can be extended as recommendations for further work. These include numerical studies and experimental investigations of the inclined Solar Chimney Power Plant as presented below.

- The development of an inclined Solar Chimney Power Plant numerical model which incorporates a far-field computational domain of the system. The simulation should be conducted at far-field condition which takes into consideration the effects of wind at different directions around the collector component and around the chimney component. The velocity of the wind should be obtained from actual meteorological and weather data with respect to various solar radiation intensities prevalent in the design location. The wind direction should be varied to study different conditions and derive a performance trend under the local environmental conditions. The energy loses associated to the wind effect will be useful for design of a real-time Inclined SCPP to operate at different environmental conditions.
- The establishment of an experimental prototype of the inclined Solar Chimney Power Plant with underneath air-vents is recommended to validate the claims of this numerical works. A supporting mathematical/analytical model should support the experimental work such that projection for commercial size plant can easily be available for investors.
- To develop a cost model of the inclined Solar Chimney Power Plant with underneath air-vents for commercial purpose considering the size of the plant.
- To investigate the performance of other types of thermal storage medium which were not considered in this study. Some examples might include wax in containers, water mixed with nano-material, and other composite materials for thermal storage.
- Future study should consider different design of turbines and guide-vanes to enhance the air attack on the turbine blade as well as the resulting power output which should be compared with the normal operating scenario.

References

Every reasonable effort has been made to acknowledge the owners of copyright material. I would be pleased to hear from any copyright owner who has been omitted or incorrectly acknowledged.

ADB. 2013. "Asian water development outlook 2013.". http://www.adb.org/publications/asian-water-development-outlook-2013.

ADB. 2014. "Climate change in Asia and the Pacific: facts and figures.". http://www.adb.org/themes/climate-change/facts-figures.

Ahmed, M Rafiuddin, and Sandeep K Patel. 2017. "Computational and experimental studies on solar chimney power plants for power generation in Pacific Island countries." Energy Conversion and Management 149:61-78.

Al-Kayiem, HH, and SI Gilani. 2013. "Simulation of a collector using waste heat energy in a solar chimney power plant system." WIT Transactions on Ecology and the Environment 179:933-944.

Al-Kayiem, Hussain H, and Ogboo Chikere Aja. 2016. "Historic and recent progress in solar chimney power plant enhancing technologies." Renewable and Sustainable Energy Reviews 58:1269-1292.

Al-Kayiem, Hussain H, How Meng Git, and Seow Lee Lee. 2009. "Experimental investigation on solar-flue gas chimney." Journal of Energy and Power Engineering 3 (9):25-31.

Al-Kayiem, Hussain H, K Yin Yin, and C Yee Sing. 2012. Numerical simulation of solar chimney integrated with exhaust of thermal power plant: WIT Press: United Kingdom.

Alrobaei, Hussain. 2007. "Hybrid Geothermal/Solar Energy Technology For Power Generation."

ANSYS, ANSYS FLUENT User's Guide. 2011. "vol. 15317, no." November. ANSYS Inc.

Ayadi, Ahmed, Zied Driss, Abdallah Bouabidi, and Mohamed Salah Abid. 2017. "Experimental and numerical study of the impact of the collector roof inclination on the performance of a solar chimney power plant." Energy and Buildings 139:263-276.

Bilgen, E, and J Rheault. 2005. "Solar chimney power plants for high latitudes." Solar Energy 79 (5):449-458.

BP. 2011. "BP Statistical Review of World Energy 2011." http://www.bp.com/assets/bp_internet/globalbp/globalbp_uk_english/reports_and_publications/statistical_energy_review_2011/STAGING/local_assets/pdf/statistical_review_of_world_energy_full_report_2011.pdf.

BP. 2012. "BP Statistical Review of World Energy 2012." http://www.bp.com/assets/bp_internet/globalbp/globalbp_uk_english/reports_and_pu

blications/statistical_energy_review_2011/STAGING/local_assets/pdf/statistical_review_of_world_energy_full_report_2012.pdf.

BP. 2013. "BP Statistical Review of World Energy 2013." http://www.bp.com/content/dam/bp/pdf/statistical-review/statistical_review_of_world_energy_2013.pdf.

BP. 2014. "BP Statistical Review of World Energy 2014." http://www.bp.com/content/dam/bp/pdf/Energy-economics/statistical-review-2014/BP-statistical-review-of-world-energy-2014-full-report.pdf.

BP. 2015. "BP Statistical Review of World Energy 2015." http://www.bp.com/content/dam/bp/pdf/Energy-economics/statistical-review-2015/bp-statistical-review-of-world-energy-2015-full-report.pdf.

BP. 2016. "BP Statistical Review of World Energy 2016." https://www.bp.com/content/dam/bp/pdf/energy-economics/statistical-review-2016/bp-statistical-review-of-world-energy-2016-full-report.pdf.

BP. 2017. "BP Statistical Review of World Energy 2017." https://www.bp.com/content/dam/bp/en/corporate/pdf/energy-economics/statistical-review-2017/bp-statistical-review-of-world-energy-2017-full-report.pdf.

Cabanyes, I. 1903. "Las chimeneas solares (Solar chimneys)." La ernergia eléctrica.

Calder, Ritchie. 1970. Leonardo & the Age of the Eye: Not Avail.

Chikere, Aja Ogboo, Hussain H Alkayiem, and Zainal Ambri Abdul Karim. 2011. "Thermal field study and analysis in hybrid solar flue gas chimney power plant." National Postgraduate Conference (NPC), 2011.

Choi, Young Jae, Dong Hoon Kam, Yoon Won Park, and Yong Hoon Jeong. 2016. "Development of analytical model for solar chimney power plant with and without water storage system." Energy 112:200-207.

Cottam, PJ, P Duffour, P Lindstrand, and P Fromme. 2016. "Effect of canopy profile on solar thermal chimney performance." Solar Energy 129:286-296.

Council, World Energy. 2013. "World Energy Issues Monitor."

Davey, RC. 2008. "Device for generating electricity from solar power." WO 22372:A1.

Dennis, Carina. 2006. "Solar energy: Radiation nation." Nature 443 (7107):23-24.

dos Santos Bernardes, Marco Aurélio. 2010. Solar Chimney Power Plants-Developments and Advancements: INTECH Open Access Publisher.

Duffie, John A, and William A Beckman. 2013. Solar engineering of thermal processes: John Wiley & Sons.

Energy, Solar. 2015. "High-temperature solar thermal energy." https://solar-energy.technology/solar-thermal/high-temperature.

Fluri, Thomas Peter. 2008. "Turbine layout for and optimization of solar chimney power conversion units." Stellenbosch: Stellenbosch University.

Ghalamchi, Mehrdad, Alibakhsh Kasaeian, Mehran Ghalamchi, and Alireza Hajiseyed Mirzahosseini. 2016. "An experimental study on the thermal performance of a solar chimney with different dimensional parameters." Renewable Energy 91:477-483.

Gholamalizadeh, Ehsan, and Jae Dong Chung. 2017. "Analysis of Fluid Flow and Heat Transfer on a Solar Updraft Tower Power Plant Coupled with a Wind Turbine using Computational Fluid Dynamics." Applied Thermal Engineering.

Gholamalizadeh, Ehsan, and Man-Hoe Kim. 2014. "Three-dimensional CFD analysis for simulating the greenhouse effect in solar chimney power plants using a two-band radiation model." Renewable energy 63:498-506.

Gholamalizadeh, Ehsan, and Man-Hoe Kim. 2016. "CFD (computational fluid dynamics) analysis of a solar-chimney power plant with inclined collector roof." Energy 107:661-667. doi: http://dx.doi.org/10.1016/j.energy.2016.04.077.

Ghorbani, Babak, Mohammad Ghashami, Mehdi Ashjaee, and Hamid Hosseinzadegan. 2015. "Electricity production with low grade heat in thermal power plants by design improvement of a hybrid dry cooling tower and a solar chimney concept." Energy Conversion and Management 94:1-11.

Gitan, Ali Ahmed, Shaymaa Husham Abdulmalek, and Salwan S Dihrab. 2015. "Tracking collector consideration of tilted collector solar updraft tower power plant under Malaysia climate conditions." Energy 93:1467-1477.

Guide, User. 2009. "Star-CCM+ Version 4.04. 11." CD adapco.

Günther, Hanns. 2012. In hundert Jahren: die künftige Energieversorgung der Welt: BoD–Books on Demand.

Guo, Peng-hua, Jing-yin Li, and Yuan Wang. 2014. "Numerical simulations of solar chimney power plant with radiation model." Renewable energy 62:24-30.

Guo, Penghua, Jingyin Li, Yunfeng Wang, and Yuan Wang. 2016. "Evaluation of the optimal turbine pressure drop ratio for a solar chimney power plant." Energy Conversion and Management 108:14-22.

Guo, Penghua, Yunfeng Wang, Jingyin Li, and Yuan Wang. 2016. "Thermodynamic analysis of a solar chimney power plant system with soil heat storage." Applied Thermal Engineering 100:1076-1084.

Haaf, W. 1984. "Solar chimneys: part ii: preliminary test results from the Manzanares pilot plant." International Journal of Sustainable Energy 2 (2):141-161.

Haaf, W, K Friedrich, G Mayr, and J Schlaich. 1983. "Solar chimneys part I: principle and construction of the pilot plant in Manzanares." International Journal of Solar Energy 2 (1):3-20.

Hamdan, Mohammad O. 2011. "Analysis of a solar chimney power plant in the Arabian Gulf region." Renewable Energy 36 (10):2593-2598.

Hanna, Magdy Bassily, Tarek Abdel-Malak Mekhail, Omar Mohamed Dahab, Mohamed Fathy Cidek Esmail, and Ahmed Rekaby Abdel-Rahman. 2016. "Experimental and Numerical Investigation of the Solar Chimney Power Plant's Turbine." Open Journal of Fluid Dynamics 6 (04):332.

Hassan, Aakash, Majid Ali, and Adeel Waqas. 2018. "Numerical investigation on performance of solar chimney power plant by varying collector slope and chimney diverging angle." Energy 142:411-425.

Höök, Mikael, Anders Sivertsson, and Kjell Aleklett. 2010. "Validity of the fossil fuel production outlooks in the IPCC Emission Scenarios." Natural Resources Research 19 (2):63-81.

Hu, Siyang, Dennis YC Leung, and John CY Chan. 2017. "Impact of the geometry of divergent chimneys on the power output of a solar chimney power plant." Energy 120:1-11.

Huang, Ming-Hua, Lei Chen, Ya-Ling He, Jun-Ji Cao, and Wen-Quan Tao. 2017. "A two-dimensional simulation method of the solar chimney power plant with a new radiation model for the collector." International Communications in Heat and Mass Transfer 85:100-106.

IPCC. 2014. "Climate Change 2014: Mitigation of Climate Change." https://www.ipcc.ch/report/ar5/wg3/.

Islamuddin, Azeemuddin, Hussain H Al-Kayiem, and Syed I Gilani. 2013. "Simulation of solar chimney power plant with an external heat source." IOP Conference Series: Earth and Environmental Science.

Kannan, Nadarajah, and Divagar Vakeesan. 2016. "Solar energy for future world:-A review." Renewable and Sustainable Energy Reviews 62:1092-1105.

Kasaeian, Alibakhsh, Amir Reza Mahmoudi, Fatemeh Razi Astaraei, and Afshin Hejab. 2017. "3D simulation of solar chimney power plant considering turbine blades." Energy Conversion and Management 147:55-65.

Kashiwa, BA, and Corey B Kashiwa. 2008. "The solar cyclone: a solar chimney for harvesting atmospheric water." Energy 33 (2):331-339.

Khan, Jibran, and Mudassar H Arsalan. 2016. "Solar power technologies for sustainable electricity generation–A review." Renewable and Sustainable Energy Reviews 55:414-425.

Koonsrisuk, Atit, and Tawit Chitsomboon. 2007. "Dynamic similarity in solar chimney modeling." Solar Energy 81 (12):1439-1446.

Koonsrisuk, Atit, and Tawit Chitsomboon. 2013. "Mathematical modeling of solar chimney power plants." Energy 51:314-322.

Kreetz, H. 1997. "'Theoretische Untersuchungen und Auslegung eines temporären Wasserspeichers für das Aufwindkraftwerk." Energieverfahrenstechnik und Umwandlungstechniken regenerativer Energien-EVUR, TU Berlin, Berlin.

Lorenzo, Elena. 2002. "DE LOS ARCHIVOS HISTÓRICOS DE LA ENERGÍA SOLAR Las chimeneas solares: De una propuesta española en 1903 a la Central de Manzanares." It reviews the history of the SUPPs technology.

Lucier, Robert E. 1978. "Utilization of solar energy." Canada Patent (1023564).

Lucier, Robert E. 1981. System for converting solar heat to electrical energy. Google Patents.

McAdams, William H. 1958. "Heat transmission."

Mehrpooya, Mehdi, Mohsen Shahsavan, and Mohammad Mehdi Moftakhari Sharifzadeh. 2016. "Modeling, energy and exergy analysis of solar chimney power plant-Tehran climate data case study." Energy 115:257-273.

Ming, Tingzhen, Jinle Gui, Renaud Kiesgen de Richter, Yuan Pan, and Guoliang Xu. 2013. "Numerical analysis on the solar updraft power plant system with a blockage." Solar Energy 98:58-69.

Nazare. 1964. Generating Artificial Cyclones. edited by France Patent.

Ng, Khai Mun. 2014. "Nor Mariah Adam, Othman Inayatullah, Mohd Zainal Abidin Ab. Kadir, Assessment of solar radiation on diversely oriented surfaces and optimum tilts for solar absorbers in Malaysian tropical latitude." Int. J. Energy Environ. Eng 5:75.

Nia, Ehsan Shabahang, and Mohsen Ghazikhani. 2015. "Numerical investigation on heat transfer characteristics amelioration of a solar chimney power plant through passive flow control approach." Energy Conversion and Management 105:588-595.

Panwar, NL, SC Kaushik, and Surendra Kothari. 2011. "Role of renewable energy sources in environmental protection: a review." Renewable and Sustainable Energy Reviews 15 (3):1513-1524.

Papageorgiou, Christos D. 2010. "Floating solar chimney technology." In Solar energy. InTech.

Pastohr, Henry, Oliver Kornadt, and Klaus Gürlebeck. 2004. "Numerical and analytical calculations of the temperature and flow field in the upwind power plant." International Journal of Energy Research 28 (6):495-510.

Pasumarthi, N, and SA Sherif. 1998. "Experimental and theoretical performance of a demonstration solar chimney model—Part I: mathematical model development." International Journal of Energy Research 22 (3):277-288.

Patel, Sandeep K, Deepak Prasad, and M Rafiuddin Ahmed. 2014. "Computational studies on the effect of geometric parameters on the performance of a solar chimney power plant." Energy Conversion and Management 77:424-431.

Pretorius, Johannes Petrus. 2007. "Optimization and control of a large-scale solar chimney power plant." Stellenbosch: University of Stellenbosch.

Rabehi, Rayan, Abla Chaker, Zeroual Aouachria, and Ming Tingzhen. 2017. "CFD Analysis on the Performance of a Solar Chimney Power Plant System: Case Study in Algeria." International Journal of Green Energy (just-accepted).

Rafindadi, Abdulkadir Abdulrashid, Zarinah Yusof, Khalid Zaman, Phouphet Kyophilavong, and Ghulam Akhmat. 2014. "The relationship between air pollution, fossil fuel energy consumption, and water resources in the panel of selected Asia-Pacific countries." Environmental Science and Pollution Research 21 (19):11395-11400.

Raithby, GD, and KGT Hollands. 1998. "Natural convection." Handbook of heat transfer 3.

Ridley. 1956. Improvements in or relating to apparatus for generating power from solarheat. edited by Great Britain Patent.

Sangi, Roozbeh, Majid Amidpour, and Behzad Hosseinizadeh. 2011. "Modeling and numerical simulation of solar chimney power plants." Solar Energy 85 (5):829-838.

Schlaich, Jörg. 1995. The solar chimney: electricity from the sun: Edition Axel Menges.

Schlaich, Jörg, Rudolf Bergermann, Wolfgang Schiel, and Gerhard Weinrebe. 2005. "Design of Commercial Solar Updraft Tower Systems—Utilization of Solar Induced Convective Flows for Power Generation." Journal of Solar Energy Engineering 127 (1):117-124. doi: 10.1115/1.1823493.

Serag-Eldin, MA. 2006. "Analysis of a new solar chimney plant design for mountainous regions." Advanced Computational Methods in Heat Transfer IX, B. Sunden, and CA Brebbia, eds., Computational Mechanics Publications Ltd, Southampton:437-446.

Shirvan, Kamel Milani, Soroush Mirzakhanlari, Mojtaba Mamourian, and Soteris A Kalogirou. 2017. "Optimization of effective parameters on solar updraft tower to achieve potential maximum power output: A sensitivity analysis and numerical simulation." Applied Energy 195:725-737.

Siraj, Muhammad Shafiq. 2012. "Energy resources—The ultimate solution." Renewable and Sustainable Energy Reviews 16 (4):1971-1976.

UNEP. 2012. "Summary for Asia and the Pacific Region: on the eve of Rio+20.". http://www.unep.org/geo/pdfs/geo5/RS_AsiaPacific_en.pdf.

Versteeg, Henk Kaarle, and Weeratunge Malalasekera. 2007. An introduction to computational fluid dynamics: the finite volume method: Pearson Education.

Wang, Qiuhuan, Jialing Zhu, and Xinli Lu. 2017. "Numerical simulation of heat transfer process in solar enhanced natural draft dry cooling tower with radiation model." Applied Thermal Engineering 114:977-983.

World-Bank. 2017. "Population growth (annual %)." http://data.worldbank.org/indicator/SP.POP.GROW.

Xu, Guoliang, Tingzhen Ming, Yuan Pan, Fanlong Meng, and Cheng Zhou. 2011. "Numerical analysis on the performance of solar chimney power plant system." Energy Conversion and Management 52 (2):876-883.

Yiping, WANG, WANG Junhong, and Z Li. 2006. "The study of sea desalination and hot wind electric power integrated system by solar chimney." Acta Energiae Solaris Sinica 27 (7):738.

Yiping, Wang, Fang Zhenlei, Zhu Li, Yang Zhiyong, Wang Junhong, and Han Lijun. 2006. "Study on the integrated utilization of seawater by solar chimney." Acta Energiae Solaris Sinica 27 (4):382.

Zhou, Xinping, Fang Wang, and Reccab M Ochieng. 2010. "A review of solar chimney power technology." Renewable and Sustainable Energy Reviews 14 (8):2315-2338.

Zhou, Xinping, Yangyang Xu, and Yong Huang. 2016. "Novel concept of enhancing the performance of sloped solar collector by using natural anabatic winds." International Journal of Heat and Mass Transfer 102:1356-1361. doi: http://dx.doi.org/10.1016/j.ijheatmasstransfer.2016.07.009.

Zhou, Xinping, and Jiakuan Yang. 2009. "A Novel Solar Thermal Power Plant with Floating Chimney Stiffened onto a Mountainside and Potential of the Power Generation in China's Deserts." Heat Transfer Engineering 30 (5):400-407. doi: 10.1080/01457630802414813.

Zhou, Xinping, Jiakuan Yang, Jinbo Wang, and Bo Xiao. 2009. "Novel concept for producing energy integrating a solar collector with a man made mountain hollow." Energy Conversion and Management 50 (3):847-854.

Zhou, Xinping, and Shuo Yuan. 2017. "Wind effects on a solar updraft power plant." Journal of Wind Engineering and Industrial Aerodynamics.

Zou, Zheng, Hengxiang Gong, Xieshi Lie, Xiaoxiao Li, and Yong Yang. 2017. "Numerical Investigation of the Crosswind Effects on the Performance of a Hybrid Cooling-Tower-Solar-Chimney System." Applied Thermal Engineering.

Zou, Zheng, and Suoying He. 2015. "Modeling and characteristics analysis of hybrid cooling-tower-solar-chimney system." Energy Conversion and Management 95:59-68.

Appendix A

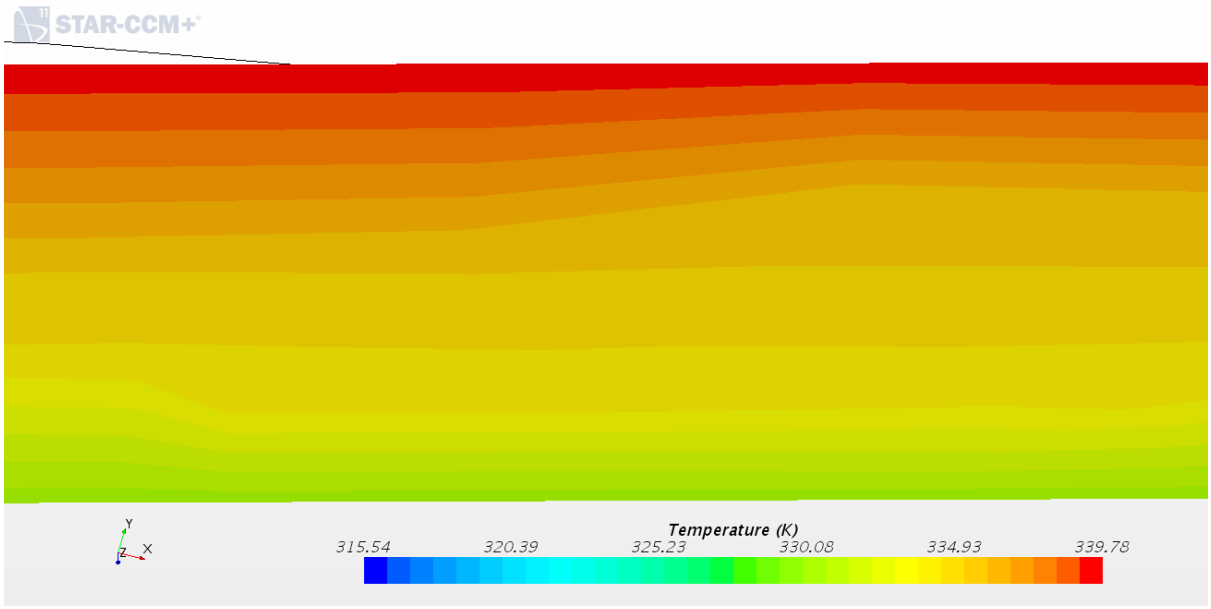

Figure A.1: Temperature Contour for 0.1 m Concrete Thickness

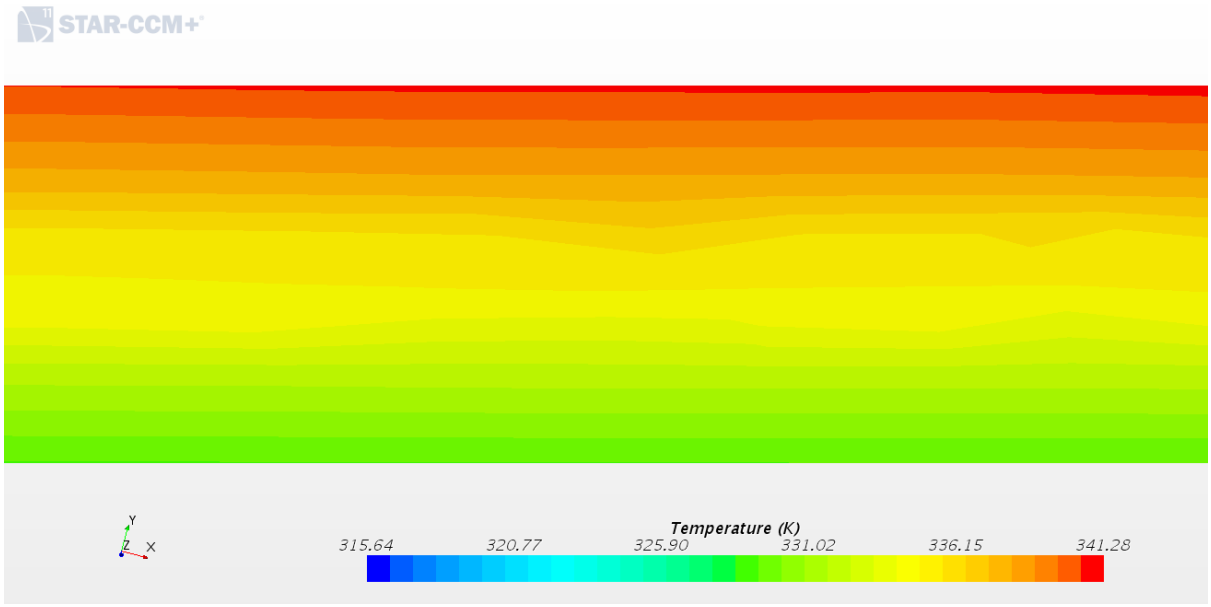

Figure A.2: Temperature Contour for 0.2 m Concrete Thickness

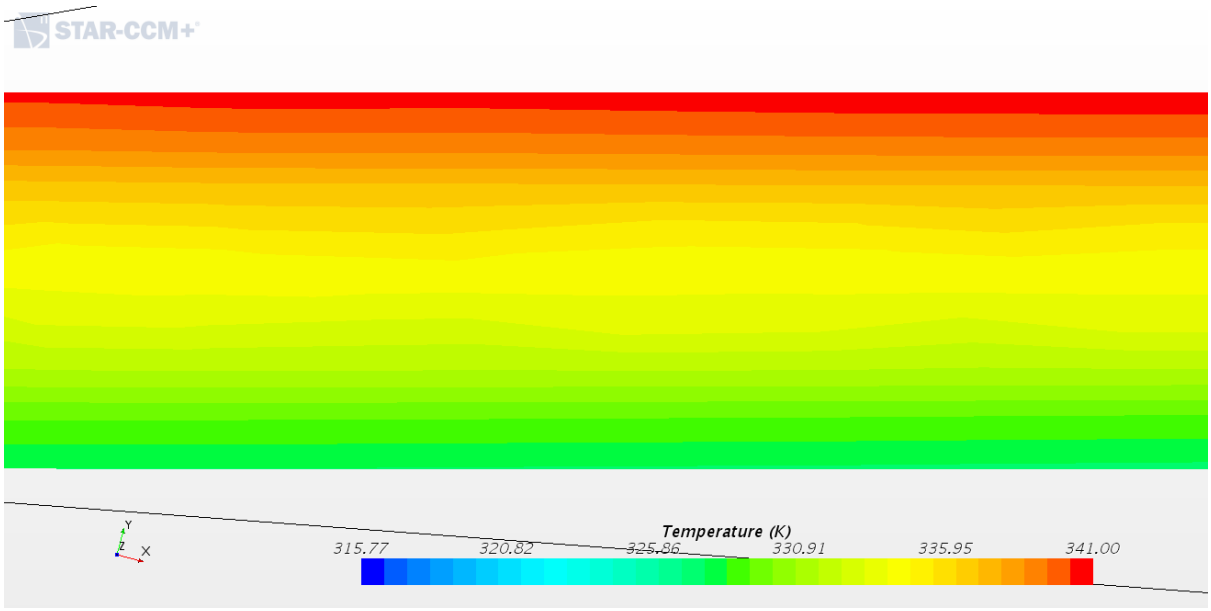

Figure A.3: Temperature Contour for 0.3 m Concrete Thickness

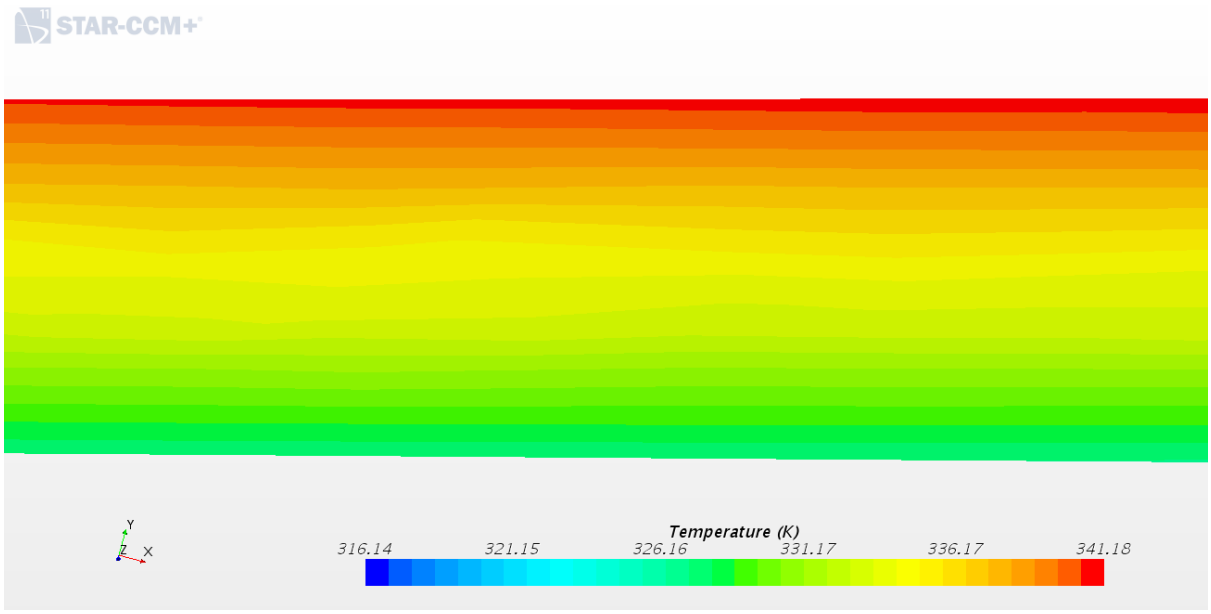

Figure A.4: Temperature Contour for 0.4 m Concrete Thickness

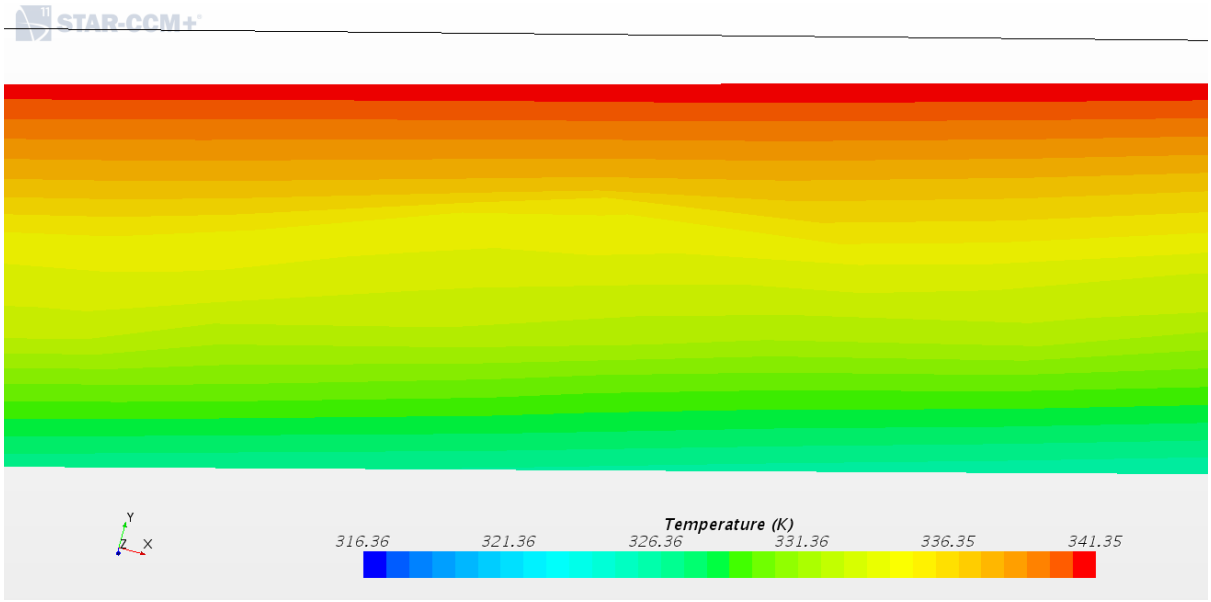

Figure A.5: Temperature Contour for 0.5 m Concrete Thickness

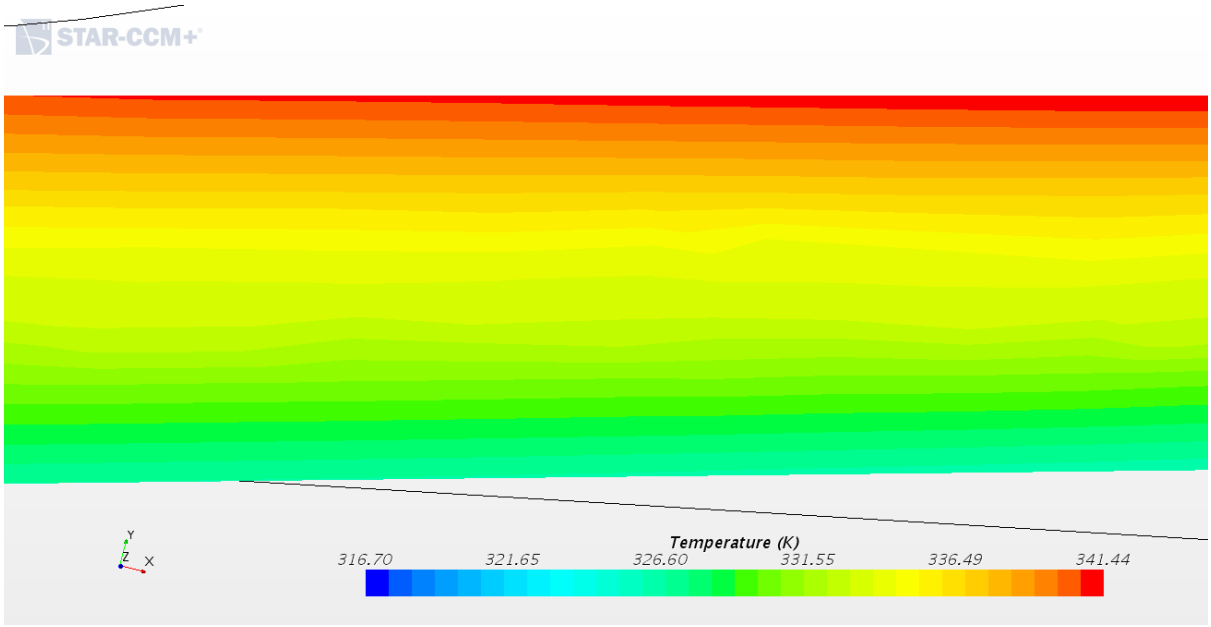

Figure A.6: Temperature Contour for 0.6 m Concrete Thickness

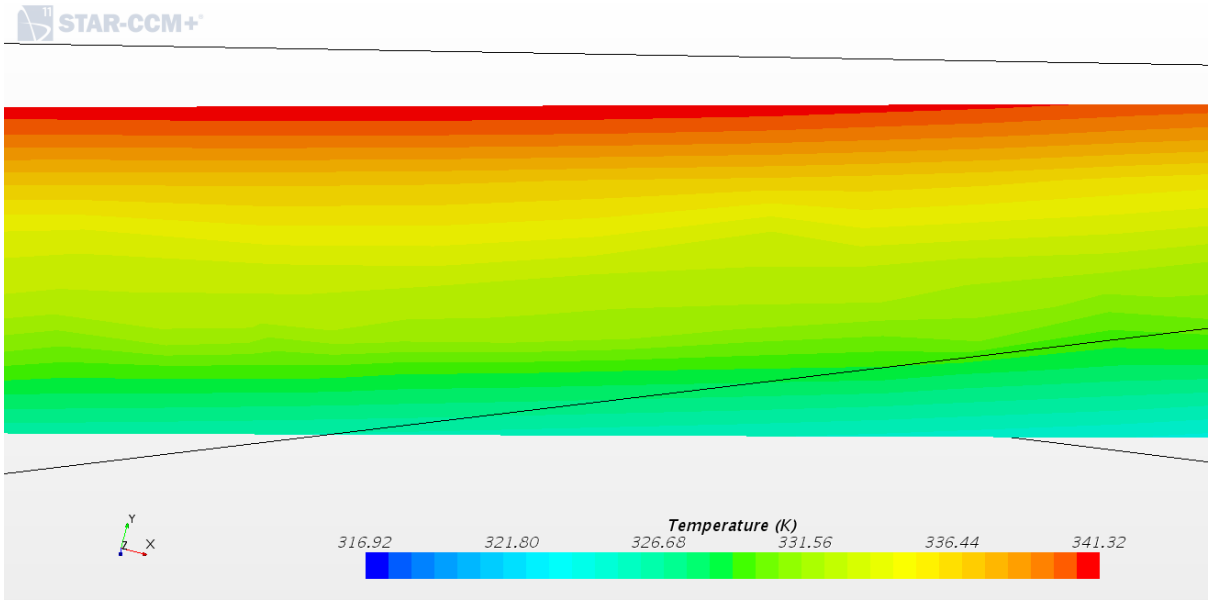

Figure A.7: Temperature Contour for 0.7 m Concrete Thickness

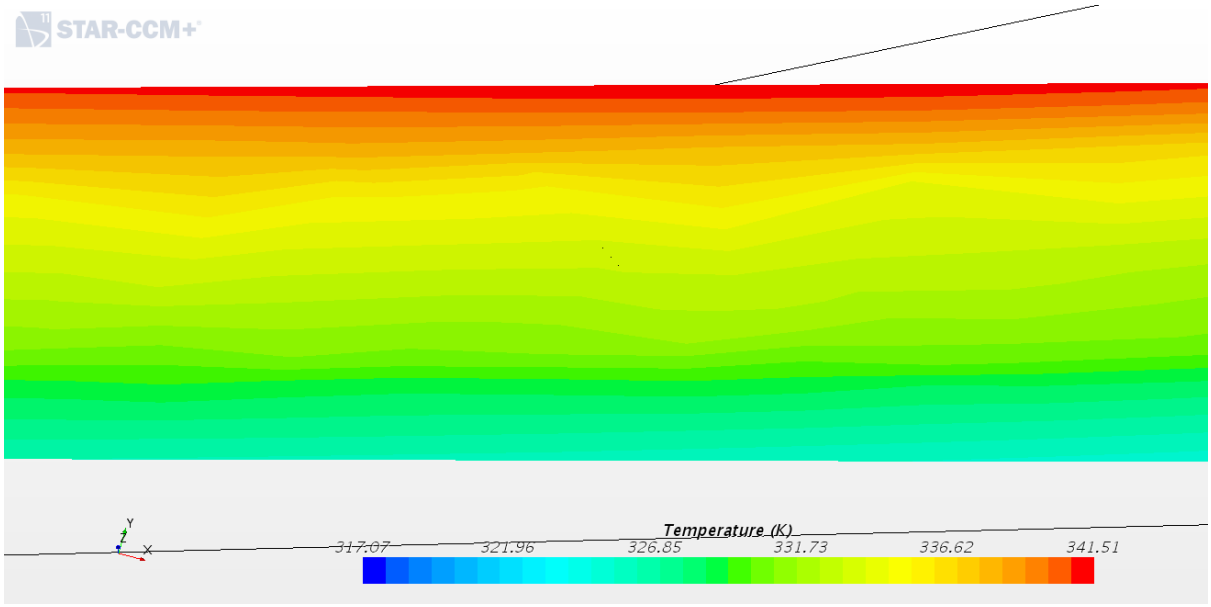

Figure A.8: Temperature Contour for 0.8 m Concrete Thickness

Appendix B

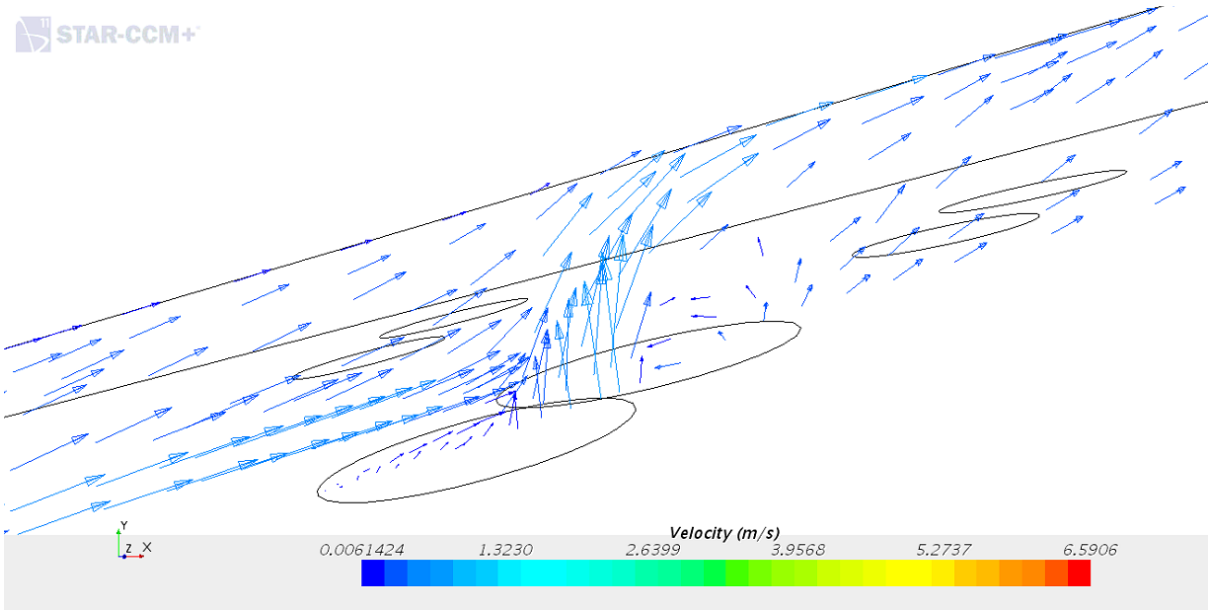

Figure B.1: Velocity vectors through the 10° vent at 1000 W/m^2

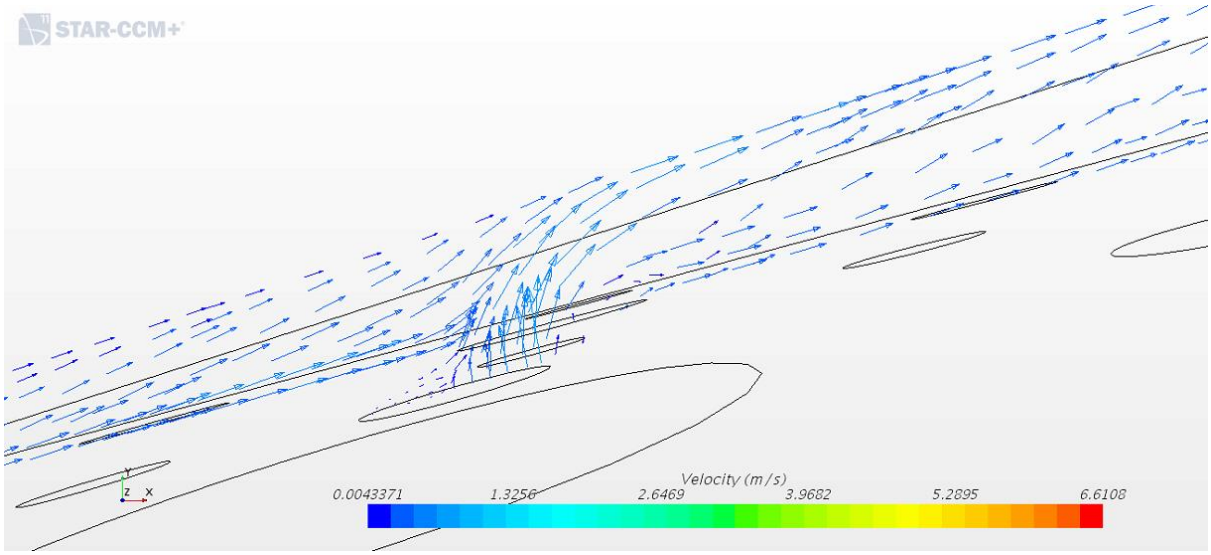

Figure B.2: Velocity vectors through the 20° vent at 1000 W/m^2

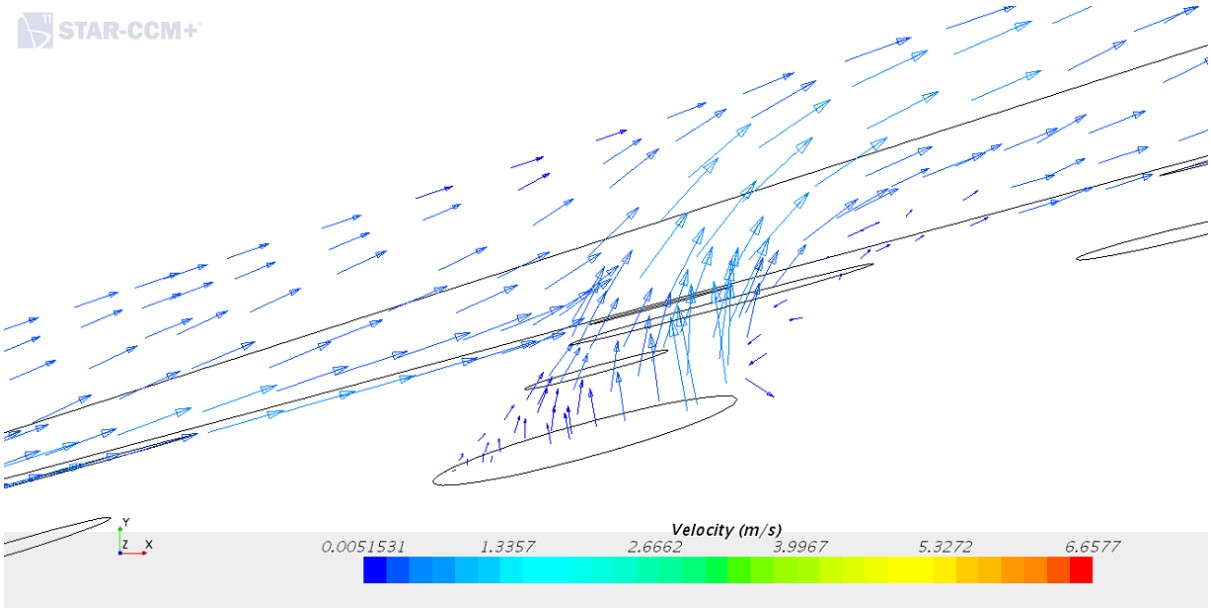

Figure B.3: Velocity vectors through the 30° vent at 1000 W/m^2

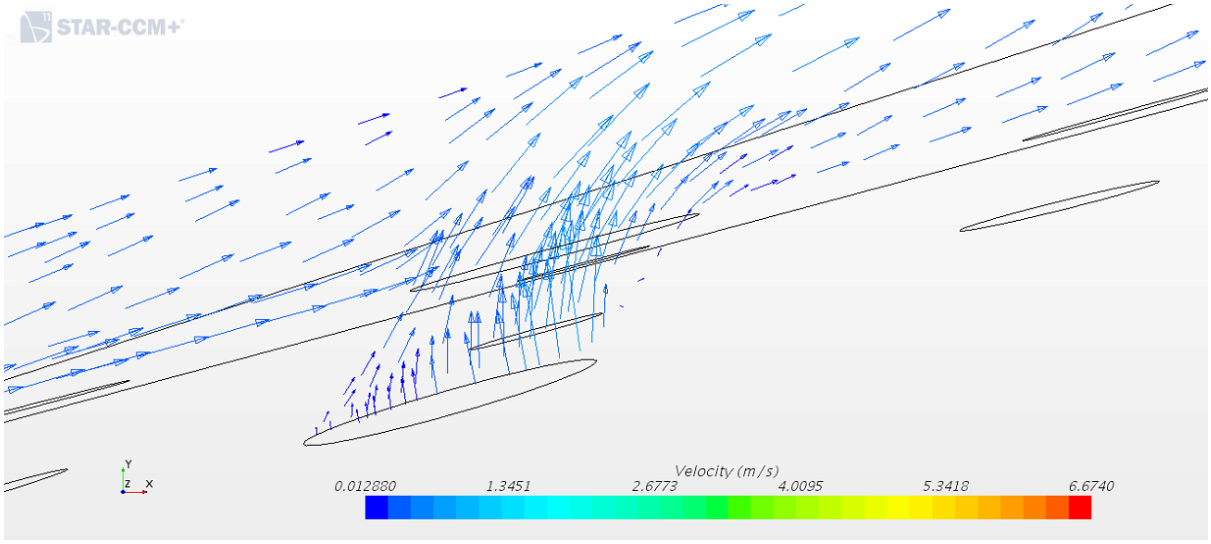

Figure B.4: Velocity vectors through the 40° vent at 1000 W/m^2

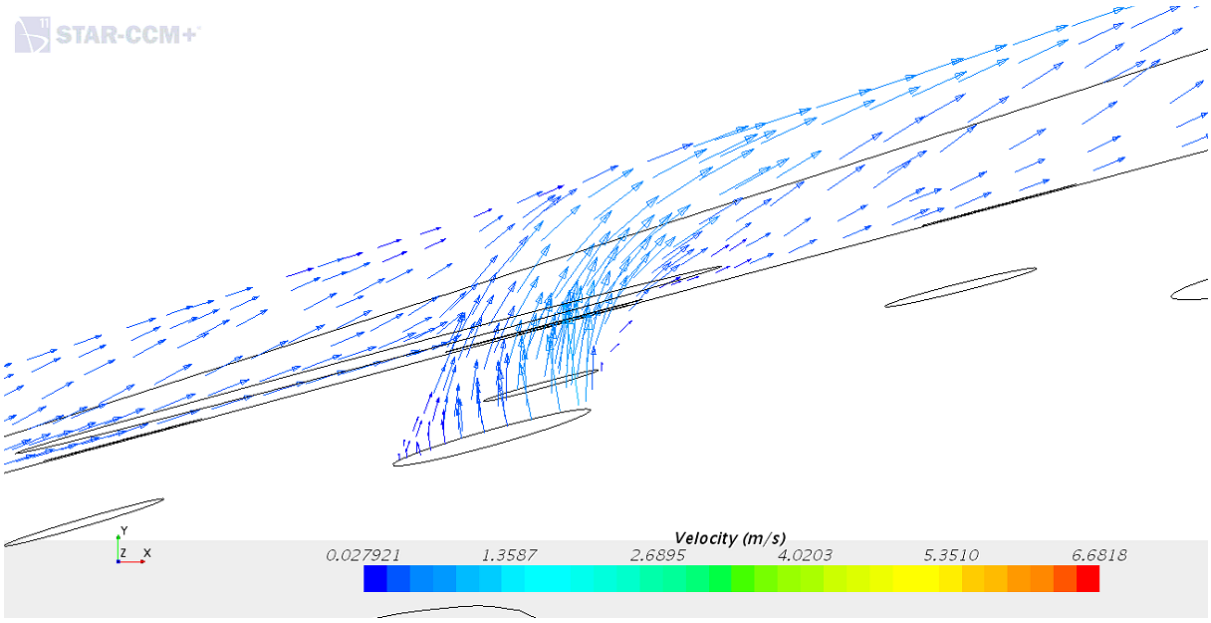

Figure B.5: Velocity vectors through the 50° vent at 1000 W/m^2

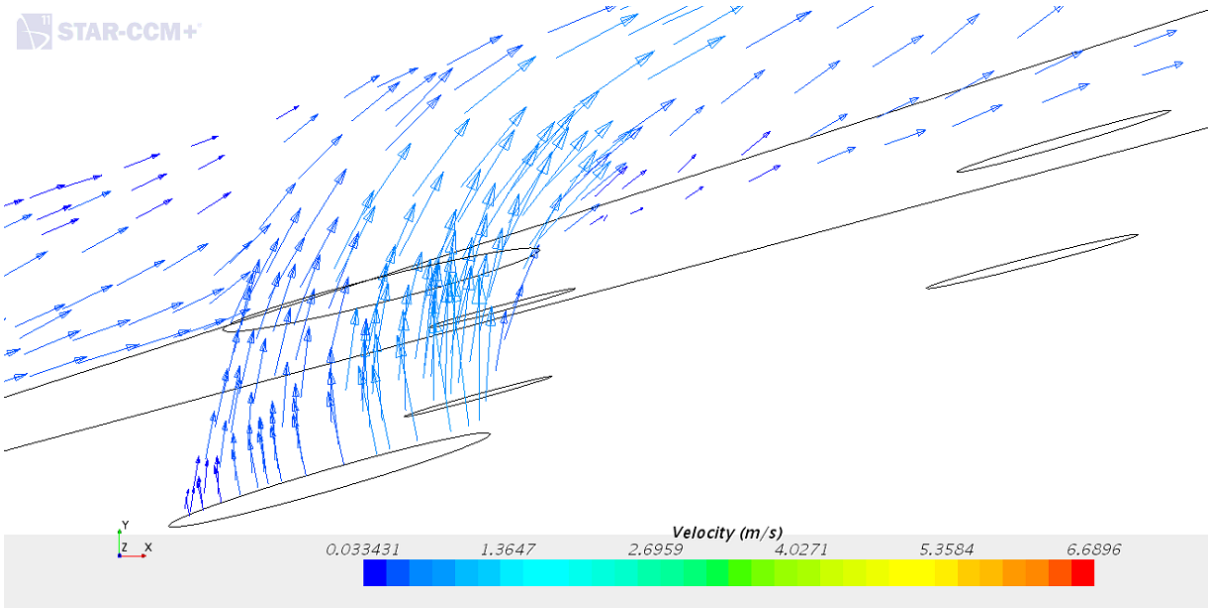

Figure B.6: Velocity vectors through the 60° vent at 1000 W/m^2

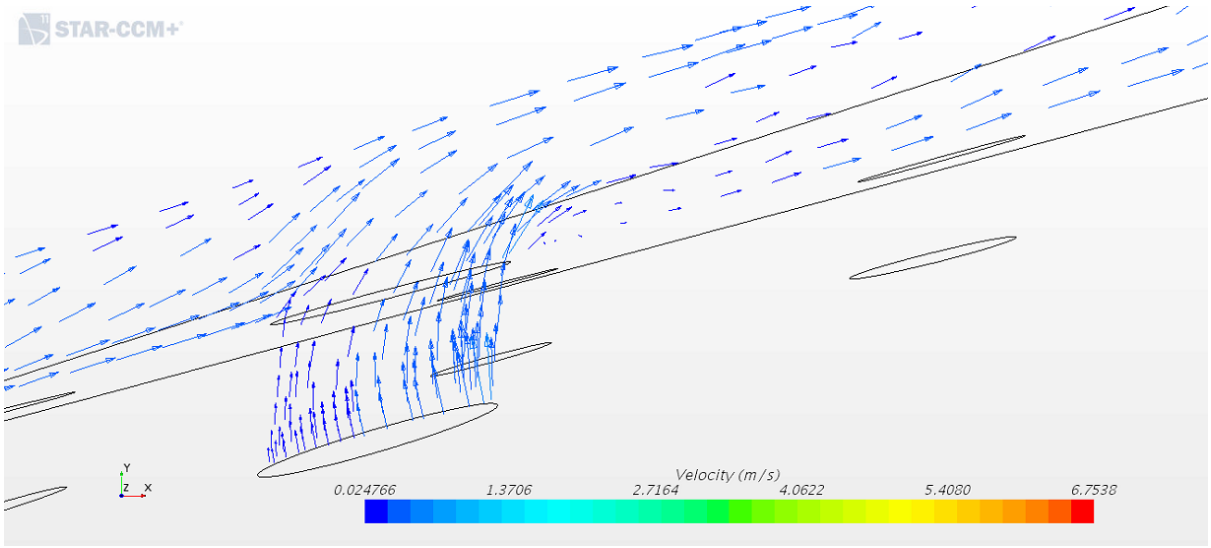

Figure B.7: Velocity vectors through the 70° vent at 1000 W/m^2

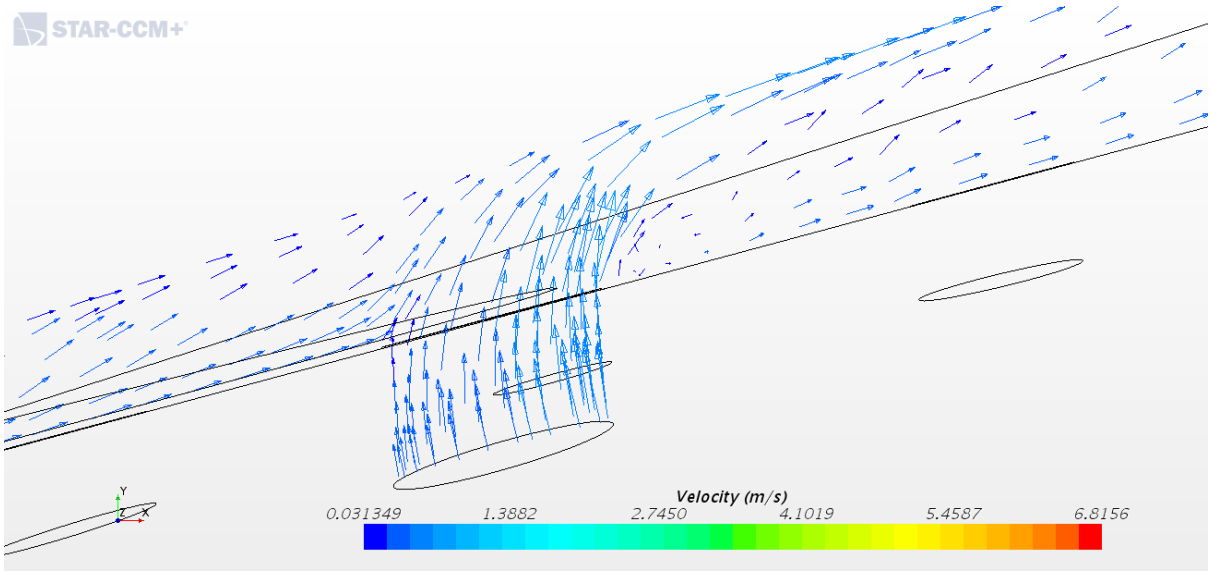

Figure B.8: Velocity vectors through the 80° vent at 1000 W/m^2

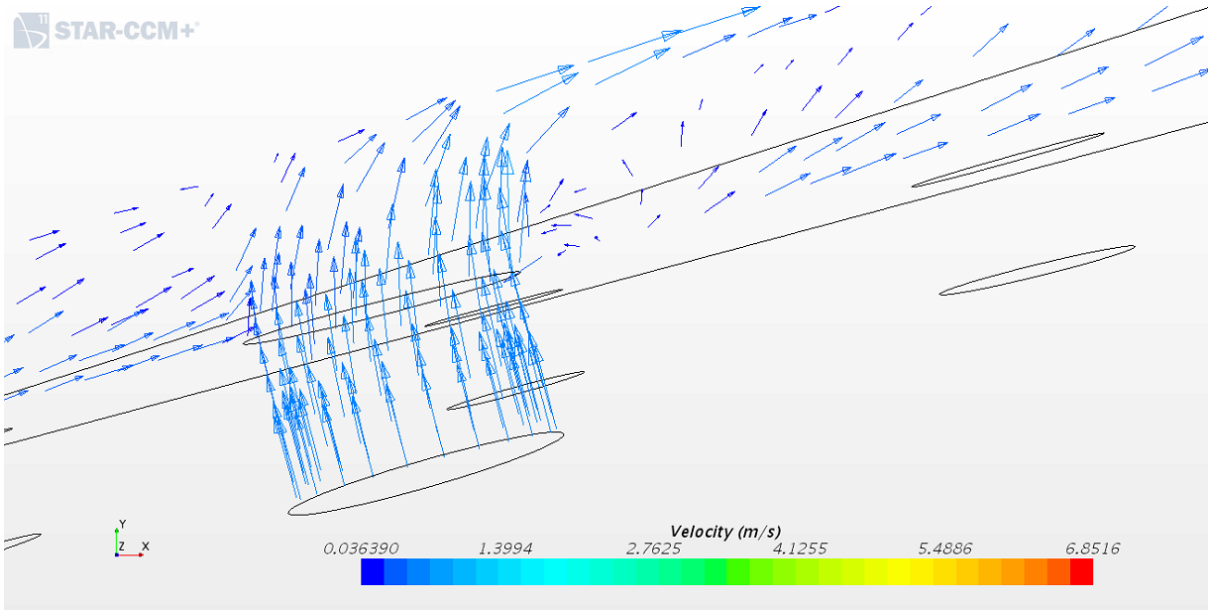

Figure B.9: Velocity vectors through the 90° vent at 1000 W/m^2

Appendix C

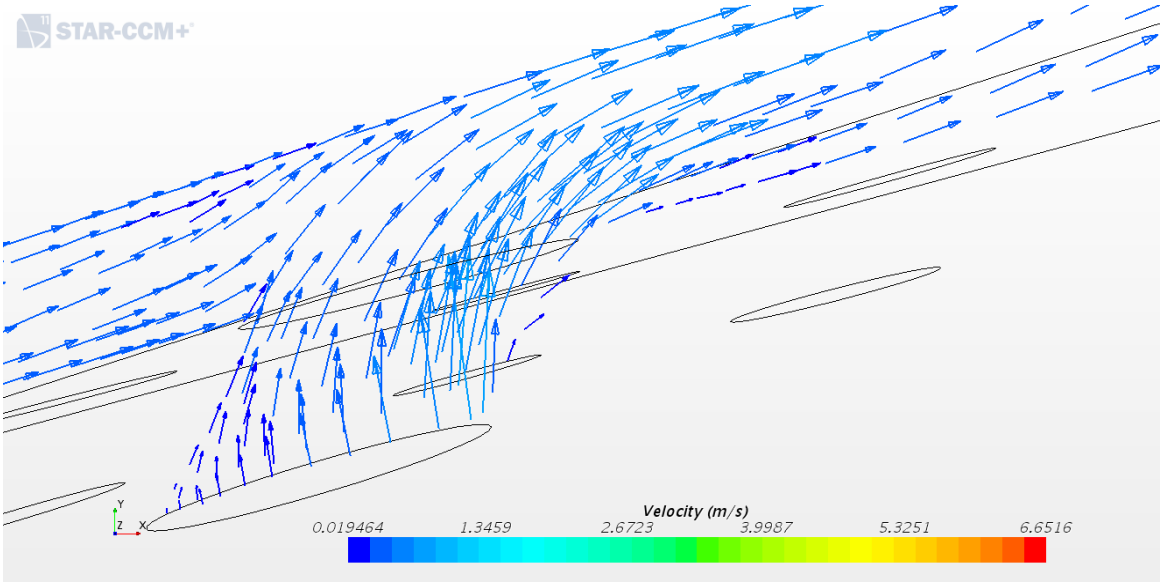

Figure C.1: Velocity Vectors for the Vents at 0 to 4 m Position

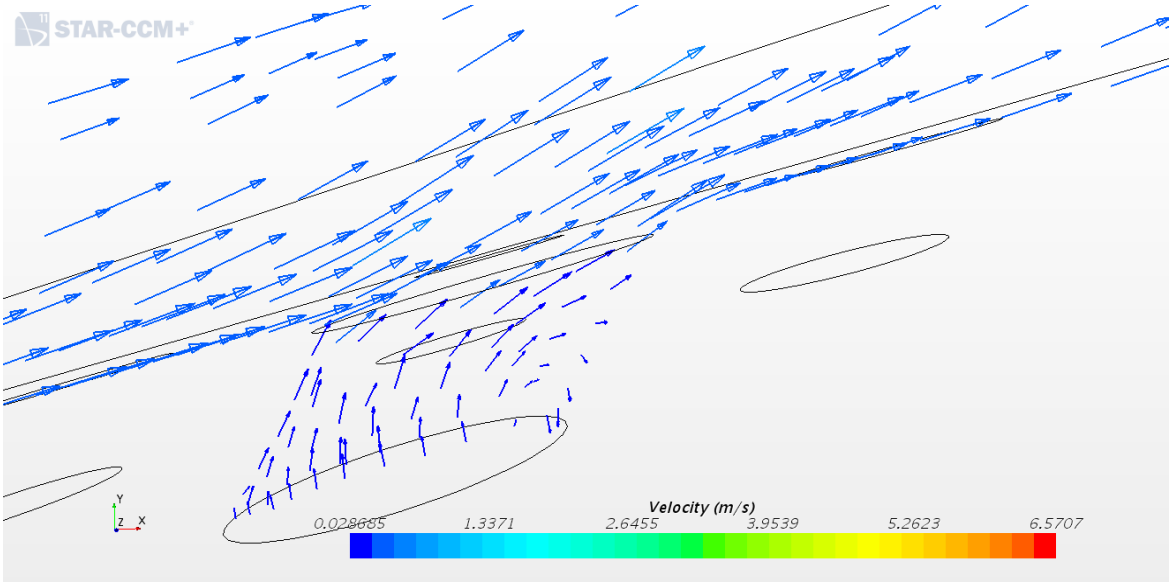

Figure C.2: Velocity Vectors for the Vents at 4 m to 8 m Position

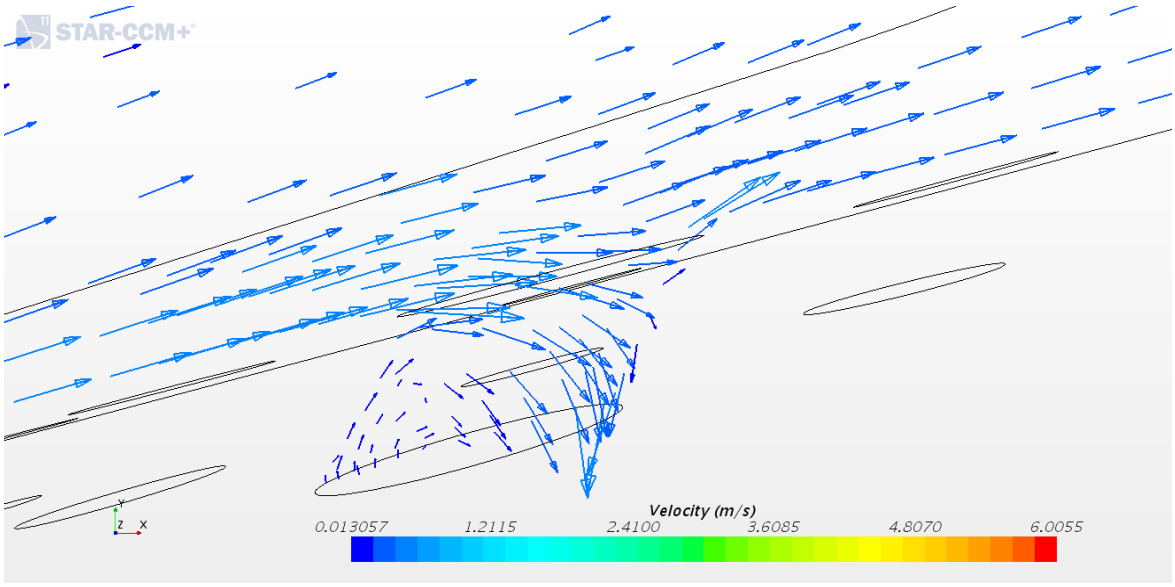

Figure C.3: Velocity Vectors for the Vents at 8 m to 12 m Position

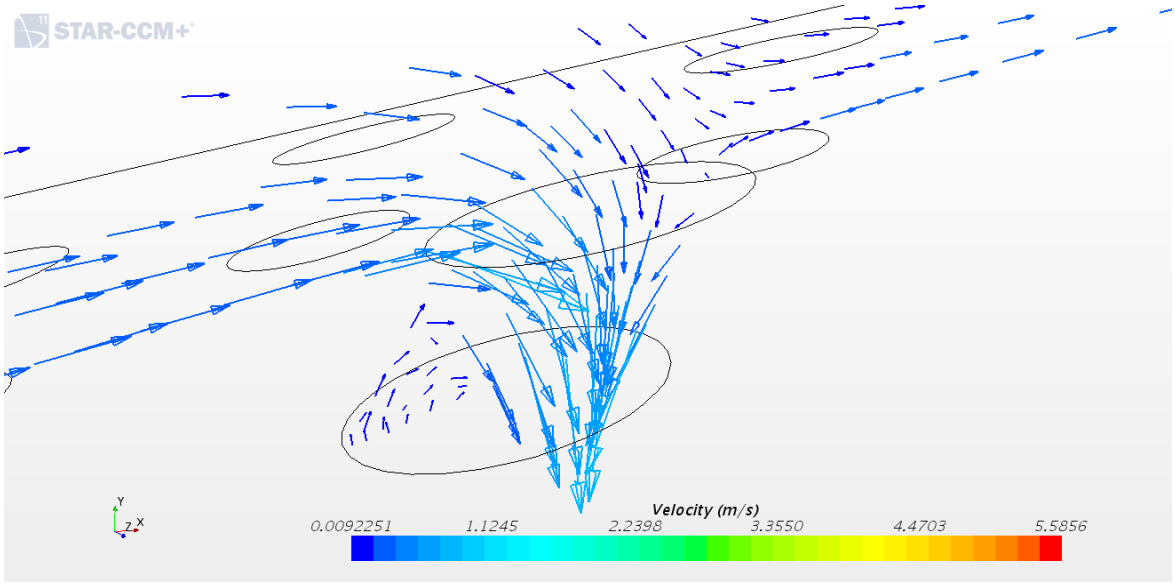

Figure C.4: Velocity Vectors for the Vents at 12 m to 16 m Position

Appendix D

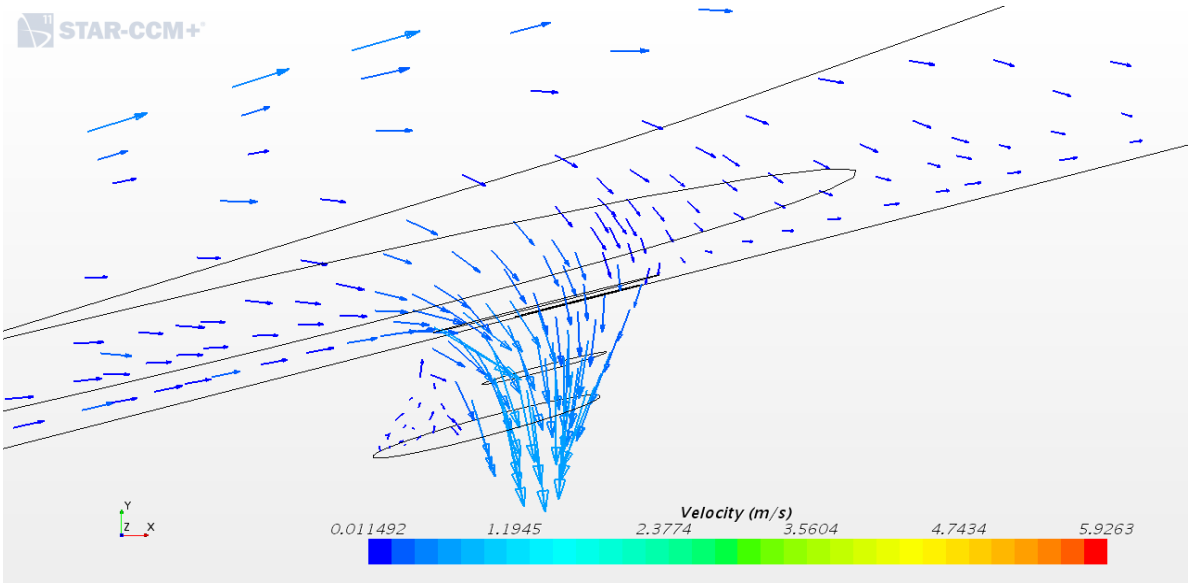

Figure D.1: Velocity vectors for the Inclined SCPP with 0.5 m chimney diameter

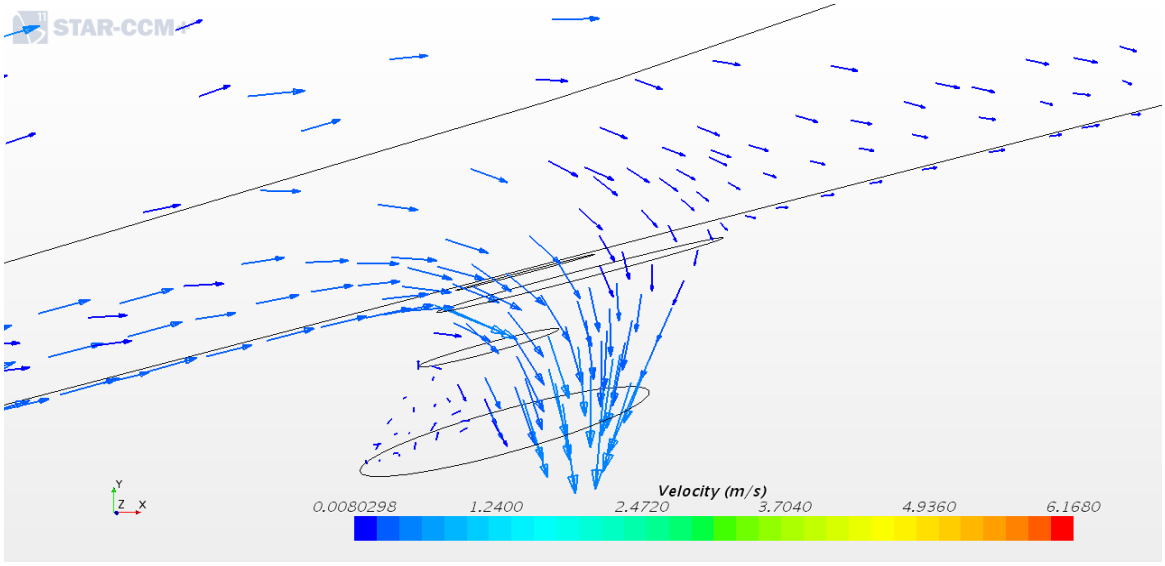

Figure D.2: Velocity vectors for the Inclined SCPP with 0.6 m chimney diameter

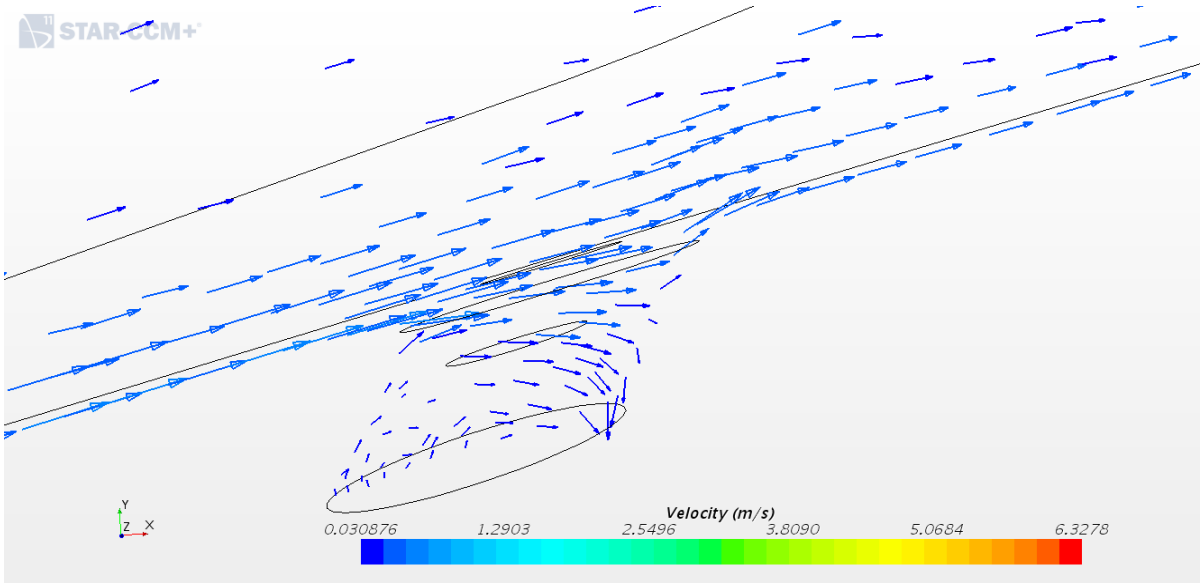

Figure D.3: Velocity vectors for the Inclined SCPP with 0.7 m chimney diameter

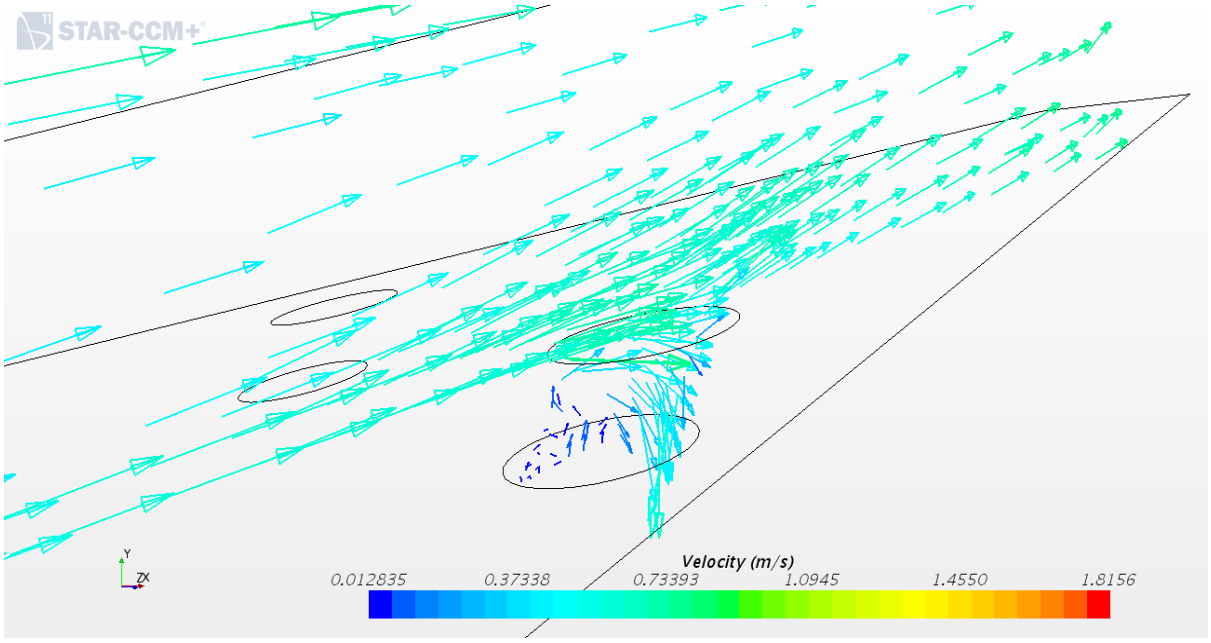

Figure D.4: Velocity vectors for the Inclined SCPP with 0.8 m chimney diameter

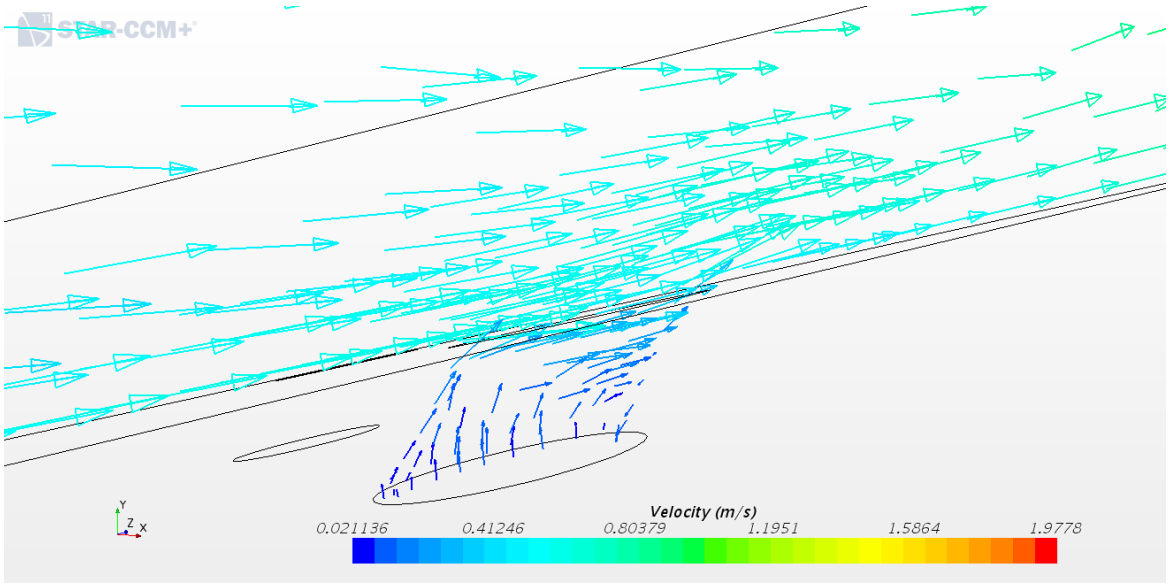

Figure D.5: Velocity vectors for the Inclined SCPP with 0.9 m chimney diameter

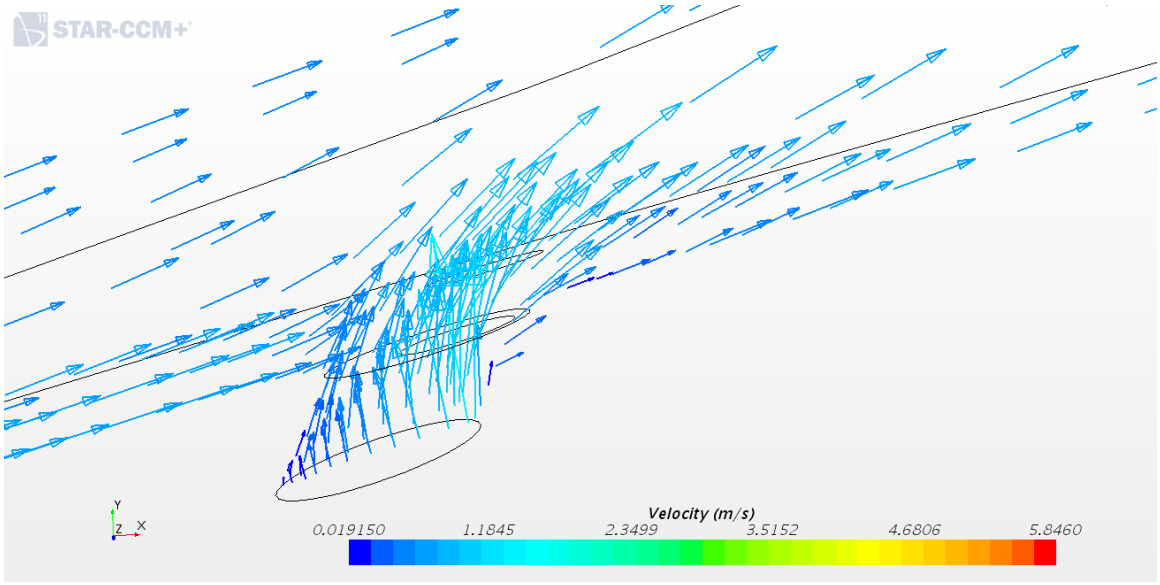

Figure D.6: Velocity vectors for the Inclined SCPP with 1.0 m chimney diameter

Appendix E

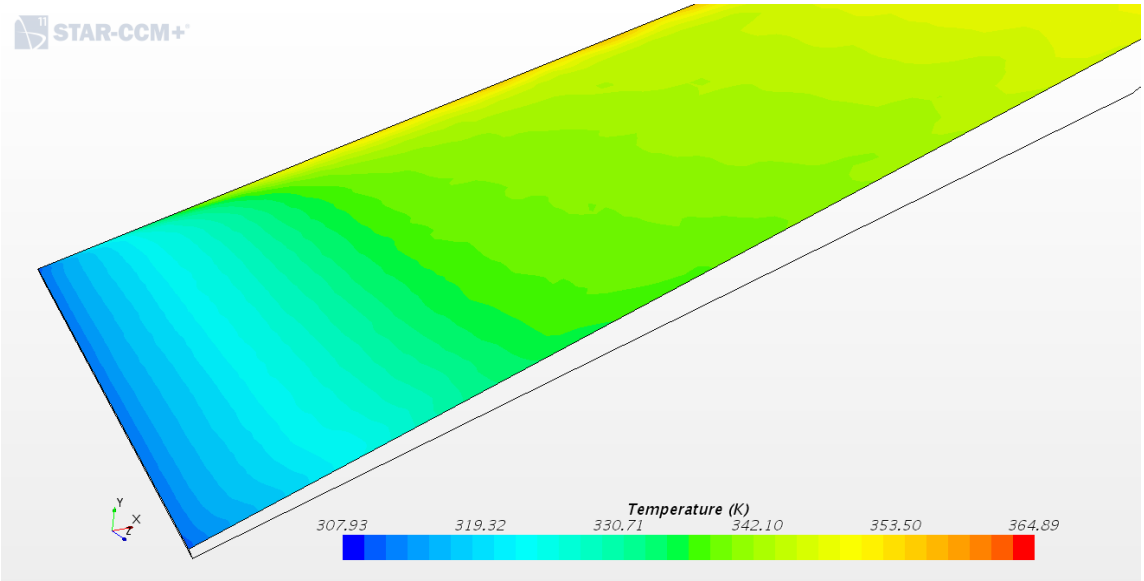

Figure E.1: Temperature Contour of the Transparent Cover of the System without Vents

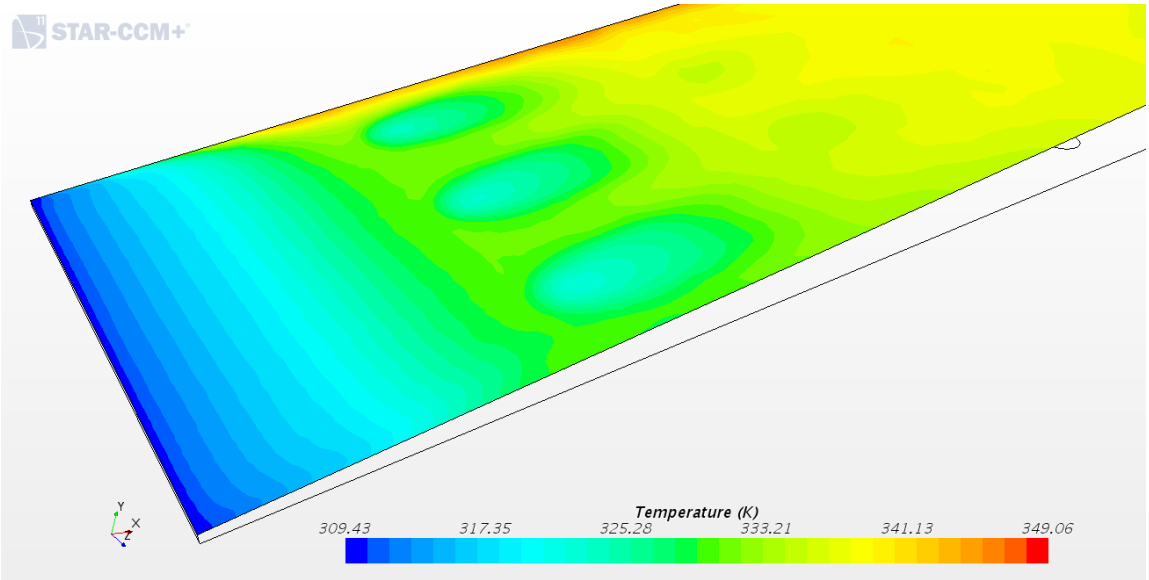

Figure E.2: Temperature Contour of the Transparent Cover of the System with Vents

Appendix F

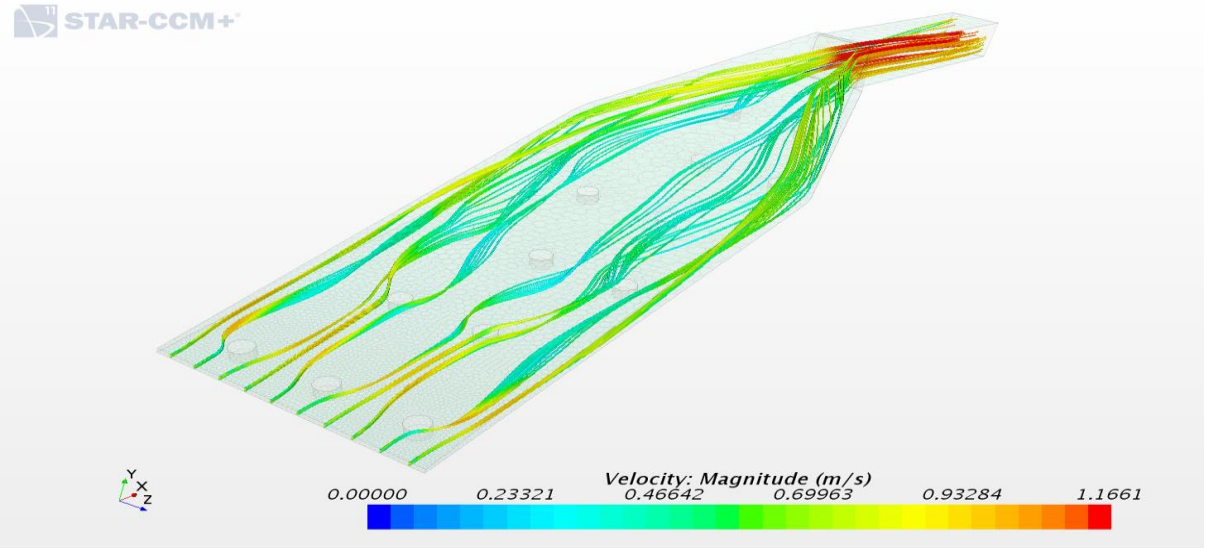

Figure F.1: Velocity Streamlines for Design A

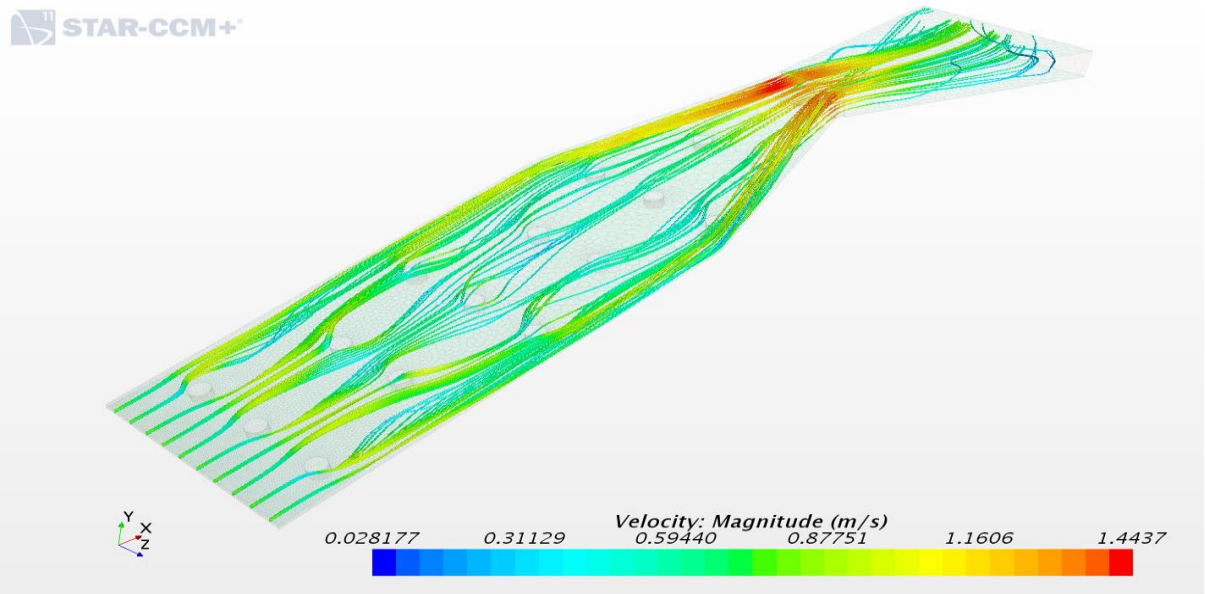

Figure F.2: Velocity Streamlines for Design B

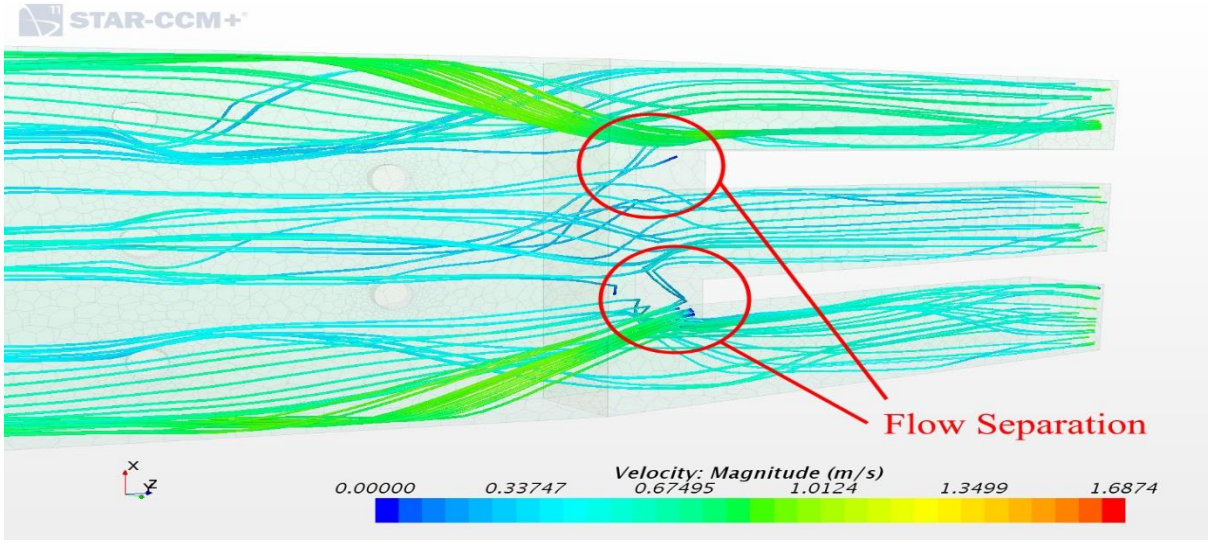

Figure F.3: Velocity Streamlines for Design C

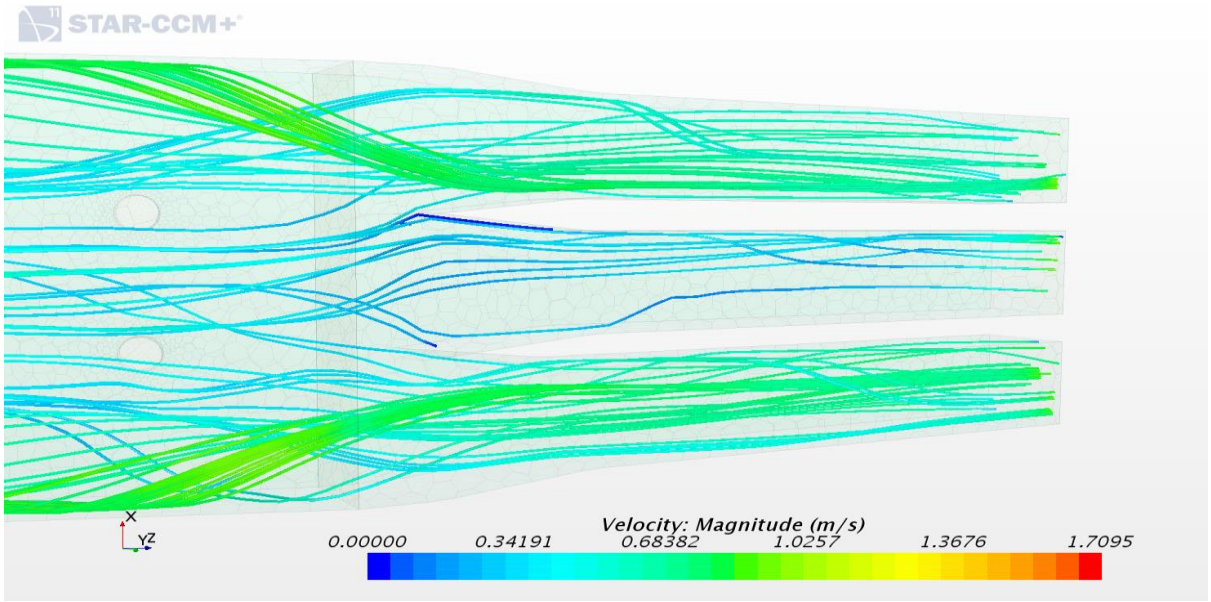

Figure F.4: Velocity Streamlines for Design D